University of Southampton
Faculty of Engineering
Department of Electronics and Computer Science
Southampton S017 1BJ

Coded Modulation Schemes For Wireless Channels

by

Soon Xin NG
B. Eng.

A doctoral thesis submitted in partial fulfilment of the
requirements for the award of Doctor of Philosophy
at the University of Southampton

October 2002

SUPERVISOR: *Professor Lajos Hanzo*
Dipl Ing, MSc, PhD, SMIEEE
Chair of Telecommunications
Department of Electronics and Computer Science
University of Southampton
Southampton SO17 1BJ
United Kingdom

UNIVERSITY OF SOUTHAMPTON

ABSTRACT

FACULTY OF ENGINEERING AND APPLIED SCIENCE
DEPARTMENT OF ELECTRONICS AND COMPUTER SCIENCE

Doctor of Philosophy

Coded Modulation Schemes For Wireless Channels

by Soon Xin Ng

In this thesis coded modulation schemes designed for transmission over mobile wireless fading channels are proposed and investigated. Specifically, coded modulation is a bandwidth efficient scheme, where the redundancy introduced by the channel coding scheme used does not expand the required bandwidth, since the parity bits are absorbed by the extended modulated signal constellation. Coded modulation schemes were designed for transmission over both Additive White Gaussian Noise (AWGN) channels and narrowband fading channels. However, typical mobile wireless channels are dispersive, where the employment of the conventional coded modulation scheme alone may be insufficient for achieving a coding gain. In this thesis, the employment of coded modulation in the context of conventional Decision Feedback Equalisers (DFE), Radial Basis Function (RBF) based equalisers and Orthogonal Frequency Division Multiplexing (OFDM) is investigated. Furthermore, coded modulation is also being investigated in a Code-Division Multiple Access (CDMA) environment, in the context of both DFE based Multi-User Detection (MUD) as well as Genetic Algorithm (GA) assisted MUD.

Another means of mitigating the effect of wideband fading channels is employing adaptive modulation techniques. More specifically, a higher-order modulation mode is employed, when the instantaneous estimated channel quality is high in order to increase the number of bits per symbol transmitted and, conversely, a more robust lower-order modulation mode is used when the instantaneous channel quality is low, in order to improve the mean Bit Error Rate (BER) performance. In this thesis, adaptive coded modulation schemes are investigated in the context of both conventional DFE schemes and DFE based MUD aided CDMA schemes. Turbo equalisation (TEQ) is another technique of mitigating the effects of wideband fading channels. Specifically, TEQ is a joint channel equalisation and channel decoding scheme, where the equaliser is fed by both the channel outputs and by the soft decisions provided by the channel decoder. This process is then invoked in a number of iterations. In this study coded modulation schemes are also amalgamated with the proposed RBF-based TEQ and with an RBF-based reduced complexity In-phase(I)/Quadrature-phase(Q) TEQ.

Finally, coded modulation is proposed for increasing the achievable diversity gain when communicating over fading channels. Specifically, IQ-interleaved coded modulation is introduced and investigated in the context of Space Time Block Coding (STBC) schemes as well as in Rake receiver based CDMA schemes. Explicitly, IQ-interleaved coded modulation is capable of achieving a novel type of diversity, namely IQ diversity, while STBC is well known for attaining both transmit and time diversity, while the Rake receiver employed is useful for achieving multipath diversity.

List of Publications

1. **S. X. Ng, T. H. Liew, L-L. Yang, L. Hanzo**, "Binary BCH Turbo Coding Performance: Union Bound and Simulation Results", Proceedings of IEEE Vehicular Technology Conference (VTC) Spring, Tokyo, Japan, May 2000, pp. 849-853.

2. **S. X. Ng, T. H. Liew, L-L. Yang and L. Hanzo**, "Comparative Study of TCM, TTCM, BICM and BICM-ID schemes", Proceedings of IEEE VTC Spring, Rhodes, Greece, May 2001, pp. 2450-2454.

3. **C. S. Lee, S. X. Ng, L. Piazzo and L. Hanzo**, "TCM, TTCM, BICM and Iterative BICM Assisted OFDM-Based Digital Video Broadcasting to Mobile Receivers", Proceedings of IEEE VTC Spring, Rhodes, Greece, May 2001, pp. 732-736.

4. **S. X. Ng, C. H. Wong and L. Hanzo**, "Burst-by-Burst Adaptive Decision Feedback Equalized TCM, TTCM, BICM and BICM-ID", Proceedings of International Conference on Communications (ICC), Helsinki, Finland, June 2001, pp. 3031-3035.

5. **P. Cherriman, S. X. Ng and L. Hanzo**, "Near-Instantaneously Adaptive Decision Feedback Equalized Coded Modulation for Wireless Video Telephony", Proceedings of IEEE Eurocon 2001, Bratislava, Slovak Republic, July 2001, pp. 6-10.

6. **S. Vlahoyiannatos, S. X. Ng and L. Hanzo**, "Combined Trellis-Coded Modulation and Blind Turbo Equalisation", Proceedings of IEEE Eurocon 2001, Bratislava, Slovak Republic, July 2001, pp. 508-512.

7. **S. X. Ng, E. L. Kuan and L. Hanzo**, "TCM, TTCM, BICM and BICM-ID Assisted Joint Detection Based CDMA", Proceedings of IEEE 4th International ITG Conference on Source and Channel Coding, Berlin, Germany, January 2002, pp. 365-369.

8. **J. Y. Chung, S. X. Ng, E. L. Kuan and L. Hanzo**, "Burst-by-burst adaptive coded modulation-aided joint detection-based CDMA for wireless video telephony", Proceedings of IEEE VTC Spring, Birmingham, USA, May 2002, vol. 3, pp. 1317-1321.

9. **S. X. Ng, L.-L. Yang and L. Hanzo**, "Space-time coding-assisted double-spread rake receiver-based cdma for dispersive rayleigh fading environments", Proceedings of IEEE VTC Spring, Birmingham, USA, May 2002, vol. 4, pp. 1670-1674.

10. **M. S. Yee, S. X. Ng and L. Hanzo**, "Iterative radial basis function assisted turbo equalisation of various coded modulation schemes", Proceedings of IEEE VTC Spring, Birmingham, USA, May 2002, vol. 4, pp. 1705-1709.

11. **S. X. Ng, K. Yen and L. Hanzo**, "TTCM Assisted Genetic-Algorithm Aided Reduced-complexity Multiuser Detection", IEE Electronics Letters, 4th of July, 2002, Vol. 38, No. 4, pp. 722-724.

12. **S. X. Ng, K. Yen and L. Hanzo**, "Coded Modulation Assisted Genetic Algorithm Based Multiuser Detection for CDMA Systems", Proceedings of Wireless 2002, Calgary, Canada, July 8-10, 2002, pp. 429-433.

13. **S. X. Ng, T. H. Liew, B. L. Yeap, E. L. Kuan and L. Hanzo**, "Single-Carrier Space-Time Trellis and Space-Time Block Coding for Dispersive Rayleigh Fading Channels", Proceedings of IEEE VTC Fall, Vancouver, Canada, September 24-28, 2002, vol. 3, pp. 1902-1906.

14. **S. X. Ng and L. Hanzo**,"Space-Time IQ-interleaved TCM and TTCM for AWGN and Rayleigh Fading Channels", IEE Electronics Letters, 21st of November, 2002, Vol. 38, No. 24, pp. 1553-1555.

15. **S. X. Ng, C. H. Wong and L. Hanzo**, "Section 5.11: Burst-by-Burst Adaptive Wideband Coded Mofulation" of **L. Hanzo and C. H. Wong and M. S. Yee**, "Adaptive Wireless Transceivers: Turbo-Coded, Turbo-Equalized and Space-Time Coded TDMA, CDMA and OFDM Systems", New York, USA: John Wiley, IEEE Press, 2002, pp. 173-186.

16. **S. X. Ng, and L. Hanzo**, "Chapter 9: Coded Modulation Theory and Performance" of **L. Hanzo, T.H. Liew and B.L. Yeap**, "Turbo Coding, Turbo Equalisation and Space Time Coding for Transmission over Wireless channels", New York, USA: John Wiley, IEEE Press, 2002, pp. 319-391.

17. **E. L. Kuan, S. X. Ng and L. Hanzo**, "Joint-detection and Interference Cancellation Based Burst-by-burst Adaptive CDMA Schemes", *accepted for* IEEE Transactions on Vehicular Technology.

18. **S. X. Ng, K. Yen and L. Hanzo**, "M-ary Coded Modulation Assisted Genetic Algorithm Based Multiuser Detection for CDMA Systems", *accepted for* IEEE Proceedings of Wireless Communications and Networking Conference (WCNC) 2003, New Orleans, Louisiana, USA, March 17-19, 2003.

19. **M. S. Yee, S. X. Ng and L. Hanzo**, "Radial Basis Function Assisted Reduced Complexity In-phase/Quadrature-phase Turbo Equalisation of Coded Modulation Schemes ", *accepted for* IEEE VTC 2003 Spring, Jeju, Korea, April 21-24, 2003.

20. **F. Guo, S. X. Ng and L. Hanzo**, "LDPC assisted Block Coded Modulation for Transmission over Rayleigh Fading Channels ", *accepted for* IEEE VTC 2003 Spring, Jeju, Korea, April 21-24, 2003.

21. **S. X. Ng and L. Hanzo**, "Space-Time Block Coded IQ-interleaved Joint Coding and Modulation for AWGN and Rayleigh Fading Channels", *accepted for* IEEE VTC 2003 Spring, Jeju, Korea, April 21-24, 2003.

22. **S. X. Ng, P. Cherriman and L. Hanzo** , "Burst-by-Burst Adaptive Decision Feedback Equalised TCM, TTCM and BICM for H.263-Assisted Wireless Video Telephony ", *submitted to* IEEE Transactions on Vehicular Technology.

23. **S. X. Ng, M. S. Yee, and L. Hanzo**, "Coded Modulation Assisted Radial Basis Function Aided Turbo Equalisation for Dispersive Rayleigh Fading Channels", *submitted to* IEEE Transactions on Wireless Communications.

Contents

Abstract ii

List of Publications iii

1 Introduction 1

1.1 A Historical Perspective on Coded Modulation 2

1.2 Organisation of Thesis and Novel Contributions 3

2 Coded Modulation Theory 6

2.1 Introduction 6

2.2 Trellis-Coded Modulation 7

2.2.1 TCM Principle 8

2.2.2 Optimum TCM Codes 13

2.2.3 TCM Code Design for Fading Channels 14

2.2.4 Set Partitioning 16

2.3 The Symbol-based MAP Algorithm 17

2.3.1 Problem Description 17

2.3.2 Detailed Description of the Symbol-based MAP Algorithm 20

2.3.3 Recursive Metric Update Formulae 22

2.3.3.1 Backward Recursive Computation of $\beta_k(i)$ 23

2.3.3.2 Forward Recursive Computation of $\alpha_k(i)$ 24

2.3.4 The MAP Algorithm in the Logarithmic-Domain 25

2.3.5 Symbol-based MAP Algorithm Summary 26

2.4 Turbo Trellis-Coded Modulation 28

2.4.1 TTCM Encoder 28

2.4.2 TTCM Decoder 30

2.5 Bit-Interleaved Coded Modulation . . . 33
2.5.1 BICM Principle . . . 34
2.5.2 BICM Coding Example . . . 37
2.6 Bit-Interleaved Coded Modulation with Iterative Decoding . . . 40
2.6.1 Labelling Method . . . 40
2.6.2 Interleaver Design . . . 42
2.6.3 BICM-ID Coding Example . . . 42
2.7 Conclusions . . . 45

3 Coded Modulation Performance in Non-dispersive Propagation Environments 46
3.1 Introduction . . . 46
3.2 Coded Modulation in Narrowband Channels . . . 46
3.2.1 System Overview . . . 46
3.2.2 Simulation Results and Discussions . . . 48
3.2.2.1 Performance over AWGN Channels . . . 49
3.2.2.2 Performance over Uncorrelated Narrowband Rayleigh Fading Channels 52
3.2.2.3 Coding Gain versus Complexity and Interleaver Block Length . . . 55
3.2.3 Conclusions . . . 59
3.3 Orthogonal Frequency Division Multiplexing . . . 59
3.3.1 Orthogonal Frequency Division Multiplexing Principle . . . 60
3.4 Coded Modulation Assisted Orthogonal Frequency Division Multiplexing . . . 61
3.4.1 Introduction . . . 61
3.4.2 System Overview . . . 63
3.4.3 Simulation Parameters . . . 64
3.4.4 Simulation Results And Discussions . . . 65
3.4.5 Conclusions . . . 67
3.5 Chapter Conclusions . . . 68

4 Coded Modulation Assisted Channel Equalised Systems 71
4.1 Introduction . . . 71
4.2 Intersymbol Interference . . . 72
4.3 Decision Feedback Equaliser . . . 72
4.3.1 Decision Feedback Equaliser Principle . . . 73

4.3.2 Equaliser Signal To Noise Ratio Loss . . . 75
4.4 Decision Feedback Equaliser Aided Adaptive Coded Modulation . . . 76
4.4.1 Introduction . . . 76
4.4.2 System Overview . . . 77
4.4.3 Fixed-Mode Based Performance . . . 80
4.4.4 System I and System II Performance . . . 83
4.4.5 Conclusions . . . 86
4.5 Radial Basis Function based Equalisation . . . 86
4.5.1 RBF based Equaliser Principle . . . 88
4.6 Turbo Equalisation using Symbol-based MAP Decoder . . . 91
4.6.1 Principle of Turbo Equalisation using Symbol-based MAP Decoder . . . 92
4.7 RBF Assisted Turbo Equalisation of Coded Modulation Schemes . . . 94
4.7.1 System Overview . . . 94
4.7.2 Simulation Results and Discussions . . . 96
4.7.3 Conclusions . . . 100
4.8 In-phase/Quadrature-phase Turbo Equalisation . . . 101
4.8.1 In-phase/Quadrature-phase Turbo Equalisation Principle . . . 103
4.9 RBF Assisted Reduced Complexity I/Q Turbo Equalisation of CM Schemes . . . 104
4.9.1 System Overview . . . 104
4.9.2 Simulation Results and Discussions . . . 105
4.9.3 Conclusions . . . 110
4.10 Chapter Conclusions . . . 111

5 Coded Modulation Assisted Code-Division Multiple Access 115

5.1 Introduction . . . 115
5.2 CM Assisted JD-MMSE-DFE Based CDMA . . . 116
5.2.1 The JD-MMSE-DFE Subsystem . . . 116
5.2.1.1 DS-CDMA System Model . . . 116
5.2.1.2 Minimum Mean Square Error Decision Feedback Equaliser Based Joint Detection Algorithm . . . 118
5.2.1.3 Algorithm Summary . . . 121
5.2.2 Simulation Parameters . . . 122
5.2.3 Simulation Results and Discussions . . . 123

5.2.4 Conclusions . . . 126
5.3 Adaptive CM Assisted JD-MMSE-DFE Based CDMA . . . 126
5.3.1 Modem Mode Adaptation . . . 127
5.3.2 Channel Model and System Parameters . . . 129
5.3.3 Performance of the Fixed Modem Modes . . . 132
5.3.4 Adaptive Modes Performance . . . 134
5.3.5 Effects of Estimation Delay and Switching Thresholds . . . 135
5.3.6 Conclusions . . . 137
5.4 CM Assisted GA Based CDMA . . . 138
5.4.1 Introduction . . . 138
5.4.2 System Overview . . . 138
5.4.3 The GA-assisted Multiuser Detector Subsystem . . . 141
5.4.4 Simulation Parameters . . . 144
5.4.5 Simulation Results And Discussions . . . 144
5.4.6 Conclusions . . . 148
5.5 Chapter Conclusions . . . 149

6 Coded Modulation Assisted Space Time Block Coding 153

6.1 Introduction . . . 153
6.2 Space-Time Block Coded IQ-Interleaved Coded Modulation . . . 154
6.2.1 Introduction . . . 154
6.2.2 System Overview . . . 154
6.2.3 Simulation Results And Discussions . . . 158
6.2.4 Conclusions . . . 162
6.3 STBC Assisted DoS-RR Based CDMA . . . 163
6.3.1 Introduction . . . 163
6.3.2 System Description . . . 164
6.3.2.1 Double-Spreading Mechanism . . . 165
6.3.2.2 Space-Time Block Coded Rake Receiver . . . 167
6.3.2.3 Channel Model and System Parameter Design . . . 169
6.3.3 Simulation Results And Discussions . . . 169
6.3.4 Conclusions . . . 174
6.4 STBC-IQ-CM assisted DoS-RR based CDMA . . . 176

6.4.1 Introduction 176
6.4.2 System Description 176
6.4.3 Simulation Results And Discussions 177
6.4.4 Conclusions 181
6.5 Chapter Conclusions 181

7 Conclusions and Future Work **185**
7.1 Summary and Conclusions 185
7.2 Suggestions for Future Work 192

List of Symbols **194**

Glossary **198**

Bibliography **202**

Index **214**

Author Index **217**

Chapter 1

Introduction

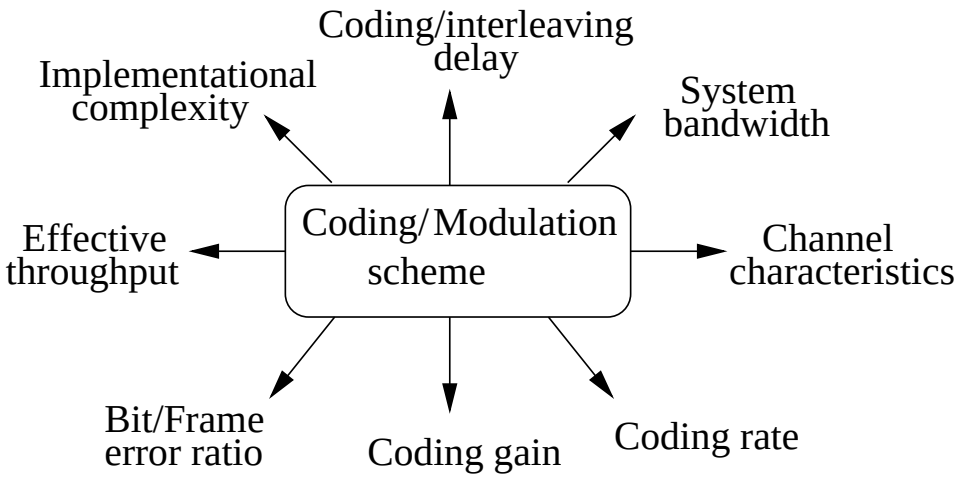

Figure 1.1: Factors affecting the design of channel coding and modulation scheme.

The objective of channel coding is to combat the effects of channel impairment and thereby aid the receiver in its decision making process. The design of a good channel coding and modulation scheme depends on a range of contradictory factors, some of which are portrayed in Figure 1.1. Specifically, given a certain transmission channel, it is always feasible to design a coding and modulation system which is capable of further reducing the Bit Error Ratio (BER) and/or Frame Error Ratio (FER) achieved. The gain quantified in terms of the bit energy reduction at a certain BER/FER, achieved by the employment of channel coding with respect to the uncoded system is termed the coding gain. However, this implies further investments in terms of the required implementational complexity and coding/interleaving delay as well as reducing the effective throughput. Different solutions accrue, when designing a coding and modulation scheme, which aim for optimising different features. For example, in a power-limited scenario, the system's bandwidth can be extended for the sake of accommodating a low rate code. By contrast, the effective throughput of the system can be reduced for the sake of absorbing more parity information. To elaborate further, in a bandwidth-limited and power-limited scenario a more complex, but a higher coding gain code can be employed. The system's effective throughput can be increased by increasing the coding rate at the cost of sacrificing the achievable transmission integrity. The coding and modulation scheme's design also depends on the channel's characteristics. More specifically, the associated bit and frame error statistics change, when the channel exhibits different statistical characteristics.

On the other hand, a joint channel coding and modulation scheme can be designed by employing high rate channel coding schemes in conjunction with multidimensional or high level modulation schemes. In this coded modulation scheme a coding gain may be achieved without bandwidth expansion. In this thesis, a variety of coded modulation assisted systems were proposed and investigated in mobile wireless propagation environments.

1.1 A Historical Perspective on Coded Modulation

The history of channel coding or Forward Error Correction (FEC) coding dates back to Shannon's pioneering work [1] in 1948, in which he showed that it is possible to design a communication system with any desired small probability of error, whenever the rate of transmission is smaller than the capacity of the channel. While Shannon outlined the theory that explained the fundamental limits imposed on the efficiency of communications systems, he provided no insights into how to actually approach these limits. This motivated the search for codes that would produce arbitrarily small probability of error. Specifically, Hamming [2] and Golay [3] were the first to develop practical error control schemes. Convolutional codes [4] were later introduced by Elias in 1955, while Viterbi [5] invented a maximum likelihood sequence estimation algorithm in 1967 for efficiently decoding convolutional codes. In 1974, Bahl proposed the more complex Maximum A-Posteriori (MAP) algorithm, which is capable of achieving the minimum achievable BER.

The first successful application of channel coding was the employment of convolutional codes [4] in deep-space probes in the 1970s. However, for years to come, error control coding was considered to have limited applicability, apart from deep-space communications. Specifically, this is a power-limited scenario, which has no strict bandwidth limitation. By contrast mobile communications systems constitute a power- and bandwidth-limited scenario. In 1987, a bandwidth efficient Trellis Coded Modulation (TCM) [6] scheme employing symbol-based channel interleaving in conjunction with Set-Partitioning (SP) [7] assisted signal labelling was proposed by Ungerböck. Specifically, the TCM scheme, which is based on combining convolutional codes with multidimensional signal sets, constitutes a bandwidth efficient scheme that has been widely recognised as an efficient error control technique suitable for applications in mobile communications [8]. Another powerful coded modulation scheme utilising bit-based channel interleaving in conjunction with Gray signal labelling, which is referred to as Bit-Interleaved Coded Modulation (BICM), was proposed by Zehavi [9] as well as by Caire, Taricco and Biglieri [10]. Another breakthrough in the history of error control coding is the invention of turbo codes by Berrou, Glavieux and Thitimajshima [11] in 1993. Convolutional codes were used as the component codes and decoders based on the MAP algorithm were employed. The results proved that a performance close to the Shannon limit can be achieved in practice with the aid of binary codes. The attractive properties of turbo codes have attracted intensive research in this area [12–14]. As a result, turbo coding has reached a state of maturity within just a few years and was standardised in the recently ratified third-generation (3G) mobile radio systems [15].

However, turbo codes often have a low coding rate and hence require considerable bandwidth expansion. Therefore, one of the objectives of turbo coding research is the design of bandwidth-efficient turbo codes. In order to equip the family of binary turbo codes with a higher spectral efficiency, BICM-based Turbo Coded Modulation (TuCM) [16] was proposed in 1994. Specifically,

TuCM uses a binary turbo encoder, which is linked to a signal mapper, after its output bits were suitably punctured and multiplexed for the sake of transmitting the desired number of information bits per transmitted symbol. In the TuCM scheme of [16] Gray-coding based signal labelling was utilised. For example, two 1/2-rate Recursive Systematic Convolutional (RSC) codes are used for generating a total of four turbo coded bits and this bit stream may be punctured for generating three bits, which are mapped to an 8PSK modulation scheme. By contrast, in separate coding and modulation scheme, any modulation schemes for example BPSK, may be used for transmitting the channel coded bits. Finally, without puncturing, 16QAM transmission would have to be used for maintaining the original transmission bandwidth. Turbo Trellis Coded Modulation (TTCM) [17] is a more recently proposed channel coding scheme that has a structure similar to that of the family of turbo codes, but employs TCM schemes as its component codes. The TTCM symbols are transmitted alternatively from the first and the second constituent TCM encoders and symbol-based interleavers are utilised for turbo interleaving and channel interleaving. It was shown in [17] that TTCM performs better than the TCM and TuCM schemes at a comparable complexity. In 1998, iterative joint decoding and demodulation assisted BICM referred to as BICM-ID was proposed in [18,19], which uses SP based signal labelling. The aim of BICM-ID is to increase the Euclidean distance of BICM and hence to exploit the full advantage of bit interleaving with the aid of soft-decision feedback based iterative decoding [19]. Many other bandwidth efficient schemes using turbo codes have been proposed in the literature [13], but we will focus our study on TCM, BICM, TTCM and BICM-ID schemes in the context of wireless channels in this thesis.

1.2 Organisation of Thesis and Novel Contributions

The outline of the thesis is presented below:

- **Chapter 2:** Four different coded modulation schemes, namely TCM, TTCM, BICM and BICM-ID are introduced. The conceptual differences amongst these four coded modulation schemes are studied in terms of their coding structure, signal labelling philosophy, interleaver type and decoding philosophy. The symbol-based MAP algorithm operating in the logarithmic domain is also highlighted.

- **Chapter 3:** The performance of the above-mentioned coded modulation schemes is studied when communicating over AWGN and narrowband fading channels. Multi-carrier Orthogonal Frequency Division Multiplexing (OFDM) is also combined with the coded modulation schemes designed for communicating over wideband fading channels. With the aid of multi-carrier OFDM the wideband channel is divided into numerous narrowband sub-channels, each associated with an individual OFDM subcarrier. The performance trends of the coded modulation schemes are studied in the context of these OFDM sub-channels and compared in terms of the associated decoding complexity, coding delay and effective throughput under the assumption of encountering non-dispersive channel conditions in each sub-channel.

- **Chapter 4:** The conventional Decision Feedback Equaliser (DFE) and a Radial Basis Function (RBF) based DFE are introduced and combined with the various coded modulation schemes

communicating over wideband fading channels. The concepts of conventional DFE based adaptive modulation as well as RBF-based turbo equalisation and a reduced complexity RBF-based In-phase(I)/Quadrature-phase(Q) turbo equalisation scheme are also presented. We will incorporate the various coded modulation schemes considered into these systems and evaluate their performance in terms of the achievable BER, FER and effective throughput, when assuming a similar bandwidth, coding rate and decoding complexity.

- **Chapter 5:** The performance of the various coded modulation schemes is also evaluated in conjunction with a Direct Sequence (DS) Code-Division Multiple Access (CDMA) system. Specifically, a DFE based Multi-User Detection (MUD) scheme is introduced for assisting the fixed-mode coded modulation schemes as well as the adaptive coded modulation schemes operating in conjunction with DS-CDMA, when communicating over wideband fading channels. The concept of Genetic Algorithm (GA) based MUD is also highlighted, which is invoked in conjunction with the coded modulation schemes for employment in the CDMA system. The performance of this MUD is compared to that of the optimum MUD.

- **Chapter 6:** IQ-interleaved Coded Modulation (IQ-CM) schemes are introduced for achieving IQ diversity. Space Time Block Coding (STBC) is also introduced for attaining additional space/transmit and time diversity. The concept of Double-Spreading aided Rake Receivers (DoS-RR) is proposed for achieving multipath diversity in a CDMA downlink, when transmitting over wideband fading channels. Finally, a STBC based IQ-CM assisted DoS-RR scheme is proposed for attaining transmit-, time-, IQ- and multipath-diversity, in a CDMA downlink, when communicating over wideband fading channels.

- **Chapter 7:** The main findings are summarised and suggestions for future research are presented.

The fundamental motivation and the rationale of the thesis was that of contriving powerful novel coded modulation schemes designed for communicating over dispersive fading channels, which are capable of achieving substantial coding gains without bandwidth expansion in return for an increased implementational complexity. This goal is achieved in a systematic approach by considering a suite of channel-equalised single-carrier, multi-carrier or OFDM as well as multiuser detected CDMA systems.

The research was concluded by systematically designing coded modulation schemes, which are capable of simultaneously attaining transmit diversity, time diversity and a novel type of diversity referred to as IQ-diversity, all in a strict performance versus complexity context.

The novel contributions of the thesis are as follows:

- Four coded modulation schemes were studied comparatively for a novel perspective, by fixing their complexity and evaluating their performance. Specifically, their simulation-based performance was evaluated when communicating over both AWGN and flat uncorrelated Rayleigh fading channels [20]. Furthermore, their performance has also been studied in the context of transmitting over dispersive channels with the aid of a novel coded modulation assisted OFDM scheme [21].

- As another design alternative, an adaptive coded modulation assisted DFE scheme was proposed for transmission over wideband fading channels [22–24]. Specifically, four coded modulation

schemes, namely TCM, TTCM, BICM and BICM-ID, were incorporated into a DFE based adaptive system. Each adaptive coded modulation scheme employed a different coding rate in conjunction with the modulation modes of 4QAM, 8PSK, 16QAM and 64QAM. The coded modulation mode switching criterion was based on the mean-squared error recorded at the output of the classic DFE.

- Coded modulation assisted RBF-based TEQ as well as IQ-TEQ schemes were contrived for transmission over wideband fading channels. Explicitly, an RBF-based TEQ scheme using the symbol-based MAP channel decoder was contrived and the performance of the proposed scheme was evaluated when communicating over wideband fading channels [25–27].

- An adaptive coded modulation assisted JD-DFE based CDMA scheme employing 4QAM, 8PSK, 16QAM and 64QAM was proposed and its performance was evaluated when communicating over the UTRA wideband fading channels [28, 29]. Specifically, the adaptive coded modulation mode switching metric was the JD-DFE's SINR output recorded for each of the users and a bitrate ranging from 23.4 $Kbit/s$ to 117 $Kbit/s$ was achieved under time variant dispersive channel conditions, whilst a near-constant FER was maintained.

- A novel reduced-complexity M-ary coded modulation assisted GA-MUD aided CDMA scheme was introduced and investigated [30–32]. The combination of the GA-MUD with coded modulation resulted in a substantial complexity reduction.

- A range of novel STBC based IQ-interleaved coded modulation schemes were proposed for simultaneously attaining transmit-diversity, time-diversity and IQ-diversity [33, 34]. Specifically, the I and Q components of the complex-valued received signals have been decoupled from each other during the STBC decoding operation and hence the I as well as Q branch metrics can be computed in isolation from each other and deinterleaved for processing by the coded modulation scheme's decoder. A DoS-RR based CDMA scheme [35] was also proposed for assisting the STBC based IQ-CM scheme's operation when communicating over a CDMA downlink in the context of wideband fading channels without sacrificing the attainable diversity gain.

Having presented an overview of the thesis, let us now commence our detailed discourse on coded modulation in the following chapter.

Chapter 2

Coded Modulation Theory

2.1 Introduction

The radio spectrum is a scarce resource. Therefore, one of the most important objectives in the design of digital cellular systems is the efficient exploitation of the available spectrum, in order to accommodate the ever-increasing traffic demands. Trellis-Coded Modulation (TCM) [36], which will be detailed in Section 2.2, was proposed originally for Gaussian channels, but it was further developed for applications in mobile communications [7, 37]. Turbo Trellis-Coded Modulation (TTCM) [38], which will be augmented in Section 2.4, is a more recent joint coding and modulation scheme that has a structure similar to that of the family of power-efficient binary turbo codes [11, 12], but employs TCM schemes as component codes. TTCM [38] requires approximately 0.5 dB lower Signal-to-Noise Ratio (SNR) at a Bit Error Ratio (BER) of 10^{-4} than binary turbo codes when communicating using 8PSK over Additive White Gaussian Noise (AWGN) channels. TCM and TTCM invoked Set Partitioning (SP) based signal labelling, as will be discussed in the context of Figure 2.7 in order to achieve a higher Euclidean distance between the unprotected bits of the constellation, as we will show during our further discourse. It was shown in [36] that parallel trellis transitions can be associated with the unprotected information bits; as we will augment in Figure 2.2(b), this reduced the decoding complexity. Furthermore, in our TCM and TTCM oriented investigations random symbol interleavers, rather than bit interleavers, were utilised, since these schemes operate on the basis of symbol, rather than bit, decisions.

Another coded modulation scheme distinguishing itself by utilising bit-based interleaving in conjunction with Gray signal constellation labelling is referred to as Bit-Interleaved Coded Modulation (BICM) [9]. More explicitly, BICM combines conventional convolutional codes with several independent bit interleavers, in order to increase the achievable diversity order to the binary Hamming distance of a code for transmission over fading channels [9], as will be shown in Section 2.5.1. The number of parallel bit interleavers equals the number of coded bits in a symbol for the BICM scheme proposed in [9]. The performance of BICM is better than that of TCM over uncorrelated or perfectly interleaved narrowband Rayleigh fading channels, but worse than that of TCM in Gaussian channels owing to the reduced Euclidean distance of the bit-interleaved scheme [9], as will be demonstrated in Section 2.5.1. Recently iterative joint decoding and demodulation assisted BICM (BICM-ID) was proposed in an effort to further increase the achievable performance [18, 20–22, 39, 40], which uses

SP-based signal labelling. The approach of BICM-ID is to increase the Euclidean distance of BICM, as will be shown in Section 2.6, and hence to exploit the full advantage of bit interleaving with the aid of soft-decision feedback-based iterative decoding [19].

In this chapter we embark on studying the properties of the above-mentioned TCM, TTCM, BICM and BICM-ID schemes in the context of Phase Shift Keying (PSK) and Quadrature Amplitude Modulation (QAM) schemes. Specifically, the code generator polynomials of 4-level QAM (4QAM) or Quadrature PSK (QPSK), 8-level PSK (8PSK), 16-level QAM (16QAM) and 64-level QAM (64QAM) will be given in Tables 2.1, 2.2, 2.3 and 2.4.

2.2 Trellis-Coded Modulation

The basic idea of TCM is that instead of sending a symbol formed by $\bar{m}$ information bits, for example two information bits for 4PSK, we introduce a parity bit, while maintaining the same effective throughput of 2 bits/symbol by doubling the number of constellation points in the original constellation to eight, i.e. by extending it to 8PSK. As a consequence, the redundant bit can be absorbed by the expansion of the signal constellation, instead of accepting a 50% increase in the signalling rate, i.e. bandwidth. A positive coding gain is achieved when the detrimental effect of decreasing the Euclidean distance of the neighbouring phasors is outweighted by the coding gain of the convolutional coding incorporated.

Ungerböck has written an excellent tutorial paper [6], which fully describes TCM, and which this section is based upon. TCM schemes employ redundant non-binary modulation in combination with a finite state Forward Error Control (FEC) encoder, which governs the selection of the coded signal sequences. Essentially the expansion of the original symbol set absorbs more bits per symbol than required by the data rate, and these extra bit(s) are used by a convolutional encoder which restricts the possible state transitions amongst consecutive phasors to certain legitimate constellations. In the receiver, the noisy signals are decoded by a trellis-based soft-decision maximum likelihood sequence decoder. This takes the incoming data stream and attempts to map it onto each of the legitimate phasor sequences allowed by the constraints imposed by the encoder. The best fitting symbol sequence having the minimum Euclidean distance from the received sequence is used as the most likely estimate of the transmitted sequence.

Simple four-state TCM schemes, where the four-state adjective refers to the number of possible states that the encoder can be in, are capable of improving the robustness of 8PSK-based TCM transmission against additive noise in terms of the required SNR by 3dB compared to conventional uncoded 4PSK modulation. With the aid of more complex TCM schemes the coding gain can reach 6 dB [6]. As opposed to traditional error correction schemes, these gains are obtained without bandwidth expansion, or without the reduction of the effective information rate. Again, this is because the FEC encoder's parity bits are absorbed by expanding the signal constellation in order to transmit a higher number of bits per symbol. The term 'trellis' is used, because these schemes can be described by a state transition diagram similar to the trellis diagrams of binary convolutional codes [41]. The difference is that in the TCM scheme the trellis branches are labelled with redundant non-binary modulation phasors, rather than with binary code symbols.

2.2.1 TCM Principle

We now illustrate the principle of TCM using the example of a four-state trellis code for 8PSK modulation, since this relatively simple case assists us in understanding the principles involved.

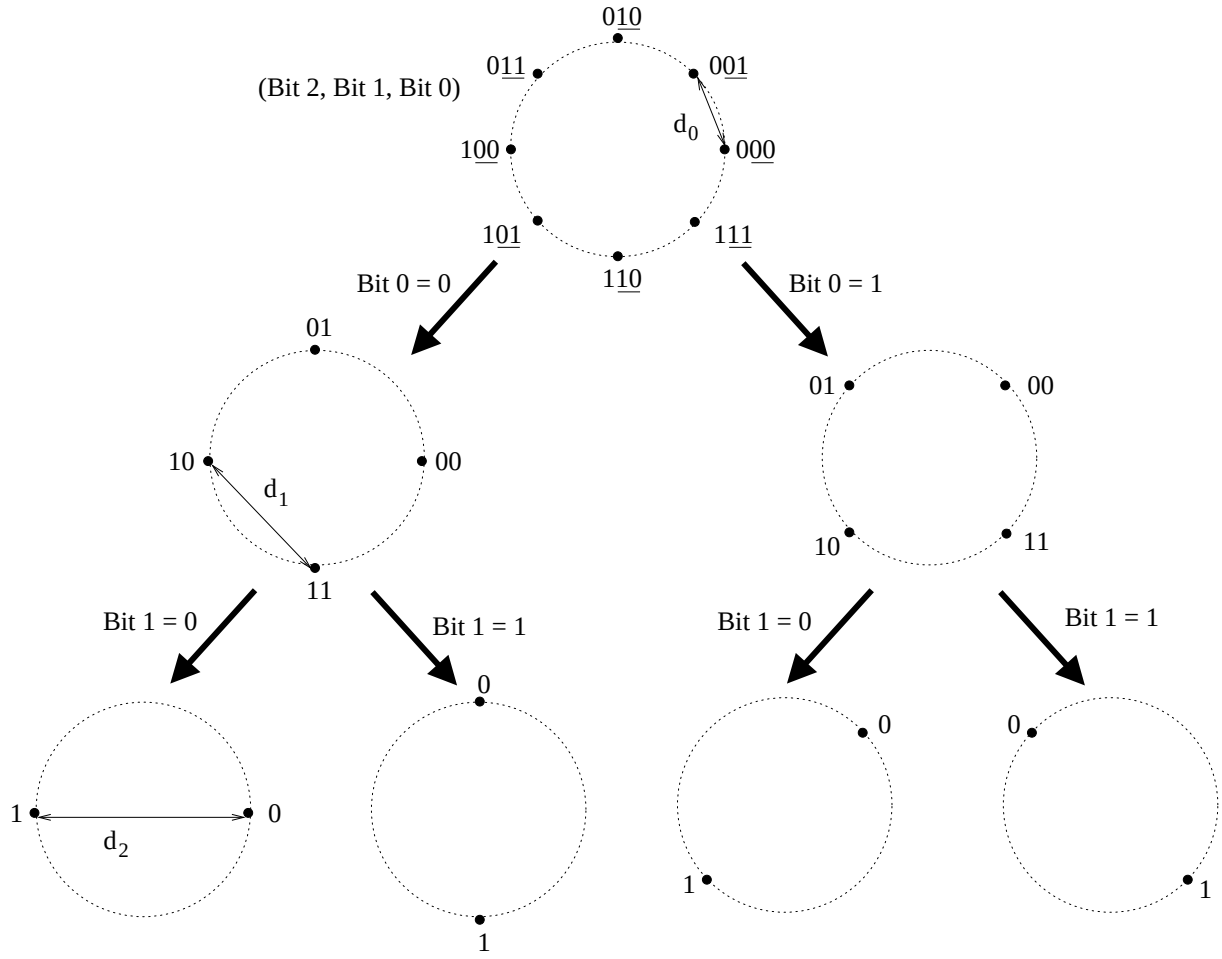

Figure 2.1: 8PSK set partitioning [36] ©IEEE, 1982, Ungerböck.

The partitioned signal set proposed by Ungerböck [6, 36] is shown in Figure 2.1, where the binary phasor identifiers are now not Gray encoded. Observe in the figure that the Euclidean distance amongst constellation points is increased at every partitioning step. The underlined last two bits, namely bit 0 and bit 1, are used for identifying one of the four partitioned sets, while bit 2 finally pinpoints a specific phasor in each partitioned set.

The signal sets and state transition diagrams for (a) uncoded 4PSK modulation and (b) coded 8PSK modulation using four trellis states are given in Figure 2.2, while the corresponding four-state encoder-based modulator structure is shown in Figure 2.3. Observe that after differential encoding bit 2 is fed directly to the 8PSK signal mapper, whilst bit 1 is half-rate convolutionally encoded by a two-stage four-state linear circuit. The convolutional encoder adds the parity bit, bit 0, to the sequence, and again these two protected bits are used for identifying which constellation subset the bits will be assigned to, whilst the more widely spaced constellation points will be selected according to the unprotected bit 2.

The trellis diagram for 4PSK is a trivial one-state trellis, which portrays uncoded 4PSK from the viewpoint of TCM. Every connected path through the trellis represents a legitimate signal sequence

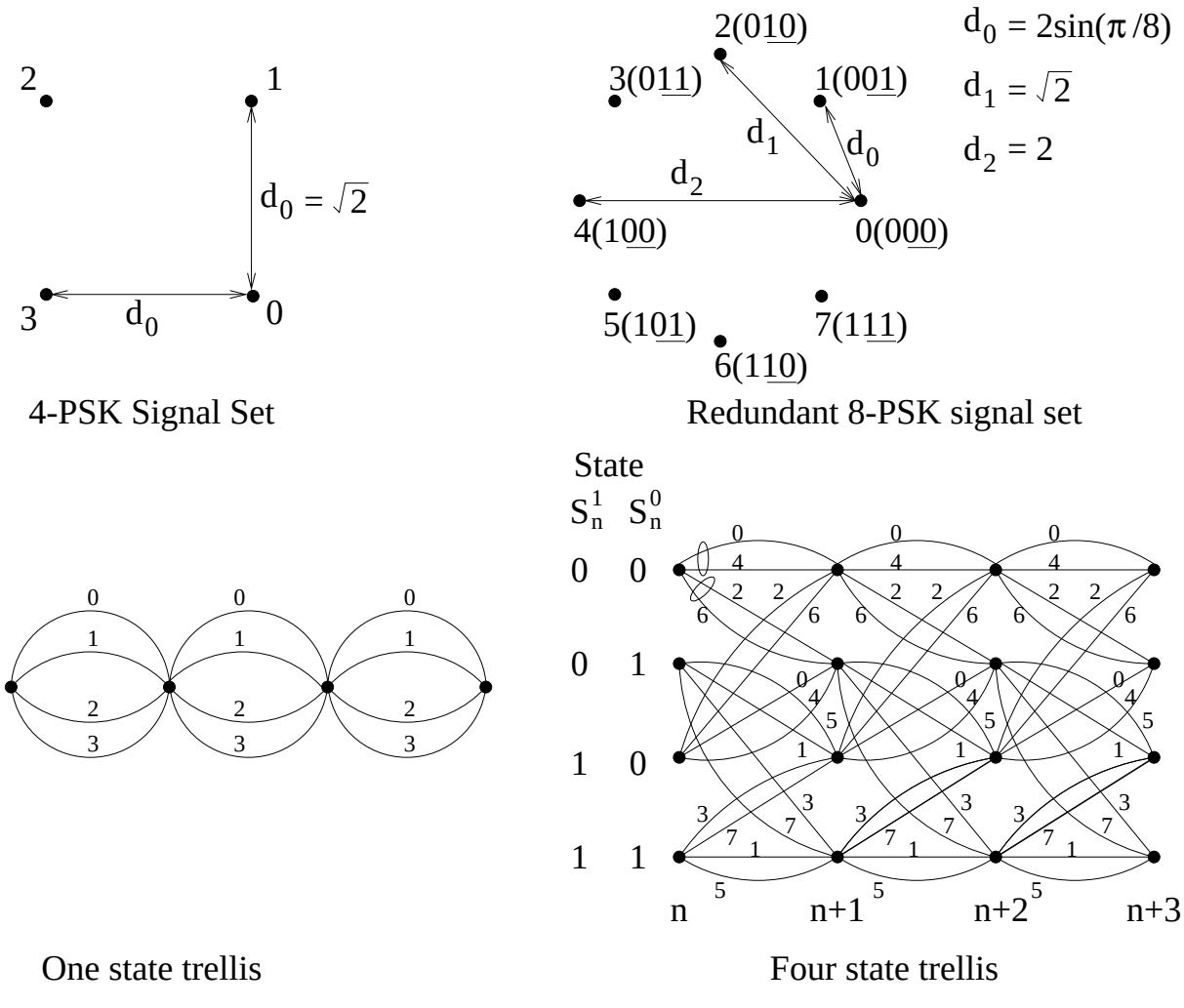

Figure 2.2: Constellation and trellis for 4- and 8PSK [6] ©IEEE, 1982, Ungerböck.

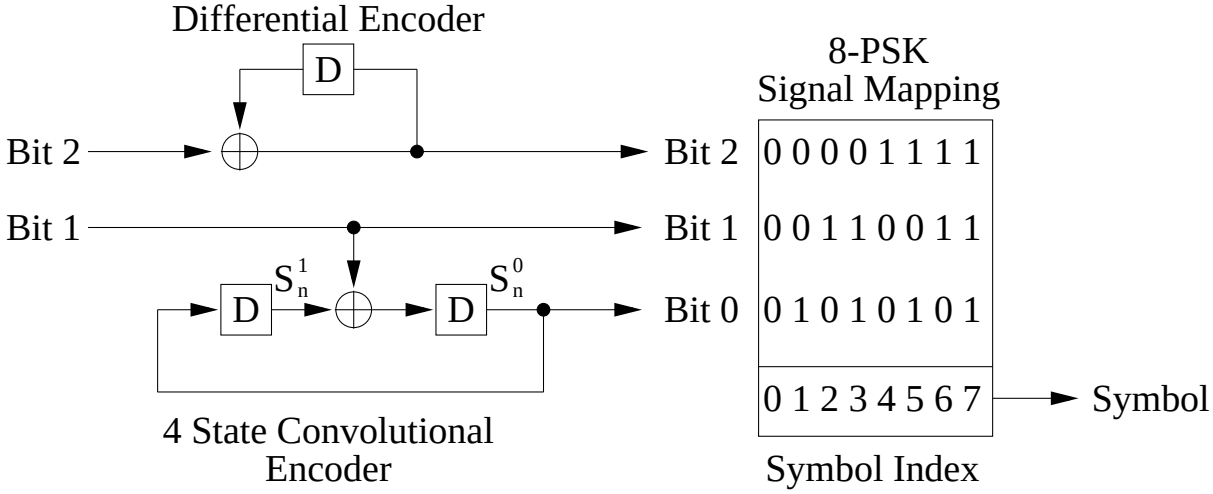

Figure 2.3: Encoder for the four-state 8PSK trellis [6] ©IEEE, 1982, Ungerböck.

where no redundancy-related transition constraints apply. In both systems, starting from any state, four transitions can occur, as required for encoding two bits/symbol. The four parallel transitions in the state trellis diagram of Figure 2.2(a) do not restrict the sequence of 4PSK symbols that can be transmitted, since there is no channel coding and therefore all trellis paths are legitimate. Hence the optimum detector can only make nearest-phasor-based decisions for each individual symbol received. The smallest distance between the 4PSK phasors is $\sqrt{2}$, denoted as d_0, and this is termed the free distance of the uncoded 4PSK constellation. Each 4PSK symbol has two nearest neighbours at this distance. Each phasor is represented by a two-bit symbol and transitions from any state to any other state are legitimate.

The situation for 8PSK TCM is a little less simplistic. The trellis diagram of Figure 2.2(b) is constituted by four states according to the four possible states of the shift-register encoder of Figure 2.3, which we represent by the four vertically stacked bold nodes. Following the elapse of a symbol period a new two-bit input symbol arrives and the convolutional encoder's shift register is clocked. This event is characterised by a transition in the trellis from state S_n to state S_{n+1}, tracking one of the four possible paths corresponding to the four possible input symbols.

In the four-state trellis of Figure 2.2(b) associated with the 8PSK TCM scheme, the trellis transitions occur in pairs and the states corresponding to the bold nodes are represented by the shift-register states S_n^0 and S_n^1 in Figure 2.3. Owing to the limitations imposed by the convolutional encoder of Figure 2.3 on the legitimate set of consecutive symbols only a limited set of state transitions associated with certain phasor sequence is possible. These limitations allow us to detect and to reject illegitimate symbol sequences, namely those which were not legitimately produced by the encoder, but rather produced by the error-prone channel. For example, when the shift register of Figure 2.3 is in state (0,0), only the transitions to the phasor points (0,2,4,6) are legitimate, whilst those to phasor points (1,3,5,7) are illegitimate. This is readily seen, because the linear encoder circuit of Figure 2.3 cannot produce a non-zero parity bit from the zero-valued input bits and hence the symbols (1,3,5,7) cannot be produced when the encoder is in the all-zero state. Observe in the 8PSK constellation of Figure 2.2(b) that the underlined bit 1 and bit 0 identify four twin-phasor subsets, where the phasors are opposite to each other in the constellation and hence have a high intra-subset separation. The unprotected bit 2 is then invoked for selecting the required phasor point within the subset. Since the redundant bit 0 constitutes also one of the shift-register state bits, namely S_n^0, from the initial states of $(S_n^1,S_n^0) = (0,0)$ or (1,0) only the even-valued phasors (0,2,4,6) having $S_n^0 = 0$ can emerge, as also seen in Figure 2.2(b). Similarly, if we have $(S_n^1,S_n^0) = (0,1)$ or (1,1) associated with $S_n^0 = 1$ then the branches emerging from these lower two states of the trellis in Figure 2.2(b) can only be associated with the odd-valued phasors of (1,3,5,7).

There are other possible codes, which would result in for example four distinct transitions from each state to all possible successor states, but the one selected here proved to be the most effective [6]. Within the 8PSK constellation we have the following distances: $d_0 = 2\sin(\pi/8)$, $d_1 = \sqrt{2}$ and $d_2 = 2$. The 8PSK signals are assigned to the transitions in the four-state trellis in accordance with the following rules:

1. Parallel trellis transitions are associated with phasors having the maximum possible distance, namely (d_2), between them, which is characteristic of phasor points in the subsets (0,4), (1,5),

(2,6) and (3,7). Since these parallel transitions belong to the same subset of Figure 2.2(b) and are controlled by the unprotected bit 2, symbols associated with them should be as far apart as possible.

2. All four-state transitions originating from, or merging into, any one of the states are labelled with phasors having a distance of *at least* $d_1 = \sqrt{2}$ between them. These are the phasors belonging to subsets (0,2,4,6) or (1,3,5,7).

3. All 8PSK signals are used in the trellis diagram with equal probability.

Observe that the assignment of bits to the 8PSK constellation of Figure 2.2(b) does not obey Gray coding and hence adjacent phasors can have arbitrary Hamming distances between them. The bit mapping and encoding process employed was rather designed for exploiting the high Euclidean distances between sets of points in the constellation. The underlined bit 1 and bit 0 of Figure 2.2(b) representing the convolutional codec's output are identical for all parallel branches of the trellis. For example, the branches labelled with phasors 0 and 4 between the identical consecutive states of (0,0) and (0,0) are associated with (bit 1)=0 and (bit 0)=0, while the uncoded bit 2 can be either '0' or '1', yielding the phasors 0 and 4, respectively. However, owing to appropriate code design this unprotected bit has the maximum protection distance, namely $d_2 = 2$, requiring the corruption of phasor 0 into phasor 4, in order to inflict a single bit error in the position of bit 2.

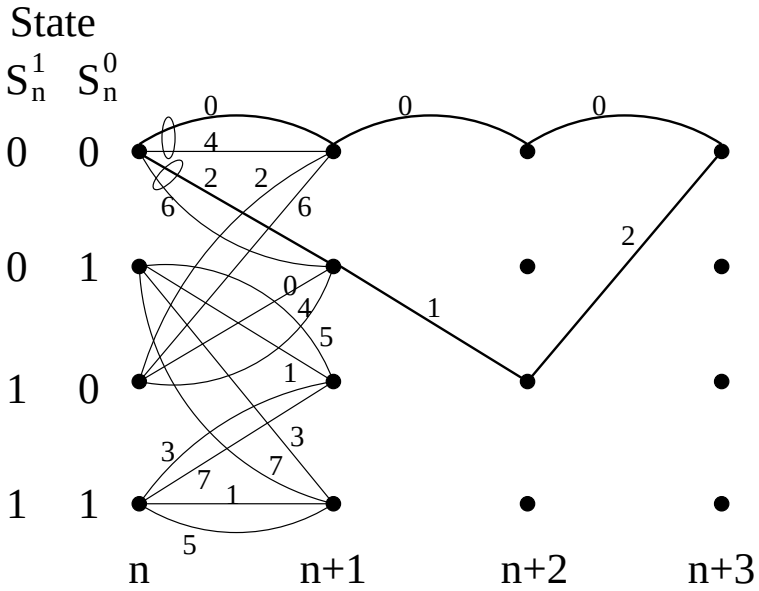

Figure 2.4: Diverging trellis paths for the computation of d_{free}. The parallel paths labelled by the symbols 0 and 4 are associated with the uncoded bits '0' and '1', respectively, as well as with the farthest phasors in the constellation of Figure 2.2(b).

The effect of channel errors exhibits itself at the decoder by diverging from the trellis path encountered in the encoder. Let us consider the example of Figure 2.4, where the encoder generated the phasors 0-0-0 commencing from state (0,0), but owing to channel errors the decoder's trellis path was different from this, since the phasor sequence 2-1-2 was encountered. The so-called free distance of a TCM scheme can be computed as the lower one of two distances. Namely, the Euclidean distances between the phasors labelling the parallel branches in the trellis of Figure 2.2(b) associated with the uncoded bit(s), which is $d_2 = 2$ in our example, as well as the distances between trellis paths diverging

and remerging after a number of consecutive trellis transitions, as seen in Figure 2.4 in the first and last of the four consecutive (0,0) states. The lower one of these two distances characterises the error resilience of the underlying TCM scheme, since the error event associated with it will be the one most frequently encountered owing to channel effects. Specifically, if the received phasors are at a Euclidean distance higher than half of the code's free distance from the transmitted phasor, an erroneous decision will be made. It is essential to ensure that by using an appropriate code design the number of decoded bit errors is minimised in the most likely error events, and this is akin to the philosophy of using Gray coding in a non-trellis-coded constellation.

The Euclidean distance between the phasors of Figure 2.2(b) associated with the parallel branches is $d_2 = 2$ in our example. The distance between the diverging trellis paths of Figure 2.2(b) labelled by the phasor sequences of 0-0-0 and 2-1-2 following the states {(0,0),(0,0),(0,0),(0,0)} and {(0,0),(0,1),(1,0),(0,0)} respectively, portrayed in Figure 2.4, is inferred from Figure 2.2(b) as d_1-d_0-d_1. By inspecting all the remerging paths of the trellis in Figure 2.2(b) we infer that this diverging path has the shortest accumulated Free Euclidean Distance (FED) that can be found, since all other diverging paths have higher accumulated FED from the error-free 0-0-0 path. Furthermore, this is the only path having the minimum free distance of $\sqrt{d_1^2 + d_0^2 + d_1^2}$. More specifically, the free distance of this TCM sequence is given by:

$$\begin{aligned} d_{free} &= min\{d_2; \sqrt{d_1^2 + d_0^2 + d_1^2}\} \\ &= min\{2; \sqrt{2 + (2.\sin\frac{\pi}{8})^2 + 2}\}. \end{aligned} \tag{2.1}$$

Explicitly, since the term under the square root in Equation 2.1 is higher than $d_2 = 2$, the free distance of this TCM scheme is given ultimately by the Euclidean distance between the parallel trellis branches associated with the uncoded bit 2, i.e.:

$$d_{free} = 2. \tag{2.2}$$

The free distance of the uncoded 4PSK constellation of Figure 2.2(a) was $d_0 = \sqrt{2}$ and hence the employment of TCM has increased the minimum distance between the constellation points by a factor of $g = \frac{d_{free}^2}{d_0^2} = \frac{2^2}{(\sqrt{2})^2} = 2$, which corresponds to 3 dB. There is only one nearest-neighbour phasor at $d_{free} = 2$, corresponding to the π-rotated phasor in Figure 2.2(b). Consequently the phasor arrangement can be rotated by π, whilst retaining all of its properties, but other rotations are not admissible.

The number of erroneous decoded bits induced by the diverging path 2-1-2 is seen from the phasor constellation of Figure 2.2(b) to be 1-1-1, yielding a total of three bit errors. The more likely event of a bit 2 error, which is associated with a Euclidean distance of $d_2 = 2$, yields only a single bit error.

Soft-decision-based decoding can be accomplished in two steps. The first step is known as subset decoding, where within each phasor subset assigned to parallel transitions, i.e. to the uncoded bit(s), the phasor closest to the received channel output in terms of Euclidean distance is determined. Having resolved which of the parallel paths was more likely to have been encountered by the encoder, we can remove the parallel transitions, hence arriving at a conventional trellis. In the second step the Viterbi algorithm is used for finding the most likely signal path through the trellis with the minimum sum of squared Euclidean distances from the sequence of noisy channel outputs received. Only the signals

already selected by the subset decoding are considered. For a description of the Viterbi algorithm the reader is referred to references [42, 43].

2.2.2 Optimum TCM Codes

Ungerböck's TCM encoder is a specific convolutional encoder selected from the family of Recursive Systematic Convolutional (RSC) codes [36], which attaches one parity bit to each information symbol. Only $\tilde{m}$ out of $\bar{m}$ information bits are RSC encoded and hence only $2^{\tilde{m}}$ branches will diverge from and merge into each trellis state. When not all information bits are RSC encoded, i.e. $\tilde{m} < \bar{m}$, $2^{\bar{m}-\tilde{m}}$ parallel transitions are associated with each of the $2^{\tilde{m}}$ branches. Therefore a total of $2^{\tilde{m}} \times 2^{\bar{m}-\tilde{m}} = 2^{\bar{m}}$ transitions occur at each trellis stage. The memory length ν of a code defines the number of shift-register stages in the encoder. Figure 2.5 shows the TCM encoder using an eight-state Ungerböck

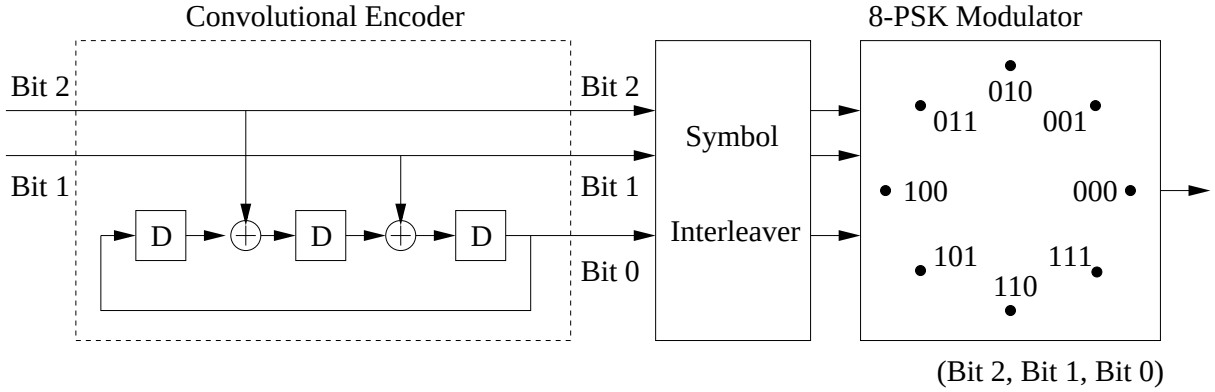

Figure 2.5: Ungerböck's RSC encoder and modulator forming the TCM encoder. The SP-based mapping of bits to the constellation points was highlighted in Figure 2.1.

code [36], which has a high FED for the sake of attaining a high performance over AWGN channels. It is a systematic encoder, which attaches an extra parity bit to the original 2-bit information word. The resulting 3-bit codewords generated by the 2-bit input binary sequence are then interleaved by a symbol interleaver in order to disperse the bursty symbol errors induced by the fading channel. Then, these 3-bit codewords are modulated onto one of the $2^3 = 8$ possible constellation points of an 8PSK modulator.

The connections between the information bits and the modulo-2 adders, as shown in Figure 2.5, are given by the generator polynomials. The coefficients of these polynomials are defined as:

$$H^j(D) := h^j_\nu.D^\nu + h^j_{\nu-1}.D^{\nu-1} + \ldots + h^j_1.D + h^j_0, \tag{2.3}$$

where D represents the delay due to one register stage. The coefficient h^j_i takes the value of '1', if there is a connection at a specific encoder stage or '0', if there is no connection. The polynomial $H^0(D)$ is the feedback generator polynomial and $H^j(D)$ for $j \geq 1$ is the generator polynomial associated with the jth information bit. Hence, the generator polynomial of the encoder in Figure 2.5 can be described in binary format as:

$$\begin{aligned} H^0(D) &= 1001 \\ H^1(D) &= 0010 \\ H^2(D) &= 0100, \end{aligned}$$

Code	State, ν	$\tilde{\mathsf{m}}$	$H^0(D)$	$H^1(D)$	$H^2(D)$
4QAM	8, 3	1	13	06	-
4QAM	64, 6	1	117	26	-
8PSK	8, 3	2	11	02	04
8PSK	32, 5	2	45	16	34
8PSK	64, 6	2	103	30	66
8PSK	128, 7	2	277	54	122
8PSK	256, 8	2	435	72	130
16QAM	64, 6	2	101	16	64

Table 2.1: Ungerböck's TCM codes [6, 36, 44, 45], where ν denotes the code memory and octal format is used for representing the generator polynomial coefficients.

or equivalently in octal format as:

$$\begin{aligned} \mathbf{H(D)} &= \left[\begin{array}{ccc} H^0(D) & H^1(D) & H^2(D) \end{array} \right] \\ &= \left[\begin{array}{ccc} 11 & 02 & 04 \end{array} \right]. \end{aligned} \tag{2.4}$$

Ungerböck suggested [36] that all feedback polynomials should have coefficients $h_\nu^0 = h_0^0 = 1$. This guarantees the realisability of the encoders shown in Figures 2.3 and 2.5. Furthermore, all generator polynomials should also have coefficients $h_\nu^j = h_0^j = 0$ for $j > 0$. This ensures that at time n the input bits of the TCM encoder have no influence on the parity bit to be generated, nor on the input of the first binary storage element in the encoder. Therefore, whenever two paths diverge from or merge into a common state in the trellis, the parity bit must be the same for these transitions, whereas the other bits differ in at least one bit [36]. Phasors associated with diverging and merging transitions therefore have at least a distance of d_1 between them, as we can see from Figure 2.2(b). Table 2.1 summarises the generator polynomials of some TCM codes, which were obtained with the aid of an exhaustive computer search conducted by Ungerböck [6], where $\tilde{\mathsf{m}}$ ($\leq \bar{\mathsf{m}}$) indicates the number of information bits to be encoded, out of the $\bar{\mathsf{m}}$ information bits in a symbol.

2.2.3 TCM Code Design for Fading Channels

It was shown in Section 2.2.1 that the design of TCM for transmission over AWGN channels is motivated by the maximisation of the FED, d_{free}. By contrast, the design of TCM concerned for transmission over fading channels is motivated by minimising the length of the shortest error event path and the product of the branch distances along that particular path [37].

The average bit error probability of TCM using M-ary PSK (MPSK) [36] for transmission over Rician channels at high SNRs is given by [37]:

$$P_b \cong \frac{1}{B} C \left(\frac{(1+\bar{K})e^{-\bar{K}}}{E_s/N_0} \right)^{\mathsf{L}} ; E_s/N_0 \gg \bar{K} \tag{2.5}$$

where C is a constant that depends on the weight distribution of the code, which quantifies the number of trellises associated with all possible Hamming distances measured with respect to the all-zero path [15]. The variable B in Equation 2.5 is the number of binary input bits of the TCM encoder

during each transmission interval, i.e the information bits per symbol, while $\bar{K}$ is the Rician fading parameter [15] and E_s/N_0 is the channel's symbol energy to noise spectral density ratio. Furthermore, L is defined as the 'length' of the shortest error event path in [46] or as the Effective Code Length (ECL) in [47, 48] or as the code's diversity in [37]. Explicity, L is expressed as the number of erroneously decoded TCM symbols asociated with the shortest error event path. Note that, in conventional TCM each trellis branch is labelled by one TCM symbol. Therefore, L can be expressed as the number of trellis branches having erroneously decoded symbol, in the shortest error event path. Most of the time, L is equal to the number of trellis branches on this path. It is clear from Equation 2.5 that P_b varies inversely proportionally with $(E_s/N_0)^{\mathsf{L}}$ and this ratio can be increased by increasing the code's diversity [37]. More specifically, in [46], the authors pointed out that the shortest error event paths

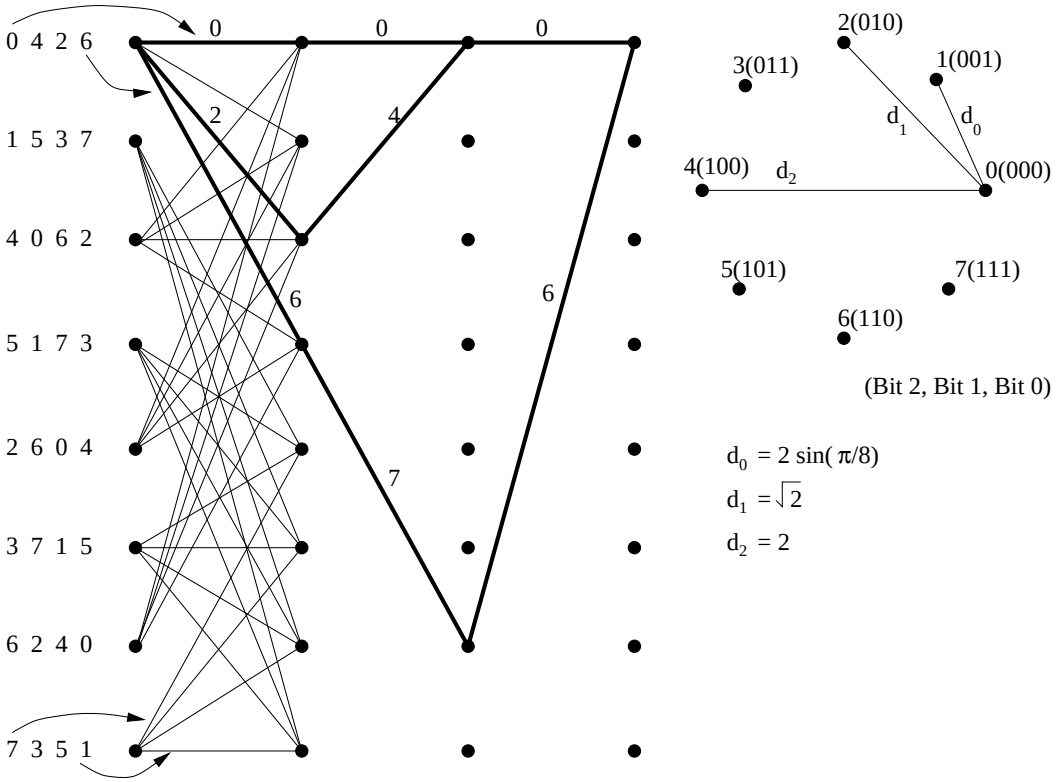

Figure 2.6: Ungerböck's 8-state 8PSK code.

are not necessarily associated with the minimum accumulated FED error events. For example, let the all-zero path be the correct path. Then the code characterised by the trellis seen in Figure 2.6 exhibits a minimum squared FED of:

$$\begin{aligned} d^2_{free} &= d^2_1 + d^2_0 + d^2_1 \\ &= 4.585, \end{aligned} \tag{2.6}$$

from the 0-0-0 path associated with the transmission of three consecutive 0 symbols from the path labelled with the transmitted symbols of 6-7-6. However, this is not the shortest error event path, since its length is $\mathsf{L} = 3$, which is longer than the path labelled with transmitted symbols of 2-4, which has a length of $\mathsf{L} = 2$ and a FED of $d^2_{free} = d^2_1 + d^2_2 = 6$. Hence, the 'length' of the shortest error event path is $\mathsf{L} = 2$ for this code, which, again, has a squared Euclidean distance of 6. In summary, the number of bit errors associated with the above $\mathsf{L} = 3$ and $\mathsf{L} = 2$ shortest error event paths is seven and two, respectively, clearly favouring the $\mathsf{L} = 2$ path, which had a higher accumulated FED of 6

than that of the 4.585 FED of the $\mathsf{L} = 3$ path. Hence, it is worth noting that if the code was designed based on the minimum FED, it may not minimise the number of bit errors. Hence, as an alternative design approach, in Section 2.5 we will study BICM, which relies on the shortest error event path L or the bit-based Hamming distance of the code and hence minimises the BER.

The design of coded modulation schemes is affected by a variety of factors. A high squared FED is desired for AWGN channels, while a high ECL and a high minimum product distance are desired for fading channels [37]. In general, a code's diversity or ECL is quantified in terms of the length of the shortest error event path L, which may be increased for example by simple repetition coding, although at the cost of reducing the effective data rate proportionately. Alternatively, space-time-coded multiple transmitter/receiver structures can be used, which increase the scheme's cost and complexity. Finally, simple interleaving can be invoked, which induces latency. In our approach, symbol-based interleaving is employed in order to increase the code's diversity.

2.2.4 Set Partitioning

As we have seen in Figure 2.4, if higher-order modulation schemes, such as 16QAM or 64QAM, are used, parallel transitions may appear in the trellis diagram of the TCM scheme, when not all information bits are convolutional channel encoded or when the number of states in the convolutional encoder has to be kept low for complexity reasons. As noted before, in order to avoid encountering high error probabilities, the parallel transitions should be assigned to constellation points exhibiting a high Euclidean distance. Ungerböck solved this problem by introducing the set partitioning technique. Specifically, the signal set is split into a number of subsets, such that the minimum Euclidean distance of the signal points in the new subset is increased at every partitioning step.

In order to elaborate a little further, Figure 2.7 illustrates the set partitioning of 16QAM. Here we used the $R = \frac{3}{4}$-rate code of Table 2.1. This is a relatively high-rate code, which would not be sufficiently powerful if we employed it for protecting all three original information bits. Moreover, if we protect for example two out of the three information bits, we can use a more potent $\frac{2}{3}$-rate code for the protection of the more vulnerable two information bits and leave the most error-resilient bit of the 4-bit constellation unprotected. This is justifiable, since we can observe in Figure 2.7 that the minimum Euclidean distance of the constellation points increases from Level 0 to Level 3 of the constellation partitioning tree. This indicates that the bits labelling or identifying the specific partitions have to be protected by the RSC code, since they label phasors that have a low Euclidean distance. By contrast, the intra-set distance at Level 3 is the highest, suggesting a low probability of corruption. Hence the corresponding bit, bit 3, can be left unprotected. The partitioning in Figure 2.7 can be continued, until there is only one phasor or constellation point left in each subset. The intra-subset distance increases as we traverse down the partition tree. The first partition level, *Level* 0, is labelled by the parity bit, and the next two levels by the coded bits. Finally, the uncoded bit labels the lowest level, *Level* 3, in the constellation, which has the largest minimum Euclidean distance.

Conventional TCM schemes are typically decoded/demodulated with the aid of the appropriately modified Viterbi Algorithm (VA) [49]. Furthermore, the VA is a maximum likelihood sequence estimation algorithm, which does not guarantee that the Symbol Error Ratio (SER) is minimised, although it achieves a performance near the minimum SER. By contrast, the symbol-based MAP algorithm [38]

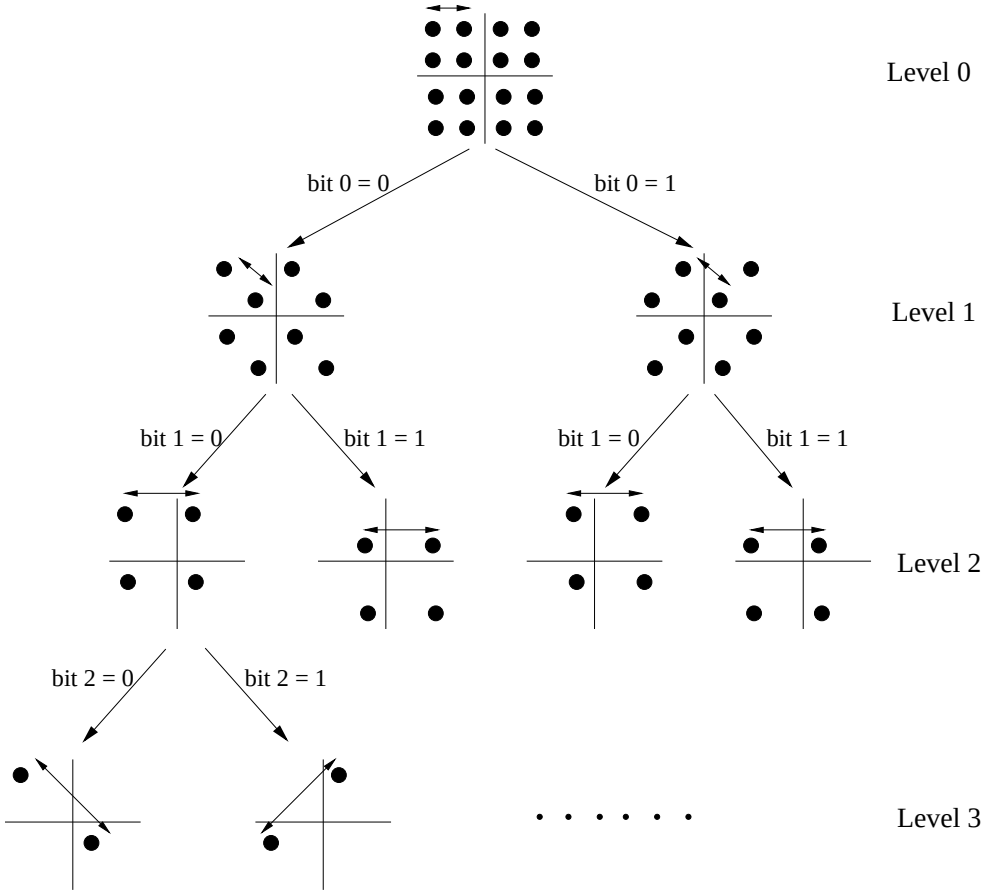

Figure 2.7: Set partitioning of a 16QAM signal constellation. The minimum Euclidean distance at a partition level is denoted by the line between the signal points [36] ©IEEE, 1982, Ungerböck.

guarantees the minimum SER, albeit at the cost of a significantly increased complexity. Hence the symbol-based MAP algorithm has been used for the decoding of TCM sequences. We will, however, in Section 2.4, also consider Turbo TCM (TTCM), where instead of the VA-based sequence estimation, symbol-by-symbol-based soft information has to be exchanged between the TCM decoders of the TTCM scheme. Hence in the next section we will present the symbol-based MAP algorithm.

2.3 The Symbol-based MAP Algorithm

In this section, the non-binary or symbol-based Maximum-A-Posteriori (MAP) decoding algorithm will be presented. The binary MAP algorithm was first presented in [50], while the non-binary MAP algorithm was proposed in [38]. A reduced-complexity version of the MAP algorithm, operating in the logarithmic domain (log-domain) after transforming the operands and the operations to this domain will also be presented. In our forthcoming discourse we use $p(x)$ to denote the probability of the event x, and, given a symbol sequence y_k, we denote by y_a^b the sequence of symbols given by $y_a, y_{a+1}, \ldots, y_b$.

2.3.1 Problem Description

The problem that the MAP algorithm has to solve is presented in Figure 2.8. An information source produces a sequence of N information symbols u_k, $k = 1, 2, \ldots, N$. Each information symbol can

assume M different values, i.e. $u_k \in \{0, 1, \ldots, M-1\}$, where M is typically a power of two, so that each information symbol carries $\bar{\mathsf{m}} = log_2 M$ information bits. We assume here that the symbols are to be transmitted over an AWGN channel. To this end, the $\bar{\mathsf{m}}$-bit symbols are first fed into an encoder for generating a sequence of N channel symbols $x_k \in X$, where X denotes the set of complex values belonging to some phasor constellations such as an increased-order QAM or PSK constellation, having M possible values carrying $\mathsf{m} = log_2 \mathsf{M}$ bits. Again, the channel symbols are transmitted over an AWGN channel and the received symbols are:

$$y_k = x_k + n_k, \tag{2.7}$$

where n_k represents the complex AWGN samples. The received symbols are fed to the decoder, which has the task of producing an estimate $\hat{u}_k$ of the $2^{\bar{\mathsf{m}}}$-ary information sequence, based on the 2^{m}-ary received sequence, where $\mathsf{m} > \bar{\mathsf{m}}$. If the goal of the decoder is that of minimising the number of symbol errors, where a symbol error occurs when $u_k \neq \hat{u}_k$, then the best decoder is the MAP decoder [50]. This decoder computes the A Posteriori Probability (APP) $A_{k,m}$ for every $2^{\bar{\mathsf{m}}}$-ary information symbol u_k that the information symbol value was m given the received sequence, i.e. computes $A_{k,m} = p(u_k = m|y_1^N)$, for $m = 0, 1, \ldots, M-1$, $k = 1, 2, \ldots, N$. Then it decides that the information symbol was the one having the highest probability, i.e. $\hat{u}_k = m$ if $A_{k,m} \geq A_{k,i}$ for $i = 0 \ldots M-1$. In order to realise a MAP decoder one has to devise a suitable algorithm for computing the APP.

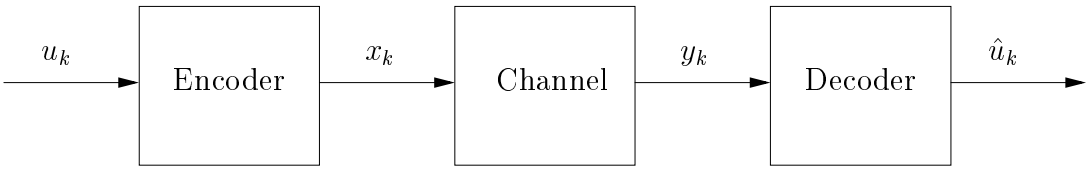

Figure 2.8: The transmission system.

In order to compute the APP, we must specify how the encoder operates. We consider a trellis encoder. The operation of a trellis encoder can be described by its trellis. The trellis seen in Figure 2.9, is constituted by $(N+1) \cdot S$ nodes arranged in $(N+1)$ columns of S nodes. There are M branches emerging from each node, which arrive at nodes in the immediately following column. The trellis structure repeats itself identically between each pair of columns.

It is possible to identify a set of paths originating from the nodes in the first column and terminating in a node of the last column. Each path will comprise exactly N branches. When employing a trellis-encoder, the input sequence unambiguously determines a single path in the trellis. This path is identified by labelling the M branches emerging from each node by the M possible values of the original information symbols, although only the labelling of the first branch at $m = 0$ and the last branch at $m = M-1$ are shown in Figure 2.9 due to space limitations. Then, commencing from a specified node in the first column, we use the first input symbol, u_1, to decide which branch is to be chosen. If $u_1 = m$, we choose the branch labeled with m, and move to the corresponding node in the second column that this branch leads to. In this node we use the second information symbol, u_2, for selecting a further branch and so on. In this way the information sequence identifies a path in the trellis. In order to complete the encoding operation, we have to produce the symbols to be transmitted over the channel, namely $x_1, x_2, \ldots, x_N$ from the information symbols $u_1, u_2, \ldots, u_N$. To

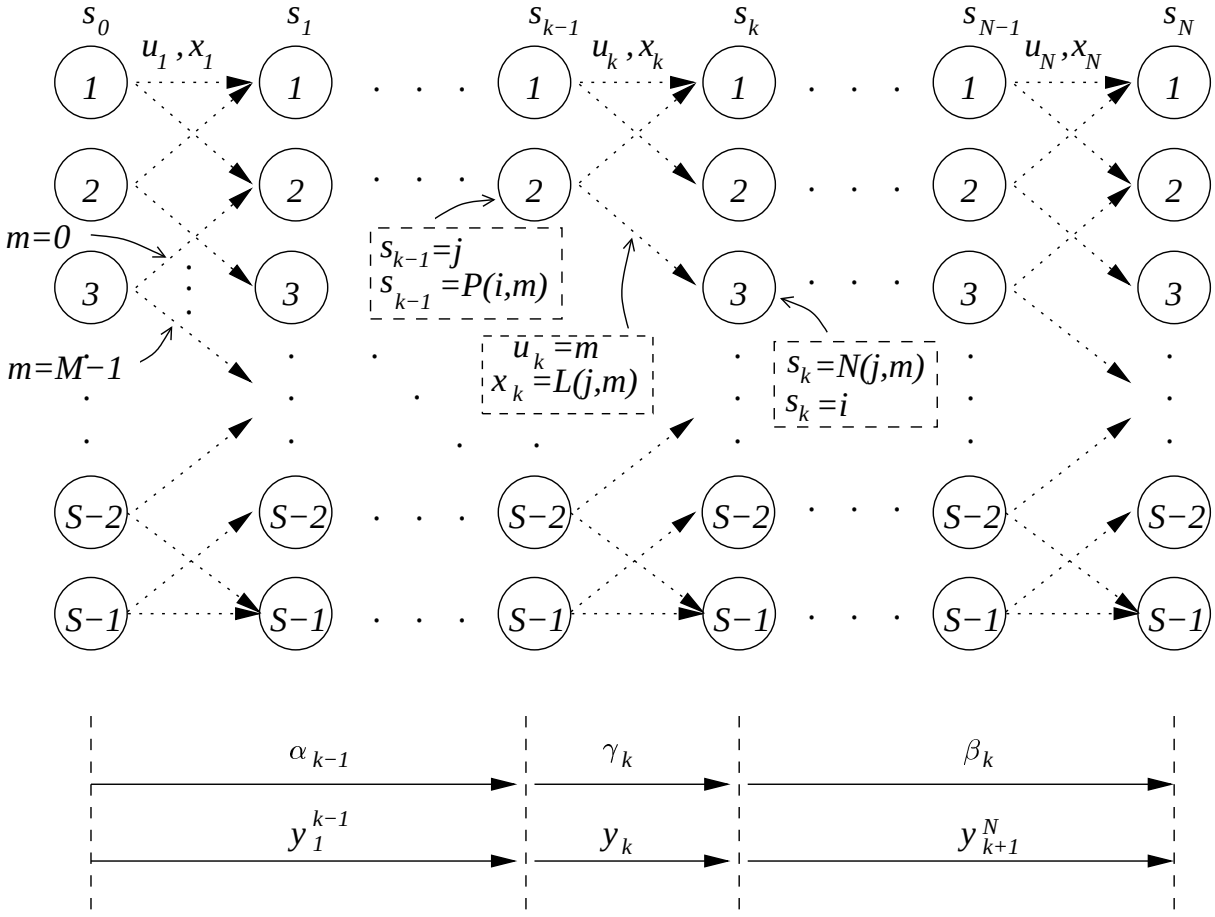

Figure 2.9: The non-binary trellis and its labelling, where there are M branches emerging from each node.

this end we add a second label to each branch, which is the corresponding phasor constellation point that is transmitted when the branch is encountered.

In a trellis it is convenient to attach a time index to each column, from 0 to N, and to number the nodes in each column from 0 to $S-1$. This allows us to introduce the concept of trellis states at time k. Specifically, during the encoding process, we say that the trellis is in state i at time k, and write $s_k = i$, if the path determined by the information sequence crosses the i-th node of the k-th column. The structure of a trellis encoder is specified by two functions. The first function is $N(j,m) \in \{0,1,\ldots,S-1\}$, which specifies the trellis' next state, namely $s_k = N(j,m)$, when the information symbol is $u_k = m$ and the previous state is $s_{k-1} = j$ as seen in Figure 2.9. In order to specify the symbol transmitted when this branch is encountered, we use the function $L(j,m) \in X$. To summarize, there is a branch leading from state $s_{k-1} = j$ to state $s_k = N(j,m)$, which is encountered if the input symbol is $u_k = m$, and the corresponding transmitted symbol is $L(j,m)$. It is useful to consider a third function, $P(i,m) \in \{0,1,\ldots,S-1\}$ specifying the previous state $s_{k-1} = P(i,m)$ of the trellis when the present state is $s_k = i$, and the last original information symbol is $u_k = m$ as seen in Figure 2.9. The aim of the MAP decoding algorithm is to find the path in the trellis that is associated with the most likely transmitted symbols, i.e. that of minimising the Symbol Error Ratio (SER). By contrast, the VA-based detection of TCM signals aims for identifying the most likely transmitted symbol sequence, which does not automatically guarantee attaining the minimum SER.

2.3.2 Detailed Description of the Symbol-based MAP Algorithm

Having described the problem to be solved by the MAP decoder and the encoder structure, we now seek an algorithm capable of computing the APP, i.e. $A_{k,m} = p(u_k = m|y_1^N)$. The easiest way of computing these probabilities is by determining the sum of a different set of probabilities, namely $p(u_k = m, s_k = i, s_{k-1} = j|y_1^N)$, where again, y_1^N denotes the symbol sequence $y_1, y_2, \ldots, y_N$. This is because we can devise a recursive way of computing the second set of probabilities, as we traverse through the trellis from state to state which reduces the detection complexity. Thus we write:

$$A_{k,m} = p(u_k = m|y_1^N) = \sum_{i,j=0}^{S-1} p(u_k = m, s_k = i, s_{k-1} = j|y_1^N), \tag{2.8}$$

where the summation implies adding all probabilities associated with the nodes j and i labeled by $u_k = m$ and the problem is now that of computing $p(u_k = m, s_k = i, s_{k-1} = j|y_1^N)$. As a preliminary consideration we note that this probability is zero, if the specific branch of the trellis emerging from state j and merging into state i is not labeled with the input symbol m. Hence, we can eliminate the corresponding terms of the summation. Thus, upon denoting the specific set of pairs i, j, by I_m for which a trellis branch labeled with m exists that traverses from state j to state i, we can rewrite Equation 2.8 as:

$$A_{k,m} = \sum_{i,j \in I_m} p(u_k = m, s_k = i, s_{k-1} = j|y_1^N). \tag{2.9}$$

If $i, j \in I_m$, then we can compute the probabilities $p(u_k = m, s_k = i, s_{k-1} = j|y_1^N)$ as [50,51]:

$$p(u_k = m, s_k = i, s_{k-1} = j|y_1^N) = \frac{1}{p(y_1^N)} \cdot \beta_k(i) \cdot \alpha_{k-1}(j) \cdot \gamma_k(j, m), \tag{2.10}$$

where

$$\begin{aligned} \beta_k(i) &= p(y_{k+1}^N|s_k = i) \\ \alpha_{k-1}(j) &= p(y_1^{k-1}, s_{k-1} = j) \\ \gamma_k(j, m) &= p(y_k, u_k = m|s_{k-1} = j). \end{aligned} \tag{2.11}$$

In order to simplify our discourse, we defer the proof of Equation 2.10 to Section 2.3.3, where we also show how the $\alpha_{k-1}(j)$ values and the $\beta_k(i)$ values can be efficiently computed using the $\gamma_k(j, m)$ values. In our forthcoming discourse we study the $\gamma_k(j, m)$ values and further simplify Equation 2.9.

The first simplification is to note that we do not necessarily need the exact $A_{k,m}$ values, but only their ratios. In fact, for a fixed k, the vector $A_{k,m}$, being a probability vector, must sum to unity. Thus, by normalising the sum in Equation 2.9 to unity, we can compute the exact value of $A_{k,m}$ from $\bar{A}_{k,m}$ with the aid of:

$$\bar{A}_{k,m} = C_k \cdot A_{k,m}. \tag{2.12}$$

For this reason we will omit the common normalisation factor of $C_k = \frac{1}{p(y_1^N)}$ in Equation 2.10. Then, upon substituting Equation 2.10 into Equation 2.9 we have:

$$\bar{A}_{k,m} = \sum_{i,j \in I_m} \beta_k(i) \cdot \alpha_{k-1}(j) \cdot \gamma_k(j, m). \tag{2.13}$$

A second simplification is to note that in Equation 2.13 the value of i is uniquely specified by the pair j and m, since $i, j \in I_m$. Specifically, since i is the state reached after emerging from state j when the

input symbol is m, we have $i = N(j,m)$ where $N(j,m)$ was defined at the end of Section 2.3.1. Thus we can rewrite [1] Equation 2.13 as:

$$\bar{A}_{k,m} = \sum_{j=0}^{S-1} \beta_k(N(j,m)) \cdot \alpha_{k-1}(j) \cdot \gamma_k(j,m). \tag{2.14}$$

Before we proceed, it is worth presenting Bayes' rule, which is applied repeatedly throughout this section. This rule gives the joint probability of "a and b", $P(a,b)$, in terms of the conditional probability of "a given b", $P(a|b)$, as:

$$P(a,b) = P(a|b) \cdot P(b) = P(b|a) \cdot P(a). \tag{2.15}$$

Two useful consequences of Bayes' rule are:

$$P(a,b,c) = P(a|b,c) \cdot P(b,c) \tag{2.16}$$

and

$$\begin{aligned} P(a,b|c) &= \frac{P(a,b,c)}{P(c)} \\ &= \frac{P(a,b,c)}{P(b,c)} \cdot \frac{P(b,c)}{P(c)} \\ &= P(a|b,c).P(b|c). \end{aligned} \tag{2.17}$$

Let us now consider the term $\gamma_k(j,m) = p(y_k, u_k = m | s_{k-1} = j)$ of Equation 2.11, which can be rewritten using the relationship of Equation 2.17 as:

$$\gamma_k(j,m) = p(y_k, u_k = m | s_{k-1} = j) = p(y_k | u_k = m, s_{k-1} = j) \cdot p(u_k = m | s_{k-1} = j) \tag{2.18}$$

Let us now study the multiplicative terms at the right of Equation 2.18, where $p(y_k|u_k = m, s_{k-1} = j)$ is the probability that we receive y_k, when the branch emerging from state $s_{k-1} = j$ of Figure 2.9 labeled with the information symbol $u_k = m$ is encountered. When this branch is encountered, the symbol transmitted is $x_k = L(j,m)$, as seen in Figure 2.9. Thus, the probability of receiving the sample y_k, given that the previous state was $s_{k-1} = j$ and the transition symbol encountered was $u_k = m$ can be written as:

$$p(y_k | u_k = m, s_{k-1} = j) = p(y_k | x_k = L(j,m)) = \eta_k(j,m). \tag{2.19}$$

By remembering that $y_k = x_k + n_k$, and that n_k is the complex AWGN, we can compute $\eta_k(j,m)$ as [52]:

$$\eta_k(j,m) = e^{\frac{-|y_k - L(j,m)|^2}{2\sigma^2}}, \tag{2.20}$$

where $\sigma^2 = N_0/2$ is the noise's variance and N_0 is the noise's Power Spectral Density (PSD). In verbal terms, Equation 2.20 indicates that the probability expressed in Equation 2.19 is a function of

[1] Equivalently, we could note that in Equation 2.13, we have $j = P(i,m)$, since $i, j \in I_m$ and rewrite Equation 2.13 as:

$$\bar{A}_{k,m} = \sum_{i=0}^{S-1} \beta_k(i) \cdot \alpha_{k-1}(P(i,m)) \cdot \gamma_k(P(i,m),m).$$

the distance between the received noisy sample y_k and the transmitted noiseless sample $x_k = L(j,m)$. Observe in Equation 2.20 that we dropped the multiplicative factor of $\frac{1}{2\pi\sigma^2}$, since it constitutes another scaling factor, which can be viewed as comprised in the constant C_k associated with $\bar{A}_{k,m} = C_k A_{k,m}$. As to the second multiplicative term at the righthand side of Equation 2.18, note that $p(u_k = m|s_{k-1} = j) = p(u_k = m)$, since the original information to be transmitted is independent of the previous trellis state. The probabilities:

$$\Pi_{k,m} = p(u_k = m) \tag{2.21}$$

are the *a priori* probabilities of the information symbols. Typically the information symbols are independent and equiprobable, hence $\Pi_{k,m} = 1/M$. However, if we have some prior knowledge about the transmitted symbols, this can be used as their *a priori* probability. As we will see, a turbo decoder will have some *a priori* knowledge about the transmitted symbols after the first iteration. We now rewrite Equation 2.18 using Equation 2.19 and the *a priori* probabilities as:

$$\gamma_k(j,m) = \Pi_{k,m} \cdot \eta_k(j,m). \tag{2.22}$$

Then, by substituting Equation 2.22 into Equation 2.14 and exchanging the order of summations we can portray the APPs in their final form, yielding:

$$\bar{A}_{k,m} = \Pi_{k,m} \cdot \sum_{j=0}^{S-1} \beta_k(N(j,m)) \cdot \alpha_{k-1}(j) \cdot \eta_k(j,m). \tag{2.23}$$

2.3.3 Recursive Metric Update Formulae

In this section we will deduce Equation 2.10. Figure 2.9 visualises the intervals, namely α_{k-1}, γ_k and β_k in the trellis for a given k, as well as the symbols received in these intervals, namely $\mathbf{y_1^{k-1}}, \mathbf{y_k}$ and $\mathbf{y_{k+1}^N}$, where γ is the so-called branch transition metric, α is the so-called forward recursive variable and β is the so-called backward recursive variable. As the first step of decoding, we have to compute all the values of γ_k using Equation 2.22, which depend only on the current received symbol y_k, for $k = 1, \cdots, N$. Then, we can compute α_{k-1} and β_k based on these γ_k values with the aid of Equation 2.11.

Now, we commence our discourse by considering the additive terms in Equation 2.9, which we formulated with the aids of Bayes' rule in Equations 2.15 to 2.17 as:

$$p(u_k = m, s_k = i, s_{k-1} = j|y_1^N) = \frac{1}{p(y_1^N)} \cdot p(y_1^N, u_k = m, s_k = i, s_{k-1} = j), \tag{2.24}$$

and consider the term $p(u_k = m, s_k = i, s_{k-1} = j, y_1^N)$. We can write

$$\begin{aligned} p(u_k = m, s_k = i, s_{k-1} = j, y_1^N) &= p(u_k = m, s_k = i, s_{k-1} = j, y_1^k, y_{k+1}^N) \\ &= p(y_{k+1}^N|u_k = m, s_k = i, s_{k-1} = j, y_1^k) \cdot p(u_k = m, s_k = i, s_{k-1} = j, y_1^k). \end{aligned} \tag{2.25}$$

Let us now simplify the first multiplicative term of Equation 2.25 by noting that if the current state s_k is known, the decoded output sequence probability is not affected by either the previous state s_{k-1}, the input symbol u_k or the previous received symbol sequence y_1^k. Thus Equation 2.25 can be rewritten as

$$p(u_k = m, s_k = i, s_{k-1} = j, y_1^N) = p(y_{k+1}^N|s_k = i) \cdot p(u_k = m, s_k = i, s_{k-1} = j, y_1^k)$$

$$= p(y_{k+1}^N | s_k = i) \cdot p(y_1^{k-1} | u_k = m, s_k = i, s_{k-1} = j, y_k) \cdot p(y_k, u_k = m, s_k = i, s_{k-1} = j). \quad (2.26)$$

Again, we simplify the second multiplicative term of Equation 2.26 by noting that, if s_{k-1} is known, the received symbol sequence y_1^{k-1} is not affected by either s_k, u_k or y_k, hence we can rewrite Equation 2.26 as

$$p(u_k = m, s_k = i, s_{k-1} = j | y_1^N) = p(y_{k+1}^N | s_k = i) \cdot p(y_1^{k-1} | s_{k-1} = j) \cdot p(y_k, u_k = m, s_k = i, s_{k-1} = j). \quad (2.27)$$

By multiplying and dividing the second and the third multiplicative term, respectively, with $p(s_{k-1} = j)$, we can rearrange Equation 2.27 to

$$p(u_k = m, s_k = i, s_{k-1} = j | y_1^N) = p(y_{k+1}^N | s_k = i) \cdot p(y_1^{k-1} s_{k-1} = j) \cdot p(y_k, u_k = m, s_k = i | s_{k-1} = j). \quad (2.28)$$

Then, by introducing

$$\beta_k(i) = p(y_{k+1}^N | s_k = i) \quad (2.29)$$

and

$$\alpha_{k-1}(j) = p(y_1^{k-1}, s_{k-1} = j) \quad (2.30)$$

we have

$$p(u_k = m, s_k = i, s_{k-1} = j | y_1^N) = \beta_k(i) \cdot \alpha_{k-1}(j) \cdot p(y_k, u_k = m, s_k = i | s_{k-1} = j). \quad (2.31)$$

If $i, j \notin I_m$, the above probability is zero, since no branch exists leading from state j to state i, when the information symbol is m. Thus we assume $i, j \in I_m$. In this case we can simplify the second multiplicative term of Equation 2.31 as

$$p(y_k, u_k = m, s_k = i | s_{k-1} = j) = p(y_k, u_k = m | s_{k-1} = j). \quad (2.32)$$

Upon defining

$$\gamma_k(j, m) = p(y_k, u_k = m | s_{k-1} = j) \quad (2.33)$$

and upon substituting Equation 2.32 and Equation 2.33 in Equation 2.31 we obtain

$$p(u_k = m, s_k = i, s_{k-1} = j, y_1^N) = \beta_k(i) \cdot \alpha_{k-1}(j) \cdot \gamma_k(j, m), \quad (2.34)$$

and upon substituting Equation 2.34 in Equation 2.24 we obtain Equation 2.10, QED.

2.3.3.1 Backward Recursive Computation of $\beta_k(i)$

Let us now highlight how the values $\beta_k(i)$ can be used, in order to 'backward' recursively compute $\beta_{k-1}(P(i, m) = j)$ from $\beta_k(i)$. With the aid of the definition in Equation 2.29 we have

$$\beta_{k-1}(j) = p(y_k^N | s_{k-1} = j) = p(y_k, y_{k+1}^N | s_{k-1} = j), \quad (2.35)$$

which can be reformulated in terms of $p(y_k, y_{k+1}^N, s_k = i | s_{k-1} = j)$, by summing these probabilities for all the trellis states $i = 0 \ldots (S-1)$, which are reached from $s_{k-1} = j$, yielding:

$$\beta_{k-1}(j) = \sum_{i=0}^{S-1} p(y_k, y_{k+1}^N, s_k = i | s_{k-1} = j).$$

This can be reformatted using Equations 2.15-2.17 as:

$$\beta_{k-1}(j) = \sum_{i=0}^{S-1} p(y_{k+1}^N | y_k, s_k = i, s_{k-1} = j) \cdot p(y_k, s_k = i | s_{k-1} = j). \quad (2.36)$$

With reference to the trellis diagram of Figure 2.9 we note that the received symbol sequence y_{k+1}^N is not affected by y_k and s_{k-1}, if s_k is given. Thus from Equations 2.36, 2.29 and 2.15-2.17 we obtain:

$$\beta_{k-1}(j) = \sum_{i=0}^{S-1} p(y_{k+1}^N | s_k = i) \cdot p(y_k, s_k = i | s_{k-1} = j) = \sum_{i=0}^{S-1} \beta_k(i) \cdot p(y_k, s_k = i | s_{k-1} = j). \quad (2.37)$$

Let us now consider the summation over the index range of $i = 0 \ldots (S-1)$, and note that for a fixed j the probability $p(y_k, s_k = i | s_{k-1} = j)$ will be non-zero only, if a branch exists that leads from state j to state i. Thus there are only M specific values of i, which contribute to the summation, namely the values of $i = N(j, m)$ for some m. We can thus rewrite Equation 2.37 as

$$\beta_{k-1}(j) = \sum_{m=0}^{M-1} \beta_k(N(j, m)) \cdot p(y_k, s_k = N(j, m) | s_{k-1} = j), \quad (2.38)$$

where for the second multiplicative term we have $p(y_k, s_k = N(j, m) | s_{k-1} = j) = p(y_k, u_k = m | s_{k-1} = j) = \gamma_k(j, m)$. Hence we can write

$$\beta_{k-1}(j) = \sum_{m=0}^{M-1} \beta_k(N(j, m)) \gamma_k(j, m). \quad (2.39)$$

Equation 2.39 facilitates the 'backward' recursive calculation of the $\beta_k(N(j, m) = i)$ values, commencing from $\beta_N(N(j, m) = i)$. In order to determine this boundary value we note that by using Equation 2.39 for computing $\beta_{N-1}(j)$ we have

$$\beta_{N-1}(j) = p(y_N | s_{N-1} = j) = \sum_{m=0}^{M-1} \beta_N(N(j, m)) \cdot p(y_N, u_N = m | s_{N-1} = j) \quad (2.40)$$

and that in order to render the above expression true we have to choose

$$\beta_N(N(j, m)) = \beta_N(i) = 1. \quad (2.41)$$

2.3.3.2 Forward Recursive Computation of $\alpha_k(i)$

In this section we recursively derive the values $\alpha_k(N(j, m) = i)$ from $\alpha_{k-1}(P(i, m) = j)$. Upon exploiting Equation 2.30 we have

$$\alpha_k(i) = p(y_1^k, s_k = i) = p(y_k, y_1^{k-1}, s_k = i). \quad (2.42)$$

We can compute the right-hand side form of Equation 2.42 using the probability $p(y_k, y_1^{k-1}, s_{k-1} = j, s_k = i)$ by summing these probabilities for all the trellis states $j = 0 \ldots (S-1)$, from which the state $s_k = i$ is reached, as follows:

$$\alpha_k(i) = \sum_{j=0}^{S-1} p(y_k, y_1^{k-1}, s_{k-1} = j, s_k = i).$$

This can be reformatted using Equations 2.15-2.17 as:

$$\alpha_k(i) = \sum_{j=0}^{S-1} p(y_k, s_k = i | s_{k-1} = j, y_1^{k-1}) \cdot p(y_1^{k-1}, s_{k-1} = j). \quad (2.43)$$

With reference to the trellis diagram of Figure 2.9 we note that the received symbol sequence y_1^{k-1} has no effect on the first multiplicative term of Equation 2.43, if s_{k-1} is given. Thus from Equation 2.43 we obtain

$$\alpha_k(i) = \sum_{j=0}^{S-1} p(y_k, s_k = i | s_{k-1} = j) \cdot p(y_1^{k-1}, s_{k-1} = j)$$

and with the aid of definition in Equation 2.30 we have:

$$\alpha_k(i) = \sum_{j=0}^{S-1} p(y_k, s_k = i | s_{k-1} = j) \cdot \alpha_{k-1}(j). \quad (2.44)$$

Let us now consider the summation over the index range of $j = 0 \ldots (S-1)$ and note that for a fixed i, the probability of $p(y_k, s_k = i | s_{k-1} = j)$ will be non-zero only, if a branch exists from state j to state i. Thus there are only M non-zero values of j, which contribute to the summation in Equation 2.44, namely the values $j = P(i, m)$ for a given m. We can thus rewrite Equation 2.44 as

$$\alpha_k(i) = \sum_{m=0}^{M-1} \alpha_{k-1}(P(i,m)) \cdot p(y_k, s_k = i | s_{k-1} = P(i,m)). \quad (2.45)$$

For the second multiplicative term of Equation 2.45 we have $p(y_k, s_k = i | s_{k-1} = P(i,m)) = p(y_k, u_k = m | s_{k-1} = P(i,m)) = \gamma_k(P(i,m), m)$, hence we can write

$$\alpha_k(i) = \sum_{m=0}^{M-1} \alpha_{k-1}(P(i,m)) \cdot \gamma_k(P(i,m), m). \quad (2.46)$$

Equation 2.46 allows the recursive calculation of the $\alpha_{k-1}(P(i,m) = j)$ values, commencing from $\alpha_0(j)$. In order to determine this boundary value we note that $\alpha_0(j) = p(s_0 = j)$, i.e. $\alpha_0(j)$ is the *a priori* probability of the first state j leading to state i. Conventionally, we commence the encoding from the first state, i.e. from state $j = 0$. In this case the boundary conditions are:

$$\alpha_0(j) = \begin{cases} 1 & \text{if } j = 0 \\ 0 & \text{if } j \neq 0 \end{cases} \quad (2.47)$$

Let us now consider how the above recursive computations can be carried out more efficiently in the logarithmic domain.

2.3.4 The MAP Algorithm in the Logarithmic-Domain

In this section we will describe the operation of the MAP algorithm in logarithmic domain (log-domain). In 1995, Robertson proposed the Log-Map algorithm [53], which dramatically reduces the complexity of the MAP algorithm, while attaining an identical performance to that of the MAP algorithm. The Max-Log-MAP algorithm constitutes a further substantial simplification, which performs

however suboptimally compared to the Log-MAP algorithm. Specifically, in the log-domain multiplications correspond to additions, which are significantly less demanding in terms of computational complexity. A further simplification accrues by using the Jacobian logarithm [53] as follows:

$$\begin{aligned} g(\Phi_1, \Phi_2) &= ln(e^{\Phi_1} + e^{\Phi_2}) \\ &= max\{\Phi_1, \Phi_2\} + ln(1 + e^{-|\Phi_1 - \Phi_2|}) \\ &= max\{\Phi_1, \Phi_2\} + f_c(|\Phi_1 - \Phi_2|), \end{aligned} \tag{2.48}$$

where the summation of $e^{\Phi_1} + e^{\Phi_2}$ is replaced by selecting the maximum of the terms Φ_1 and Φ_2 and adding a correction term f_c that depends on the Euclidean distance of both terms. For the summation of more than two terms, i.e. for example for the summations seen in Equations 2.39 and 2.46, nesting of the $g(\Phi_1, \Phi_2)$ terms in Equation 2.48 can be carried out as follows:

$$ln(\sum_{i=1}^{I} e^{\Phi_i}) = g(\Phi_I, g(\Phi_{I-1}, \ldots g(\Phi_3, g(\Phi_2, \Phi_1)) \ldots)). \tag{2.49}$$

The correction term f_c in Equation 2.48 can be determined with the aid of three different methods:

- The Exact-Log-MAP algorithm, which is characterised by calculating the exact value of the correction term f_c as:

  $$f_c = ln(1 + e^{-|\Phi_1 + \Phi_2|}). \tag{2.50}$$

  The corresponding performance is identical to that of the MAP algorithm.

- The Approx-Log-MAP algorithm invokes an approximation of the correction term f_c. Robertson [53] found that a look-up table containing eight values for f_c, ranging between 0 and 5, gives practically the same performance as the Exact-Log-MAP algorithm.

- The Max-Log-MAP algorithm, which retains only the maximum value in Equation 2.48, hence ignoring the correction term f_c. However, the Approx-Log-MAP algorithm is only marginally more complex, than the Max-Log-MAP algorithm, although it has a superior performance.

For these reasons, our simulations have been carried out by employing the Approx-Log-MAP algorithm. Explicitly, an addition operation is substituted with an addition, a subtraction, a table look-up and a maximum-search operation according to Equation 2.48, when the Approx-Log-MAP algorithm is employed.

2.3.5 Symbol-based MAP Algorithm Summary

Let us now summarize the operations of the symbol-based MAP algorithm using Figure 2.10. We assume that the *a priori* probabilities $\Pi_k(i)$ in Equation 2.21 were known. These are either all equal to $1/M$ or they are constituted by additional external information. The first step is to compute the set of probabilities $\eta_k(i, m)$ from Equation 2.20 as:

$$\eta_k(j, m) = e^{\frac{-|y_k - L(j,m)|^2}{2\sigma^2}}. \tag{2.51}$$

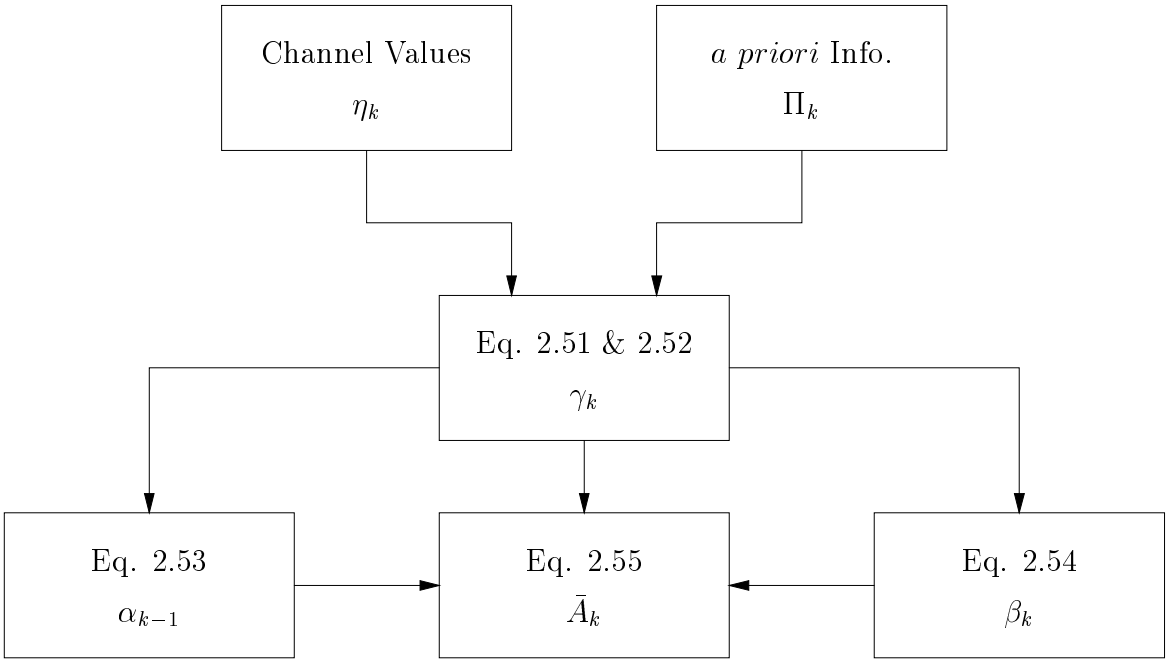

Figure 2.10: Summary of the symbol-based MAP algorithm operations.

From these and the *a priori* probabilities, the $\gamma_k(i,m)$ values are computed according to Equation 2.22 as

$$\gamma_k(j,m) = \Pi_{k,m} \cdot \eta_k(j,m). \tag{2.52}$$

The above values are then used to recursively compute the values $\alpha_{k-1}(j)$ employing Equations 2.46 and 2.47 as

$$\alpha_k(i) = \sum_{m=0}^{M-1} \alpha_{k-1}(P(i,m)) \cdot \gamma_k(P(i,m),m), \tag{2.53}$$

and the values $\beta_k(i)$ using Equations 2.39 and 2.41 as

$$\beta_{k-1}(j) = \sum_{m=0}^{M-1} \beta_k(N(j,m)) \cdot \gamma_k(j,m). \tag{2.54}$$

Finally, the APP can be obtained using Equation 2.23

$$\bar{A}_{k,m} = \Pi_{k,m} \cdot \sum_{j=0}^{S-1} \beta_k(N(j,m)) \cdot \alpha_{k-1}(j) \cdot \eta_k(j,m). \tag{2.55}$$

When considering the implementation of the MAP algorithm, one can opt for computing and storing the $\eta_k(j,m)$ values, and use these values together with the *a priori* probabilities for determining the values $\gamma_k(j,m)$ during decoding. In order to compute the probabilities $\eta_k(j,m)$ it is convenient to separately evaluate the exponential function of Equation 2.51 for every k and for every possible value of the transmitted symbol. As described in Section 2.3.1, a sequence of N information symbols was produced by the information source and each information symbol can assume M possible values, while the number of encoder states is S. There are $\mathsf{M} = 2 \cdot M$ possible transmitted symbols, since the size of the original signal constellation was doubled by the trellis encoder. Thus $N \cdot 2 \cdot M$ evaluations of the exponential function of Equation 2.51 are needed. Using the online computation of the $\gamma_k(j,m)$ values, two multiplications are required for computing one additive term in each of Equation 2.53

and 2.54, and there are $N \cdot S$ terms to be computed, each requiring M terms to be summed. Hence $2 \cdot N \cdot M \cdot S$ multiplications and $N \cdot M \cdot S$ additions are required for computing the forward recursion α or the backward recursion β. Approximately three multiplications are required for computing each additive term in Equation 2.55, and there are $N \cdot M$ terms to be computed, each requiring S terms to be summed. Hence, the total implementational complexity entails $7 \cdot N \cdot M \cdot S$ multiplications, $3 \cdot N \cdot M \cdot S$ summations and $N \cdot 2 \cdot M$ exponential function evaluations, which is directly proportional to the length N of the transmitted sequence, to the number of code states S and to the number of different values M assumed by the input symbols.

The computational complexity can be reduced by implementing the algorithm in the log-domain, where the evaluation of the exponential function in Equation 2.51 is avoided. The multiplications and additions in Equations 2.52 to 2.55 are replaced by additions and Jacobian comparisons, respectively. Hence the total implementational complexity imposed is $7 \cdot N \cdot M \cdot S$ additions and $3 \cdot N \cdot M \cdot S$ Jacobian comparisons.

When implementing the MAP decoder presented here it is necessary to control the dynamic range of the likelihood terms computed in Equations 2.53 to 2.55. This is because these values tend to become lower and lower due to the multiplication of small values. The dynamic range can be controlled by normalising the sum of the $\alpha_k(i)$ and the $\beta_k(i)$ values to unity at every particular k symbol. The resulting symbol values will not be affected, since the normalization only affects the scaling factors C_k in Equation 2.12. However, this problem can be avoided, when the MAP algorithm is implemented in the log-domain.

To conclude, let us note that the MAP decoder presented here is suitable for the decoding of finite-length, preferably short, sequences. When long sequences are transmitted, the employment of this decoder is impractical, since the associated memory requirements increase linearly with the sequence-length. In this case the MAP decoder has to be modified. A MAP decoder designed for long sequences was first presented in [54]. An efficient implementation, derived by adapting the algorithm of [50], was proposed by Piazzo in [55]. Having described the symbol-based MAP algorithm, let us now consider Turbo TCM (TTCM) and the way it invokes the MAP procedure.

2.4 Turbo Trellis-Coded Modulation

2.4.1 TTCM Encoder

It is worth describing the signal set dimensionality ($\bar{D}$) [56, 57] before we proceed. For a specific $2\bar{D}$ code, we have one $2\bar{D}$ symbol per codeword. For a general multidimensional code having a dimensionality of $\mathsf{D} = 2 \cdot n$ where $n > 0$ is an integer, one $\mathsf{D}\bar{D}$ codeword is comprised of n $2\bar{D}$ sub-codewords. The basic concept of the multidimensional signal mapping [56] is to assign more than one $2\bar{D}$ symbol to one codeword, in order to increase the spectral efficiency, which is defined as the number of information bits transmitted per channel symbol. For instance, a $2\bar{D}$ 8PSK TCM code seen in Table 2.2 maps $n = \frac{\mathsf{D}}{2} = 1$ three-bit $2\bar{D}$ symbol to one $2\bar{D}$ codeword, where the number of information bits per $2\bar{D}$ codeword is $\bar{\mathsf{m}} = 2$ yielding a spectral efficiency of $\bar{\mathsf{m}}/n = 2$ information bits per symbol. However, a $4\bar{D}$ 8PSK TCM code seen in Table 2.2 maps $n = \frac{\mathsf{D}}{2} = 2$ three-bit $2\bar{D}$ symbols to one six-bit $4\bar{D}$ codeword using the mapping rule of [56], where the number of information bits

per $4\bar{D}$ codeword is $\bar{\mathsf{m}} = 5$, yielding a spectral efficiency of $\bar{\mathsf{m}}/n = 2.5$ information bits per symbol. However, during our further discourse we only consider $2\bar{D}$ signal sets.

Employing TTCM [38] avoids the obvious disadvantage of rate loss that one would incur when applying the principle of parallel concatenation to TCM without invoking puncturing. Specifically, this is achieved by puncturing the parity information in a particular manner, so that all information bits are sent only once, and the parity bits are provided alternatively by the two component TCM encoders. The TTCM encoder is shown in Figure 2.11, which comprises two identical TCM encoders linked by a symbol interleaver.

Let the memory of the interleaver be N symbols. The number of modulated symbols per block is $N.n$, where $n = \frac{\mathsf{D}}{2}$ is an integer and D is the number of dimensions of the signal set. The number of information bits transmitted per block is $N.\bar{\mathsf{m}}$, where $\bar{\mathsf{m}}$ is the number of information bits per symbol. The encoder is clocked at a rate of $n.T$, where T is the symbol duration of each transmitted $2^{(\bar{\mathsf{m}}+1)/n}$-ary $2\bar{D}$ symbol. At each step, $\bar{\mathsf{m}}$ information bits are input to the TTCM encoder and n symbols each constituted by $\bar{\mathsf{m}}+1$ bits are transmitted, yielding a coding rate of $\frac{\bar{\mathsf{m}}}{\bar{\mathsf{m}}+1}$.

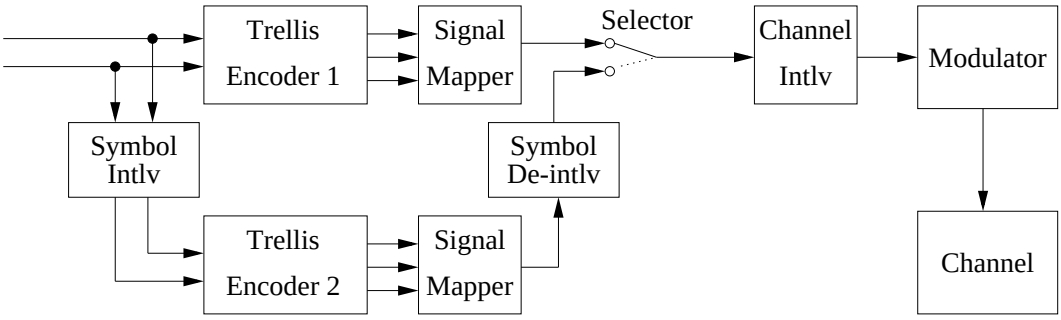

Figure 2.11: Schematic of the TTCM encoder. The selector enables the transmission of the information bits only once and selects alternative parity bits from the constituent encoders seen at the top and bottom [38] ©IEEE, 1998, Robertson and Wörz.

Each component TCM encoder consists of an Ungerböck encoder and a signal mapper. The first TCM encoder operates on the original input bit sequence, while the second TCM encoder manipulates the interleaved version of the input bit sequence. The signal mapper translates the codewords into complex symbols using the SP-based labelling method of Section 2.2.4. A complex symbol represents the amplitude and phase information passed to the modulator in the system seen in Figure 2.11. The complex output symbols of the signal mapper at the bottom of Figure 2.11 are symbol de-interleaved according to the inverse operation of the interleaver. Again, the interleaver and de-interleaver are symbol interleavers [58]. Owing to invoking the de-interleaver of Figure 2.11 at the output of the component encoder seen at the bottom, the TTCM codewords of both component encoders have identical information bits before the selector. Hence, the selector that alternatively selects the symbols of the upper and lower component encoders is effectively a puncturer that punctures the parity bits of the output symbols.

The output of the selector is then forwarded to the channel interleaver, which is, again, another symbol interleaver. The task of the channel interleaver is to effectively disperse the bursty symbol errors experienced during transmission over fading channels. This increases the diversity order of the code [37, 46]. Finally, the output symbols are modulated and transmitted through the channel.

Code	State, ν	$\tilde{\mathsf{m}}$	$H^0(D)$	$H^1(D)$	$H^2(D)$	$H^3(D)$	$d^2_{free}/\triangle^2_0$
$2\bar{D}$, 8PSK	4, 2	2	07	02	04	-	
$2\bar{D}$, 8PSK	8, 3	2	11	02	04	-	3
$4\bar{D}$, 8PSK	8, 3	2	11	06	04	-	3
$2\bar{D}$, 8PSK	16, 4	2	23	02	10	-	3
$4\bar{D}$, 8PSK	16, 4	2	23	14	06	-	3
$2\bar{D}$, 16QAM	8, 3	3	11	02	04	10	2
$2\bar{D}$, 16QAM	16, 4	3	21	02	04	10	3
$2\bar{D}$, 64QAM	8, 3	2	11	04	02	-	3
$2\bar{D}$, 64QAM	16, 4	2	21	04	10	-	4

Table 2.2: 'Punctured' TCM codes exhibiting the best minimum distance for 8PSK, 16QAM and 64QAM, where octal format is used for specifying the generator polynomials [38] ©IEEE, 1998, Robertson and Wörz. The notation $\bar{D}$ denotes the dimensionality of the code, ν denotes the code memory, $\triangle^2_0$ denotes the squared Euclidean distance of the signal set itself and d^2_{free} denotes the squared FED of the TCM code.

Table 2.2 shows the generator polynomials of some component TCM codes that can be employed in the TTCM scheme. These generator polynomials were obtained by Robertson and Wörz [38] using an exhaustive computer search of all polynomials and finding the one that maximises the minimal Euclidean distance, taking also into account the alternative selection of parity bits for the TTCM scheme. In Table 2.2, $\tilde{\mathsf{m}}$ denotes the number of information bits to be encoded out of the total $\bar{\mathsf{m}}$ information bits in a symbol, $\triangle^2_0$ denotes the squared Euclidean distance of the signal set itself, i.e. after TCM signal expansion, and d^2_{free} denotes the squared FED of the TCM constituent codes, as defined in Section 2.2.1. Since $d^2_{free}/\triangle^2_0 > 0$, the 'punctured' TCM codes constructed in Table 2.2 exhibit a positive coding gain in comparison to the uncoded but expanded signal set, although not necessarily in comparison to the uncoded and unexpanded original signal set. Nonetheless, the design target is to provide a coding gain also in comparison to the uncoded and unexpanded original signal set at least for the targeted operational SNR range of the system.

Considering the 8PSK example of Table 2.2, where $\triangle^2_0 = d^2_{8PSK}$ applies, we have $d^2_{free}/d^2_{8PSK} = 3$. However, when we compare the 'punctured' 8PSK TCM codes to the original uncoded QPSK, signal set we have $d^2_{free}/d^2_{QPSK} = d^2_{free}/2 = 0.878$ [38], which implies attaining a negative coding gain. However, when the iterative decoding scheme of TTCM is invoked, we attain a significant positive coding gain, as we will demonstrate in the following chapters.

2.4.2 TTCM Decoder

The concept of *a priori*, *a posteriori* and *extrinsic* information is illustrated in Figure 2.12. The associated concept is portrayed in more detail in Figure 2.13. The TTCM decoder structure of Figure 2.13(b) is similar to that of binary turbo codes shown in Figure 2.13(a), except that there is a difference in the nature of the information passed from one decoder to the other and in the treatment of the very first decoding step. Specifically, each decoder alternately processes its corresponding encoder's channel-impaired output symbol, and then the other encoder's channel-impaired output symbol.

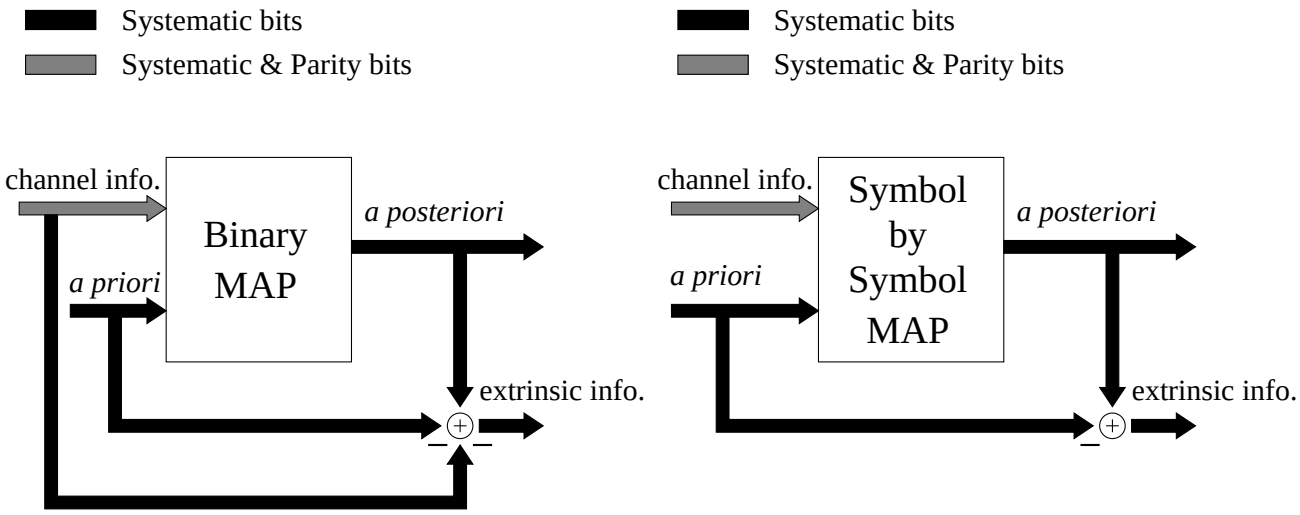

(a) A binary turbo component decoder.

(b) A non-binary TTCM component decoder.

Figure 2.12: Schematic of the component decoders for binary turbo codes and non-binary TTCM.

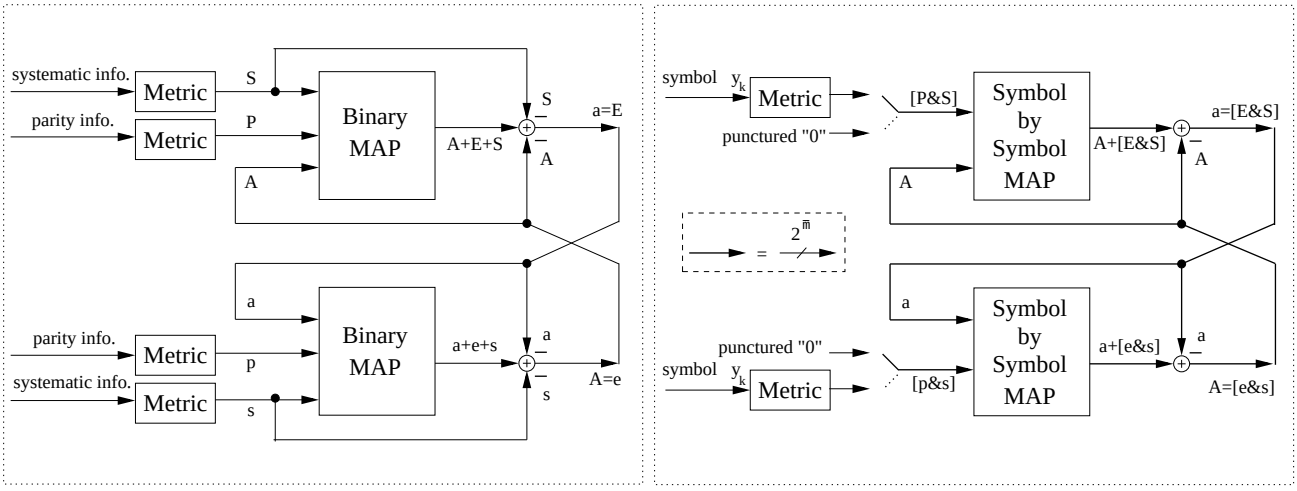

(a) Binary Turbo Decoder at step k

(b) TTCM Decoder at step k

Figure 2.13: Schematic of the decoders for binary turbo codes and TTCM. Note that the labels and arrows apply only to one specific information bit for the binary turbo decoder, or a group of $\bar{m}$ information bits for the TTCM decoder [38] ©IEEE, 1998, Robertson and Wörz. The interleavers/de-interleavers are not shown and the notations P, S, A and E denote the parity information, systematic information, *a priori* probabilities and *extrinsic* probabilities, respectively. Upper (lower) case letters represent the probabilities of the upper (lower) component decoder.

In a binary turbo coding scheme the component encoders' output can be split into three additive parts for each information bit u_k at step k, when operating in the logarithmic or LLR domain [53] as shown in Figure 2.13(a), which are:

1. the systematic component (S/s), i.e. the corresponding received systematic value for bit u_k;
2. the *a priori* or *intrinsic* component (A/a), i.e. the information provided by the other component decoder for bit u_k; and
3. the *extrinsic* information component related to bit u_k (E/e), which depends not on bit u_k itself but on the surrounding bits.

These components are impaired by independent noise and fading effects. In turbo codes, only the *extrinsic* component should be passed on to the other component decoder, so that the *intrinsic* information directly related to a bit is not reused in the other component decoder [11]. This measure is necessary in turbo codes for avoiding the prevention of achieving iterative gains, due to the dependence of the constituent decoders' information on each other.

However, in a symbol-based non-binary TTCM scheme the $\bar{\mathsf{m}}$ systematic information bits and the parity bit are transmitted together in the same non-binary symbol. Hence, the systematic component of the non-binary symbol, namely the original information bits, cannot be separated from the *extrinsic* component, since the noise and/or fading that affects the parity component also affects the systematic component. Therefore, in this scenario the symbol-based information can be split into only two components:

1. the *a priori* component of a non-binary symbol (A/a), which is provided by the other component decoder, and
2. the inseparable *extrinsic* as well as systematic component of a non-binary symbol ($[E\&S]/[e\&s]$), as can be seen from Figure 2.13(b).

Each decoder passes only the latter information to the next component decoder while the *a priori* information is removed at each component decoder's output, as seen in Figure 2.13(b), where, again, the *extrinsic* and systematic components are inseparable.

As described in Section 2.4.1, the number of modulated symbols per block is $N \cdot n$, with $n = \frac{\mathsf{D}}{2}$, where D is the number of dimensions of the signal set. Hence for a $2\bar{D}$ signal set we have $n = 1$ and the number of modulated symbols per block is N. Therefore the symbol interleaver of length N will interleave a block of N complex symbols. Let us consider $2\bar{D}$ modulation having a coding rate of $\frac{\bar{\mathsf{m}}}{\bar{\mathsf{m}}+1}$ for the following example.

The received symbols are input to the 'Metric' block of Figure 2.14, in order to generate a set of $\mathsf{M} = 2^{\bar{\mathsf{m}}+1}$ symbol probabilities for quantifying the likelihood that a certain symbol of the M-ary constellation was transmitted. The selector switches seen at the input of the 'Symbol by Symbol MAP' decoder select the current symbol's reliability metric, which is produced at the output of the 'Metric' block, if the current symbol was not punctured by the corresponding encoder. Otherwise puncturing will be applied where the probabilities of the various legitimate symbols at index k are set to 1 or

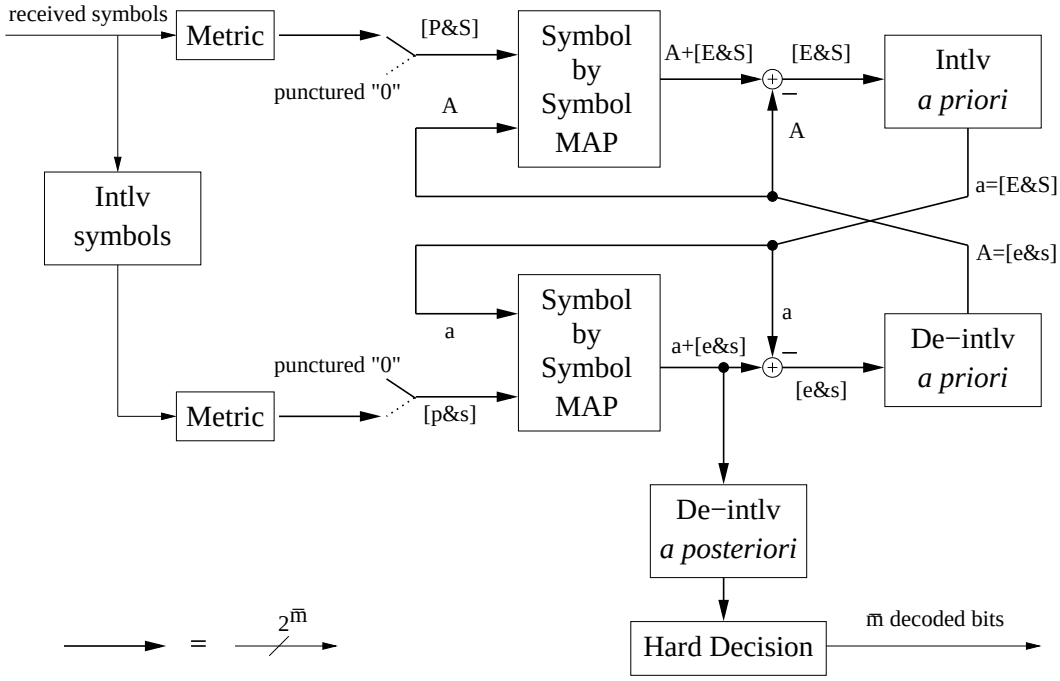

Figure 2.14: Schematic of the TTCM decoder. P, S, A and E denote the parity information, systematic information, *a priori* probabilities and *extrinsic* probabilities, respectively. Upper (lower) case letters represent the probabilities of the upper (lower) component decoder.

to 0 in the log-domain. The upper (lower) case letters denote the set of probabilities of the upper (lower) component decoder, as shown in the figure. The 'Metric' block provides the decoder with the inseparable parity and systematic ($[P\&S]$ *or* $[p\&s]$) information, and the second input to the decoder is the *a priori* (A *or* a) information provided by the other component decoder. The MAP decoder then provides the *a posteriori* ($A + [E\&S]$ *or* $a + [e\&s]$) information at its output. Then A (*or* a) is subtracted from the *a posteriori* information, so that the same information is not used more than once in the other component decoder, since otherwise the component decoders' corresponding information would become dependent on each other, which would preclude the achievement of iteration gains. The resulting $[E\&S$ *or* $e\&s]$ information is symbol interleaved (or de-interleaved) in order to present the a (*or* A) input for the other component decoder in the required order. This decoding process will continue iteratively, in order to offer an improved version of the set of symbol reliabilities for the other component decoder. One iteration comprises the decoding of the received symbols by both the component decoders once. Finally, the *a posteriori* information of the lower component decoder will be de-interleaved in order to extract $\bar{m}$ decoded information bits per symbol. Hard decision implies selecting the specific symbol which exhibits the maximum *a posteriori* probability associated with the $\bar{m}$-bit information symbol out of the $2^{\bar{m}}$ probability values. Having described the operation of the symbol-based TTCM technique, which does not protect all transmitted bits of the symbols, let us now consider bit-interleaved coded modulation as a design alternative.

2.5 Bit-Interleaved Coded Modulation

Bit-Interleaved Coded Modulation (BICM) was proposed by Zehavi [9] with the aim of increasing the diversity order of Ungerböck's TCM schemes which was quantified in Section 2.2.3. Again, the

diversity order of a code is defined as the 'length' of the shortest error event path expressed in terms of the number of trellis stages encountered, before remerging with the all-zero path [46] or, equivalently, defined as the minimum Hamming distance of the code [10] where the diversity order of TCM using a symbol-based interleaver is the minimum number of different symbols between the erroneous path and the correct path along the shortest error event path. Hence, in a TCM scenario having parallel transitions, as shown in Figure 2.4, the code's diversity order is one, since the shortest error event path consists of one branch. This implies that parallel transitions should be avoided in TCM codes if it was possible, and if there were no parallel branches, any increase in diversity would be obtained by increasing the constraint length of the code. Unfortunately no TCM codes exist where the parallel transitions associated with the unprotected bits are avoided. In order to circumvent this problem, Zehavi's idea [9] was to render the code's diversity equal to the smallest number of different bits, rather than to that of the different channel symbols, by employing bit-based interleaving, as will be highlighted below.

2.5.1 BICM Principle

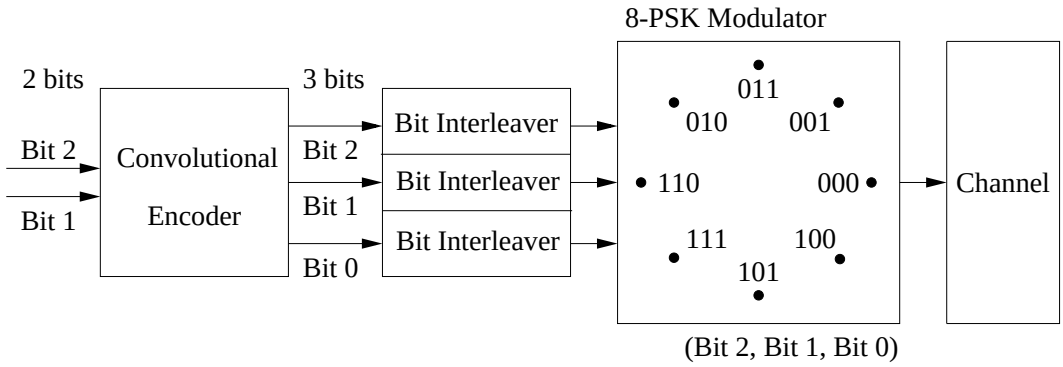

Figure 2.15: BICM encoder schematic employing independent bit interleavers and and protecting all transmitted bits. Instead of the SP-based labelling of TCM in Figure 2.1 here Gray labelling is employed [9] ©IEEE, 1992, Zehavi.

The BICM encoder is shown in Figure 2.15. In comparison to the TCM encoder of Figure 2.5, the differences are that BICM uses independent bit interleavers for all the bits of a symbol and non-systematic convolutional codes, rather than a single symbol-based interleaver and systematic RSC codes protecting some of the bits. The number of bit interleavers equals the number of bits assigned to the non-binary codeword. The purpose of bit interleaving is:

- to disperse the bursty errors induced by the correlated fading and to maximise the diversity order of the system;
- to render the bits associated with a given transmitted symbol uncorrelated or independent of each other.

The interleaved bits are then grouped into non-binary symbols, where Gray-coded labelling is used for the sake of optimising the performance of the BICM scheme. The BICM encoder uses Paaske's non-systematic convolutional code proposed on page 331 of [59], which exhibits the highest possible free Hamming distance, hence attaining optimum performance over Rayleigh fading channels. Figure

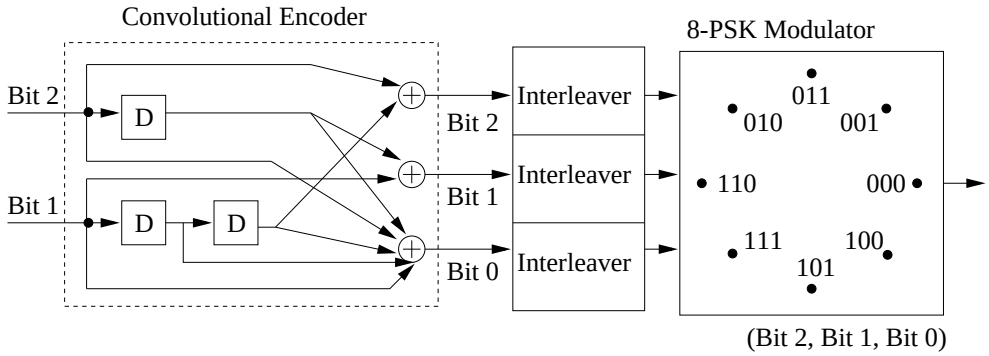

Figure 2.16: Paaske's non-systematic convolutional encoder, bit-based interleavers and modulator forming the BICM encoder [9,59], where none of the bits are unprotected and instead of the SP-based labelling as seen in Figure 2.1 here Gray labelling is employed.

2.16 shows Paaske's non-systematic eight-state code of rate-2/3, exhibiting a free bit-based Hamming distance of four. The BICM decoder implements the inverse process, as shown in Figure 2.17. In the

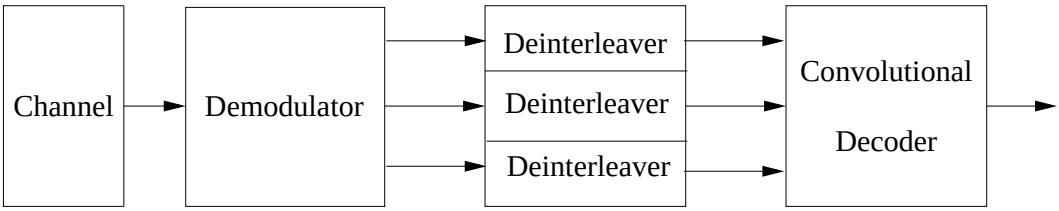

Figure 2.17: BICM decoder [9].

demodulator module six bit metrics associated with the three bit positions, each having binary values of 0 and 1, are generated from each channel symbol. These bit metrics are de-interleaved by three independent bit de-interleavers, in order to form the estimated codewords. Then the convolutional decoder of Figure 2.17 is invoked for decoding these codewords, generating the best possible estimate of the original information bit sequence.

From Equation 2.5 we know that the average bit error probability of a coded modulation scheme using MPSK over Rayleigh fading channels at high SNRs is inversely proportional to $(E_s/N_0)^{\mathsf{L}}$, where E_s/N_0 is the channel's symbol energy to noise spectral density ratio and L is the minimum Hamming distance or the code's diversity order. When bit-based interleavers are employed in BICM instead of the symbol-based interleaver employed in TCM, the minimum Hamming distance of BICM is quantified in terms of the number of different bits between the erroneous path in the shortest error event and the correct path. Since in BICM the bit-based minimum Hamming distance is maximised, BICM will give a lower bit error probability in Rayleigh fading channels than that of TCM that maximises the FED. Again, the design of BICM is aimed at providing maximum minimum Hamming distance, rather than providing maximum FED, as in TCM schemes. Moreover, we note that attaining a maximum FED is desired for transmission over Gaussian channels, as shown in Section 2.2.1. Hence, the performance of BICM is not as good as that of TCM in AWGN channels. The reduced FED of BICM is due to the 'random' modulation imposed by the 'random' bit interleavers [9], where the m-bit BICM symbol is randomised by the m number of bit interleavers. Again, $\bar{\mathsf{m}}$ denotes the number of information bits, while m denotes the total number of bits in a 2^{m}-ary modulated symbol.

Table 2.3 summarises the parameters of a range of Paaske's non-systematic codes utilised in BICM.

Rate	State, ν	$g^{(1)}$	$g^{(2)}$	$g^{(3)}$	$g^{(4)}$	d_{free}
1/2	8, 3	15	17	-	-	5
(4QAM)	16, 4	23	35	-	-	7
	64, 6	133	171	-	-	10
2/3	8, 3	4	2	6	-	4
(8PSK)		1	4	7	-	
	16, 4	7	1	4	-	5
		2	5	7	-	
	64, 6	64	30	64	-	7
		30	64	74	-	
3/4	8, 3	4	4	4	4	4
(16QAM)		0	6	2	4	
		0	2	5	5	
	32, 5	6	2	2	6	5
		1	6	0	7	
		0	2	5	5	
	64, 6	6	1	0	7	6
		3	4	1	6	
		2	3	7	4	

Table 2.3: Paaske's non-systematic convolutional codes, page 331 of [59], where ν denotes the code memory and d_{free} denotes the free Hamming distance. Octal format is used for representing the generator polynomial coefficients.

Rate	State, ν	$g^{(1)}$	$g^{(2)}$	puncturing matrix	d_{free}
5/6	8, 3	15	17	1 0 0 1 0	3
(64QAM)				0 1 1 1 1	
	64, 6	133	171	1 1 1 1 1	3
				1 0 0 0 0	

Table 2.4: Rate-Compatible Punctured Convolutional (RCPC) codes [60, 61], where ν denotes the code memory and d_{free} denotes the free Hamming distance. Octal format is used for representing the generator polynomial coefficients.

For a rate-k/n code there are k generator polynomials, each having n coefficients. For example, $\mathbf{g_i} = (g^0,\ g^1,\ \ldots,\ g^n),\ i \leq k$, is the generator polynomial associated with the ith information bit. The generator matrix of the encoder seen in Figure 2.16 is:

$$\mathbf{G(D)} = \begin{bmatrix} 1 & D & 1+D \\ D^2 & 1 & 1+D+D^2 \end{bmatrix}, \tag{2.56}$$

while the equivalent polynomial expressed in octal form is given by:

$$\mathbf{g_1} = \begin{bmatrix} 4 & 2 & 6 \end{bmatrix} \quad \mathbf{g_2} = \begin{bmatrix} 1 & 4 & 7 \end{bmatrix}. \tag{2.57}$$

Observe in Table 2.3 that Paaske generated codes of rate-1/2, 2/3 and 3/4, but not 5/6. In order to study rate-5/6 BICM/64QAM, we created the required punctured code from the rate-1/2 code of Table 2.3. Table 2.4 summarises the parameters of the Rate-Compatible Punctured Convolutional (RCPC) codes that can be used in rate=5/6 BICM/64QAM schemes. Specifically, rate-1/2 codes were punctured according to the puncturing matrix of Table 2.4 in order to obtain the rate-5/6 codes, following the approach of [60, 61]. Let us now consider the operation of BICM with the aid of an example.

2.5.2 BICM Coding Example

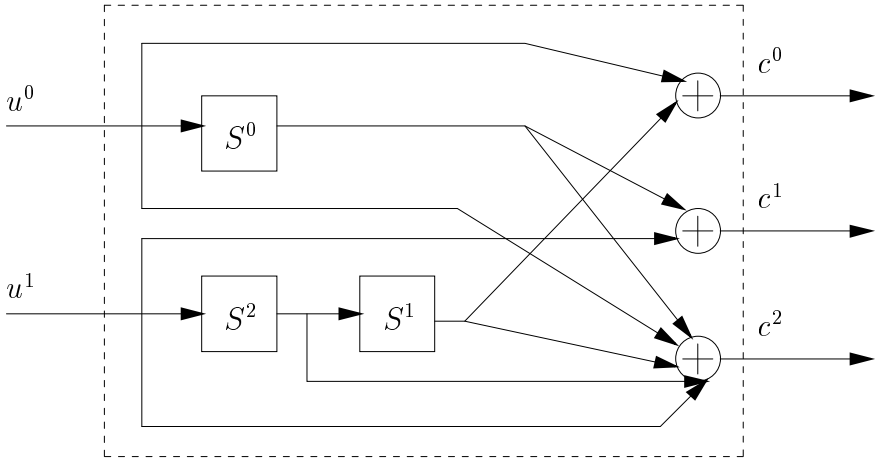

Figure 2.18: Paaske's non-systematic convolutional encoder [59].

Considering Paaske's eight-state convolutional code [59] in Figure 2.18 as an example, the BICM encoding process is illustrated here. The corresponding generator polynomial is shown in Equation 2.57. A two-bit information word, namely $u = (u^1,\ u^0)$, is encoded in each cycle in order to form a three-bit codeword, $c = (c^2,\ c^1,\ c^0)$. The encoder has three shift registers, namely S^0, S^1 and S^2, as shown in the figure. The three-bit binary contents of these registers represent eight states, as follows:

$$S = (S^2,\ S^1,\ S^0) \in \{000,\ 001,\ \ldots,\ 111\} = \{0,\ 1,\ \ldots,\ 7\}. \tag{2.58}$$

The input sequence, u, generates a new state S and a new codeword c at each encoding cycle. Table 2.5 illustrates the codewords generated and the associated state transitions. The encoding process can also be represented with the aid of the trellis diagram of Figure 2.19. Specifically, the top part of Table 2.19 contains the codewords $c = (c^2,\ c^1, c^0)$ as a function of the encoder state

State $S = (S^2, S^1, S^0)$	Information Word $u = (u^1,\ u^0)$			
	$00 = 0$	$01 = 1$	$10 = 2$	$11 = 3$
$000 = 0$	$000 = 0$	$101 = 5$	$110 = 6$	$011 = 3$
$001 = 1$	$110 = 6$	$011 = 3$	$000 = 0$	$101 = 5$
$010 = 2$	$101 = 5$	$000 = 0$	$011 = 3$	$110 = 6$
$011 = 3$	$011 = 3$	$110 = 6$	$101 = 5$	$000 = 0$
$100 = 4$	$100 = 4$	$001 = 1$	$010 = 2$	$111 = 7$
$101 = 5$	$010 = 2$	$111 = 7$	$100 = 4$	$001 = 1$
$110 = 6$	$001 = 1$	$100 = 4$	$111 = 7$	$010 = 2$
$111 = 7$	$111 = 7$	$010 = 2$	$001 = 1$	$100 = 4$
Codeword $c = (c^2,\ c^1, c^0)$				
$000 = 0$	$000 = 0$	$001 = 1$	$100 = 4$	$101 = 5$
$001 = 1$	$000 = 0$	$001 = 1$	$100 = 4$	$101 = 5$
$010 = 2$	$000 = 0$	$001 = 1$	$100 = 4$	$101 = 5$
$011 = 3$	$000 = 0$	$001 = 1$	$100 = 4$	$101 = 5$
$100 = 4$	$010 = 2$	$011 = 3$	$110 = 6$	$111 = 7$
$101 = 5$	$010 = 2$	$011 = 3$	$110 = 6$	$111 = 7$
$110 = 6$	$010 = 2$	$011 = 3$	$110 = 6$	$111 = 7$
$111 = 7$	$010 = 2$	$011 = 3$	$110 = 6$	$111 = 7$
Next State $S = (S^2,\ S^1,\ S^0)$				

Table 2.5: The codeword generation and state transition table of the non-systematic convolutional encoder of Figure 2.18. The state transition diagram is seen in Figure 2.19.

$S = (S^2, S^1, S^0)$ as well as that of the information word $u = (u^1,\ u^0)$, while the bottom section contains the next states, again as a function of S and u. For example, if the input is $u = (u^1,\ u^0) = (1, 1) = 3$ when the shift register is in state $S = (S^2, S^1, S^0) = (1, 1, 0) = 6$, the shift register will change its state to state $S = (S^2, S^1, S^0) = (1, 1, 1) = 7$ and $c = (c^2,\ c^1, c^0) = (0, 1, 0) = 2$ will be the generated codeword. Hence, if the input binary sequence is $\{01\ 10\ 01\ 00\ 10\ 10 \rightarrow\}$ with the rightmost being the first input bit, the corresponding information words are $\{1\ 2\ 1\ 0\ 2\ 2 \rightarrow\}$. Before any decoding takes place, the shift register is initialised to zero. Therefore, as seen at the right of Figure 2.19, when the first information word of $u_1 = 2$ arrives, the state changes from $S^{-1} = 0$ to $S = 4$, generating the first codeword $c_1 = 6$ as seen in the bottom and top sections of Table 2.5, respectively. Then the second information word of $u_2 = 2$ changes the state from $S^{-1} = 4$ to $S = 6$, generating the second codeword of $c_2 = 2$. The process continues in a similiar manner according to the transition table, namely Table 2.5. The codewords generated as seen at the right of Figure 2.19 are $\{4\ 0\ 0\ 1\ 2\ 6 \rightarrow\}$, and the state transitions are $\{2 \leftarrow 4 \leftarrow 1 \leftarrow 2 \leftarrow 6 \leftarrow 4 \leftarrow 0\}$. Then the bits constituting the codeword sequence are interleaved by the three bit interleavers of Figure 2.16, before they are assigned to the corresponding 8PSK constellation points.

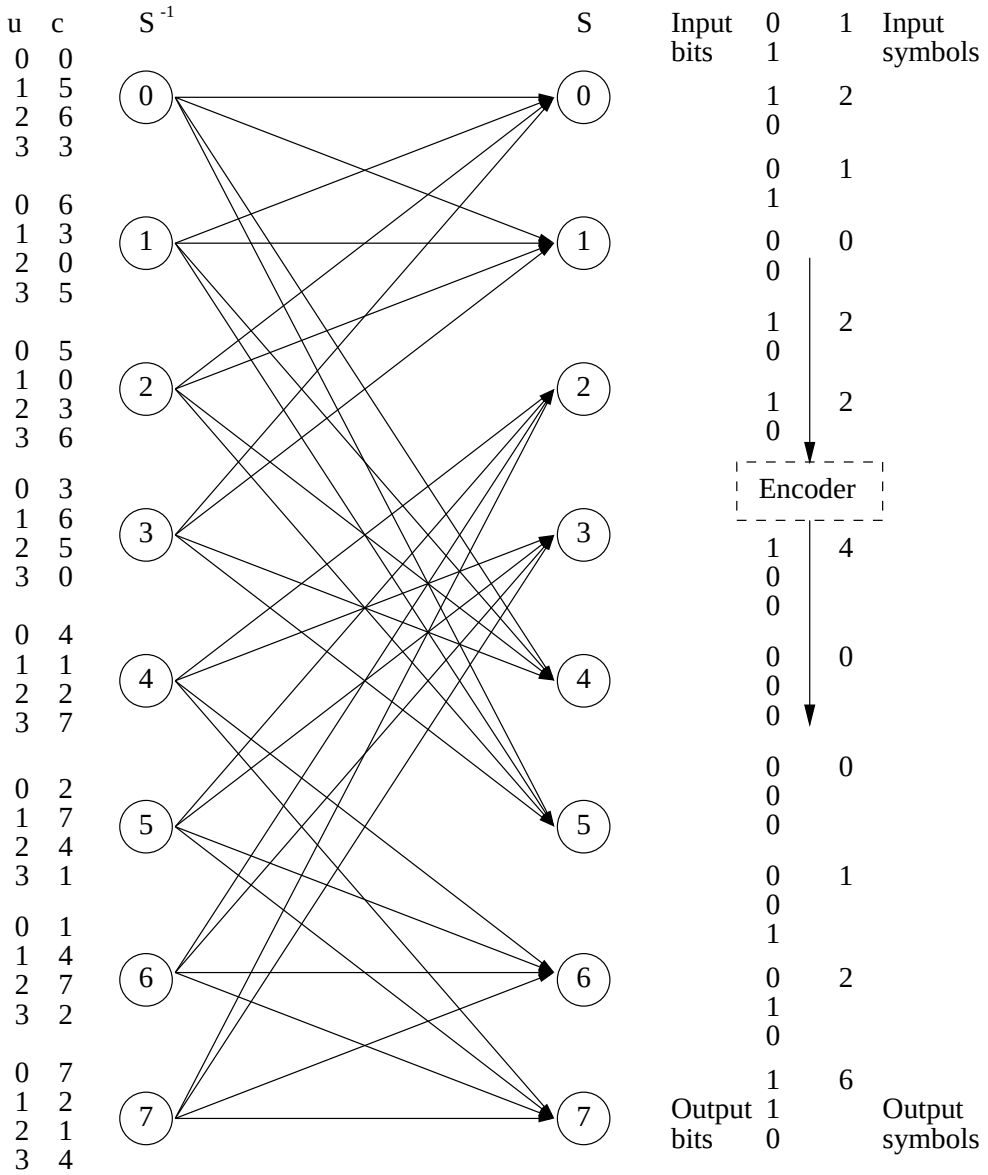

Figure 2.19: Trellis diagram for Paaske's eight-state convolutional code, where u indicates the information word, c indicates the codeword, S^{-1} indicates the previous state and S indicates the current state. As an example, the encoding of the input bit sequence of $\{011001001010 \rightarrow\}$ is shown at the right. The encoder schematic is portrayed in Figure 2.18, while the state transitions are summarised in Table 2.5.

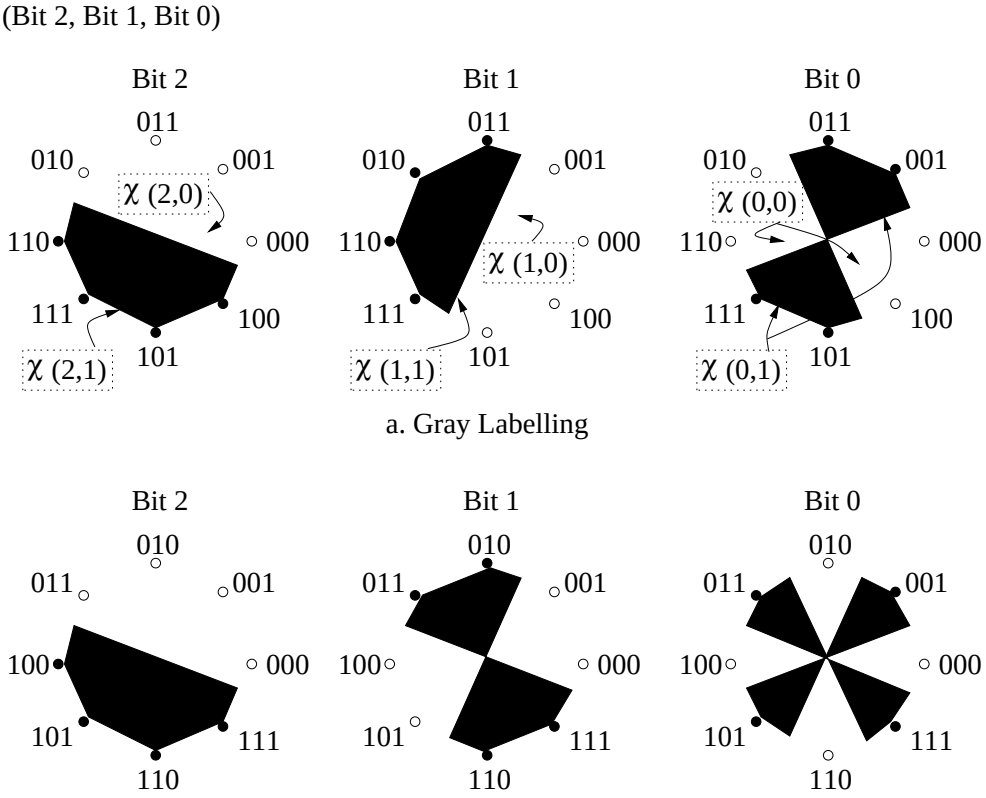

Figure 2.20: SP and Gray labelling methods for 8PSK and the corresponding subset partitioning for each bit, where $\chi(i,b)$ defined in Equation 2.64 refers to the subset of the modulation constellation for Bit i where Bit $i = b \in \{0,1\}$ [18] ©IEEE, 1999, Li and Ritcey.

2.6 Bit-Interleaved Coded Modulation with Iterative Decoding

BICM using Iterative Decoding (BICM-ID) was proposed by Li [18,39] for further improving the FED of Zehavi's BICM scheme, although BICM already improved the diversity order of Ungerböck's TCM scheme. This FED improvement can be achieved with the aid of combining SP-based constellation labelling, as in TCM, and by invoking soft-decision feedback from the decoder's output to the demodulator's input, in order to exchange soft-decision-based information between them. As we will see below, this is advantageous, since upon each iteration the channel decoder improves the reliability of the soft information passed to the demodulator.

2.6.1 Labelling Method

Let us now consider the mapping of the interleaved bits to the phasor constellation in this section. Figure 2.20 shows the process of subset partitioning for each of the three bit positions for both Gray labelling and in the context of SP labelling. The shaded regions shown inside the circle correspond to the subset $\chi(i,1)$ defined in Equation 2.64, and the unshaded regions to $\chi(i,0)$, $i = 0,1,2$, where i indicates the bit position in the three-bit BICM/8PSK symbol. These are also the decision regions for each bit, if hard-decision-based BICM demodulation is used for detecting each bit individually. The two labelling methods seen in Figure 2.20 have the same intersubset distances, although a different

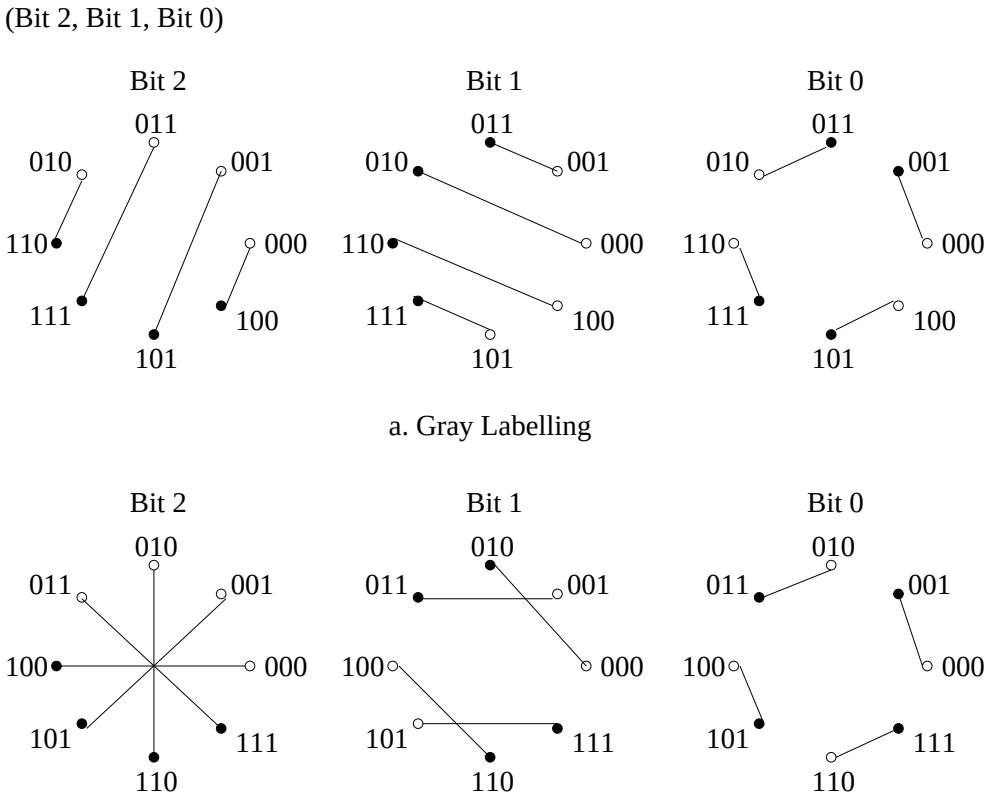

Figure 2.21: Iterative decoding translates the 8PSK scheme into three parallel binary sub-channels, each associated with a BPSK constellation selected from the four possible signal sets [18] ©IEEE, 1999, Li and Ritcey.

number of nearest neighbours. For example, $\chi(0,1)$, which denotes the region where bit 0 equals to 1, is divided into two regions in the context of Gray labelling, as can be seen in Figure 2.20(a). By contrast, in the context of SP labelling seen in Figure 2.20(b), $\chi(0,1)$ is divided into four regions. Clearly, Gray labelling has a lower number of nearest neighbours compared to SP-based labelling. The higher the number of nearest neighbours, the higher the chances for a bit to be decoded into the wrong region. Hence, Gray labelling is a more appropriate mapping during the first decoding iteration, and hence it was adopted by the non-iterative BICM scheme of Figure 2.17.

During the second decoding iteration in BICM-ID, given the feedback information representing Bit 1 and Bit 2 of the coded symbol, the constellation associated with Bit 0 is confined to a pair of constellation points, as shown at the right of Figure 2.21. Therefore, as far as Bit 0 is concerned, the 8PSK phasor constellation is translated into four binary constellations, where one of the four possible specific BPSK constellations is selected by the feedback Bit 1 and Bit 2. The same is true for the constellations associated with both Bit 1 and Bit 2, given the feedback information of the corresponding other two bits.

In order to optimise the second-pass decoding performance of BICM-ID, one must maximise the minimum Euclidean distance between any two points of all the $2^{m-1} = 4$ possible phasor pairs at the left (Bit 2), centre (Bit 1) and the right (Bit 0) of Figure 2.21. Clearly, SP-based labelling serves this aim better, when compared to Gray labelling, since the corresponding minimum Euclidean distance of

SP-based labelling is higher than that of Gray labelling for both Bit 1 and Bit 2, as illustrated at the left and the centre of Figure 2.21. Although the first-pass performance is important, in order to prevent error precipitation due to erroneous feedback bits, the error propagation is effectively controlled by the soft feedback of the decoder. Therefore, BICM-ID assisted by soft decision feedback uses SP labelling.

Specifically, the desired high Euclidean distance for Bit 2 in Figure 2.21(b) is only attainable when Bit 1 and Bit 0 are correctly decoded and fed back to the SP-based demodulator. If the values to be fed back are not correctly decoded, the desired high Euclidean distance will not be achieved and error propagation will occur. On the other hand, an optimum convolutional code having a high binary Hamming distance is capable of providing a high reliability for the decoded bits. Therefore, an optimum convolutional code using appropriate signal labelling is capable of 'indirectly' translating the high binary Hamming distance between coded bits into a high Euclidean distance between the phasor pairs portrayed in Figure 2.21. In short, BICM-ID converts a 2^{m}-ary signalling scheme to m independent parallel binary schemes by the employment of m number of independent bit interleavers and involves an iterative decoding method. This simultaneously facilitates attaining a high diversity order with the advent of the bit interleavers, as well as achieving a high FED with the aid of the iterative decoding and SP-based labelling. Hence, BICM-ID effectively combines powerful binary codes with bandwidth-efficient modulation.

2.6.2 Interleaver Design

The interleaver design is important as regards the performance of BICM-ID. In [40], Li introduced certain constraints on the design of the interleaver, in order to maximise the minimum Euclidean distance between the two points in the $2^{\mathsf{m}-1}$ possible specific BPSK constellations. However, we advocate a more simple approach, where the m number of interleavers used for the 2^{m}-ary modulation scheme are generated randomly and separately, without any interactions between them. The resultant minimum Euclidean distance is less than that of the scheme proposed in [40], but the error bursts inflicted by correlated fading are expected to be randomised effectively by the independent bit interleavers. This was expected to give a better performance over fading channels at the cost of a slight performance degradation over AWGN channels, when compared to Li's scheme [40]. However, as we will demonstrate in the context of our simulation results in Section 3.2.2, our independent random interleaver design and Li's design perform similarly.

Having described the labelling method and the interleaver design in the context of BICM-ID, let us now consider the operation of BICM-ID with the aid of an example.

2.6.3 BICM-ID Coding Example

The BICM-ID scheme using soft-decision feedback is shown in Figure 2.22. The interleavers used are all bit-based, as in the BICM scheme of Figure 2.16, although for the sake of simplicity here only one interleaver is shown. A Soft-Input Soft-Output (SISO) [62] decoder is used in the receiver module and the decoder's output is fed back to the input of the demodulator. The SISO decoder of the BICM-ID scheme is actually a MAP decoder that computes the *a posteriori* probabilities for the non-systematically channel-coded bits and the original information bits.

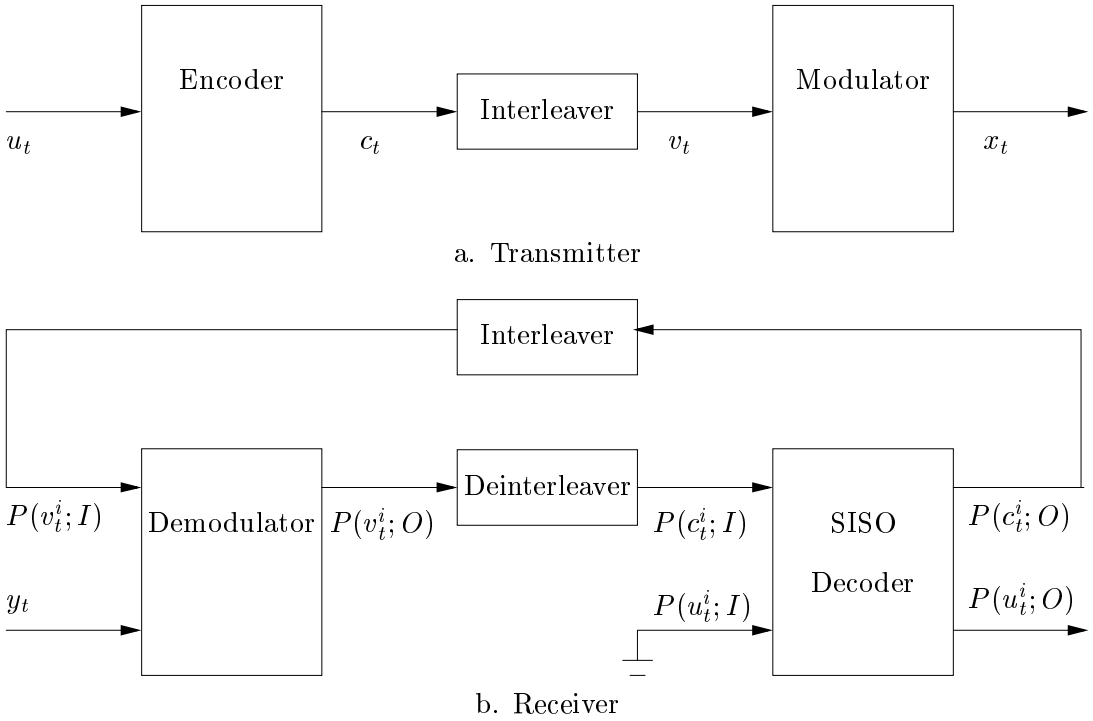

Figure 2.22: The transmitter and receiver modules of the BICM-ID scheme using soft-decision feedback [39] ©IEEE, 1998, Li.

For an $(n,\ k)$ binary convolutional code the encoder's input symbol at time t is denoted by $u_t = [u_t^0,\ u_t^1,\ \ldots,\ u_t^{k-1}]$ and the coded output symbol by $c_t = [c_t^0,\ c_t^1,\ \ldots,\ c_t^{n-1}]$, where u_t^i or c_t^i is the ith bit in a symbol as defined in the context of Table 2.5 and Figure 2.19. The coded bits are interleaved by m independent bit interleavers, then m interleaved bits are grouped together in order to form a channel symbol $v_t = [v_t^0,\ v_t^1,\ \ldots,\ v^{\mathsf{m}-1}]$ as seen in Figure 2.22(a), for transmission using 2^{m}-ary modulation. Let us consider 8PSK modulation, i.e. $\mathsf{m} = 3$ as an example.

A signal labelling method μ maps the symbol v_t to a complex phasor according to $x_t = \mu(v_t)$, $x_t \in \chi$, where the 8PSK signal set is defined as $\chi = \{\sqrt{E_s}\ e^{j2n\pi/8},\ n = 0, \ldots, 7\}$ and E_s is the energy per transmitted symbol. In conjunction with a rate-2/3 code, the energy per information bit is $E_b = E_s/2$. For transmission over Rayleigh fading channels using coherent detection, the received discrete time signal is:

$$y_t = \rho_t x_t + n_t, \tag{2.59}$$

where ρ_t is the Rayleigh-distributed fading amplitude [15] having an expectation value of $\mathrm{E}[\rho_t^2] = 1$, while n_t is the complex AWGN exhibiting a variance of $\sigma^2 = N_0/2$ where N_0 is the noise's PSD. For AWGN channels we have $\rho_t = 1$ and the Probability Density Function (PDF) of the non-faded but noise-contaminated received signal is expressed as [52]:

$$P(y_t|x_t, \rho_t) = \frac{1}{2\pi\sigma^2}\ e^{-\frac{1}{2}\left(\frac{n_t}{\sigma}\right)^2}, \tag{2.60}$$

where $\sigma^2 = N_0/2$ and the constant multiplicative factor of $\frac{1}{2\pi\sigma^2}$ does not influence the shape of the distribution and hence can be ignored when calculating the branch transition metric η, as described in Section 2.3.5. For AWGN channels, the conditional PDF of the received signal can be written as:

$$P(y_t|x_t) = e^{-\frac{|y_t\ -\ x_t|^2}{2\sigma^2}}. \tag{2.61}$$

Considering AWGN channels, the demodulator of Figure 2.22(b) takes y_t as its input for computing the confidence metrics of the bits using the maximum APP criterion [19]:

$$P(v_t^i = b|y_t) = \sum_{x_t \in \chi(i,b)} P(x_t|y_t), \tag{2.62}$$

where $i \in \{0,1,2\}$, $b \in \{0,1\}$ and $x_t = \mu(v_t)$. Furthermore, the signal after the demodulator of Figure 2.22 is described by the demapping of the bits $[\nabla^0(x_t), \nabla^1(x_t), \nabla^2(x_t)]$ where $\nabla^i(x_t) \in \{0,1\}$ is the value of the ith bit of the three-bit label assigned to x_t. With the aid of Bayes' rule in Equations 2.15 to 2.17 we obtain:

$$P(v_t^i = b|y_t) = \sum_{x_t \in \chi(i,b)} P(y_t|x_t)P(x_t), \tag{2.63}$$

where the subset $\chi(i,b)$ is described as:

$$\chi(i,b) = \{\mu([\nabla^0(x_t), \nabla^1(x_t), \nabla^2(x_t)]) \mid \nabla^j(x_t) \in \{0,1\}, j \neq i\}, \tag{2.64}$$

which contains all the phasors for which $\nabla^i(x_t) = b$ holds. For 8PSK, where $\mathsf{m} = 3$, the size of each such subset is $2^{\mathsf{m}-1} = 4$ as portrayed in Figure 2.20. This implies that only the *a priori* probabilities of $\mathsf{m} - 1 = 2$ bits out of the total of $\mathsf{m} = 3$ bits per channel symbol have to be considered, in order to compute the bit metric of a particular bit.

Now using the notation of Benedetto *et al.* [62], the *a priori* probabilities of an original uncoded information bit at time index t and bit index i, namely u_t^i being 0 and 1, are denoted by $P(u_t^i = 0; I)$ and $P(u_t^i = 1; I)$ respectively, while I refers to the *a prIori* probabilities of the bit. This notation is simplified to $P(u_t^i; I)$, when no confusion arises, as shown in Figure 2.22. Similarly, $P(c_t^i; I)$ denotes the *a priori* probabilities of a legitimate coded bit at time index t and position index i. Finally, $P(u_t^i; O)$ and $P(c_t^i; O)$ denote the *extrinsic a pOsteriori* information of the original information bits and coded bits, respectively.

The *a priori* probability $P(x_t)$ in Equation 2.63 is unavailable during the first-pass decoding, hence an equal likelihood is assumed for all the 2^{m} legitimate symbols. This renders the *extrinsic a posteriori* bit probabilities, $P(v_t^i = b; O)$, equal to $P(v_t^i = b|y_t)$, when ignoring the common constant factors. Then, the SISO decoder of Figure 2.22(b) is used for generating the *extrinsic a posteriori* bit probabilities $P(u_t^i; O)$ of the information bits, as well as the *extrinsic a posteriori* bit probabilities $P(c_t^i; O)$ of the coded bits, from the de-interleaved probabilities $P(v_t^i = b; O)$, as seen in Figure 2.22(b). Since $P(u_t^i; I)$ is unavailable, it is not used in the entire decoding process.

During the second iteration $P(c_t^i; O)$ is interleaved and fed back to the input of the demodulator in the correct order in the form of $P(v_t^i; I)$, as seen in Figure 2.22(b). Assuming that the probabilities $P(v_t^0; I)$, $P(v_t^1; I)$ and $P(v_t^2; I)$ are independent by the employment of three independent bit interleavers, we have for each $x_t \in \chi$:

$$\begin{aligned} P(x_t) &= P(\mu([\nabla^0(x_t), \nabla^1(x_t), \nabla^2(x_t)])) \\ &= \prod_{j=0}^{2} P(v_t^j = \nabla^j(x_t); I), \end{aligned} \tag{2.65}$$

where $\nabla^j(x_t) \in \{0,1\}$ is the value of the jth bit of the three-bit label for x_t. Now that we have the *a priori* probability $P(x_t)$ of the transmitted symbol x_t, the *extrinsic a posteriori* bit probabilities

for the second decoding iteration can be computed using Equations 2.63 and 2.65, yielding:

$$\begin{aligned} P(v_t^i = b; O) &= \frac{P(v_t^i = b|y_t)}{P(v_t^i = b; I)} \\ &= \sum_{x_t \in \chi(i,b)} \left(P(y_t|x_t) \prod_{j \neq i} P(v_t^j = \nabla^j(x_t); I) \right) \\ & \quad i \in \{0,1,2\}, \quad b \in \{0,1\}. \end{aligned} \tag{2.66}$$

As seen from Equation 2.66, in order to recalculate the metric for a bit we only need the *a priori* probabilities of the other two bits in the same channel symbol. After interleaving in the feedback loop of Figure 2.22, the regenerated bit metrics are tentatively soft demodulated again and the process of passing information between the demodulator and decoder is continued. The final decoded output is the hard-decision-based *extrinsic* bit probability $P(u_t^i; O)$.

2.7 Conclusions

In this chapter we have studied the conceptual differences between four coded modulation schemes in terms of coding structure, signal labelling philosophy, interleaver type and decoding philosophy. The symbol-based non-binary MAP algorithm was also highlighted, when operating in the log-domain.

In the next chapter, we will proceed to study the performance of TCM, BICM, TTCM and BICM-ID over non-dispersive propagation environments.

Chapter 3

Coded Modulation Performance in Non-dispersive Propagation Environments

3.1 Introduction

Having described the operating principles of the TCM, BICM, TTCM and BICM-ID schemes in Chapter 2, in Section 3.2 their performance will be initially evaluated for transmission over non-dispersive narrowband channels. By contrast, in Section 3.4 we will investigate their performance, when communicating over wideband fading channels in the context of multi-carrier Orthogonal Frequency Division Multiplexing (OFDM) system [63]. However, we will assume that the number of subcarriers is sufficiently high for assuming that each OFDM subcarrier experiences narrowband, non-dispersive channel conditions.

3.2 Coded Modulation in Narrowband Channels

In this section, a comparative study of TCM, TTCM, BICM and BICM-ID schemes over both Gaussian and uncorrelated narrowband Rayleigh fading channels is presented in the context of 8PSK, 16QAM and 64QAM. We comparatively study the associated decoding complexity, the effects of the encoding block length and the achievable bandwidth efficiency. It will be shown that TTCM constitutes the best compromise scheme, followed by BICM-ID.

3.2.1 System Overview

The schematic of the coded modulation schemes under consideration is shown in Figure 3.1. The source generates random information bits, which are encoded by one of the TCM, TTCM or BICM encoders. The coded sequence is then appropriately interleaved and used for modulating the waveforms according to the symbol mapping rules. For a narrowband Rayleigh fading channel in conjunction with coherent detection, the relationship between the transmitted discrete time signal x_t and the received

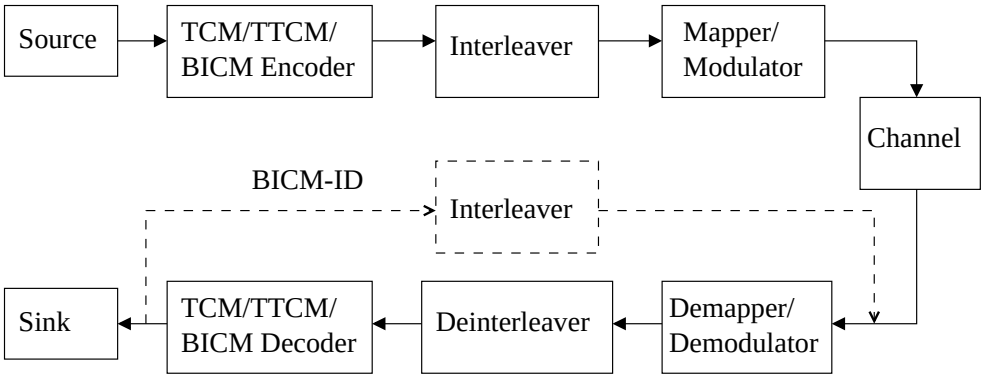

Figure 3.1: System overview of different coded modulation schemes.

discrete time signal y_t is given by:

$$y_t = \rho_t x_t \ + \ n_t, \tag{3.1}$$

where ρ_t is the Rayleigh-distributed fading amplitude having an expected value of $\mathrm{E}[\rho_t^2] = 1$, while n_t is the complex AWGN having a variance of $\sigma^2 = N_0/2$ where N_0 is the noise's Power Spectral Density (PSD). For AWGN channels we have $\rho_t = 1$. The receiver consists of a coherent demodulator followed by a de-interleaver and one of the TCM, TTCM or BICM decoders. TTCM schemes consist of two component TCM encoders and two parallel decoders. In BICM-ID schemes the decoder output is appropriately interleaved and fed back to the demodulator input, as shown in Figure 3.1.

The log-domain branch metric required for the maximum likelihood decoding of TCM and TTCM over fading channels is given by the squared Euclidean distance between the faded transmitted symbol x_t and the noisy received symbol y_t, which is formulated as:

$$\pi_t = |y_t - \rho_t x_t|^2. \tag{3.2}$$

By contrast, the corresponding branch metric for BICM and BICM-ID is formed by summing the de-interleaved bit metrics λ of each coded bit v_t^i which quantifies the reliability of the corresponding symbol, yielding:

$$\pi_t = \sum_{i=0}^{\bar{\mathsf{m}}} \lambda(v_t^i = b), \tag{3.3}$$

where i is the bit position of the coded bit in a constellation symbol, $\bar{\mathsf{m}}$ is the number of information bits per symbol and $b \ \in (0, 1)$. The number of coded bits per symbol is $(\bar{\mathsf{m}} + 1)$, since the coded modulation schemes add one parity bit to the $\bar{\mathsf{m}}$ information bits by doubling the original constellation size, in order to maintain the same spectral efficiency of $\bar{\mathsf{m}}$ bits/s/Hz. The BICM bit metrics $\tilde{\lambda}$ before the de-interleaver are defined as [18]:

$$\tilde{\lambda}(v_t^i = b) = \sum_{x \in \chi(i,b)} |y_t - \rho_t x|^2, \tag{3.4}$$

where $\chi(i, b)$ is the signal set, for which the bit i of the symbol has a binary value b.

To elaborate a little further, the coded modulation schemes that we comparatively studied are Ungerböck's TCM [36], Robertson's TTCM [38], Zehavi's BICM [9] and Li's BICM-ID [19]. Table 3.1 shows the generator polynomials of both the TCM and TTCM codes in octal format. These are

Rate	State	$\tilde{\mathsf{m}}$	H^0	H^1	H^2	H^3
2/3	8	2	11	02	04	-
(8PSK)	64 *	2	103	30	66	-
3/4	8	3	11	02	04	10
(16QAM)	64 *	3	101	16	64	-
5/6	8	2	11	02	04	-
(64QAM)	64 *	2	101	16	64	-

Table 3.1: 'Punctured' TCM codes with best minimum distance for PSK and QAM, ©Robertson and Wörz [38]. '*' indicates Ungerböck's TCM codes [36]. Two-dimensional ($2\bar{D}$) modulation is utilised. Octal format is used for representing the generator polynomials H^i and $\tilde{\mathsf{m}}$ denotes the number of coded information bits out of the total $\bar{\mathsf{m}}$ information bits in a modulated symbol.

Recursive Systematic Convolutional (RSC) codes that add one parity bit to the information bits. Hence, the coding rate of a $2^{\bar{\mathsf{m}}+1}$-ary PSK or QAM signal is $R = \frac{\bar{\mathsf{m}}}{\bar{\mathsf{m}}+1}$. The number of decoding states associated with a code of memory ν is 2^ν. When the number of protected/coded information bits $\tilde{\mathsf{m}}$ is less than the total number of original information bits $\bar{\mathsf{m}}$, there are $(\bar{\mathsf{m}} - \tilde{\mathsf{m}})$ uncoded information bits and $2^{\bar{\mathsf{m}}-\tilde{\mathsf{m}}}$ parallel transitions in the trellis of the code. Parallel transitions assist in reducing the decoding complexity and the memory required, since the dimensionality of the corresponding trellis is smaller than that of a trellis having no parallel branches.

Table 3.2 shows the generator polynomials for the BICM and BICM-ID codes in octal format. These codes are non-systematic convolutional codes having a maximum free Hamming distance. Again, only one extra bit is added to the information bits. Hence, the achievable coding rate and the bandwidth efficiency are similar to that of TCM and TTCM for the $2^{\bar{\mathsf{m}}+1}$-ary modulation schemes used. In order to reduce the required decoding memory, the BICM and BICM-ID schemes based on 64QAM were obtained by puncturing the rate-1/2 codes following the approach of [61], since for a non-punctured rate-5/6 code there are $2^{(\bar{\mathsf{m}}=5)} = 32$ branches emerging from each trellis state for a block length of L_B, whereas for the punctured rate-1/2 code, there are only $2^{(\bar{\mathsf{m}}=1)} = 2$ branches emerging from each trellis state for a block length of $\bar{\mathsf{m}}L_B = 5L_B$. Therefore the required decoding memory is reduced by a factor of $\frac{2^{\bar{\mathsf{m}}} \cdot L_B}{2^1 \cdot \bar{\mathsf{m}} \cdot L_B} = 3.2$.

Soft-decision trellis decoding utilising the Log-Maximum A Posteriori (Log-MAP) algorithm [53] was invoked for the decoding of the coded modulation schemes. As discussed in Section 2.3.5, the Log-MAP algorithm is a numerically stable version of the MAP algorithm operating in the log-domain, in order to reduce its complexity and to mitigate the numerical problems associated with the MAP algorithm [50].

3.2.2 Simulation Results and Discussions

In this section we study the performance of TCM, TTCM, BICM and BICM-ID using computer simulations. The complexity of the coded modulation schemes is compared in terms of the number of decoding states, and the number of decoding iterations. For a TCM or BICM code of memory ν, the corresponding complexity is proportional to the number of decoding states namely to $S = 2^\nu$. Since TTCM schemes invoke two component TCM codes, a TTCM code with t iterations and using an S-

Rate	State	g^1	g^2	g^3	g^4	d_{free}
2/3	8	4	2	6	-	4
(8PSK)	(ν=3)	1	4	7	-	
	16	7	1	4	-	5
	(ν=4)	2	5	7	-	
	64	15	6	15	-	7
	(ν=6)	6	15	17	-	
3/4	8	4	4	4	4	4
(16QAM)	(ν=3)	0	6	2	4	
		0	2	5	5	
	32	6	2	2	6	5
	(ν=5)	1	6	0	7	
		0	2	5	5	

Rate	State	g^1	g^2	Puncturing	d_{free}
5/6	8	15	17	1 0 0 1 0	3
(64QAM)	(ν=3)			0 1 1 1 1	
	64	133	171	1 1 1 1 1	3
	(ν=6)			1 0 0 0 0	

Table 3.2: Top table shows the generator polynomials of Paaske's code, p. 331 of [59]. Bottom table shows those of the rate-compatible puncture convolutional codes [61]. ν is the code memory and d_{free} is the free Hamming distance. Octal format is used for the polynomial coefficients g^i, while '1' and '0' in the puncturing matrix indicate the position of the unpunctured and punctured coded bits, respectively.

state component code exhibits a complexity proportional to $2.t.S$ or $t.2^{\nu+1}$. As for BICM-ID schemes, only one decoder is used but the demodulator is invoked in each decoding iteration. However, the complexity of the demodulator is assumed to be insignificant compared to that of the channel decoder. Hence, a BICM-ID code with t iterations using an S-state code exhibits a complexity proportional to $t.S$ or $t.2^{\nu}$.

3.2.2.1 Performance over AWGN Channels

It is important to note that in terms of the total number of trellis states the decoding complexity of 64-state TCM and 8-state TTCM using two TCM decoders in conjunction with four iterations can be considered similar. The same comments are valid also for 16-state BICM-ID using four iterations or for 8-state BICM-ID using eight iterations. In our forthcoming discourse we will always endeavour to compare schemes of similar decoding complexity, unless otherwise stated. Figure 3.2 illustrates the effects of interleaving block length on the TCM, TTCM and BICM-ID performance in an 8PSK scheme over AWGN channels. It is clear from the figure that a high interleaving block length is desired for the iterative TTCM and BICM-ID schemes. The block length does not affect the BICM-ID performance during the first pass, since it constitutes a BICM scheme using SP-based phasor labelling. However, if we consider four iterations, the performance improves, converging faster to the Error-Free-Feedback

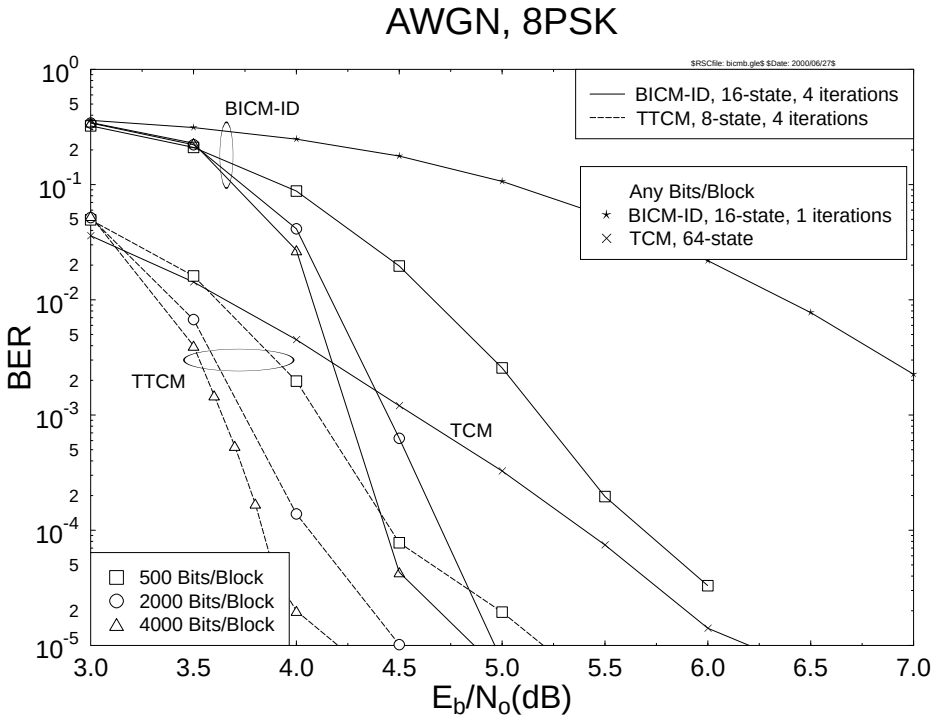

Figure 3.2: Effects of block length on the TCM, TTCM and BICM-ID performance in the context of an 8PSK scheme for transmissions over AWGN channels.

(EFF) bound[1] [18] for larger block lengths. At a BER of 10^{-4} a 500-bit block length was about 1 dB inferior in terms of the required SNR to the 2000-bit block length in the context of the BICM-ID scheme. A slight further SNR improvement was obtained for the 4000-bit block length. In other words, the advantage of BICM-ID over TCM for transmissions over AWGN channels is more significant for larger block lengths. The 8-state TTCM performance also improves, when using four iterations, as the block length is increased and, on the whole, TTCM is the best performer in this scenario.

Figure 3.3 shows the effects of the decoding complexity on the TCM, TTCM, BICM and BICM-ID schemes' performance in the context of an 8PSK scheme for transmissions over AWGN channels using a block length of 4000 information bits (2000 symbols). Again, the 64-state TCM, 64-state BICM, 8-state TTCM using four iterations and 16-state BICM-ID along with four iterations exhibit a similar decoding complexity. At a BER of 10^{-4}, TTCM requires about 0.6 dB lower SNR than BICM-ID, 1.6 dB less energy than TCM and 2.5 dB lower SNR than BICM. When the decoding complexity is reduced such that 8-state codes are used in the TCM, BICM and BICM-ID schemes, their corresponding performance becomes worse than that of the 64-state codes, as shown in Figure 3.3. In order to be able to compare the associated performance with that of 8-state BICM-ID using four iterations, 8-state TTCM along with two iterations is employed. Observe that due to the insufficient number of iterations, TTCM exhibits only marginal advantage over BICM-ID.

Figure 3.4 shows the performance of TCM, TTCM and BICM-ID invoking 16QAM for transmissions over AWGN channels using a block length of 6000 information bits (2000 symbols). Upon comparing 64-state TCM with 32-state BICM-ID using two iterations, we observed that BICM-ID outperforms TCM for E_b/N_0 values in excess of 6.8 dB. However, 8-state BICM-ID using an increased

[1]The EFF bound is defined as the BER upper bound performance achieved for the idealised situation, when the decoded values fed back to the demodulator in Figure 3.1 are error free.

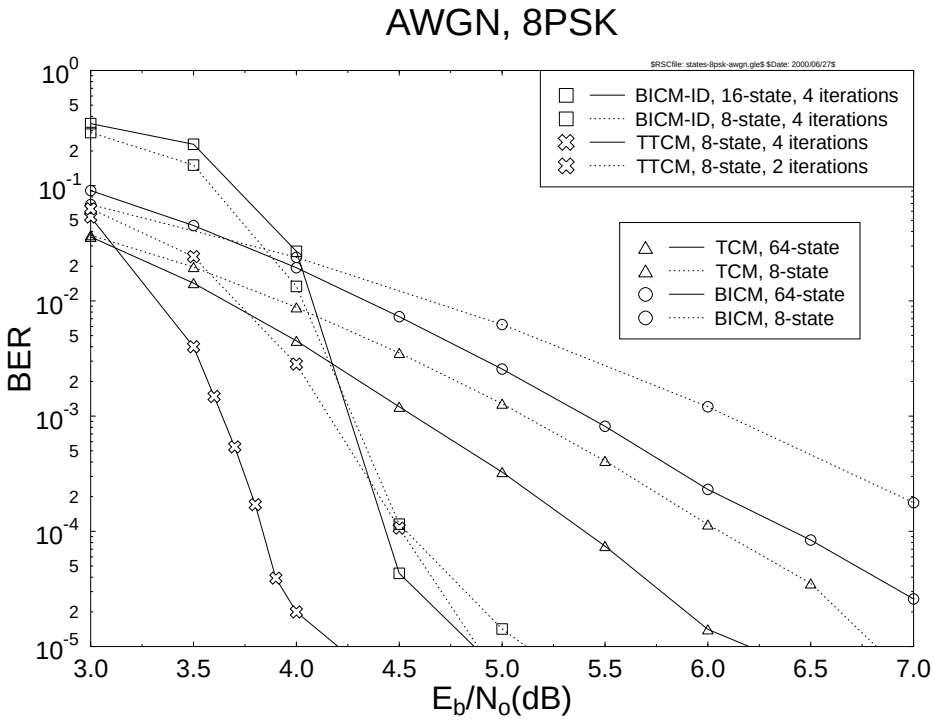

Figure 3.3: Effects of decoding complexity on the TCM, TTCM, BICM and BICM-ID schemes' performance in the context of an 8PSK scheme for transmissions over AWGN channels using a block length of 4000 information bits (2000 symbols).

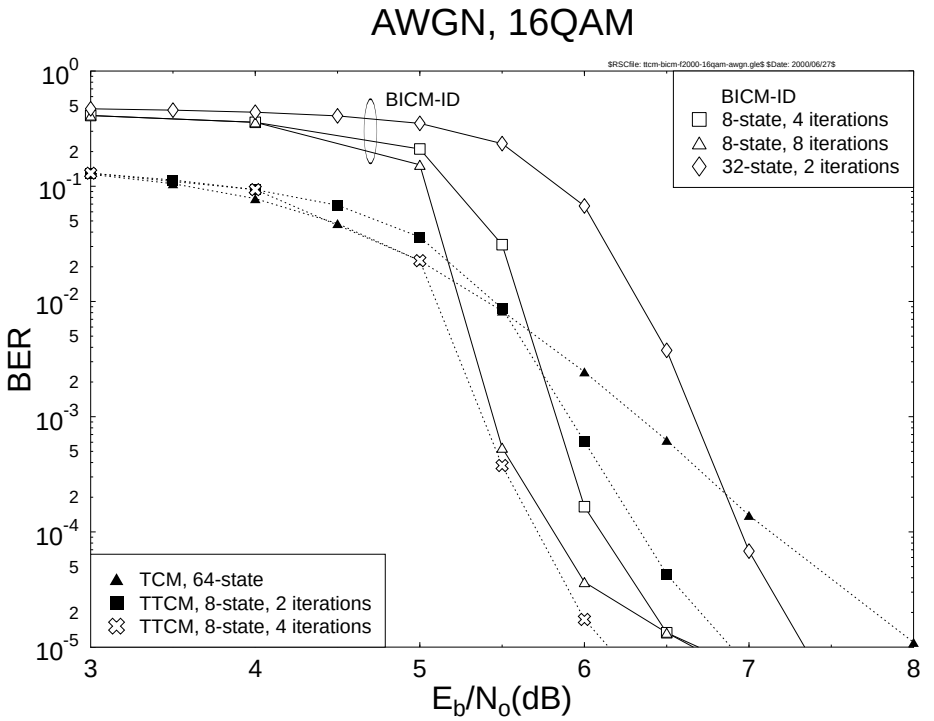

Figure 3.4: Performance comparison of TCM, TTCM and BICM-ID employing 16QAM for transmissions over AWGN channels using a block length of 6000 information bits (2000 symbols).

number of iterations, such as eight, outperforms the similar complexity 32-state BICM-ID scheme employing two iterations as well as 64-state TCM. An approximately 1.2 dB E_b/N_0 gain was obtained at a BER of 10^{-4} for 8-state BICM-ID using eight iterations over 64-state TCM at a similar decoding complexity. Comparing 8-state TTCM using two iterations and 8-state BICM-ID employing four iterations reveals that BICM-ID performs better for the E_b/N_0 range of 5.7 dB to 7 dB. When the number of iterations is increased to four for TTCM and to eight for BICM-ID, TTCM exhibits a better performance, as seen in Figure 3.4.

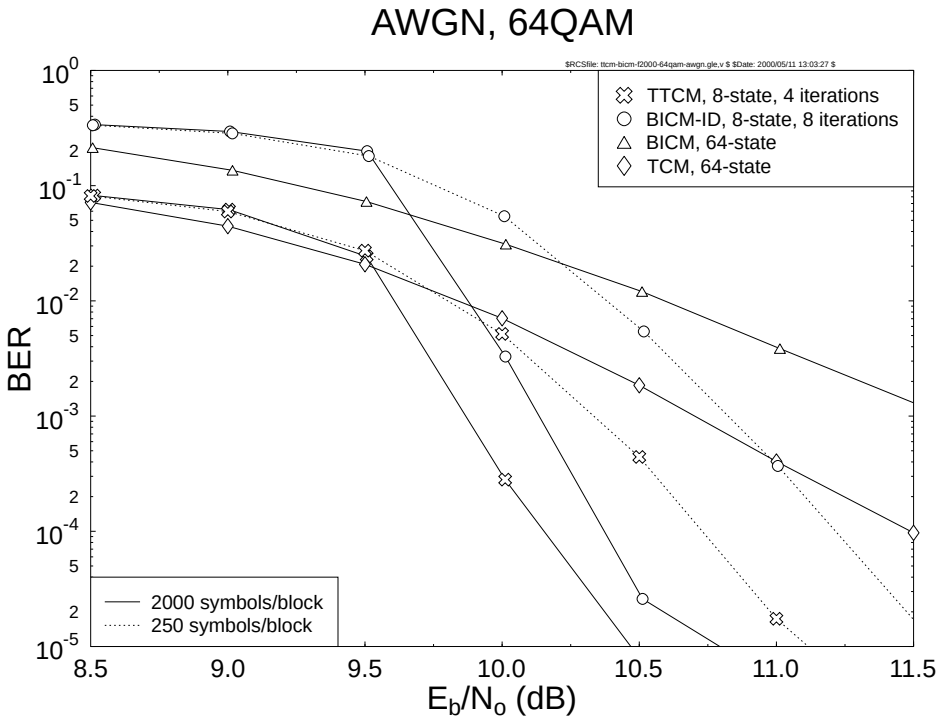

Figure 3.5: Performance comparison of TCM, TTCM, BICM and BICM-ID using 64QAM over AWGN channels.

Owing to the associated SP, the intra-subset distance of TCM and TTCM increases as we traverse down the partition tree of Figure 2.7, for example. It was shown in [38] that we only need to encode $\tilde{m} = 2$ out of $\bar{m} = 5$ information bits in the 64QAM/TTCM to attain target BERs around 10^{-5} in AWGN channels. Hence in this scenario there are $2^{\bar{m}-\tilde{m}} = 8$ parallel transitions due to the $\bar{m} - \tilde{m} = 3$ uncoded information bits in the trellis of 64QAM/TTCM. Figure 3.5 illustrates the performance of TCM, TTCM, BICM and BICM-ID using 64QAM over AWGN channels. When using a block length of 10000 information bits (2000 symbols), 8-state TTCM invoking four iterations is the best candidate, followed by the similar complexity 8-state BICM-ID scheme employing eight iterations. Again, TCM performs better than BICM in AWGN channels. When a block length of 1250 information bits (250 symbols) was used, both TTCM and BICM-ID experienced a performance degradation. It is also seen in Figure 3.5 that BICM-ID performs close to TTCM, when a longer block length is used.

3.2.2.2 Performance over Uncorrelated Narrowband Rayleigh Fading Channels

The uncorrelated Rayleigh fading channels implied using an infinite-length interleaver over narrowband Rayleigh fading channels. Figure 3.6 shows the performance of 64-state TCM, 64-state BICM, 8-state

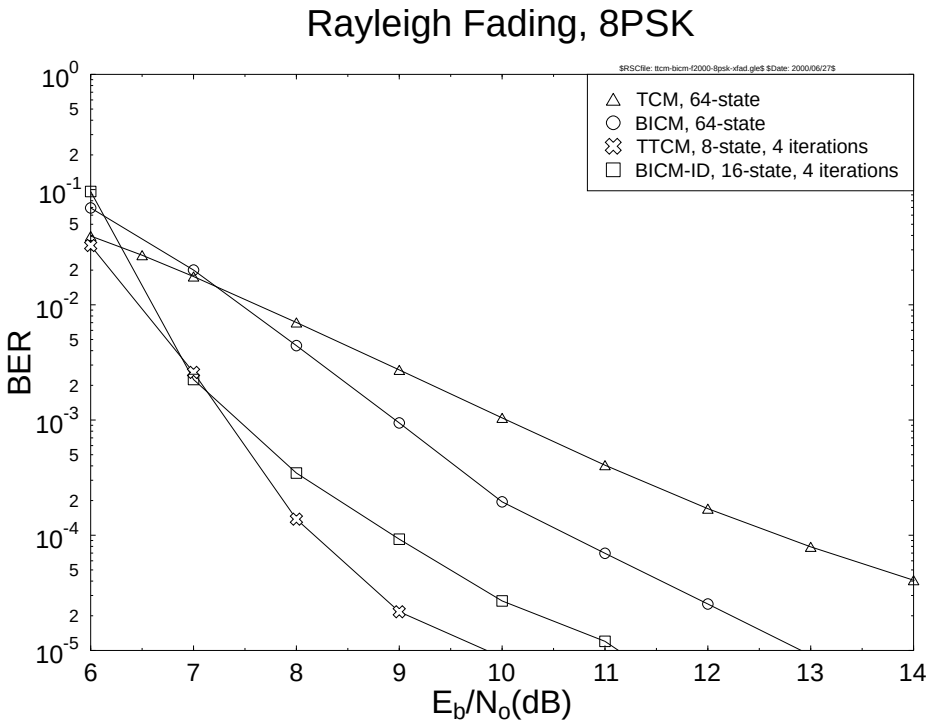

Figure 3.6: Performance comparison of TCM, TTCM, BICM and BICM-ID for 8PSK transmissions over uncorrelated Rayleigh fading channels using a block length of 4000 information bits (2000 symbols).

TTCM using four iterations and 16-state BICM-ID employing four iterations in the context of an 8PSK scheme communicating over uncorrelated narrowband Rayleigh fading channels using a block length of 4000 information bits (2000 symbols). These four coded modulation schemes have a similar complexity. As can be seen from Figure 3.6, TTCM performs best, followed by BICM-ID, BICM and TCM. At a BER of 10^{-4}, TTCM performs about 0.7 dB better in terms of the required E_b/N_0 value than BICM-ID, 2.3 dB better than BICM and 4.5 dB better than TCM. The error floor of TTCM [38] was lower than the associated EFF bound of BICM-ID. However, the BERs of TTCM and BICM-ID were identical at $E_b/N_0 = 7$ dB.

Figure 3.7 compares the performance of TCM, TTCM and BICM-ID invoking 16QAM for communicating over uncorrelated narrowband Rayleigh fading channels using a block length of 6000 information bits (2000 symbols). Observe that 32-state BICM-ID using two iterations outperforms 64-state TCM for E_b/N_0 in excess of 9.6 dB. At the same complexity, 8-state BICM-ID invoking eight iterations outperforms 64-state TCM beyond $E_b/N_0 = 8.2$ dB. Similarly to 8PSK, the coding gain of BICM-ID over TCM in the context of 16QAM is more significant over narrowband Rayleigh fading channels compared to AWGN channels. Near E_b/N_0 of 11 dB the 8-state BICM-ID scheme approaches the EFF bound, hence 32-state BICM-ID using two iterations exhibits a better performance due to its lower EFF bound. Observe also that 8-state BICM-ID using four iterations outperforms 8-state TTCM employing two iterations in the range of $E_b/N_0 = 8.5$ dB to 12.1 dB. Increasing the number of iterations only marginally improves the performance of BICM-ID, but results in a significant gain for TTCM. The performance of 8-state TTCM using four iterations is better than that of 8-state BICM-ID along with eight iterations for E_b/N_0 values in excess of 9.6 dB.

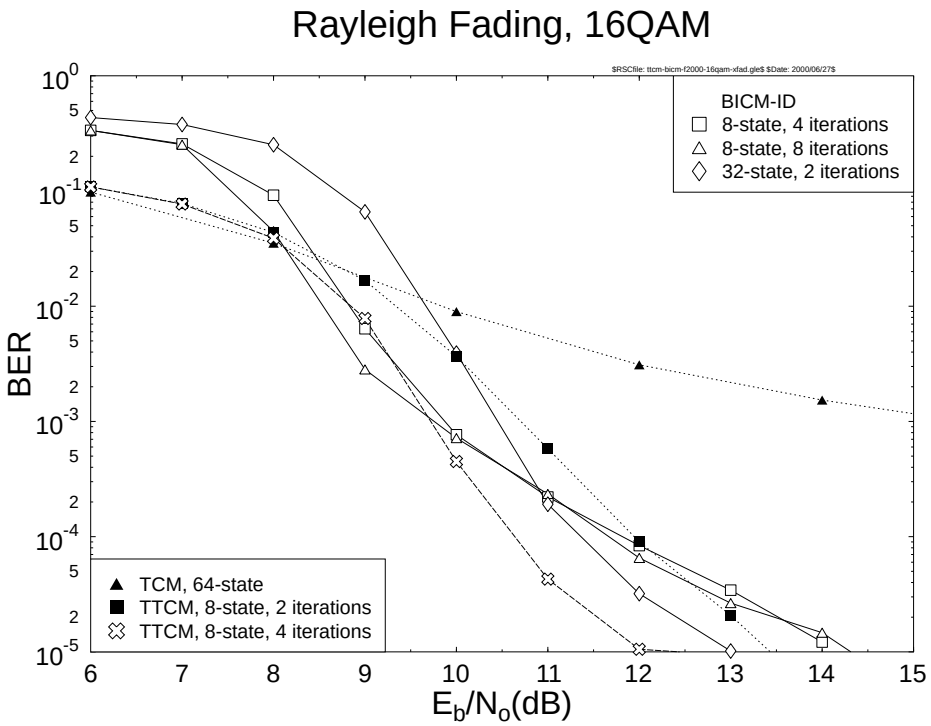

Figure 3.7: Performance comparison of TCM, TTCM and BICM-ID for 16QAM transmissions over uncorrelated narrowband Rayleigh fading channels transmitting 2000 symbols/block (6000 information bits/block).

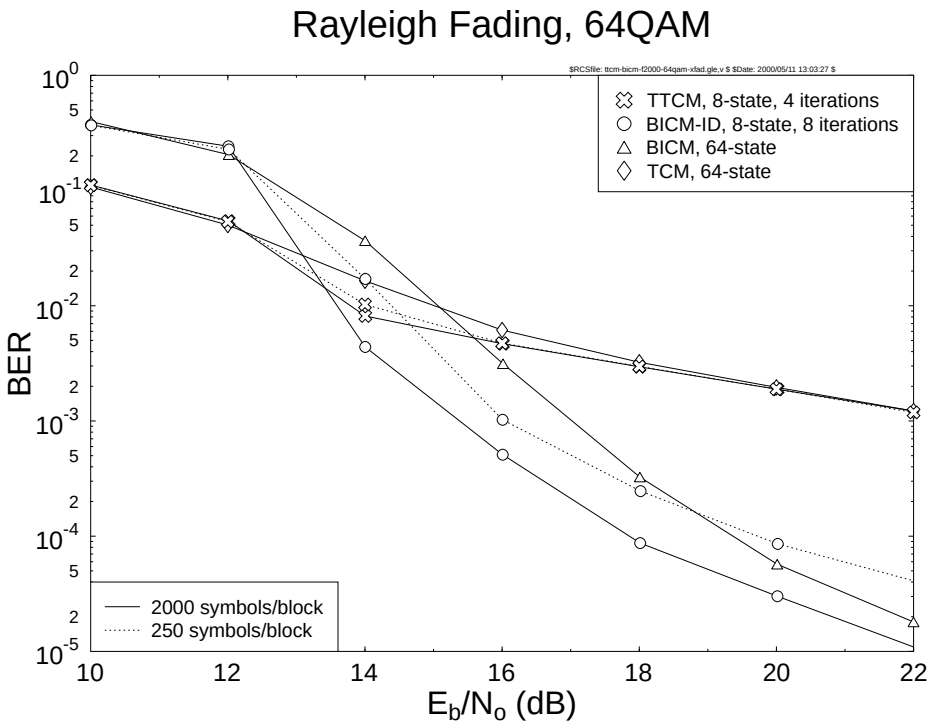

Figure 3.8: Performance comparison of TCM, TTCM, BICM and BICM-ID using 64QAM for transmissions over uncorrelated narrowband Rayleigh fading channels.

Figure 3.8 illustrates the performance of TCM, TTCM, BICM and BICM-ID when invoking 64QAM for communicating over uncorrelated narrowband Rayleigh fading channels. Using a block length of 10000 information bits (2000 symbols), 64-state BICM performs better than 64-state TCM for E_b/N_0 values in excess of 15 dB. BICM-ID exhibits a lower error floor than TTCM in this scenario, since BICM-ID protects all the five information bits, while TTCM protects only two information bits of the six-bit 64QAM symbol. The three unprotected information bits of TCM and TTCM render these schemes less robust to the bursty error effects of the uncorrelated fading channel. If we use a TCM or TTCM code generator that encodes all the five information bits, a better performance is expected. Reducing the block length from 2000 symbols to 250 symbols resulted in a small performance degradation for TTCM, but yielded a significant degradation for BICM-ID.

3.2.2.3 Coding Gain versus Complexity and Interleaver Block Length

In this section, we will investigate the coding gain (G) of the coded modulation schemes utilising an 8PSK scheme versus the Decoding Complexity (DC) and the Interleaver Block Length (IL) at a BER of 10^{-4}. The coding gain G is measured by comparing to the uncoded 4PSK scheme, which exhibits a BER of 10^{-4} at $E_b/N_0 = 8.35$ dB and $E_b/N_0 = 35$ dB for transmissions over AWGN channels and uncorrelated narrowband Rayleigh fading channels, respectively. Again, the DC is measured using the associated number of decoding states and the notations S and t represent the number of decoding states and the number of decoding iterations, respectively. Hence, the relative complexity of TCM, BICM, TTCM and BICM-ID is given by S, S, $2tS$ and tS, respectively. The IL is measured in terms of the number of information bits in the interleaver.

Figure 3.9 portrays the coding gain G versus DC plot of the coded modulation schemes for 8PSK transmissions over (a) AWGN channels and (b) uncorrelated narrowband Rayleigh fading channels, using an IL of 4000 information bits (2000 symbols). At a DC as low as 8, the non-iterative TCM scheme exhibits the highest coding gain G for transmissions over AWGN channels, as seen in Figure 3.9(a). By contrast, the BICM scheme exhibits the highest coding gain G for transmissions over uncorrelated narrowband Rayleigh fading channels, as seen in Figure 3.9(b). However, for a DC higher than 16, the iterative TTCM and BICM-ID schemes exhibit higher coding gains than their non-iterative counterparts for transmission over both channels.

For the iterative schemes different combinations of t and S may yield different performances at the same DC. For example, the coding gain G of BICM-ID in conjunction with $tS = 8 \times 8$ is better than that of $tS = 4 \times 16$ at DC=64 for transmissions over AWGN channels, as seen in Figure 3.9(a), since BICM-ID invoking a constituent code associated with $S = 16$ has not reached its optimum performance at iteration $t = 4$. However, the coding gain G of BICM-ID in conjunction with $tS = 4 \times 16$ is better than that of $tS = 8 \times 8$ at DC=64, when communicating over uncorrelated narrowband Rayleigh fading channels, as seen in Figure 3.9(b). This is because BICM-ID invoking a constituent code associated with $S = 8$ has reached its EFF bound at iteration $t = 4$, while BICM-ID invoking a constituent code associated with $S = 16$ has not reached its EFF bound, because the EFF bound for code associated with $S = 16$ is lower than that of a code associated with $S = 18$. In general, the coding gain G of TTCM is the highest for DC values in excess of 32 for transmissions over both channels.

Figure 3.10 portrays the coding gain G versus IL plot of the coded modulation schemes for 8PSK

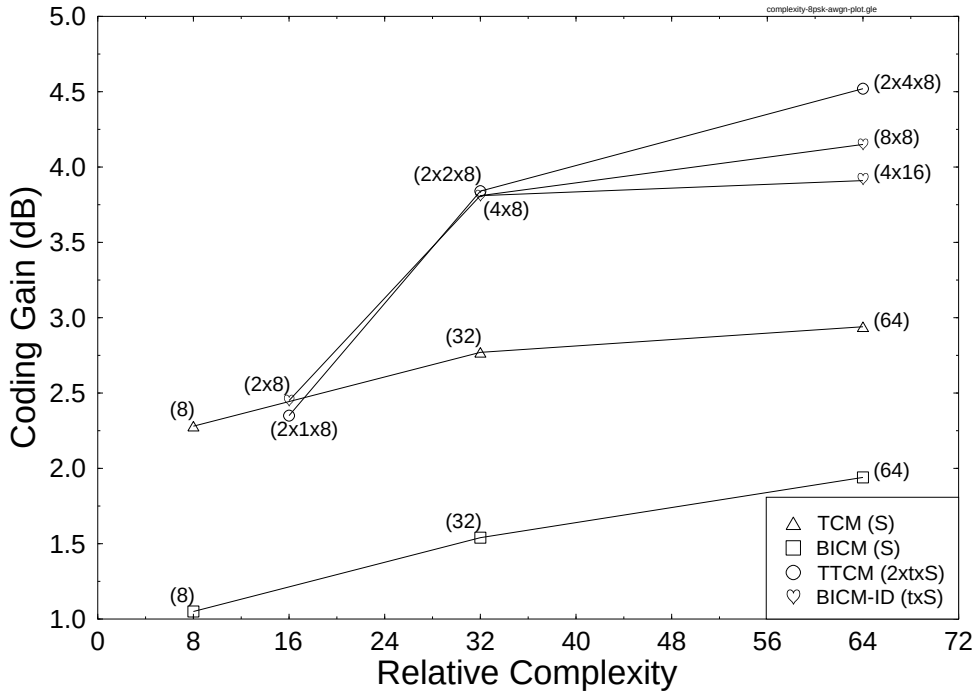

(a) AWGN channels

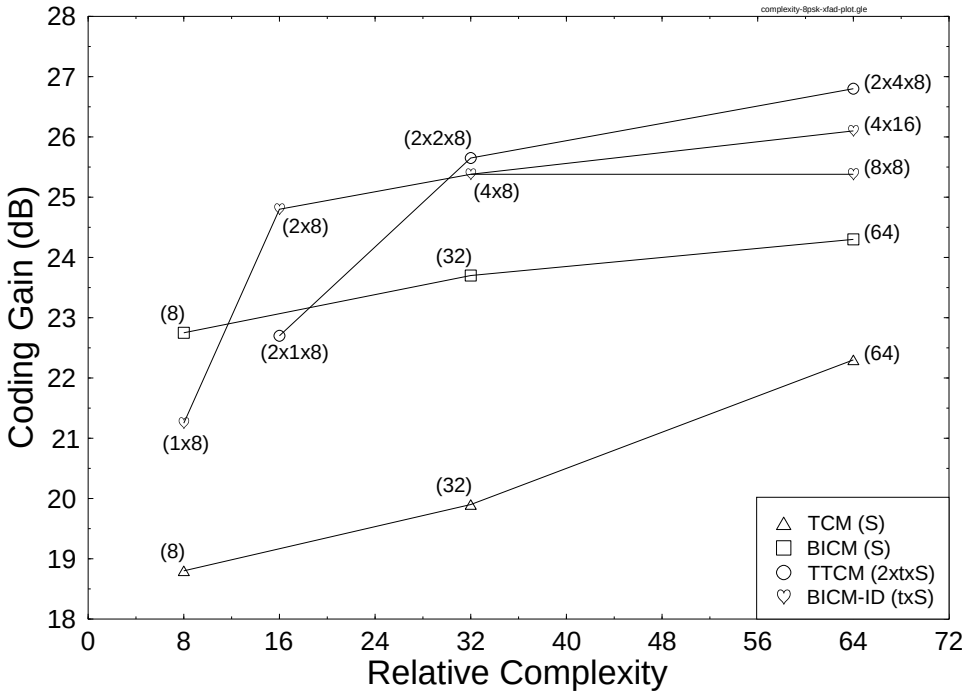

(b) uncorrelated narrowband Rayleigh fading channels

Figure 3.9: Coding gain at BER=10^{-4} over the uncoded 4PSK scheme, against the decoding complexity of TCM, TTCM, BICM and BICM-ID for 8PSK transmissions over (a) AWGN channels and (b) uncorrelated narrowband Rayleigh fading channels, using an interleaver block length of 4000 information bits (2000 symbols). The notations S and t represent the number of decoding states and the number of decoding iterations, respectively.

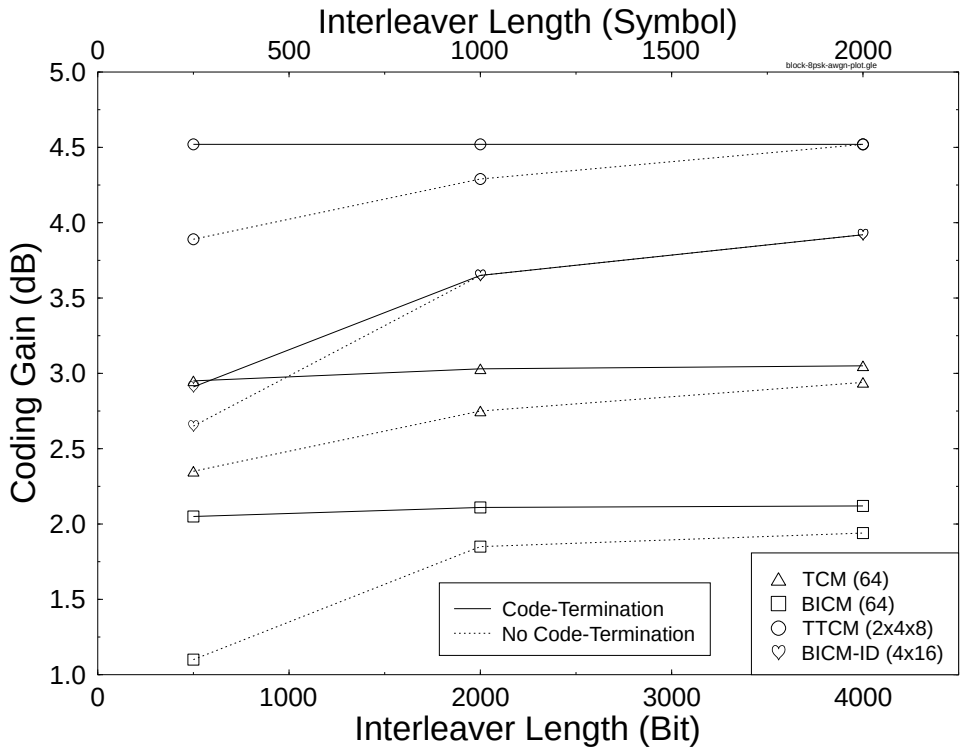

(a) AWGN channels

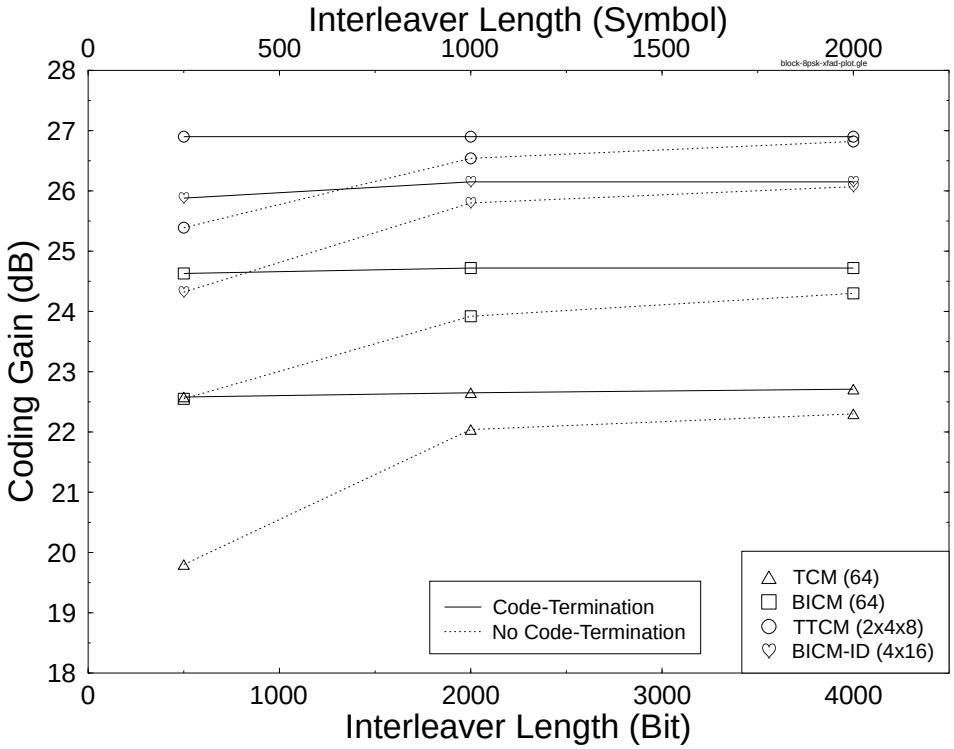

(b) uncorrelated narrowband Rayleigh fading channels

Figure 3.10: Coding gain at a BER of 10^{-4} over the uncoded 4PSK scheme, against the IL of TCM, TTCM, BICM and BICM-ID for 8PSK transmissions over (a) AWGN channels and (b) uncorrelated narrowband Rayleigh fading channels, invoking a DC of 64 applying code termination or no code termination.

transmissions over (a) AWGN channels and (b) uncorrelated narrowband Rayleigh fading channels in conjunction with a DC of 64 both with and without code termination [8]. We can observe in Figure 3.10(a) that IL affects the performance of the schemes using no code termination, since the shorter the IL, the higher the probability for the decoding trellis to end at a wrong state. For transmissions over AWGN channels and upon using code-terminated schemes, only the performance of the BICM-ID scheme is affected by the IL, since the performance of the scheme communicating over AWGN channels depends on the FED, while the high FED of BICM-ID depends on the reliability of the feedback values. Therefore, when the IL is short, BICM-ID suffers from a performance degradation. However, the other schemes are not affected by the IL when communicating over AWGN channels, as seen in Figure 3.10(a), since there are no bursty channel errors to be dispersed by the interleaver and hence there is no advantage in utilising a long IL. To elaborate a little further, as seen in Figure 3.10 for transmissions over uncorrelated narrowband Rayleigh fading channels using code-terminated schemes, the IL does not significantly affect the performance of the schemes, since the error events are uncorrelated in the uncorrelated Rayleigh fading scenario. These results constitute the upper bound performance achievable when an infinitely long interleaver is utilised for rendering the error events uncorrelated.

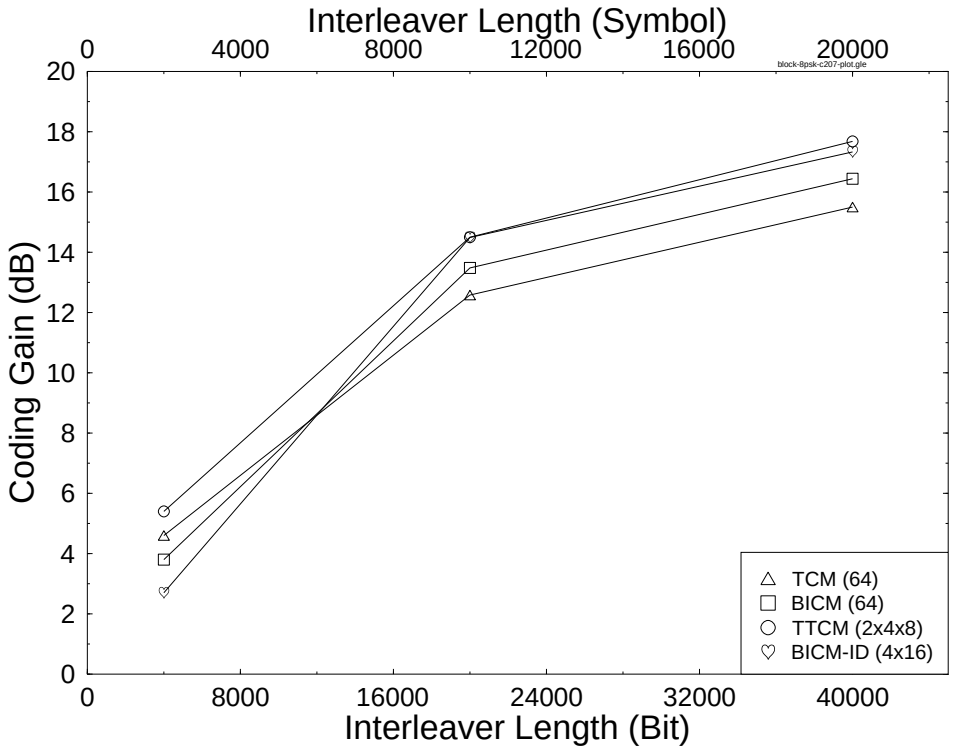

Figure 3.11: Coding gain at a BER of 10^{-4} over the uncoded 4PSK scheme, against the IL of TCM, TTCM, BICM and BICM-ID for 8PSK transmissions over correlated narrowband Rayleigh fading channels, invoking a DC of 64 applying code termination. The normalised Doppler frequency of the channel is 3.25×10^{-5}, which corresponds to a Baud rate of 2.6 MBaud, a carrier frequency of 1.9 GHz and a vehicular speed of 30 mph.

Figure 3.11 portrays the coding gain G versus IL plot of the coded modulation schemes for 8PSK transmissions over correlated narrowband Rayleigh fading channels, in conjunction with a decoding complexity of 64, when applying code termination. The normalised Doppler frequency of the channel

is 3.25×10^{-5}, which corresponds to a Baud rate of 2.6 MBaud, a carrier frequency of 1.9 GHz and a vehicular speed of 30 mph. This is a slow fading channel and hence the fading envelope is highly correlated. It is demonstrated by Figure 3.11 that the coding gain G of all coded modulation schemes improves as the IL increases. This is because the MAP decoder is unable to perform at its best when the channel errors occur in bursts. However, the performance improves when the error bursts are dispersed by the employment of a long interleaver. In general, TTCM is the best performer for a variety of IL values. However, BICM-ID is the worst performer for an IL of 4000 bits, while performing similarly to TTCM for long IL values.

On one hand, TCM performs better than BICM for short IL values, which follows the performance trends observed for transmissions over AWGN channels, as shown in Figure 3.10(a). This is because slowly fading channels are highly correlated and hence they behave as near-Gaussian channels, where TCM is at its best, since TCM was designed for Gaussian channels. By contrast, although BICM was designed for fading channels, when the channel-induced error bursts are inadequately dispersed owing to the employment of a short IL, the performance of BICM suffers. In other words, when communicating over slowly fading channels, extremely long interleavers may be necessary for over-bridging the associated long fades and for facilitating the dispersion of bursty transmission errors, which is a prerequisite for the efficient operation of channel codecs.

On the other hand, BICM performs better than TCM for long IL values, which is reminiscent of the performance trends observed when communicating over uncorrelated Rayleigh fading channels, as evidenced by Figure 3.10(b). This is justified, since the correlation of the fading channel is broken when a long IL is employed for dispersing the error bursts.

3.2.3 Conclusions

In conclusion, at a given complexity TCM performs better than BICM in AWGN channels, but worse in uncorrelated narrowband Rayleigh fading channels. However, BICM-ID using soft-decision feedback outperforms TCM and BICM for transmissions over both AWGN and uncorrelated narrowband Rayleigh fading channels at the same DC. TTCM has shown superior performance over the other coded modulation schemes studied, but exhibited a higher error floor for the 64QAM scheme due to the presence of uncoded information bits for transmissions over uncorrelated narrowband Rayleigh fading channels. Comparing the coding gain against the DC, the iterative decoding schemes of TTCM and BICM-ID are capable of providing a high coding gain even in conjunction with a constituent code exhibiting a short memory length, although only at the cost of a sufficiently high number of decoding iterations, which may imply a relatively high decoding complexity. Comparing the achievable coding gain against the IL, TTCM is the best performer for a variety of ILs, while the performance of BICM-ID is highly dependent on the IL for transmissions over both AWGN and Rayleigh fading channels.

3.3 Orthogonal Frequency Division Multiplexing

Owing to the Inter-Symbol Interference (ISI) inflicted by wideband channels, the employment of channel equalisers is essential in supporting the operation of the coded modulation schemes considered.

However, the employment of channel equalisers will be discussed only at a later stage, namely, in Chapter 4. As an attractive design alternative, here a Discrete Fourier Transform (DFT) based multi-carrier OFDM scheme [63] will be utilised for removing the ISI. Specifically, as long as the OFDM subcarrier signalling rate is sufficiently low since the number of subcarriers is sufficiently high, the individual OFDM subchannels experience non-dispersive narrowband fading conditions.

3.3.1 Orthogonal Frequency Division Multiplexing Principle

In this section we briefly introduce Frequency Division Multiplexing (FDM), also referred to as Orthogonal Multiplexing (OMPX), as a means of dealing with the problems of frequency-selective fading encountered when transmitting over a high-rate wideband radio channel. The fundamental principle of orthogonal multiplexing originates from Chang [64], and over the years a number of researchers have investigated this technique [65, 66]. Despite its conceptual elegance, until recently its employment has been mostly limited to military applications because of the associated implementational difficulties. However, it has recently been adopted as the new European Digital Audio Broadcasting (DAB) standard; it is also a strong candidate for Digital Terrestrial Television Broadcast (DTTB) and for a range of other high-rate applications, such as 155 Mbit/s wireless Asynchronous Transfer Mode (ATM) local area networks. These wide-ranging applications underline its significance as an alternative technique to conventional channel equalisation in order to combat signal dispersion [67–69].

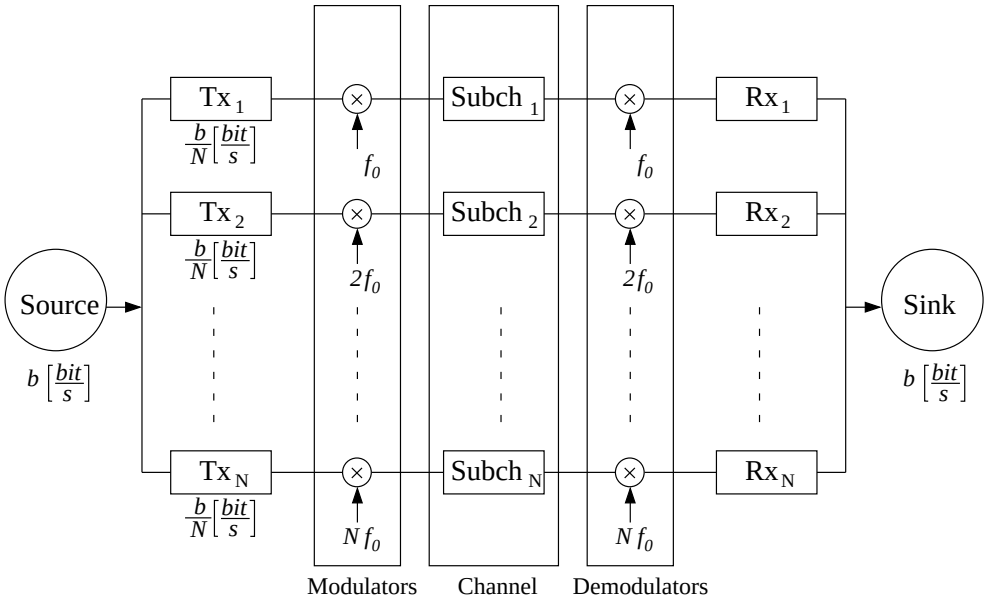

Figure 3.12: Simplified block diagram of the orthogonal parallel modem.

In the FDM scheme of Figure 3.12 the serial data stream of a traffic channel is passed through a serial-to-parallel converter, which splits the data into a number of parallel sub-channels. The data in each sub-channel are applied to a modulator, such that for N channels there are N modulators whose carrier frequencies are f_0, f_1, ..., f_{N-1}. The centre frequency difference between adjacent channels is Δf and the overall bandwidth W of the N modulated carriers is $N\Delta f$.

These N modulated carriers are then combined to give a FDM signal. We may view the serial-to-parallel converter as applying every Mth symbol to a modulator. This has the effect of interleaving the symbols entered into each modulator, hence symbols $S_0, S_N, S_{2N}, \ldots$ are applied to the modulator

whose carrier frequency is f_0. At the receiver the received FDM signal is demultiplexed into N frequency bands, and the N modulated signals are demodulated. The baseband signals are then recombined using a parallel-to-serial converter.

The main advantage of the above FDM concept is that because the symbol period has been increased, the channel's delay spread is a significantly shorter fraction of a symbol period than in the serial system, potentially rendering the system less sensitive to ISI than the conventional N times higher-rate serial system. In other words, in the low-rate sub-channels the signal is no longer subject to frequency-selective fading, hence no channel equalisation is necessary.

A disadvantage of the FDM approach shown in Figure 3.12 is its increased complexity in comparison to the conventional system caused by employing N modulators and filters at the transmitter and N demodulators and filters at the receiver. It can be shown that this complexity can be reduced by employing the DFT, typically implemented with the aid of the Fast Fourier Transform (FFT) [63]. The sub-channel modems can use almost any modulation scheme, and 4- or 16-level QAM is an attractive choice in many situations.

The FFT-based QAM/FDM modem's schematic is portrayed in Figure 3.13. The bits provided by the source are serial/parallel converted in order to form the n-level Gray-coded symbols, N of which are collected in TX buffer 1, while the contents of TX buffer 2 are being transformed by the IFFT in order to form the time-domain modulated signal. The Digital-to-Analogue (D/A) converted, low-pass filtered modulated signal is then transmitted via the channel and its received samples are collected in RX buffer 1, while the contents of RX buffer 2 are being transformed to derive the demodulated signal. The twin buffers are alternately filled with data to allow for the finite FFT-based demodulation time. Before the data are Gray coded and passed to the data sink, they can be equalised by a low-complexity method, if there are some dispersions within the narrow sub-bands. For a deeper tutorial exposure the interested reader is referred to reference [63].

3.4 Coded Modulation Assisted Orthogonal Frequency Division Multiplexing

3.4.1 Introduction

The coded modulation schemes of Chapter 2 are here amalgamated with an OFDM modem. Specifically, the coded symbols are mapped to the OFDM modulator at the transmitter, while the symbols output by the OFDM demodulator are channel decoded at the receiver.

When the channel is frequency selective and OFDM modulation is used, the received symbol is given by the product of the transmitted frequency-domain OFDM symbol and the frequency-domain transfer function of the channel. This direct relationship facilitates the employment of simple frequency-domain channel equalisation techniques. Essentially, if an estimate of the complex frequency-domain transfer function H_k is available at the receiver, channel equalisation can be performed by dividing each received value by the corresponding frequency-domain channel transfer function estimate. The channel's frequency-domain transfer function can be estimated with the aid of known frequency-domain pilot subcarriers inserted into the transmitted signal's spectrum [63]. These

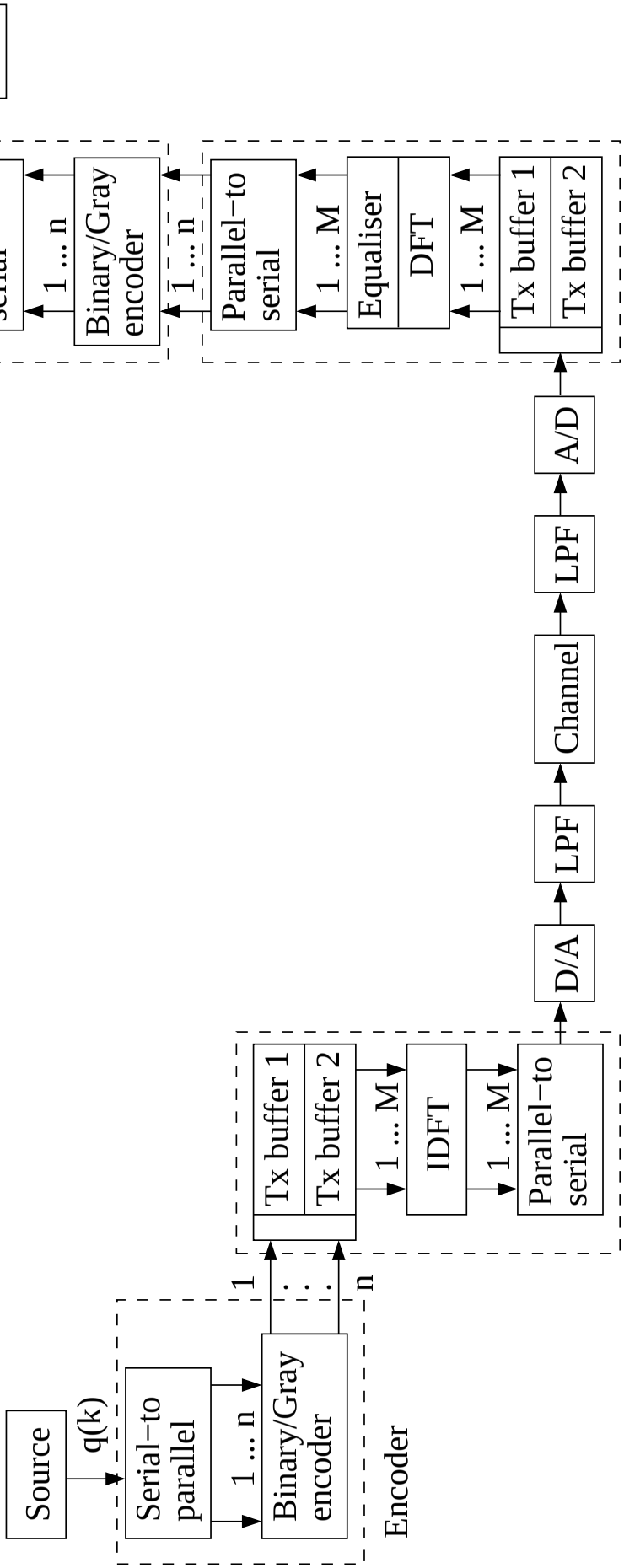

Figure 3.13: FFT-based OFDM modem schematic ©Webb, Hanzo, 1994, [63]

known pilots effectively sample the channel's frequency-domain transfer function according to the Nyquist frequency. These frequency-domain samples then allow us to recover the channel's transfer function between the frequency-domain pilots with the aid of interpolation. In addition to this simple form of channel equalisation, another advantage of the OFDM-based modulation is that it turns a channel exhibiting memory into a memoryless one, where the memory is the influence of the past transmitted symbols on the value of the present symbol.

In the literature the performance of TCM and TTCM assisted OFDM modems has been investigated in [70] when communicating over various dispersive Rayleigh fading channels. In [71], a multilevel coding and BICM assisted OFDM modem employing noncoherent reception was investigated in dispersive Rayleigh fading environments. In this section, the performance of TCM, TTCM, BICM and BICM-ID schemes will be investigated using the Pan-European Digital Video Broadcasting (DVB) standard's OFDM scheme [63] for transmissions over the 12-path COST207 [72] Hilly Terrain (HT) Rayleigh fading channels, which characterise a rather hostile, strongly dispersive environment.

3.4.2 System Overview

The encoder produces a block of N_i channel symbols to be transmitted. These symbols are transmitted by the OFDM modulator. As the OFDM modulator transmits N_u modulated symbols per OFDM symbol, if $N_u = N_i$ then the whole block of N_u modulated symbols can be transmitted in a single OFDM symbol. We refer to this case as the single-symbol mapping based scenario. By contrast, if $N_u < N_i$, then more than one OFDM symbol is required for the transmission of the channel-coded block. We refer to this case as the multiple-symbol mapping based scenario. Both the single- and the multiple-symbol scenarios are interesting. The single-symbol scenario is more appealing from an implementation point of view, as it is significantly more simple. However, it is well known that the performance of a turbo-coded scheme improves upon increasing the IL. Since the number of subcarriers in an OFDM system is limited by several factors, such as for example the oscillator's frequency stability, by using the single-symbol solution we would be limited in terms of the TTCM block length as well. Thus the multiple-symbol solution also has to be considered in order to fully exploit the advantages of the TTCM scheme. Since the single-symbol based scheme is conceptually more simple, we will consider this scenario first. Its extension to the multiple-symbol scenario is straightforward.

In the single carrier system discussed in Section 4.3.1 the received signal is given by $y_k = x_k * h_k + n_k$, where $*$ denotes the convolution of the transmitted sequence x_k with the channel's impulse response h_k. An equaliser is used for removing the ISI before channel decoding, giving $\tilde{y}_k = \tilde{x}_k + \tilde{n}_k$. The associated branch metrics can be computed as:

$$\begin{aligned} P(\tilde{y}_k|\tilde{x}_k) &= e^{-\frac{|\tilde{n}|^2}{2\sigma^2}} \\ &= e^{-\frac{|\tilde{y}_k-\tilde{x}_k|^2}{2\sigma^2}}. \end{aligned} \tag{3.5}$$

However, in a multi-carrier OFDM system, the received signal is given by $Y_k = X_k \cdot H_k + N_k$, which facilitates joint channel equalisation and channel decoding by computing the branch metrics as:

$$P(y_k|x_k) = e^{-\frac{|Y_k - H_k \cdot X_k|^2}{2\sigma^2}}, \tag{3.6}$$

where H_k is the channel's frequency-domain transfer function at the centre frequency of the kth subcarrier. Hence, as long as the the channel transfer function estimation is of sufficiently high quality, simple frequency-domain equalisation could be invoked during the decoding process. If iterative channel decoding is invoked, the channel transfer function estimation is expected to improve during the consecutive iterative steps, in a fashion known in the context of turbo equalisation [73]. Indeed, a performance as high as that in conjunction with perfect channel estimation can be attained [74].

Let us now consider the effect of the channel interleaver. When the channel is frequency selective, it exhibits frequency-domain nulls, which may obliterate several OFDM subcarriers. Thus the quality of several consecutive received subcarrier symbols will be low. If the quality is inferior, the channel decoder is unable to correctly estimate the transmitted symbols. When, however, a channel interleaver is present, the received symbols are shuffled before channel decoding and hence these clusters of corrupted subcarriers are dispersed. Thus, after the channel interleaver we expect to have only isolated low-quality subcarriers surrounded by unimpaired ones. In this case the decoder is more likely to be able to recover the symbol transmitted on the corrupted subcarrier, using the redundancy added by the channel coding process, conveyed by the surrounding unimpaired subcarriers.

Finally, we consider the multiple-symbol scenario. The system requires only a minor modification. When more than one OFDM symbol is required for transmitting the block of channel-coded symbols, the OFDM demodulator has to store both the demodulated symbols and the channel transfer function estimates in order to form a whole channel-coded block. This block is then fed to the channel interleaver and then to the channel decoder, together with the channel transfer function estimate. Exactly the same MAP decoder as in the single-symbol case can be used for performing the joint channel equalisation and channel decoding. Similarly, the function of the channel interleaver is the same as in the single-symbol scenario.

3.4.3 Simulation Parameters

OFDM Parameters	
Total number of subcarriers, N	2048 (2K mode)
Number of effective subcarriers, N_u	1705
OFDM symbol duration T_s	224 μs
Guard interval	$T_s/4 = 56\mu$s
Total symbol duration (inc. guard interval)	280 μs
Consecutive subcarrier spacing $1/T_s$	4464 Hz
DVB channel spacing	7.61 MHz
QPSK and QAM symbol period	7/64 μs
Baud rate	9.14 MBaud

Table 3.3: Parameters of the OFDM module [75].

The DVB standard's OFDM scheme [63] was used for this study. The parameters of the OFDM DVB system are presented in Table 3.3. Since the OFDM modem has 2048 subcarriers, the subcarrier signalling rate is effectively 2000 times lower than the maximum DVB transmission rate of 20

Mbit/s, corresponding to about 10 kbit/s. At this sub-channel rate, the individual sub-channels can be considered nearly frequency-flat.

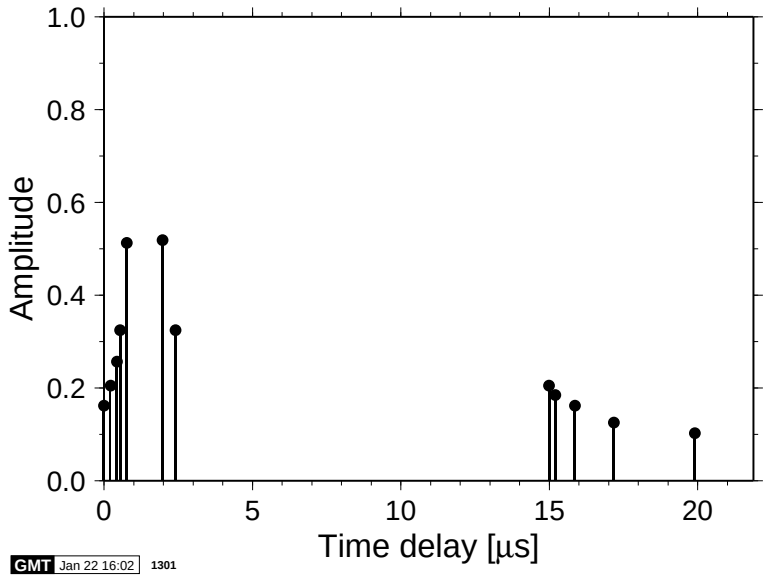

Figure 3.14: COST207 Hilly Terrain (HT) type of impulse response [72].

The channel model employed is the 12-path COST207 [72] HT type of impulse response, exhibiting a maximum relative path delay of 19.9 μs. The unfaded impulse response is depicted in Figure 3.14. The carrier frequency is 500 MHz and the sampling rate is 7/64 μs. Each of the channel paths was faded independently, obeying a Rayleigh fading distribution, according to a normalised Doppler frequency of 10^{-5} [15]. This corresponds to a worst-case vehicular velocity of about 200 km/h.

3.4.4 Simulation Results And Discussions

In this section, the system performance of the OFDM-based coded modulation schemes is evaluated using QPSK, 8PSK and 16QAM. The coding rate of the coded modulation schemes changes according to the modem mode used. Hence the effective throughput for QPSK is 1 bit/subcarrier, for 8PSK it is 2 bits/subcarrier and finally for 16QAM it is 3 bits/subcarrier.

Figure 3.15 shows the performance of the integrated systems in conjunction with a channel interleaver of 5000 symbols using a QPSK modem. We can see from Figure 3.15 that at a BER of 10^{-4} BICM performs about 1.5 dB better than TCM. When the iterative schemes of TTCM and BICM-ID are used, a better performance is achieved. Specifically, in conjunction with eight iterations, TTCM and BICM-ID approach their best achievable performance. Clearly, in this scenario TTCM is superior to BICM-ID.

Figure 3.16 illustrates the performance of the systems considered, which maintain an effective throughput of 2 bits/subcarrier using a channel interleaver length of 5000 symbol duration. All schemes exhibit a similar complexity, however, TTCM using eight iterations is slightly more complex. Specifically, in order to be able to compare the associated complexities we assumed that the number of decoder trellis states determined the associated implementation/decoding complexity. For example, a memory-length $\nu = 3$ TTCM scheme had $2^{\nu} = 8$ trellises per decoding iteration and there are two decoders. Hence, after four iterations we encounter a total of $8 \cdot 2 \cdot 4 = 64$ trellis states. Therefore

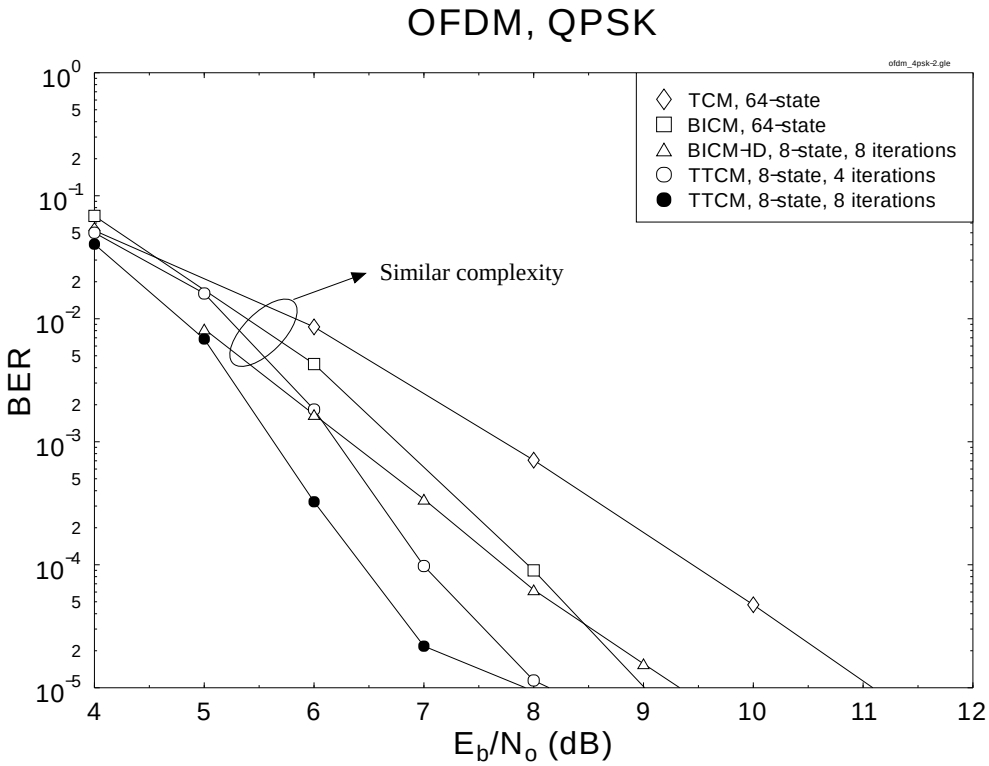

Figure 3.15: Comparison of TCM, TTCM, BICM and BICM-ID using QPSK-OFDM modem for transmissions over the Rayleigh fading COST207 HT channel of Figure 3.14 at a normalised Doppler frequency of 10^{-5}. The OFDM parameters are listed in Table 3.3, while the coded modulation parameters were summarised in Section 3.2.1.

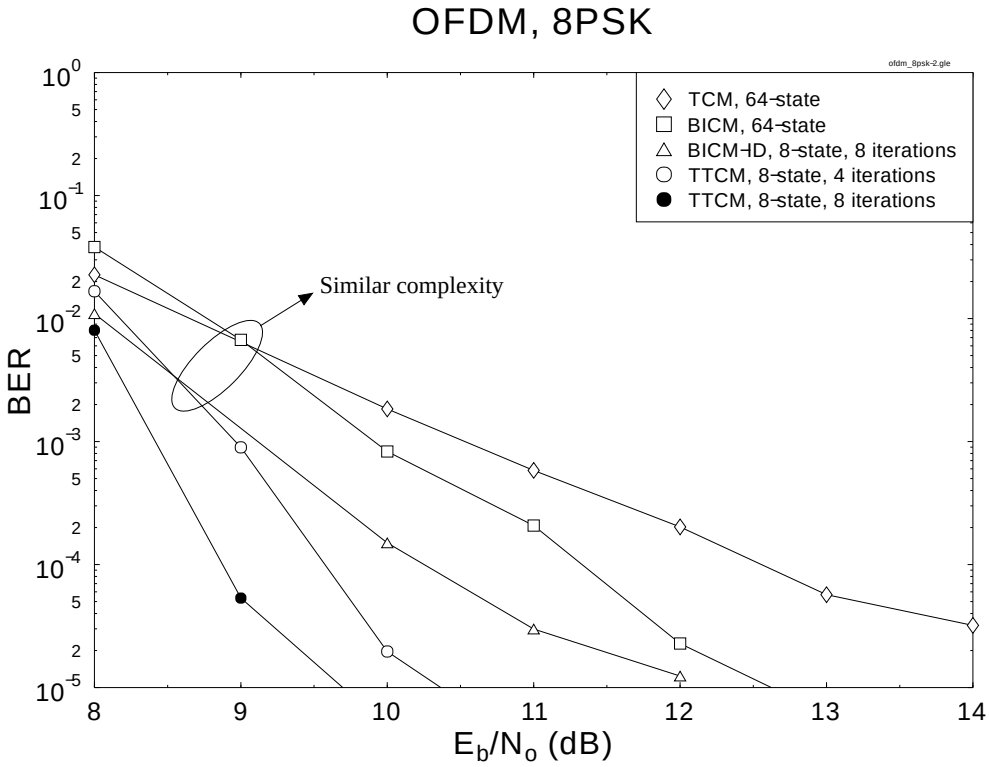

Figure 3.16: Comparison of TCM, TTCM, BICM and BICM-ID using 8PSK-OFDM modem for transmissions over the Rayleigh fading COST207 HT channel of Figure 3.14 at a normalised Doppler frequency of 10^{-5}. The OFDM parameters are listed in Table 3.3 while the coded modulation parameters were summarised in Section 3.2.1.

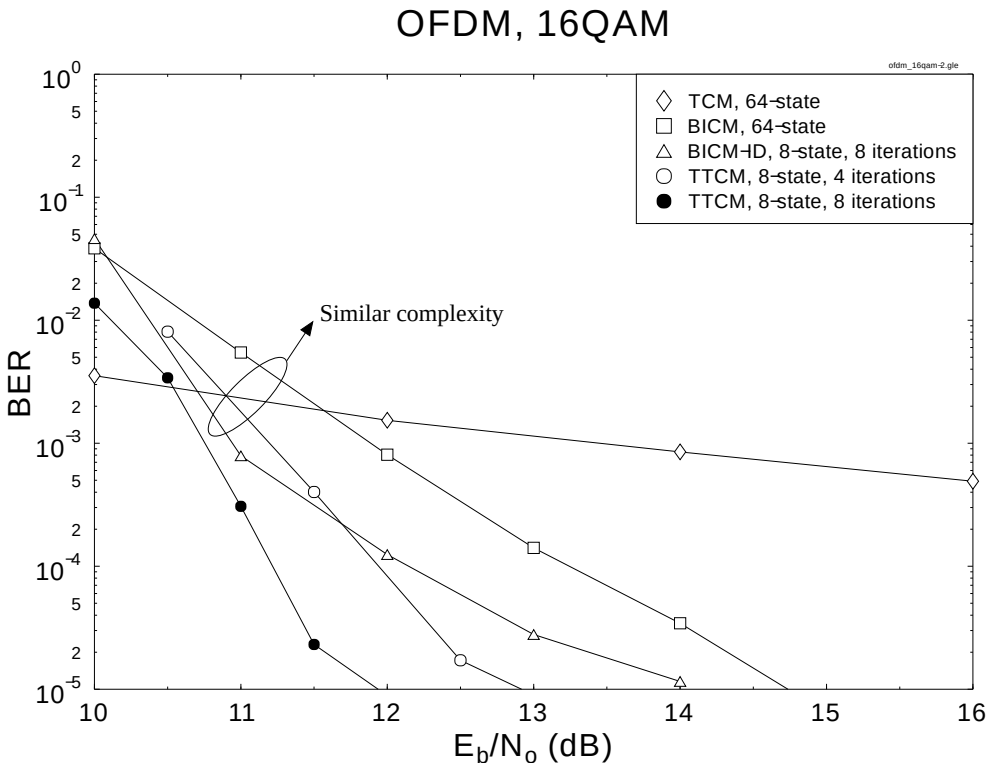

Figure 3.17: Comparison of TCM, TTCM, BICM and BICM-ID using 16QAM-OFDM modem for transmissions over the Rayleigh fading COST207 HT channel of Figure 3.14 at a normalised Doppler frequency of 10^{-5}. The OFDM parameters are listed in Table 3.3 while the coded modulation parameters were summarised in Section 3.2.1.

a 64-state, $\nu = 6$ TCM scheme has a similar complexity to a $\nu = 4$ TTCM arrangement using four iterations. Again, TTCM is the best scheme. At a BER of 10^{-4}, TTCM performs about 0.7 dB better than BICM-ID, 1.8 dB better than BICM and 3.0 dB better than TCM at a similar complexity. Another 0.6 dB gain was attained by TTCM, when the number of turbo iteration was increased from four to eight.

Figure 3.17 compares the performance of the systems maintaining a throughput of 3 bits/subcarrier using a channel interleaver of 5000 symbols. Again, the systems exhibited a similar complexity, except for TTCM employing eight iterations. There is one uncoded information bit in the 4-bit 16QAM symbol of the rate-3/4 TCM scheme having 64 states, as can be seen from its generator polynomial in Table 3.1. For this reason, this TCM scheme is only potent at lower SNRs, while exhibiting modest performance improvements in the higher SNR region, as demonstrated by Figure 3.17. The rest of the schemes do not have uncoded information bits in their 16QAM symbols. BICM-ID outperforms BICM for E_b/N_0 values in excess of about 1.2 dB, while it is inferior in comparison to TTCM by about 0.2 dB at a BER of 10^{-4}. Note that BICM-ID starts to exhibit an error floor at a BER around 10^{-4}, while TTCM starts to exhibit an error floor at a BER around 10^{-5}.

3.4.5 Conclusions

In this section OFDM was integrated with the coded modulation schemes of Chapter 2. The performance of TCM, TTCM, BICM and BICM-ID assisted OFDM was investigated for transmissions over

the dispersive COST207 HT Rayleigh fading channel of Figure 3.14 using QPSK, 8PSK and 16QAM modulation modes. TTCM was found to be the best compromise scheme, followed by BICM-ID, BICM and TCM.

3.5 Chapter Conclusions

In Section 3.2 the performance of four coded modulation schemes was evaluated for transmissions over AWGN and narrowband fading channels. Explicitly, it was shown in Sections 3.2.2.1 and 3.2.2.2 that at a given complexity TCM performed better than BICM in AWGN channels, but performed worse than BICM in uncorrelated narrowband Rayleigh fading channels. However, BICM-ID outperformed TCM and BICM for transmissions over both AWGN and uncorrelated narrowband Rayleigh fading channels at the same decoding complexity. TTCM, however, has shown superior performance over the other coded modulation schemes studied. By contrast, in Section 3.4 we evaluated the performance of the coded modulation schemes when communicating over the wideband COST207 HT Rayleigh fading channels, by assuming that the number of subcarriers was sufficiently high for maintaining narrowband channel conditions in each OFDM subchannel. In the context of 8PSK-based OFDM, TTCM performs about 0.7 dB better than BICM-ID, 1.8 dB better than BICM and 3.0 dB better than TCM at a BER of 10^{-4}, as evidenced by Figure 3.16.

The TTCM assisted scheme was found to represent the most attractive trade-off in terms of its performance versus complexity balance, closely followed by the BICM-ID assisted scheme, both in the context of the conventional single carrier system of Section 3.2 as well as in the multi-carrier OFDM system of Section 3.4, when communicating over non-dispersive propagation environment.

In summary, the coding gain values exhibited by the coded modulation schemes studied in this chapter were tabulated in Tables 3.4 and 3.5. Specifically, we summarised the performance gain exhibited by the various coded modulation schemes of Section 3.2, when communicating over non-dispersive AWGN channels and uncorrelated Rayleigh fading channels in Table 3.4. The coding gains exhibited by the OFDM-based coded modulation schemes of Section 3.4 communicating over the COST207 HT Rayleigh fading channels were tabulated in Table 3.5.

Code	Modulation/ BPS	AWGN Channels				Flat Uncorrelated Rayleigh Fading Channels			
		E_b/N_o (dB)		Gain (dB)		E_b/N_o (dB)		Gain (dB)	
		BER				BER			
		10^{-3}	10^{-5}	10^{-3}	10^{-5}	10^{-3}	10^{-5}	10^{-3}	10^{-5}
Uncoded	BPSK/1	6.75	9.52	0.00	0.00	24.00	43.50	0.00	0.00
TCM	QPSK/1	2.81	4.42	3.94	5.10	6.29	9.88	17.71	33.62
TTCM	QPSK/1	**1.27**	**1.90**	5.48	7.62	**3.40**	**4.28**	20.60	39.22
BICM	QPSK/1	2.60	4.16	4.15	5.36	5.00	7.46	19.00	36.04
BICM-ID	QPSK/1	2.00	4.07	4.75	5.45	5.05	8.50	18.95	35.00
Uncoded	QPSK/2	6.75	9.52	0.00	0.00	24.00	43.50	0.00	0.00
TCM	8PSK/2	4.57	6.20	2.18	3.32	10.05	17.00	13.95	26.50
TTCM	8PSK/2	**3.64**	**4.20**	3.11	5.32	**7.32**	**9.84**	16.68	33.66
BICM	8PSK/2	5.41	7.46	1.34	2.06	8.95	12.90	15.05	30.60
BICM-ID	8PSK/2	4.25	4.86	2.50	4.66	7.43	11.12	16.57	32.38
Uncoded	8PSK/3	10.02	12.95	0.00	0.00	26.15	46.00	0.00	0.00
TCM	16QAM/3	6.32	8.01	3.70	4.94	15.54	34.00	10.61	12.00
TTCM	16QAM/3	**5.38**	**6.15**	4.64	6.80	**9.72**	**12.10**	16.43	33.90
BICM	16QAM/3	8.50	10.10	1.52	2.85	12.76	15.50	13.39	30.50
BICM-ID	16QAM/3	5.45	6.65	4.57	6.30	9.75	14.30	16.40	31.70
Uncoded	16QAM/4	10.51	13.37	–	–	26.78	47.00	–	–
TCM	64QAM/5	10.70	12.20	–	–	22.80	43.00	–	–
TTCM	64QAM/5	**9.86**	**10.46**	–	–	22.80	43.00	–	–
BICM	64QAM/5	11.60	13.50	–	–	**17.02**	23.50	–	–
BICM-ID	64QAM/5	10.14	10.78	–	–	15.38	**22.00**	–	–
Uncoded	64QAM/6	14.74	17.72	–	–	30.37	50.00	–	–

Table 3.4: Coding gain values of the various coded modulation schemes studied in this chapter, when communicating over non-dispersive AWGN channels and uncorrelated Rayleigh fading channels. All of the coded modulation schemes exhibited a similar decoding complexity in terms of the number of decoding states, which was equal to 64 states. An interleaver block length of 2000 symbols was employed. The performance of the best scheme is printed in bold.

Code	Modulation/ BPS	OFDM, COST207 HT Rayleigh fading channels			
		E_b/N_o (dB)		Gain (dB)	
		BER			
		10^{-3}	10^{-5}	10^{-3}	10^{-5}
uncoded	BPSK/1	24.18	43.70	0.00	0.00
TCM	QPSK/1	7.72	10.07	16.46	33.63
TTCM	QPSK/1	**6.20**	**8.12**	17.98	35.58
BICM	QPSK/1	6.75	9.00	17.43	34.70
BICM-ID	QPSK/1	6.32	9.31	17.86	34.39
uncoded	QPSK/2	24.18	43.70	0.00	0.00
TCM	8PSK/2	10.53	15.68	13.65	28.02
TTCM	8PSK/2	**8.96**	**10.36**	15.22	33.34
BICM	8PSK/2	9.91	12.61	14.27	31.09
BICM-ID	8PSK/2	9.11	12.20	15.07	31.50
uncoded	8PSK/3	26.47	46.02	0.00	0.00
TCM	16QAM/3	11.19	33.90	15.28	12.12
TTCM	16QAM/3	13.42	**12.90**	13.05	33.12
BICM	16QAM/3	11.88	14.73	14.59	31.29
BICM-ID	16QAM/3	**10.94**	14.10	15.53	31.92
uncoded	16QAM/4	27.17	46.60	–	–
uncoded	64QAM/6	30.65	50.10	–	–

Table 3.5: Coding gain values of the various OFDM-based coded modulation schemes studied in this chapter, when communicating over COST207 HT Rayleigh fading channels. All of the coded modulation schemes exhibited a similar decoding complexity in terms of the number of decoding states, which was equal to 64 states. An interleaver block length of 5000 symbols was employed and the corresponding simulation parameters were shown in Table 3.3. The performance of the best scheme is printed in bold.

Chapter 4

Coded Modulation Assisted Channel Equalised Systems

4.1 Introduction

In this chapter we will further investigate the performance of the TCM, BICM, TTCM and BICM-ID coded modulation schemes in the context of single carrier systems communicating over wideband fading channels. Owing to the Inter-Symbol Interference (ISI) inflicted by wideband channels, the employment of channel equalisers is essential. Hence the conventional Decision Feedback Equaliser (DFE) is introduced in Section 4.3.1, while in Section 4.4 we will evaluate the performance of a conventional DFE-aided wideband burst-by-burst adaptive coded modulation system. Specifically, in this adaptive coded modulation scheme [76] a higher-order modulation mode is employed, when the instantaneous estimated channel quality is high in order to increase the number of Bit Per Symbol (BPS) transmitted and, conversely, a more robust lower-order modulation mode is employed when the instantaneous channel quality is low, in order to improve the mean BER performance.

As another design alternative, the channel equalisation procedure can be formulated as a symbol classification problem with the advent of employing a Radial Basis Function (RBF) based equaliser [77]. The performance of this system can be further improved with the aid of *turbo equalisation* (TEQ) [14]. More specifically, turbo equalisation is a joint channel equalisation and channel decoding scheme, where the equaliser is fed both by the channel outputs plus the soft decisions provided by the channel decoder. This process is invoked for a number of iterations. An overview of RBF based channel equalisation is given in Section 4.5.1, while the TEQ scheme utilising a symbol-based MAP decoder is introduced in Section 4.6. A novel RBF-TEQ based CM scheme is presented in Section 4.7. Our discussions evolve further by introducing the reduced-complexity I/Q-TEQ philosophy in Section 4.8, while a reduced complexity RBF-I/Q-TEQ based CM scheme is proposed in Section 4.9.

Let us now commence our discourse by studying the nature of the ISI in the following section.

4.2 Intersymbol Interference

The mobile radio channels [15] can be typically characterised by band-limited linear filters. If the modulation bandwidth exceeds the coherence bandwidth of the radio channel, ISI occurs and the modulation pulses are spread or dispersed in the time domain. The ISI, inflicted by band-limited frequency, selective time-dispersive channels, distorts the transmitted signals. At the receiver, the linearly distorted signal has to be equalised in order to recover the information.

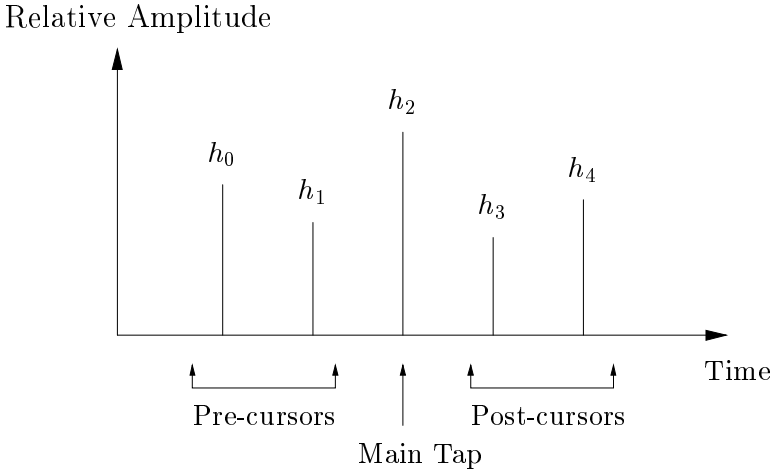

Figure 4.1: Channel Impulse Response (CIR) having pre-cursors, the main tap and post-cursors.

The linearly distorted instantaneous signal received over the dispersive channel can be visualised as the superposition of the channel's response due to several information symbols in the past and in the future. Figure 4.1 shows the Channel's Impulse Response (CIR) exhibiting three distinct parts. The main tap h_2 possesses the highest relative amplitude. The taps before the main tap, namely h_0 and h_1, are referred to as pre-cursors, whereas those following the main tap, namely h_3 and h_4, are referred to as post-cursors.

The energy of the wanted signal is received mainly over the path described by the main channel tap. However, some of the received energy is contributed by the convolution of the pre-cursors with future symbols and the convolution of the post-cursor with past symbols, which are termed pre-cursor ISI and post-cursor ISI, respectively. Thus the received signal is constituted by the superposition of the wanted signal, pre-cursor ISI and post-cursor ISI.

4.3 Decision Feedback Equaliser

Channel equalisers that are utilised for compensating the effects of ISI can be classified structurally as linear equalisers or DFEs. They can be distinguished also on the basis of the criterion used for optimising their coefficients. When applying the Minimum Mean Square Error (MMSE) criterion, the equaliser is optimised such that the mean squared error between the distorted signal and the actual transmitted signal is minimised. For time varying dispersive channels, a range of adaptive algorithms can be invoked for updating the equaliser coefficients and for tracking the channel variations [63].

4.3.1 Decision Feedback Equaliser Principle

The simple Zero Forcing Equaliser (ZFE) [78] forces all the impulse response contributions of the concatenated system constituted by the channel and the equaliser to zero at the signalling instants nT for $n \neq 0$, where T is the signalling interval duration. The ZFE provides gain in the frequency domain at frequencies where the channel's transfer function experiences attenuation and vice versa. However, both the signal and the noise are enhanced simultaneously and hence the ZFE is ineffective owing to the associated noise enhancement effects. Furthermore, no finite-gain ZFE can be designed for channels that exhibit spectral nulls [63, 79].

Linear MMSE equalisers [78] are designed for mitigating both the pre-cursor ISI and the post-cursor ISI, as defined in Section 4.2. The MMSE equaliser is more intelligent than the ZFE, since it jointly minimises the effects of both the ISI and noise. Although the linear MMSE equaliser approaches the same performance as the ZFE at high SNRs, an MMSE solution does exists for all channels, including those that exhibit spectral nulls.

The idea behind the DFE [63, 78, 79] is that once an information symbol has been detected and decided upon, the ISI that these detected symbols inflicted on future symbols can be estimated and the corresponding ISI can be cancelled before the detection of subsequent symbols.

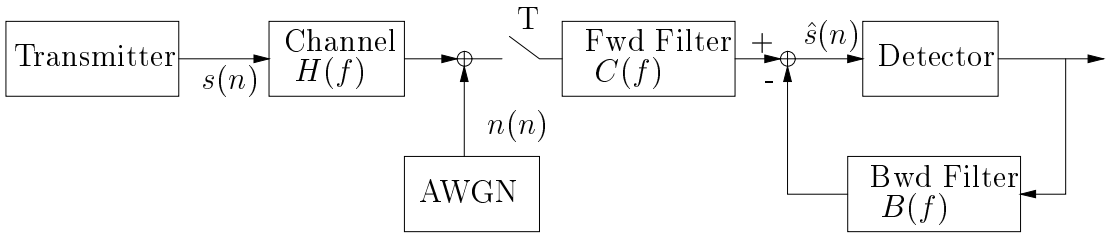

Figure 4.2: Schematic of the transmission system portraying the feedforward (Fwd) and backward (Bwd) oriented filter of the DFE, where $C(f)$ and $B(f)$ are the corresponding frequency-domain transfer functions, respectively.

The DFE employs a feedforward filter and a backward-oriented filter for combating the effects of dispersive channels. Figure 4.2 shows the general block diagram of the transmission system employing a DFE. The forward-oriented filter partially eliminates the ISI introduced by the dispersive channel. The feedback filter, in the absence of decision errors, is fed with the ISI-free transmitted signal in order to further reduce the ISI.

The feedback filter, denoted as the Bwd Filter in Figure 4.2, receives the detected symbol. Its output is then subtracted from the estimates generated by the forward filter, denoted as the Fwd Filter, in order to produce the detector's input. Since the feedback filter uses the ISI-free signal as its input, the feedback loop mitigates the ISI without introducing enhanced noise into the system. The drawback of the DFE is that when wrong decisions are fed back into the feedback loop, error propagation is inflicted and the BER performance of the equaliser is degraded.

The detailed DFE structure is shown in Figure 4.3. The feedforward filter is constituted by the coefficients or taps labelled as $C_0 \rightarrow C_{N_f-1}$, where N_f is the number of taps in the feedforward filter, as shown in the figure. The causal feedback filter is constituted by N_b feedback taps, denoted as $b_1 \rightarrow b_{N_b}$. Note that the feedforward filter contains only the present input signal r_k, and future

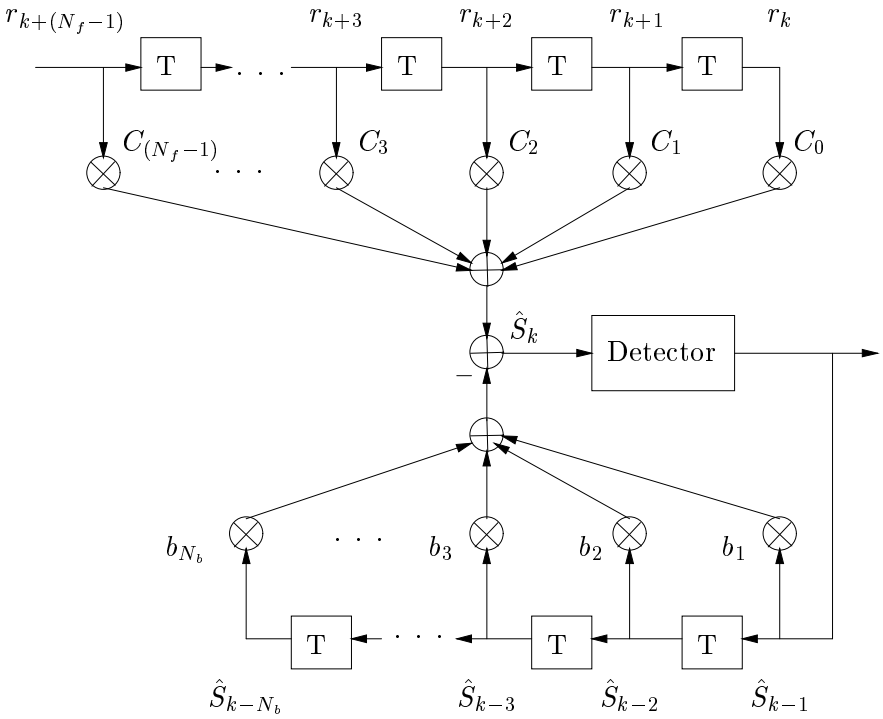

Figure 4.3: Structure of the DFE where r_k and $\hat{S}_k$ denote the received signal and detected symbol, respectively, while C_m, b_q represent the coefficient taps of the forward- and backward-oriented filters, respectively.

input signals $r_{k+1} \dots r_{k+(N_f+1)}$, which implies that no latency is inflicted. Therefore, the feedforward filter eliminates only the pre-cursor ISI, but not the post-cursor ISI. By contrast, the feedback filter mitigates the ISI caused by the past data symbols, i.e. post-cursor ISI. Since the feedforward filter only eliminates the pre-cursor ISI, the noise enhancement effects are less problematic in DFEs compared to the linear MMSE equaliser.

Here, the MMSE criterion [78] is used for deriving the optimum coefficients of the feedforward section of the DFE. The Mean Square Error (MSE) between the transmitted signal, s_k, and its estimate, $\hat{s}_k$, at the equaliser's output is formulated as:

$$MSE = E[|s_k - \hat{s}_k|^2], \tag{4.1}$$

where $E[|s_k - \hat{s}_k|^2]$ denotes the expected value of $|s_k - \hat{s}_k|^2$. In order to minimise the MSE, the orthogonality principle [80] is applied, stating that the residual error of the equaliser, $e_k = s_k - \hat{s}_k$, is orthogonal to the input signal of the equaliser, r_k, when the equaliser taps are optimal, yielding:

$$E[e_k r^*_{k+l}] = 0, \tag{4.2}$$

where the superscript * denotes conjugation. Following Cheung's approach [63, 81], the optimum coefficient of the feedforward section can be derived from the following set of N_f equations:

$$\sum_{m=0}^{N_f-1} C_m \left[\sum_{v=0}^{l} h^*_v h_{v+m-l} \sigma^2_S + N_0 \delta_{m-l} \right] = h^*_l \sigma^2_S, \; l = 0 \; \dots N_f - 1, \tag{4.3}$$

where σ^2_S and $N_0/2$ are the signal and noise variance, respectively, while h^* denotes the complex conjugate of the CIR and δ is the delta function. By solving these N_f simultaneous equations, the

equaliser coefficients, C_m, can be obtained. For the feedback filter the following set of N_b equations were used, in order to derive the optimum feedback coefficient, b_q [81]:

$$b_q = \sum_{m=0}^{N_f-1} C_m h_{m+q}, \ q = 1 \ \ldots N_b. \tag{4.4}$$

4.3.2 Equaliser Signal To Noise Ratio Loss

The equaliser's performance can be measured in terms of the equaliser's SNR loss, BER performance and MSE [79]. Here the SNR loss is considered, since this parameter will be used in next section.

The SNR loss of the equaliser was defined by Cheung [81] as:

$$SNR_{loss} = SNR_{input} - SNR_{output}, \tag{4.5}$$

where SNR_{input} is the SNR measured at the equaliser's input, given by:

$$SNR_{input} = \frac{\sigma_S^2}{2\sigma_N^2}, \tag{4.6}$$

with σ_S^2 being the average received signal power, assuming wide sense stationary conditions, and σ_N^2 is the variance of the AWGN.

The equaliser's output contains the wanted signal, the effective Gaussian noise, the residual ISI and the ISI caused by the past data symbols. In order to simplify the calculation of SNR_{output}, we assume that the SNR is high and hence we consider the low-BER range, where effectively correct bits are fed back to the DFE's feedback filter. Thus the post-cursor ISI is completely eliminated from the equaliser's output. Hence SNR_{output} is given by [81]:

$$SNR_{output} = \frac{\text{Wanted Signal Power}}{\text{Residual ISI Power } + \text{ Effective Noise Power}}, \tag{4.7}$$

where the residual ISI is assumed to be an extra noise source that possessed a Gaussian distribution. Therefore, we have:

$$\text{Wanted Signal Power} = E\left[\left| s_k \sum_{m=0}^{N_f-1} C_m h_m \right|^2 \right], \tag{4.8}$$

$$\text{Effective Noise Power} = N_0 \sum_{i=0}^{N_f-1} |C_i|^2, \tag{4.9}$$

and:

$$\text{Residual ISI Power} = \sum_{q=-(N_f-1)}^{-1} E\left[|f_q s_{k-q}|^2 \right], \tag{4.10}$$

where $f_q = \sum_{m=0}^{N_f-1} C_m h_{m+q}$ and the remaining notations are accrued from Figure 4.3. By substituting Equations 4.8, 4.9 and 4.10 into 4.7, the SNR_{output} can be written as [79]:

$$SNR_{output} = \frac{E\left[\left| s_k \sum_{m=0}^{N_f-1} C_m h_m \right|^2 \right]}{\sum_{q=-(N_f-1)}^{-1} E\left[|f_q s_{k-q}|^2 \right] \ + \ N_0 \sum_{i=0}^{N_f-1} |C_i|^2}. \tag{4.11}$$

Following this rudimentary introduction to channel equalisation, we focus our attention on quantifying the performance of various wideband Coded Modulation (CM) schemes, referring the reader to [63] for an in-depth discourse on channel equalisation.

4.4 Decision Feedback Equaliser Aided Adaptive Coded Modulation

In this section, DFE-aided wideband Burst-by-Burst (BbB) adaptive TCM, TTCM, BICM and BICM-ID schemes are proposed and characterised in performance terms, when communicating over the COST207 Typical Urban (TU) wideband fading channel. These schemes are evaluated using a practical near-instantaneous modem mode switching regime, in the context of **System I** which invokes channel interleaving over one transmission burst and **System II** which invokes channel interleaving over four transmission bursts. Explicitly, **System I** exhibited a factor four lower delay in overall modem mode signalling, and hence it was capable of more prompt modem mode reconfiguration. By contrast, **System II** was less agile in terms of modem mode reconfiguration, but benefited from a longer interleaver delay. We will show in Section 4.4.4 that a substantially improved BPS and BER performance was achieved by **System II** in comparison to **System I**. We will also show that BbB adaptive TTCM is the best performer in comparison to other adaptive CM schemes, in the context of **System II** at a similar decoding complexity, when aiming for a target BER of below 0.01%.

4.4.1 Introduction

In general fixed-mode transceivers fail to adequately counteract the time varying nature of the mobile radio channel and hence typically result in bursts of transmission errors. By contrast, in BbB adaptive schemes [76] a higher-order modulation mode is employed when the instantaneous estimated channel quality is high in order to increase the number of BPS transmitted and, conversely, a more robust lower-order modulation mode is employed when the instantaneous channel quality is low, in order to improve the mean BER performance. In the literature the performance of adaptive schemes was investigated mostly in the context of narrowband Rayleigh fading channels. Specifically, the performance of uncoded adaptive schemes and coded adaptive schemes has been investigated for transmissions over narrowband Rayleigh fading channels in [76, 82–86] and [87–94], respectively. By contrast, a turbo-coded wideband adaptive scheme assisted by a DFE was investigated in [95]. In this section, a DFE-based coded modulation assisted wideband adaptive scheme is investigated.

In our practical approach the transmitter A obtains the channel quality estimate generated by receiver B upon receiving the transmission of transmitter B. In other words, the modem mode required by receiver B is superimposed on the transmission burst of transmitter B. Hence a delay of one transmission burst duration is incurred. In the literature, adaptive coding designed for time varying channels using outdated fading estimates has been investigated in [91].

Over wideband fading channels the DFE employed will eliminate most of the ISI. Consequently, the MSE at the output of the DFE can be calculated and used as the metric invoked for switching the modulation modes [86]. This ensures that the performance is optimised by employing equalisation and BbB adaptive CM jointly, in order to combat both the signal power fluctuations and the time variant ISI of the wideband channel.

In Section 4.4.2, the system's schematic is outlined. In Section 4.4.3, the performance of various fixed-mode CM schemes is evaluated, while Section 4.4.4 contains the detailed characterisation of the BbB adaptive CM schemes in the context of **System I** and **System II**. Finally, we will conclude with our findings in Section 4.4.5.

4.4.2 System Overview

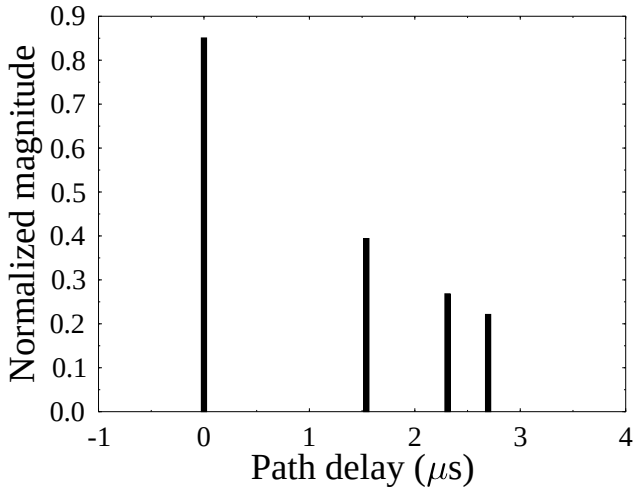

Figure 4.4: The impulse response of a COST207 Typical Urban (TU) channel [96].

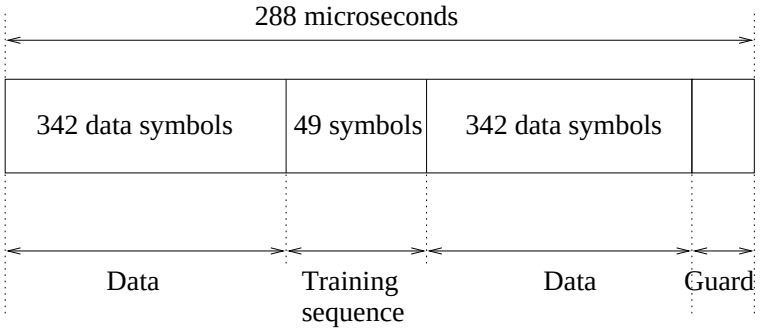

non-spread data burst

Figure 4.5: Transmission burst structure of the FMA1 non-spread data as specified in the FRAMES proposal [97].

The multipath channel model is characterised by its discretised symbol-spaced COST207 Typical Urban (TU) CIR [96], as shown in Figure 4.4. Each path is faded independently according to a Rayleigh distribution and the corresponding normalised Doppler frequency is 3.25×10^{-5}, the system's Baud rate is 2.6 MBaud, the carrier frequency is 1.9 GHz and the vehicular speed is 30 mph. The DFE incorporated 35 feed forward taps and 7 feedback taps and the transmission burst structure used is shown in Figure 4.5. When considering a Time Division Multiple Access (TDMA)/Time Division Duplex (TDD) system providing 16 slots per 4.615 ms TDMA frame, the transmission burst duration is 288 μs, as specified in the Pan-European FRAMES proposal [97].

The following assumptions are stipulated. First, we assume that the equaliser is capable of estimating the CIR perfectly with the aid of the equaliser training sequence of Figure 4.5. Second, the CIR is time-invariant for the duration of a transmission burst, but varies from burst to burst according to the normalised Doppler frequency, which corresponds to assuming that the CIR is slowly varying. We refer to this scenario as encountering burst-invariant fading. The error propagation imposed by erroneous decisions of the DFE will degrade the estimated performance, but the effect of error propa-

gation is left for further study. Here we assumed that correct symbol decisions are input to the DFE's feedback filter in order to obtain the upper bound performance of the system. It is expected that the more vulnerable higher-throughput modem modes are more prone to error propagation effects, but their influence may be compensated by slightly increasing the switching thresholds. This allows us to maintain the target BER but reduces the throughput. At the receiver, the CIR is estimated, and is then used for calculating the DFE coefficients [63]. Subsequently, the DFE is used for equalising the ISI-corrupted received signal. In addition, both the CIR estimate and the DFE feedforward coefficients are utilised for computing the SNR at the output of the DFE. More specifically, by assuming that the residual ISI is near-Gaussian distributed and that the probability of decision feedback errors is negligible, the SNR at the output of the DFE, γ_{dfe}, is calculated as [81]:

$$\begin{aligned}\gamma_{dfe} &= \frac{\text{Wanted Signal Power}}{\text{Residual ISI Power + Effective Noise Power}}. \\ &= \frac{E\left[\left|s_k \sum_{m=0}^{N_f} C_m h_m\right|^2\right]}{\sum_{q=-(N_f-1)}^{-1} E\left[\left|\sum_{m=0}^{N_f-1} C_m h_{m+q} s_{k-q}\right|^2\right] + N_0 \sum_{m=0}^{N_f} |C_m|^2},\end{aligned} \tag{4.12}$$

where C_m and h_m denote the DFE's feedforward coefficients and the CIR, respectively. The transmitted signal is represented by s_k and N_0 denotes the noise spectral density. Finally, the number of DFE feedforward coefficients is denoted by N_f.

The equaliser's SNR, γ_{dfe}, in Equation 4.12, is then compared against a set of adaptive modem mode switching thresholds f_n, and subsequently the appropriate modulation mode is selected [86, 98]. The modem mode required by receiver B is then fed back to transmitter A. The modulation modes that are utilised in this scheme are 4QAM, 8PSK, 16QAM and 64QAM [63].

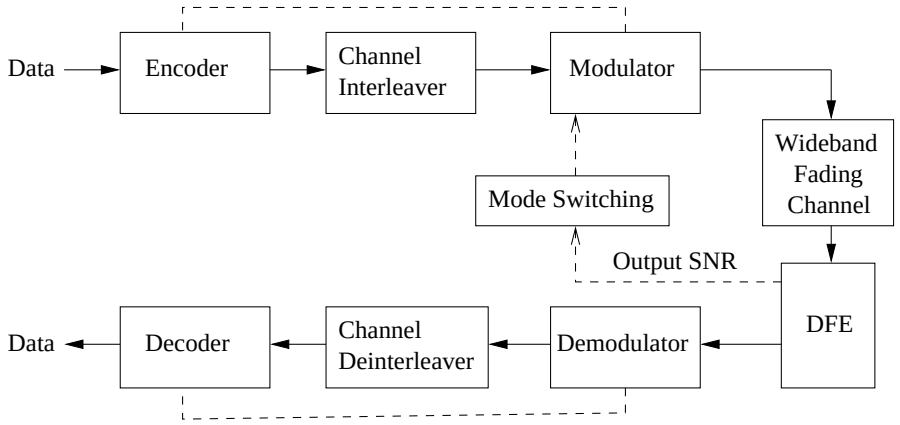

Figure 4.6: **System I** employing channel interleaving over one transmission burst. The equaliser's output SNR is used for selecting a suitable modulation mode, which is fed back to the transmitter on a burst-by-burst basis.

The simplified block diagram of the BbB adaptive CM **System I** is shown in Figure 4.6, where channel interleaving over one transmission burst is employed. Transmitter A extracts the modulation mode required by receiver B from the reverse-link transmission burst in order to adjust the adaptive CM mode suitable for the currently experienced instantaneous channel quality. This incurs one TDMA/TDD frame delay between estimating the actual channel condition at receiver B and the selected modulation mode of transmitter A. Better channel quality prediction can be achieved using the techniques proposed in [99]. We invoke four encoders, each adding one parity bit to each information

symbol, yielding the coding rate of 1/2 in conjunction with the CM mode of 4QAM, 2/3 for 8PSK, 3/4 for 16QAM and 5/6 for 64QAM.

The design of CM schemes contrived for fading channels relies on the time and space diversity provided by the associated channel coder [37, 46]. Diversity may be achieved by repetition coding, which reduces the effective data rate, space-time coded multiple transmitter/receiver structures [100], which increases cost and complexity, or by simple interleaving, which induces latency. In [101] adaptive TCM schemes were designed for narrowband fading channels utilising repetition-based transmissions during deep fades along with ideal channel interleavers and assuming zero delay for the feedback of the channel quality information.

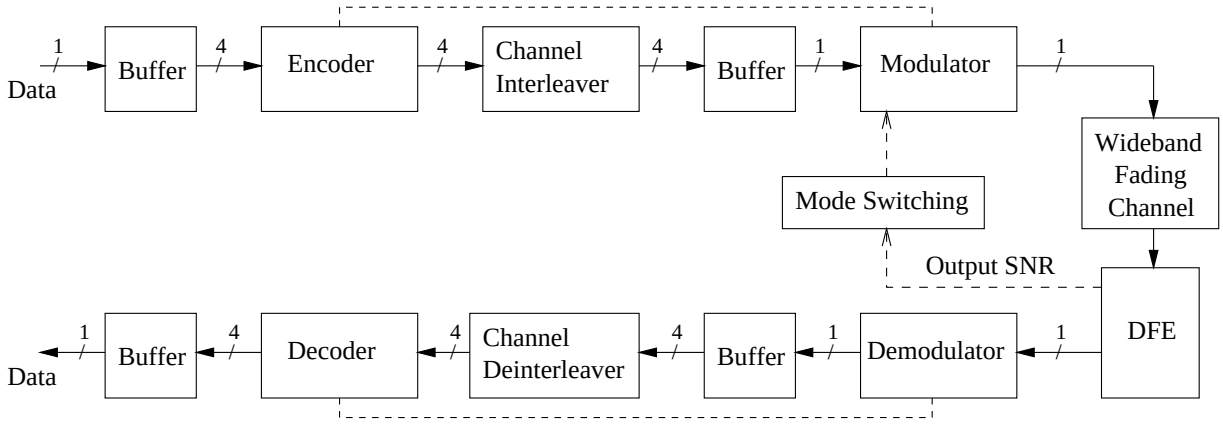

Figure 4.7: **System II** employing a channel interleaver length of four TDMA/TDD bursts. Data are entered into the input buffer on a burst-by-burst basis and the modulator modulates coded data read from the output buffer for transmission on a burst-by-burst basis. The encoder and channel interleaver as well as the decoder and channel de-interleaver operate on a four-burst basis. The equaliser's output SNR during the fourth burst is used for selecting a suitable modulation mode and fed back to the transmitter on the reverse-link burst.

Figure 4.7 shows the block diagram of **System II**, where symbol-based channel interleaving over four transmission bursts, or equivalently 4×684 symbols is utilised, in order to disperse the bursty symbol errors. Hence, the coded modulation module assembles four bursts using an identical modulation mode, so that they can be interleaved using the symbol-by-symbol random channel interleaver without the need of adding dummy bits. Then, these four-burst CM packets are transmitted to the receiver. Once the receiver has received the fourth burst, the equaliser's output SNR for this most recent burst is used for choosing a suitable modulation mode. The selected modulation mode is fed back to the transmitter on the reverse-link burst. Upon receiving the modulation mode required by receiver B (after one TDMA frame delay), the coded modulation module assembles four bursts of data from the input buffer for coding and interleaving, which are then stored in the output buffer ready for the next four bursts' transmission. Thus the first transmission burst exhibits one TDMA/TDD frame delay and the fourth transmission burst exhibits a delay of four frames which is the worst-case scenario.

4.4.3 Fixed-Mode Based Performance

Before characterising the proposed wideband BbB adaptive scheme, the BER performance of the fixed modem modes of 4QAM, 8PSK, 16QAM and 64QAM are studied in the context of **System I** where channel interleaving over one transmission burst is utilised and **System II** where channel interleaving over four transmission bursts is invoked. These results are shown in Figure 4.8 for TCM,

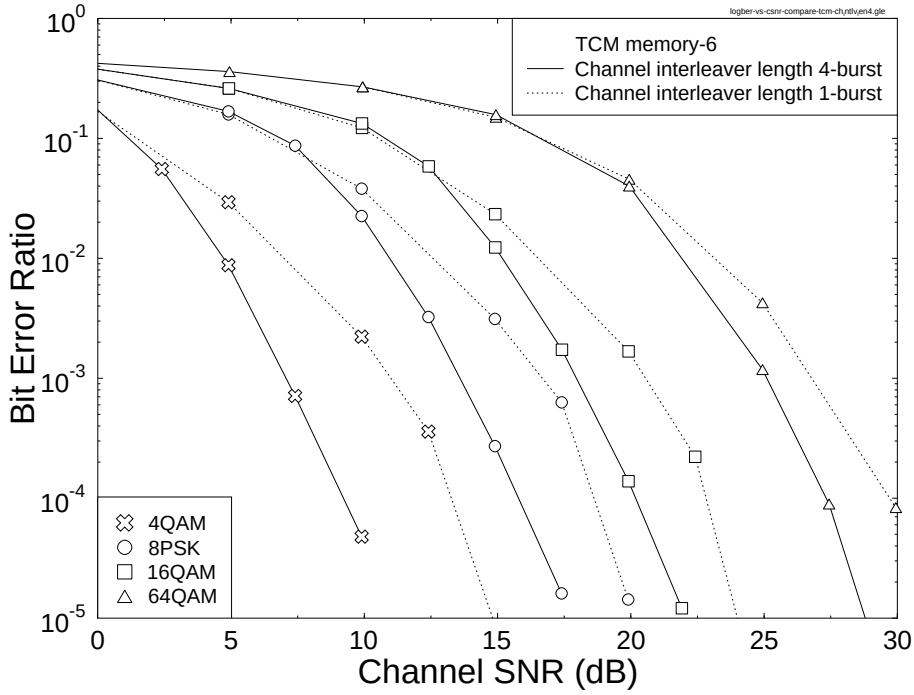

Figure 4.8: TCM performance of each individual modulation mode over the Rayleigh fading COST207 TU channel of Figure 4.4. A TCM code memory of 6 was used, since it had a similar decoding complexity to TTCM in conjunction with four iterations using a component TCM code memory of 3. The normalised Doppler frequency was 3.25×10^{-5}.

and in Figure 4.9 for TTCM. The random TTCM symbol-interleaver memory was set to 684 symbols, corresponding to the number of data symbols in the transmission burst structure of Figure 4.5, where the resultant number of bits was the $BPS \times 684$. A channel interleaver of 4×684 symbols was utilised for **System II**, where the number of coded bits was $(BPS + 1) \times 4 \times 684$ bits, since one parity bit was added to each CM symbol.

As expected, in Figures 4.8 and 4.9 the BER performance of **System II** was superior compared to that of **System I**, although at the cost of an associated higher transmission delay. The SNR gain difference between **System II** and **System I** was about 5 dB in the TTCM/4QAM mode, but this difference reduced for higher-order modulation modes. Again, this gain was obtained at the cost of a four-burst channel interleaving delay. This SNR gain difference shows the importance of time diversity in CM schemes.

TTCM has been shown to be more efficient than TCM for transmissions over AWGN channels and narrowband fading channels [38, 70]. Here, we illustrate the advantage of TTCM in comparison to TCM over the dispersive or wideband Gaussian CIR of Figure 4.4, as seen in Figure 4.10. In

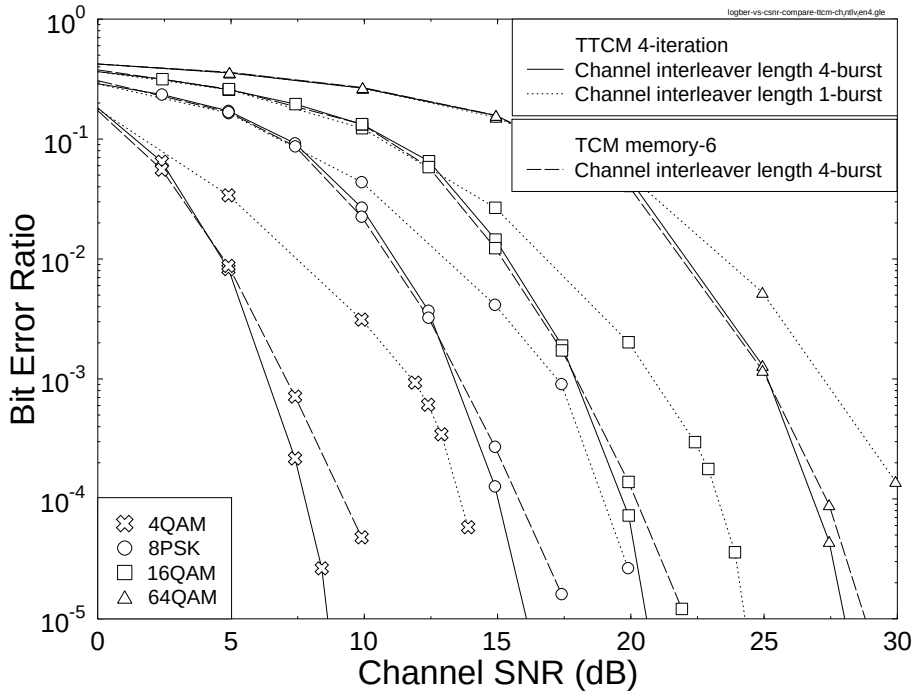

Figure 4.9: TTCM performance of each individual modulation mode over the Rayleigh fading COST207 TU channel of Figure 4.4. A component TCM code memory of 3 was used and the number of turbo iterations was four. The performance of the TCM code with memory 6 utilising a channel interleaver was also plotted for comparison. The normalised Doppler frequency was 3.25×10^{-5}.

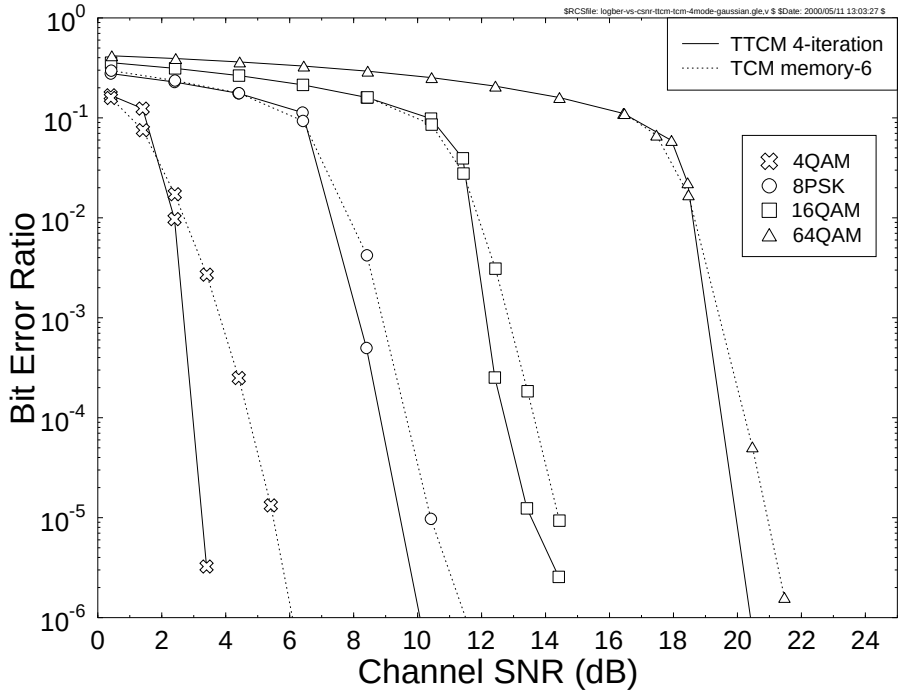

Figure 4.10: TTCM and TCM performance of each individual modulation mode for transmissions over the unfaded COST207 TU channel of Figure 4.4. The TTCM scheme used component TCM codes of memory 3 and the number of turbo iterations was four. The performance of the TCM scheme in conjunction with memory 6 was plotted for comparison with the similar-complexity TTCM scheme.

conclusion, TTCM is superior to TCM in a variety of channels.

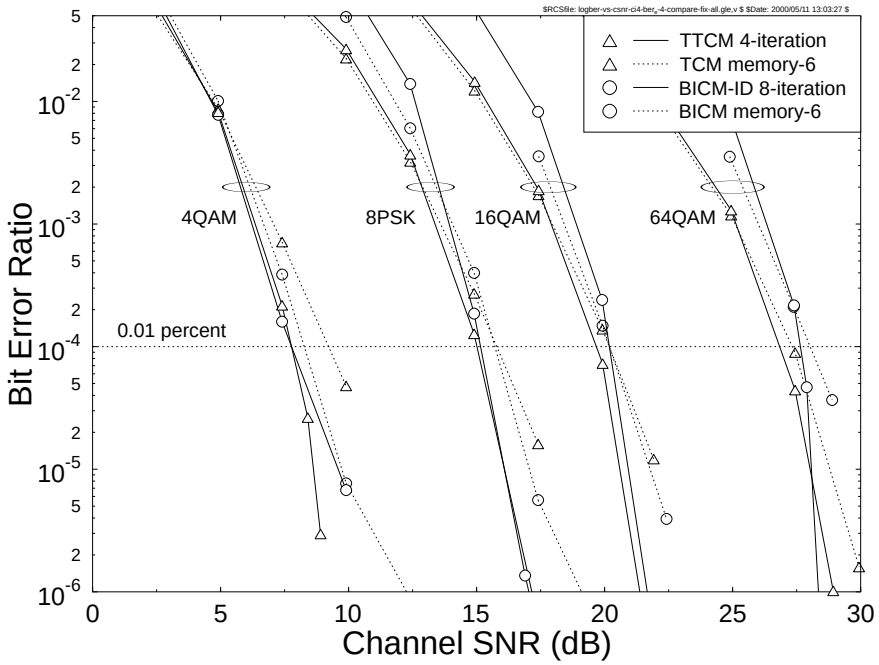

Figure 4.11: BER performance of the fixed modem modes of 4QAM, 8PSK, 16QAM and 64QAM utilising TCM, TTCM, BICM and BICM-ID schemes in the context of **System II** for transmissions over the COST207 TU channel of Figure 4.4. For the sake of maintaining a similar decoding complexity, we used a TCM code memory of 6, TTCM code memory of 3 in conjunction with four turbo iterations, BICM code memory of 6 and a BICM-ID code memory of 3 in conjunction with eight decoding iterations. However, BICM-ID had a slightly higher complexity than the other systems, since the demodulator module was invoked eight times as compared to only once for its counterparts during each decoding process. The normalised Doppler frequency was 3.25×10^{-5}.

Figure 4.11 shows the fixed modem modes' performance for TCM, TTCM, BICM and BICM-ID in the context of **System II**. For the sake of a fair comparison of the decoding complexity, we used a TCM code memory of 6, TTCM code memory of 3 in conjunction with four turbo iterations, BICM code memory of 6 and a BICM-ID code memory of 3 in conjunction with eight decoding iterations. However, BICM-ID had a slightly higher decoding complexity, since the demodulator was invoked in each BICM-ID iteration, whereas in the BICM, TCM and TTCM schemes the demodulator was only visited once in each decoding process. As illustrated in the figure, the BICM scheme performed marginally better than the TCM scheme at a BER below 0.01%, except in the 64QAM mode. Hence, adaptive BICM is also expected to be better than adaptive TCM in the context of **System II**, when a target BER of less than 0.01% is desired. This is because when the channel interleaver depth is sufficiently high, the diversity gain of the BICM's bit interleaver is higher than that of the TCM's symbol interleaver [9, 10].

Let us now compare the performance of the BbB adaptive CM **system I** and **II**.

4.4.4 System I and System II Performance

The modem mode switching mechanism of the adaptive schemes is characterised by a set of switching thresholds, the corresponding random TTCM symbol interleavers and the component codes, as follows:

$$\text{Modulation Mode} = \begin{cases} 4QAM, I_0 = 684, R_0 = 1/2 & \text{if } \gamma_{DFE} \leq f_1 \\ 8PSK, I_1 = 1368, R_1 = 2/3 & \text{if } f_1 < \gamma_{DFE} \leq f_2 \\ 16QAM, I_2 = 2052, R_2 = 3/4 & \text{if } f_2 < \gamma_{DFE} \leq f_3 \\ 64QAM, I_3 = 3420, R_3 = 5/6 & \text{if } \gamma_{DFE} > f_3, \end{cases} \tag{4.13}$$

where $f_n, n = 1 \ldots 3$, are the equaliser's output SNR thresholds, while I_n represents the random TTCM symbol interleaver size in terms of the number of bits, which is not used for the other CM schemes. The switching thresholds f_n were chosen experimentally, in order to maintain a BER of below 0.01%, and these thresholds are listed in Table 4.1.

BER < 0.01 % Adaptive System Type		Switching Thresholds		
		f_1	f_2	f_3
TCM, Memory 3	System I	19.56	23.91	30.52
	System II	17.17	21.91	29.61
TCM, Memory 6	System I	19.56	23.88	30.07
	System II	17.14	21.45	29.52
TTCM, 4 iterations	System I	19.69	23.45	30.29
	System II	16.66	21.40	28.47
BICM, Memory 3	System I	19.94	24.06	31.39
BICM-ID, 8 iterations	System II	16.74	21.45	28.97

Table 4.1: The switching thresholds were set experimentally for transmissions over the COST207 TU channel of Figure 4.4, in order to achieve a target BER of below 0.01%. **System I** utilises a channel interleaver length of one TDMA/TDD burst, while **System II** uses a channel interleaver length of four TDMA/TDD bursts.

Let us consider the adaptive TTCM scheme in order to investigate the performance of **System I** and **System II**. The performance of **System I** employing channel interleaving over one transmission burst was found to be identical to that of the same scheme employing no channel interleaving. This is because in the context of the burst-invariant fading scenario the channel behaves like a dispersive Gaussian channel, encountering a specific fading envelope and phase trajectory across a transmission burst. The CIR is then faded at the end or at the commencement of each transmission burst. Hence the employment of a channel interleaver having a memory of one transmission burst would not influence the distribution of the channel errors experienced by the decoder. The BER and BPS performances of both adaptive TTCM systems using four iterations are shown in Figure 4.12, where we observed that the throughput of **System II** was superior to that of **System I**. Furthermore, the overall BER of **System II** was lower than that of **System I**. In order to investigate the switching dynamics of both systems, the mode switching together with the equaliser's output SNR was plotted versus time at an average channel SNR of 25 dB in Figures 4.13 and 4.14. Observe in Table 4.1 that the switching thresholds f_n of **System II** are lower than those of **System I**, since the fixed-mode-based results of **System II** in Figure 4.9 were better. Hence higher-order modulation modes were chosen more

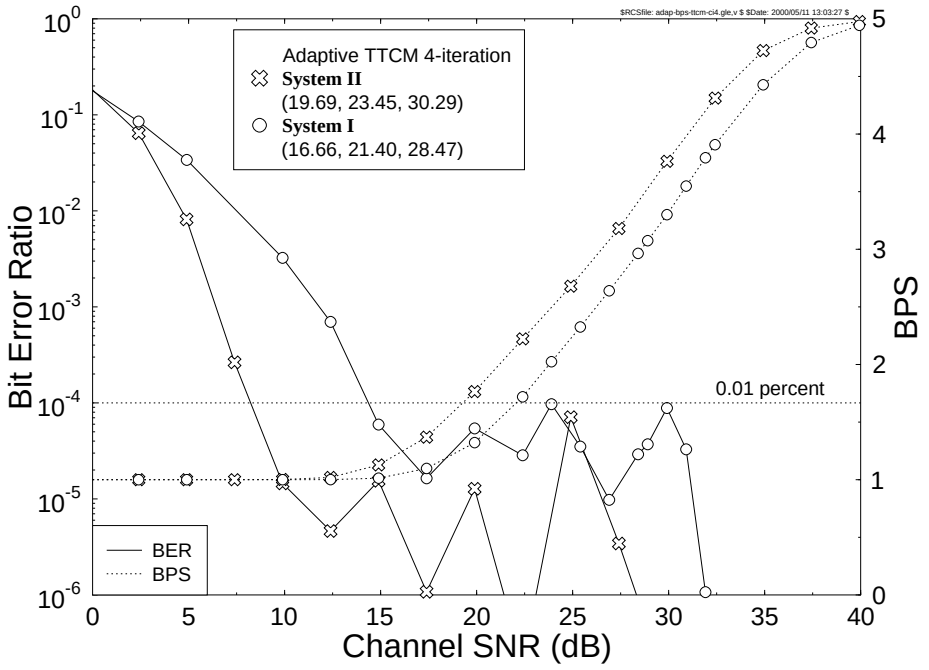

Figure 4.12: BER and BPS performance of adaptive TTCM for transmissions over the COST207 TU channel of Figure 4.4, using four turbo iterations in **System I** (with a channel interleaver length of one burst) and in **System II** (with a channel interleaver length of four bursts) for a target BER of less than 0.01%. The legends indicate the associated switching thresholds expressed in dB, as seen in the brackets. The normalised Doppler frequency was 3.25×10^{-5}.

frequently than in **System I**, giving a better BPS throughput. From Figures 4.13 and 4.14, it is clear that **System I** was more flexible in terms of mode switching, while **System II** benefited from higher diversity gains due to the four-burst channel interleaver. This diversity gain compensated for the loss of switching flexibility, ultimately providing a better performance in terms of BER and BPS, as seen in Figure 4.12.

In our next endeavour, the adaptive CM schemes of **System I** and **System II** are compared. Figure 4.15 shows the BER and BPS performance of **System I** for adaptive TTCM using four iterations, adaptive TCM of memory 3 (which was the component code of our TTCM scheme), adaptive TCM of memory 6 (which had a similar decoding complexity to our TTCM scheme) and adaptive BICM of memory 3. As can be seen from the fixed-mode results of Figures 4.8 and 4.9 in the previous section, TCM and TTCM performed similarly in terms of their BER, when channel interleaving over one transmission burst was used for the slow fading wideband COST207 TU channel of Figure 4.4. Hence, they exhibited a similar performance in the context of the adaptive schemes of **System I**, as shown in Figure 4.15. Even the TCM scheme of memory 3 associated with a lower complexity could give a similar BER and BPS performance. This shows that the equaliser plays a dominant role in **System I**, where the coded modulation schemes could not benefit from sufficient diversity due to the lack of interleaving. Also shown in Figure 4.15 is that adaptive TCM exhibited a better BPS throughput and BER performance than adaptive BICM, due to employing an insufficiently high channel interleaving depth for the BICM scheme, for transmissions over our slow fading wideband channels.

When channel interleaving over four transmission bursts is introduced in **System II**, the bursty

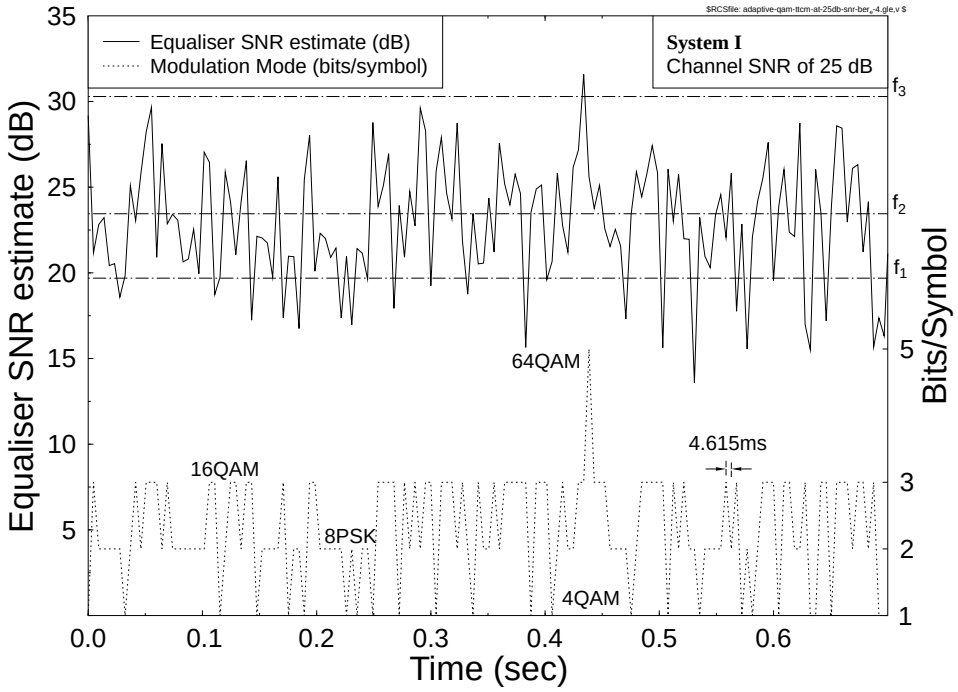

Figure 4.13: Channel SNR estimate and BPS versus time plot for adaptive TTCM for transmissions over the COST207 TU channel of Figure 4.4, using four turbo iterations in **System I** at an average channel SNR of 25 dB, where the modulation mode switching is based upon the equaliser's output SNR, which is compared to the switching thresholds f_n defined in Table 4.1. The duration of one TDMA/TDD frame is 4.615 ms. The TTCM mode can be switched after one frame duration.

symbol errors are dispersed. Figure 4.16 illustrates the BER and BPS performance of **System II** for adaptive TTCM using four iterations, adaptive TCM of memory 3, adaptive TCM of memory 6 and adaptive BICM-ID of memory 3 in conjuction with eight decoding iterations. The performance of all these schemes improved in the context of **System II**, as compared to the corresponding schemes in **System I**. The TCM scheme of memory 6 had a lower BER than TCM of memory 3, and also exhibited a small BPS improvement. As observed in Figure 4.11, we noticed that BICM-ID had the worst performance at low SNRs in each modulation modes compared to other CM schemes. However, it exhibited a steep slope and therefore at high SNRs it approached the performance of the TTCM scheme. As shown in Figure 4.16, the adaptive TTCM scheme exhibited a better BPS throughput than adaptive BICM-ID, since TTCM had a better performance in fixed modem modes at a BER of 0.01%. However, adaptive BICM-ID exhibited a lower BER performance than adaptive TTCM owing to the high steepness of the BER curve of BICM-ID in its fixed modem modes.

In summary, we have observed BER and BPS gains for the adaptive CM schemes of **System II** in comparison to the adaptive CM schemes of **System I**. Adaptive TTCM exhibited a superior BPS performance in comparison to other adaptive CM schemes in the context of **System II**.

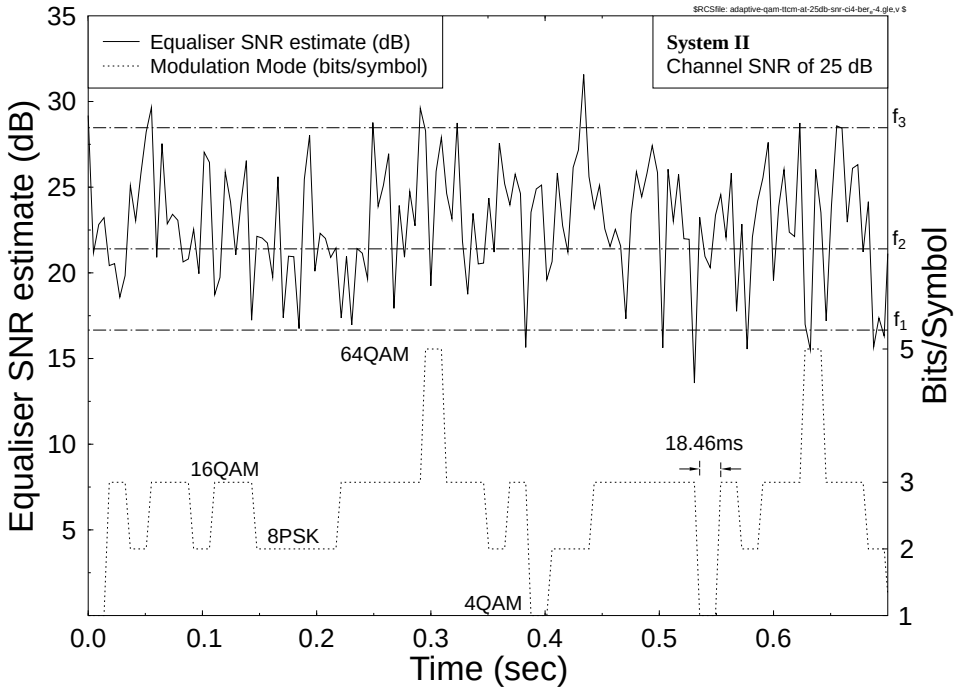

Figure 4.14: Channel SNR estimate and BPS versus time plot for adaptive TTCM for transmissions over the COST207 TU channel of Figure 4.4, using four turbo iterations in **System II** at an average channel SNR of 25 dB, where the modulation mode switching is based upon the equaliser's output SNR which is compared to the switching thresholds f_n defined in Table 4.1. The duration of one TDMA/TDD frame is 4.615 ms. The TTCM mode is maintained for four frame durations, i.e. for 18.46 ms.

4.4.5 Conclusions

In this section, BbB adaptive TCM, TTCM, BICM and BICM-ID were proposed for transmissions over wideband fading channels and they were characterised in performance terms when communicating over the COST207 TU fading channel. When channel interleaving over one transmission burst is invoked in **System I**, the performance of the system was dominant by the channel equaliser. Nonetheless, adaptive TCM still outperformed adaptive BICM in the context of **System I**, as shown in Figure 4.15. When observing the associated BPS curves, adaptive TTCM exhibited up to 2.5 dB SNR gain when the channel interleaver depth was increased from one to four transmission bursts, as evidenced in Figure 4.12. Upon comparing the BPS curves, adaptive TTCM also exhibited up to 0.7 dB SNR gain compared to adaptive TCM of the same complexity in the context of **System II** for a target BER of less than 0.01%, as shown in Figure 4.16. Finally, the BPS performance of adaptive BICM-ID was only marginally worse than that of adaptive TTCM in the context of **System II**, as illustrated in Figure 4.16.

4.5 Radial Basis Function based Equalisation

In the forthcoming sections, we will further investigate the Coded Modulation (CM) schemes in the context of a Radial Basis Function (RBF) assisted turbo equalised system.

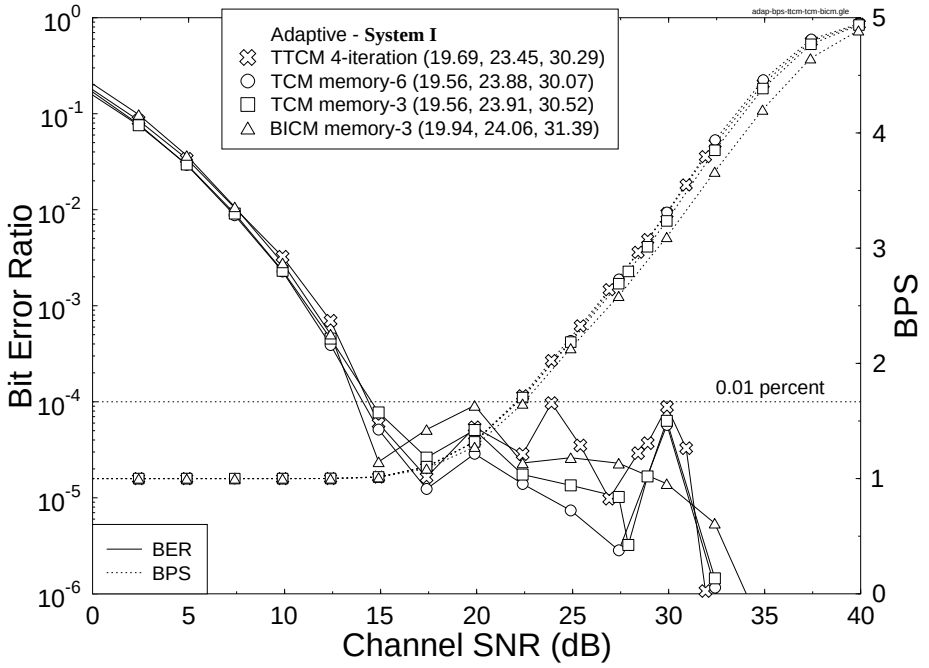

Figure 4.15: BER and BPS performance of adaptive TCM, TTCM and BICM in the context of **System I**, for transmissions over the Rayleigh fading COST207 TU channel of Figure 4.4. The switching mechanism was characterised by Equation 4.13. The switching thresholds were set experimentally, in order to achieve a BER of below 0.01%, as shown in Table 4.1. The normalised Doppler frequency was 3.25×10^{-5}.

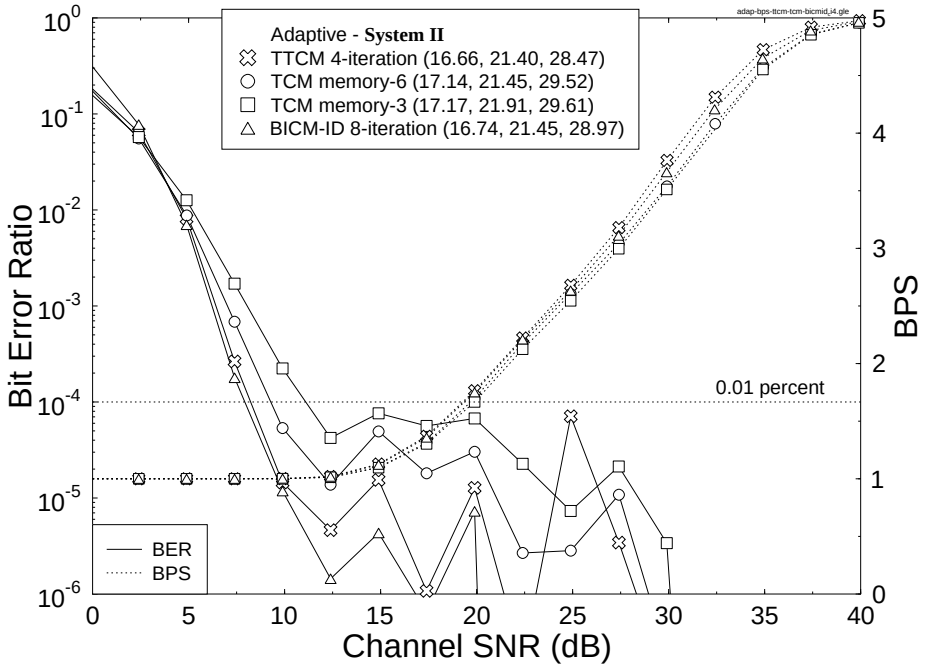

Figure 4.16: BER and BPS performance of adaptive TCM, TTCM and BICM-ID in the ccontext of **System II**, for transmissions over the Rayleigh fading COST207 TU channel of Figure 4.4. The switching mechanism was characterised by Equation 4.13. The switching thresholds were set experimentally, in order to achieve a BER of below 0.01%, as shown in Table 4.1. The normalised Doppler frequency was 3.25×10^{-5}.

The RBF based equaliser [77] studied constitutes a non-linear equalisation scheme, which formulates the channel equalisation procedure as a classification problem. More explicitly, in conventional equalisers of Section 4.3.1 the received signal is linearly filtered with the aid of the channel equaliser, which is aiming for mimicking the inverse of the CIR. By contrast, given the CIR, the RBF based equaliser determines all possible channel outputs engendered by the set of legitimate transmitted symbols and then classifies each received symbol into the nearest legitimate channel output, which allows us to infer the specific symbol transmitted. The application of non-linear RBF based equalisers has been studied in conjunction with channel codecs [102, 103], space-time codecs [104] as well as turbo equalisation [105]. The BER performance of RBF-based Turbo Equalisation (RBF-TEQ) was presented in [105] in the context of Quadrature Amplitude Modulation (QAM), which was found similar to that of the Conventional Trellis-based Turbo Equalisation (CT-TEQ) [106]. The RBF-assisted schemes are however capable of maintaining a lower complexity than their conventional trellis-based counterparts, when communicating over both dispersive Gaussian and Rayleigh fading channels, while maintaining a similar performance. The complexity of the RBF-TEQ scheme can be further reduced by invoking the In-phase/Quadrature-phase Turbo Equalisation (I/Q-TEQ) technique, while maintaining a similar performance to that of the CT-TEQ [103]. Explicitly the philosophy of carrying out the equalisation of the in phase and quadrature phase components separately is appealing, since the dimensionality of the I and Q components is significantly lower than that of the complex constellation, which reduces the equaliser's complexity. However, this principal can only be invoked in conjunction with turbo equalisation where the associated gross simplification of considering the I and Q components in isolation and hence disregarding their channel-induced cross-coupling is compensated by the turbo-equaliser's consecutive iterations [14].

4.5.1 RBF based Equaliser Principle

As already mentioned above, the characteristics of the transmitted sequence can be exploited by capitalising on the finite-duration CIR and by considering the channel equalisation process as a geometric classification problem. This approach was first expounded by Gibson, Siu and Cowan [107], who investigated utilising nonlinear structures offered by neural networks as channel equalisers [103].

After filtering the received signal with the aid of a filter mimicking the inverse of the CIR, a linear equaliser performs the classification into symbols in conjunction with a decision device, which is often a simple sign function. The decision boundary is constituted by the locus of all noisy channel outputs, where the output of the linear equaliser is zero. In general, the linear equaliser invokes a hyperplane as its decision boundary, and hence it implements a sub-optimum classification strategy. Gibson *et. al.* [107] have shown examples of linearly non-separable channels, when the decision delay is zero and the channel is of non-minimum phase nature. The linear separability of the channel outputs depends on the equaliser order, m, on the decision delay τ and in situations where the channel characteristics are time varying, it may not be possible to specify appropriate values of m and τ, which will guarantee linear separability.

According to Chen, Gibson and Cowan [108], the above shortcomings of the linear equaliser are circumvented by a Bayesian approach [109] to obtaining an optimal equalisation solution. In general, the optimal Bayesian decision boundary is constituted by a hyper-surface, rather than just a hyper-

plane in the m-dimensional observation space and the realisation of this nonlinear boundary requires a nonlinear decision capability, which can be provided by neural networks. The so-called Radial Basis Function (RBF) network is ideal for channel equalisation applications, since it is capable of realising the optimal Bayesian equalisation solution [110]. Therefore, RBF equalisers can be derived directly from theoretical considerations related to optimal detection and all our prior knowledge concerning detection problems [109] can be exploited.

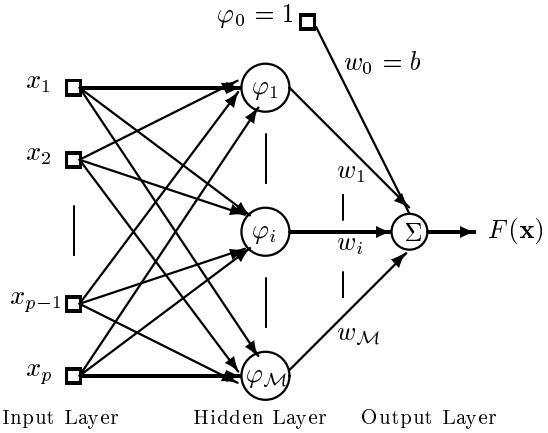

Figure 4.17: Architecture of a radial basis function based network.

Briefly, the structure of the RBF network [111] consists of three different layers, as shown in Figure 4.17. The input layer is constituted by p source nodes. A set of $\mathcal{M}$ nonlinear activation functions $\varphi_i, i = 1, \ldots, \mathcal{M}$, constitutes the hidden second layer where $\mathcal{M}$ is the number of independent basis functions of the RBF network. The output of the RBF network is provided by the third layer, which is comprised of output nodes. Figure 4.17 shows only one output node. This construction is based on the fundamentals of neural network design [111]. As suggested by the terminology, the activation functions in the hidden layer take the form of radial basis functions [111], each centred around one of the $\mathcal{M}$ independent basis functions of the RBF network.

Radial functions are characterised by their responses that decrease or increase monotonically with distance from a central point, $\mathbf{c}$, i.e. as the Euclidean norm $\|\mathbf{x} - \mathbf{c}\|$ is increased, where $\mathbf{x} = [x_1 \; x_2 \; \ldots \; x_p]^T$ is the input vector of the RBF network. The central points in the vector $\mathbf{c}$ are often referred to as the RBF centres. Therefore, the radial basis functions take the form of:

$$\varphi_i(\mathbf{x}) = \varphi(\|\mathbf{x} - \mathbf{c}_i\|), \qquad i = 0, \ldots, \mathcal{M}. \tag{4.14}$$

This justifies the 'radial' terminology. Referring to Figure 4.17, the RBF network can be represented mathematically as follows:

$$F(\mathbf{x}) = \sum_{i=0}^{\mathcal{M}} w_i \varphi_i(\mathbf{x}), \tag{4.15}$$

where w_i is the ith weight of the RBF network. The additive bias b in Figure 4.17 is absorbed into the summation as w_0 by including an extra basis function φ_0, whose activation function is set to 1. For a detailed description of the RBF network design, the interested reader is referred to [103] for example.

The architecture of the RBF equaliser designed for an M-ary multilevel modem scenario is shown

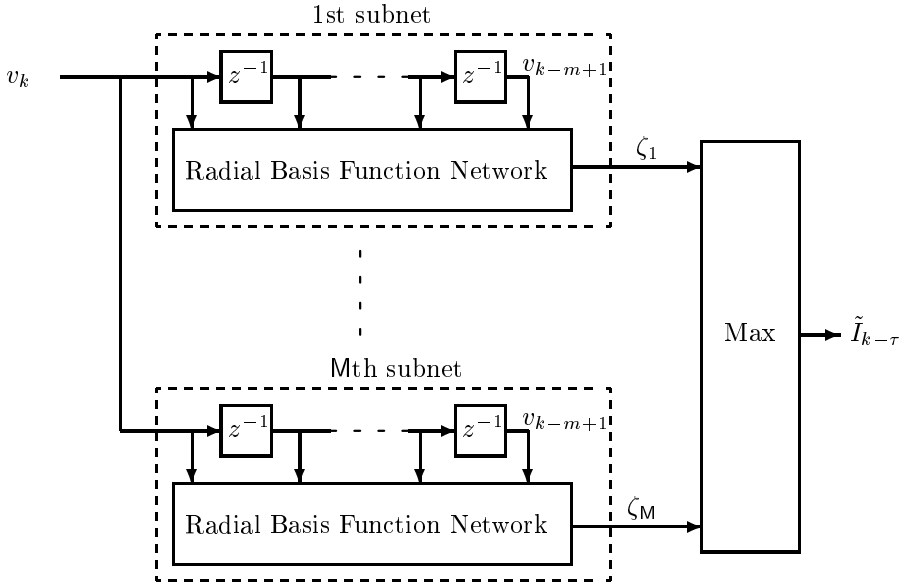

Figure 4.18: RBF equaliser for M-level modems, where $\{v_k\}$ is the channel output sequence, $\tilde{I}_{k-\tau}$ is the estimate of the transmitted signal $I_{k-\tau}$ and ζ_i is the conditional density function of the ith sub-RBF network.

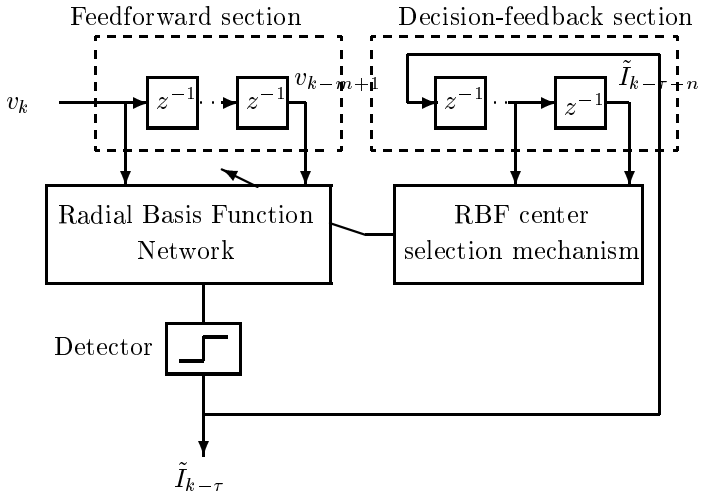

Figure 4.19: RBF equaliser with decision feedback.

in Figure 4.18[1]. Observe in Figure 4.18 that each of the M possible symbols has a dedicated sub-RBF network. Note furthermore that the output of each sub-RBF network gives the corresponding conditional density function ζ_i and this output value can be used for generating soft decision channel decoder inputs in conjunction with error correction techniques [14]. Figure 4.19 illustrates the RBF assisted Decision Feedback Equaliser (RBF-DFE) for the specific scenario of a binary modulation scheme. This is also equivalent to one sub-RBF network of M-level modems. Observe in the figure that in contrast to conventional DFEs, where the output of the feedback section is subtracted from that of the feedforward section for the sake of cancelling the ISI component imposed by the symbols that have already been detected, here the feedback section is employed for assisting the operation of the feedforward section where a subset of centres was selected for a particular decision based

[1]Explicitly, M determines the number of possible symbols constituted by $\mathsf{m} = \log_2(\mathsf{M})$ bits, while $\mathcal{M}$ is the number of RBF centres, which is determined by all possible combinations of the legitimate transmitted symbols and by the length of the CIR.

on the feedback symbol vector. More explicitly, some of the channel outputs can be eliminated from further classification-related comparisons, since the corresponding symbols have already been determined [103]. The structure of RBF-DFE is specified by the equaliser's decision delay τ, the feedforward order m and the feedback order n.

Determine the feedback state	
$n_{s,i}(m+2) - 2\mathsf{M} + n_{s,f}$	subtraction and addition
$n_{s,f}$	multiplication
$n_{s,f}$	division
$n_{s,i} - \mathsf{M} + 1$	max
$n_{s,i} - \mathsf{M}$	table look-up

Table 4.2: Reduced computational complexity per equalised output sample of an M-ary Jacobian RBF DFE based on scalar centres. The Jacobian RBF DFE has m inputs and $n_{s,i}$ hidden RBF nodes, which are derived from the $n_{s,f}$ number of scalar centres.

The Bayesian-based RBF equaliser has a high computational complexity imposed by the evaluation of the nonlinear exponential functions in Equation 4.19 and owing to the high number of additions/subtractions and multiplications/divisions required for the estimation of each symbol. However, the output of the RBF network can be generated in the logarithmic domian by using the Jacobian logarithm [53] described in Section 2.3.4, in order to avoid the computation of exponentials and to reduce the number of multiplications performed. The RBF equaliser using the Jacobian logarithm is referred to as the *Jacobian RBF equaliser*. The complexity of the Jacobian RBF equaliser can be further reduced by exploiting the fact that the elements of the vector of noiseless channel outputs constituting the channel states $\mathbf{r}_i, i = 1, \ldots, n_s$ correspond to the convolution of a sequence of $(\bar{L}+1)$ transmitted symbols and $(\bar{L}+1)$ CIR taps. These vector elements are referred to as the scalar channel states $r_l, l = 1, \ldots, n_{s,f}(= \mathsf{M}^{\bar{L}+1})$ and we could use Patra's and Mulgrew's method [112] to reduce the computational load [103]. Following the procedure of Sections 8.10 and 10.2 in [103], it can be shown that the corresponding computional complexity per equalised output sample of an M-ary Jacobian RBF DFE is given by the values shown in Table 4.2. All systems presented in this chapter employed the reduced complexity M-ary Jacobian RBF-DFE of [103].

Having presented a brief overview of the RBF equaliser, we will proceed to introduce the turbo equalisation technique using the symbol-based MAP decoder of Section 2.3.

4.6 Turbo Equalisation using Symbol-based MAP Decoder

In the RBF DFE based systems discussed in Section 4.5.1 channel equalisation and channel decoding ensued independently. However, it is possible to improve the receiver's performance, if the equaliser is fed by the channel outputs plus the soft decisions provided by the channel decoder, invoking a number of iterative processing steps. This novel receiver scheme was first proposed by Douillard *et. al.* [73] for a convolutional coded Binary Phase Shift Keying (BPSK) system, using a similar principle to that of turbo codes and hence it was termed *turbo equalisation* [14]. This scheme is illustrated in Figure 4.21, which will be detailed during our forthcoming discourse. Gertsman and Lodge [113] extended this

work and showed that the iterative process of turbo equalisation is capable of compensating for the performance degradation imposed by imperfect channel estimation. In [114] turbo equalisation was implemented in conjunction with turbo coding, rather than conventional convolutional coding, by Raphaeli and Zarai, which demonstrated an increased performance gain owing to turbo coding as well as with the advent of enhanced ISI mitigation achieved by turbo equalisation.

4.6.1 Principle of Turbo Equalisation using Symbol-based MAP Decoder

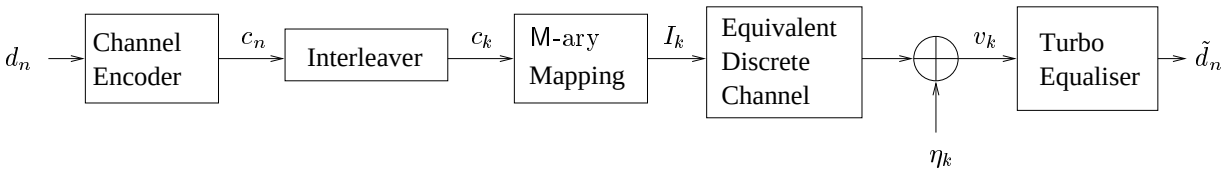

Figure 4.20: Serially concatenated coded M-ary system using the turbo equaliser, which performs the equalisation, demodulation and channel decoding iteratively.

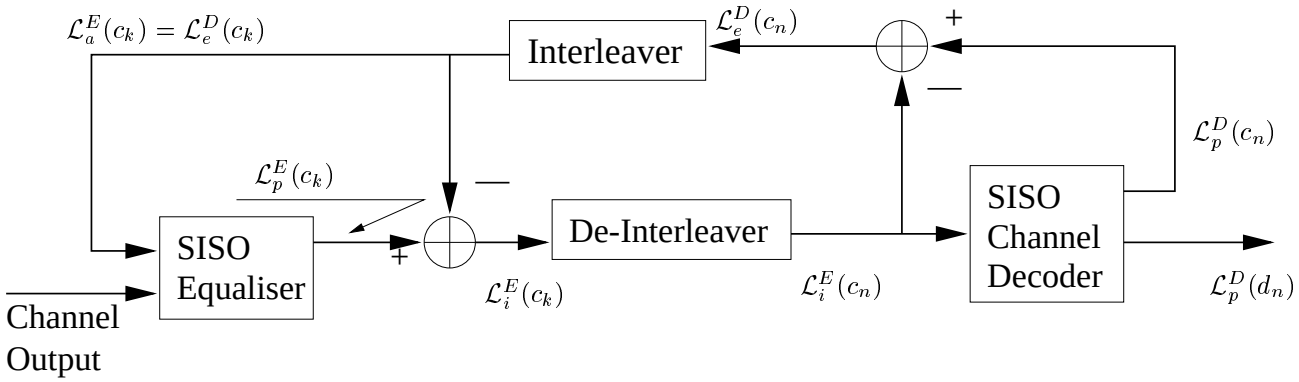

Figure 4.21: Iterative turbo equalisation schematic.

The principles of bit-based iterative turbo decoding [115] were modified appropriately for employment of the symbol-based M-ary coded modulation system of Figure 4.20. As seen in the figure, a data symbol d_n is fed into the channel encoder in order to yield a channel encoded symbol c_n of $\mathsf{m} = \log_2(\mathsf{M})$ bits. Then the interleaved channel encoded symbol c_k is mapped to an M-ary symbol before transmission. In this scheme the channel is viewed as an 'inner encoder' of a serially concatenated arrangement, since it can be modelled with the aid of a tapped delay line similar to that of a convolutional encoder [73, 116], as it was also demonstrated in Section 16.5 of [14]. At the receiver the equaliser and decoder employ a Soft-In Soft-Out (SISO) algorithm, such as the optimal Maximum *A Posteriori* (MAP) algorithm [14, 50] or the Log-MAP algorithm [14, 53]. The SISO equaliser processes the *a priori* information associated with the coded symbol c_k transmitted over the channel and – in conjunction with the channel output values v_k – computes the *a posteriori* information concerning the coded symbol. The soft values of the coded bits constituting the channel coded symbol c_k are normally quantified in the form of the log-likelihood ratio [73], however, here we will quantify them in the form of the symbol probabilities using the symbol-based MAP decoder of Section 2.3. Note that in the context of turbo equalisation the *a posteriori* information concerning all the *coded* bits is required,

whereas in the context of conventional turbo channel decoding only the *a posteriori* information of the *information* bits are computed.

In our description of the turbo equaliser depicted in Figure 4.21 [2], we have used the notation $\mathcal{L}^E$ and $\mathcal{L}^D$ for denoting the Log-domain Probability (LP) values output by the SISO equaliser and SISO decoder, respectively. The subscripts e, i, a and p were used to represent the *extrinsic* LP, the combined channel and *extrinsic* LP, the *a priori* LP and the *a posteriori* LP, respectively. Referring to Figure 4.21, the SISO equaliser processes the channel outputs and the *a priori* information $\mathcal{L}_a^E(c_k)$ of the coded symbol, and generates the *a posteriori* LP values $\mathcal{L}_p^E(c_k)$ of the interleaved coded symbol c_k seen in Figure 4.20. Before passing the above *a posteriori* LPs generated by the SISO equaliser to the SISO decoder of Figure 4.21, the contribution of the decoder — which is represented in the form of the *a priori* information $\mathcal{L}_a^E(c_k)$ — accruing from the previous iteration must be removed, in order to yield the combined channel and *extrinsic* information $\mathcal{L}_i^E(c_k)$ seen in Figure 4.21. To expound a little further, the channel and *extrinsic* information are referred to as 'combined', since they are intrinsically bound and cannot be separated. However, note that at the initial iteration stage no *a priori* information is available yet. To elaborate further, the *a priori* information $\mathcal{L}_a^E(c_k)$ was removed at this stage, in order to prevent the decoder from processing its own output information, which would result in overwhelming the decoder's current reliability-estimation characterising the coded bits, *i.e.* the *extrinsic* information. The combined channel and *extrinsic* LP values are channel-deinterleaved – as seen in Figure 4.21 – in order to yield $\mathcal{L}_i^E(c_n)$, which is then passed to the SISO channel decoder. Subsequently, the channel decoder computes the *a posteriori* LP values $\mathcal{L}_p^D(c_n)$ of the coded symbol. The *a posteriori* LPs generated at the output of the channel decoder are constituted by the *extrinsic* LP $\mathcal{L}_e^D(c_n)$ and the channel-deinterleaved combined channel and *extrinsic* LP $\mathcal{L}_i^E(c_n)$ extracted from the equaliser's *a posteriori* LP $\mathcal{L}_p^E(c_k)$. The *extrinsic* part can be interpreted as the incremental information concerning the current symbol obtained through the decoding process from all the information available due to all surrounding symbols imposed by the code constraints, but excluding the information directly conveyed by the symbol. This information can be calculated by subtracting on a symbol-by-symbol basis the LP values $\mathcal{L}_i^E(c_n)$ at the input of the decoder from the *a posteriori* LP values $\mathcal{L}_p^D(c_n)$ at the channel decoder's output, as seen also in Figure 4.21, yielding:

$$\mathcal{L}_e^D(c_n) = \mathcal{L}_p^D(c_n) - \mathcal{L}_i^E(c_n). \tag{4.16}$$

The *extrinsic* information $\mathcal{L}_e^D(c_n)$ of the coded symbol is then interleaved as shown in Figure 4.21, in order to yield $\mathcal{L}_e^D(c_k)$, which is fed back in the required symbol-order to the channel equaliser, where it is used as the *a priori* information $\mathcal{L}_a^E(c_k)$ in the next equalisation iteration. This constitutes the first iteration. Again, it is important that only the channel-interleaved *extrinsic* part – *i.e.* $\mathcal{L}_e^D(c_k)$ of $\mathcal{L}_p^D(c_n)$ – is fed back to the equaliser, since the interdependence between the *a priori* information $\mathcal{L}_a^E(c_k) = \mathcal{L}_e^D(c_k)$ used by the equaliser and the previous decisions of the equaliser should be minimised. This independence assists in obtaining the equaliser's reliability-estimation of the coded symbols for the current iteration, without being 'influenced' by its previous estimations. Ideally, the *a priori* information should be based on an independent estimation. As argued above, this is the reason that

[2]The SISO channel decoder block may contain any of the coded modulation decoders such as the TCM, BICM, TTCM and BICM-ID decoders. The TTCM and BICM-ID decoders themselves have a number of inner iterations and the number of inner and outer iterations is adjusted such that all the different schemes encounter the same total number of trellis stages.

the *a priori* information $\mathcal{L}_a^E(c_k)$ is subtracted from the *a posteriori* LP value $\mathcal{L}_p^E(c_k)$ at the output of the channel equaliser in Figure 4.21, before passing the LP values to the channel decoder. In the final iteration, the *a posteriori* LPs $\mathcal{L}_p^D(d_n)$ of the information symbols are computed by the channel decoder.

Previous turbo equalisation research has implemented the SISO equaliser using the Soft-Output Viterbi Algorithm (SOVA) [73], the optimal MAP algorithm [106] and linear filters [117]. We will now introduce the RBF based equaliser as the SISO equaliser, which will be employed in the context of turbo equalisation using the symbol-based MAP algorithm.

4.7 RBF Assisted Turbo Equalisation of Coded Modulation Schemes

The RBF network based equaliser is capable of utilising the *a priori* information $\mathcal{L}_a^E(c_k)$ provided by the channel decoder of Figure 4.21, in order to improve its performance. This *a priori* information can be assigned namely to the weights of the RBF network [118]. In turn, the RBF equaliser provides the decoder with the *a posteriori* information $\mathcal{L}_p^E(c_k)$ concerning the coded symbol. We will now provide a brief overview of symbol-based coded modulation assisted, RBF aided turbo equalisation. Note that this procedure is different from the separate bit-based channel coding and modulation philosophy outlined in Section 11.2 of [103].

4.7.1 System Overview

The conditional Probability Density Function (PDF) of the ith symbol, $i = 1, \ldots, \mathsf{M}$, associated with the ith subnet of the M-ary RBF channel equaliser having a feedforward order of m is given by [103]:

$$f_{RBF}^i(\mathbf{v}_k) = \sum_{j=1}^{n_{s,i}} w_j^i \varphi(|\mathbf{v}_k - \mathbf{c}_j^i|), \tag{4.17}$$

$$w_j^i = p_j^i (2\pi\sigma_N^2)^{-m/2}, \tag{4.18}$$

$$\varphi(x) = \exp\left(\frac{-x^2}{2\sigma_N^2}\right) \tag{4.19}$$

$$i = 1, \ldots, \mathsf{M}, \qquad j = 1, \ldots, n_{s,i}$$

where $\mathbf{c}_j^i$, w_j^i, $\varphi(\cdot)$ and $2\sigma_N^2$ are the RBF's centres, weights, activation function and width, respectively, and σ_N^2 is the noise variance of the channel. The actual number of channel states $n_{s,i}$ is determined by the specific design of the algorithm invoked, but in general we aim for reducing the number of channel states from the optimum number of $\mathsf{M}^{m+\bar{L}-1}$, where m is the equaliser feedforward order and $\bar{L}+1$ is the (CIR) duration [112, 119, 120], to a lower value for the sake of reducing the computational complexity.

The term $\mathbf{v}_k$ in Equation 4.17 is the received symbol sequence, as shown in Figure 4.20. Explicitly, $\mathbf{v}_k$ hosts the channel outputs observed by the mth order equaliser, which can be expressed in an m-dimensional vectorial form as:

$$\mathbf{v}_k = \begin{bmatrix} v_k & v_{k-1} & \ldots & v_{k-m+1} \end{bmatrix}^T. \tag{4.20}$$

The channel input states are hosted by the vector $\mathbf{s}_j$, which is also referred to as the channel input vector. Explicitly, this vector is given by the jth possible combination of the $(\bar{L}+m)$ number of transmitted symbols, namely by:

$$\mathbf{s}_j = \begin{bmatrix} s_{j1} & \dots & s_{jp} & \dots & s_{j(\bar{L}+m)} \end{bmatrix}^T. \tag{4.21}$$

In order to arrive at the Bayesian equalisation solution [14, 110] the RBF centres $\mathbf{c}_j^i$ are assigned the values of the channel output states $\mathbf{r}_j^i$. The channel output states $\mathbf{r}_j$ is the product of the CIR matrix $\mathbf{H}$ and the channel input states $\mathbf{s}_j$. $\mathbf{r}_j$ is also referred to as the channel output vector and it is represented as [14]:

$$\mathbf{r}_j = \mathbf{H}\mathbf{s}_j, \tag{4.22}$$

where the z-transform of the CIR $h(t)$ having a memory of $\bar{L}$ symbols is represented by $H(z) = \sum_{n=0}^{\bar{L}} h_n z^{-n}$ and $\mathbf{H}$ is an $m \times (m+\bar{L})$ matrix given by the CIR taps as follows:

$$\mathbf{H} = \begin{bmatrix} h_0 & h_1 & \dots & h_{\bar{L}} & \dots & 0 \\ 0 & h_0 & \dots & h_{\bar{L}-1} & \dots & 0 \\ \vdots & \vdots & & & & \vdots \\ 0 & 0 & h_0 & \dots & h_{\bar{L}-1} & h_{\bar{L}} \end{bmatrix}. \tag{4.23}$$

The RBF weights w_j^i correspond to the *a priori* probability of the channel states $p_j^i = P(\mathbf{r}_j^i)$, $i = 1, \dots, \mathsf{M}$, $j = 1, \dots, n_{s,i}$, as shown in Equation 4.18. The probability p_j^i of the channel states $\mathbf{r}_j^i$, and therefore the weights of the RBF equaliser can be derived from the *a priori* information $\mathcal{L}_a^E(c_k)$ estimated by the symbol-based MAP channel decoder. Explicitly, $\mathcal{L}_a^E(c_k)$ is the interleaved version of the extrinsic information $\mathcal{L}_e^D(c_n)$ in Equation 4.16. More specifically, we derived the *a posteriori* LP value of the $\mathsf{m}(= \log_2 \mathsf{M})$-bit coded symbol as:

$$\mathcal{L}_p^D(c_n) = \begin{cases} \ln(\bar{A}_{n,d}), & \text{if } c_n = L(j,d) \text{ exist}, \\ \ln(0), & \text{otherwise}, \end{cases} \tag{4.24}$$

where $\bar{A}_{n,d}$ is the *a posteriori* probability of the information symbol d defined in Equation 2.55, while $ln(0) = -\infty$ can be substituted by a large negative value, $L(j,d)$ is the corresponding coded symbol when the information symbol is d and the previous trellis state is j. Explicitly, we have $d = \{0, \dots, 2^{\mathsf{m}-1} - 1\}$ when a rate-$(\mathsf{m}-1)/\mathsf{m}$ channel codec is employed.

Based on Equation 4.22 – for a time-invariant CIR and assuming that the symbols in the sequence $\mathbf{s}_j$ are statistically independent of each other – the probability of the received channel output states $\mathbf{r}_j$ is given by:

$$\begin{aligned} P(\mathbf{r}_j) &= P(\mathbf{s}_j) \\ &= P(s_{j1} \cap \dots s_{jp} \cap \dots s_{j(\bar{L}+m)}) \\ &= \prod_{p=1}^{\bar{L}+m} P(s_{jp}) \qquad j = 1, \dots, n_{s,i}. \end{aligned} \tag{4.25}$$

The transmitted symbol vector component s_{jp} – i.e. the pth symbol in the vector of Equation 4.21– is given by $\mathsf{m} = \log_2 \mathsf{M}$ number of bits $b_{jp1}, b_{jp2}, \dots, b_{jp\mathsf{m}}$, which constitute the coded symbol c_k.

Explicitly, the transmitted symbol vector component s_{jp} is mapped to the coded symbol c_k. Therefore we have:

$$P(s_{jp}) = \exp\left(\mathcal{L}_a^E(c_k)\right), \qquad s_{jp} = c_k. \tag{4.26}$$

Note that the probability $P(\mathbf{r}_j)$ of the channel output states and therefore also the RBF weights defined in Equation 4.18 are time-variant, since the values of $\mathcal{L}_p^D(c_n)$ are time-variant. Hence, referring to Equations 4.25 and 4.26, the probability $P(\mathbf{r}_j)$ of the channel output states can be represented in terms of the symbol LP $\mathcal{L}_a^E(c_k)$ as follows:

$$\begin{aligned} P(\mathbf{r}_j) &= P(\mathbf{s}_j) \\ &= \prod_{\substack{p=1 \\ s_{jp}=c_k}}^{\bar{L}+m} \exp\left(\mathcal{L}_a^E(c_k)\right) \qquad j = 1, \ldots, n_{s,i}. \end{aligned} \tag{4.27}$$

In summary, the computation of the PDF $f_{RBF}^i(\mathbf{v}_k)$ of the ith symbol in Equation 4.17, $i = 1, \ldots, \mathsf{M}$, which is associated with the ith subnet of the M-ary RBF channel equaliser, requires the knowledge of the channel states' *a priori* probability p_j^i, when determining the RBF weights w_j^i, as shown in Equation 4.18. Explicitly, we have $p_j^i = P(\mathbf{r}_j^i)$ and note that for a specific subnet i we can suppress the index i for the sake of brevity. Finally, $P(\mathbf{r}_j)$ can be computed from Equation 4.27 using the *a priori* information $\mathcal{L}_a^E(c_k)$. Explicitly, $\mathcal{L}_a^E(c_k)$ is the interleaved version of the extrinsic information $\mathcal{L}_e^D(c_n)$ of Equation 4.16, and the *a posteriori* information $\mathcal{L}_p^D(c_n)$ can be obtained from Equation 4.24. Therefore, we have demonstrated how the soft output $\mathcal{L}_a^E(c_k)$ provided by the symbol-based MAP channel decoder of Figure 4.21 can be utilised by the RBF equaliser.

On the other hand, the ith subnet of the M-ary RBF equaliser provides the *a posteriori* LP value of the ith coded symbol c_k^i according to:

$$\mathcal{L}_p^E(c_k^i) = \ln\left(\frac{f_{RBF}^i(\mathbf{v}_k)}{\sum_{all\ l} f_{RBF}^l(\mathbf{v}_k)}\right), \qquad l = 1, \ldots, \mathsf{M}. \tag{4.28}$$

where $f_{RBF}^i(\mathbf{v}_k)$ was defined by Equation 4.17, while the term $\sum_{all\ l} f_{RBF}^l(\mathbf{v}_k)$ is a normalisation factor, ensuring that we have $\sum_{all\ i} \exp(\mathcal{L}_p^E(c_k^i)) = 1$ and the received sequence $\mathbf{v}_k$ is defined in Equation 4.20.

4.7.2 Simulation Results and Discussions

We employed the Jacobian RBF-DFE of [103, 121], which reduced the complexity of the RBF equaliser by utilising the Jacobian logarithmic function [53] and decision feedback assisted RBF-centre selection [103, 118] as well as a TEQ scheme using a symbol-based MAP channel decoder. The parameters used for the RBF-DFE scheme are: τ=2, m=3 and n=1. The transmitted $(\mathsf{m}-1)$-bit information symbols are encoded by the rate-$(\mathsf{m}-1)/\mathsf{m}$ CM encoder, interleaved and mapped to an M-ary modulated symbol where $\mathsf{M} = 2^{\mathsf{m}}$. We utilised 16QAM in order to obtain an effective transmission throughput of $\mathsf{m}-1$=3 information Bits Per Symbol (BPS). All the 16QAM-based CM schemes employed exhibited a similar decoding complexity for the sake of a fair comparison. More specifically, a component TCM (or BICM) code memory of 3 was used for the TTCM (or BICM-ID) scheme. The number of iterations for TTCM (BICM-ID) was fixed to 4 (8) and hence the iterative scheme exhibited a similar decoding

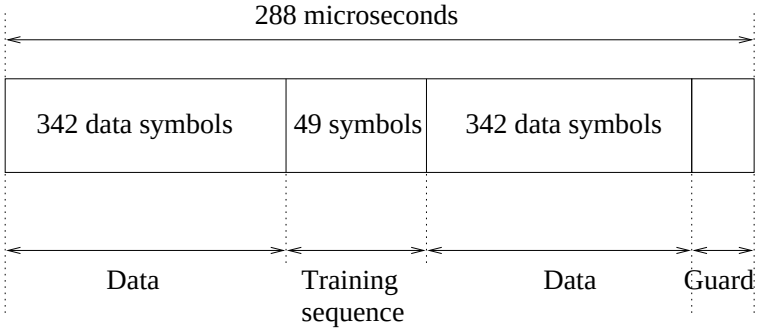

Figure 4.22: Transmission burst structure of the FMA1 non-spread speech burst of the FRAMES proposal [97].

complexity to that of the TCM (BICM) code of memory 6 when quantified in terms of the number of coding states according to the explanations given in Section 3.2.2. Their corresponding generator polynomials can be found from Tables 2.1, 2.2, 2.3 and 2.4.

The transmission burst structure used in this system is the FMA1 non-spread data burst specified by the Pan-European FRAMES proposal [97], which is shown in Figure 4.22. When considering a Time Division Multiple Access (TDMA) system having 16 slots per $4.615ms$ TDMA frame, the transmission burst length is 288 μs, as shown in Figure 4.22. In our investigations, the transmission delay was limited to approximately $8 \times 4.615ms = 37ms$. This corresponds to a transmission delay of 8 TDMA frames and a channel interleaver depth of $8 \times 684 = 5472$ symbols can be employed.

A two-path, symbol-spaced CIR of equal tap weights was used, which can be expressed as $h(t) = 0.707 + 0.707z^{-1}$, where $\bar{L} = 1$ and the Rayleigh fading statistics obeyed a normalised Doppler frequency of 3.25×10^{-5}. The fading magnitude and phase was kept constant for the duration of a transmission burst, a condition which we refer to as employing transmission burst-invariant fading. The Least Mean Square (LMS) algorithm [122] was employed for estimating the CIR based on the training sequence of the transmission burst, as seen in Figure 4.22. Iterative CIR estimation was invoked, where the initial LMS CIR estimation step-size used was 0.05, which was reduced to 0.01 for the second and the subsequent iterations. This LMS-aided CIR estimation was outlined in details in [103].

Figures 4.23 to 4.26 illustrate the BER and FER versus channel SNR performance of the RBF-TEQ scheme assisted by 16QAM-based TCM, TTCM, BICM and BICM-ID, when communicating over the equally-weighted two-path Rayleigh fading CIR. As we can see from the figures, the systems employing CIR estimations, rather than perfect CIR knowledge, exhibited some performance loss compared to the ideal systems employing perfect CIR estimation, but the associated losses reduced rapidly, when the number of TEQ iteration was increased. The BER and FER performance of the identical-throughput uncoded 8PSK scheme communicating over non-dispersive AWGN channels was used as a benchmarker for the 16QAM-based RBF-TEQ arrangement using various CM schemes, when communicating over dispersive Rayleigh fading channels. We found that the BER curves of the TTCM, BICM and BICM-ID assisted schemes are only about 2 dB away from the benchmarker at a BER of 10^{-5}. However, the TCM assisted scheme suffers from an error floor owing to the existence of unprotected bits in the TCM coded symbols. On the other hand, the FER performance of the TTCM, BICM and BICM-ID assisted RBF-TEQ schemes was found in Figures 4.24 to 4.26 to be better than

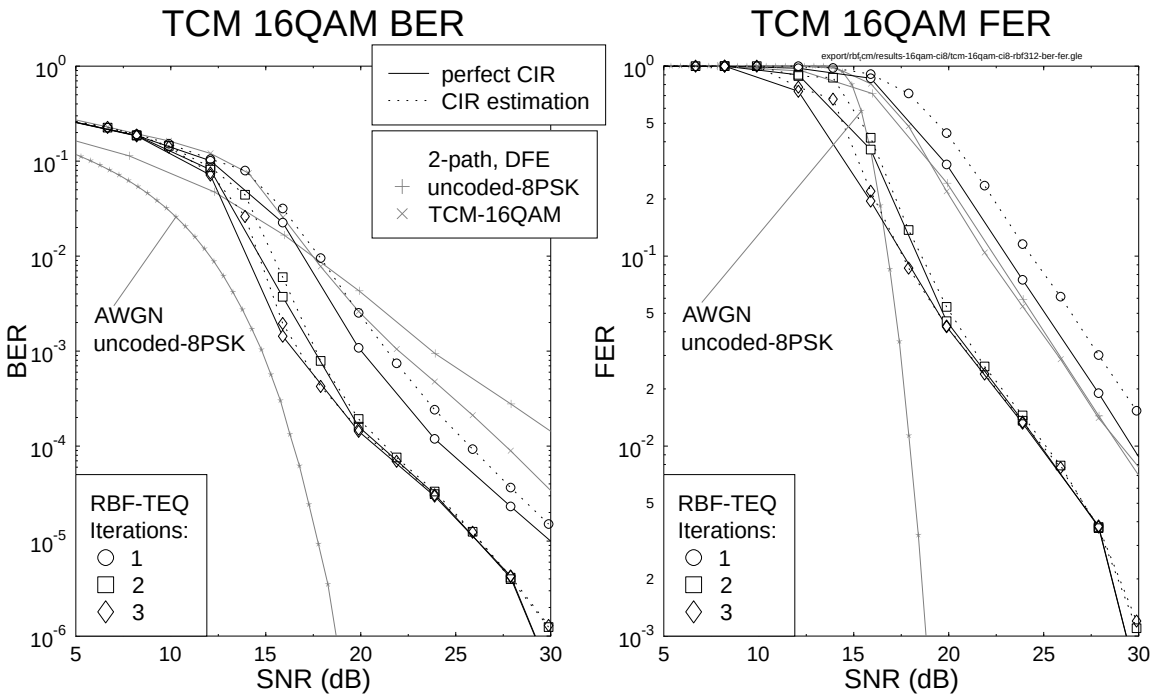

Figure 4.23: The BER and FER versus channel SNR performance of the **RBF-TEQ-TCM** 16QAM scheme, when communicating over the equally-weighted two-path Rayleigh fading CIR. The initial LMS CIR estimation step-size used was 0.05, which was reduced to 0.01 for the second and the subsequent iterations. Our simulation results using perfect CIR estimation are also shown for comparison. The normalised Doppler frequency was 3.25×10^{-5}.

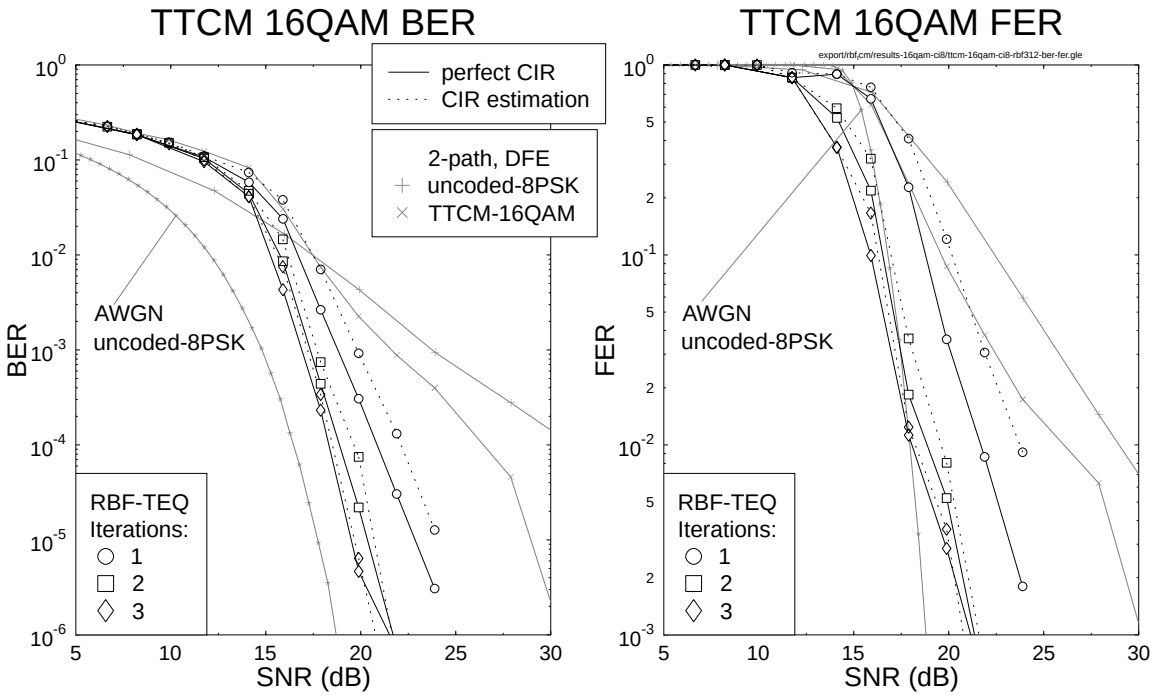

Figure 4.24: The BER and FER versus channel SNR performance of the **RBF-TEQ-TTCM** 16QAM scheme, when communicating over the equally-weighted two-path Rayleigh fading CIR. The initial LMS CIR estimation step-size used was 0.05, which was reduced to 0.01 for the second and the subsequent iterations. Our simulation results using perfect CIR estimation are also shown for comparison. The normalised Doppler frequency was 3.25×10^{-5}.

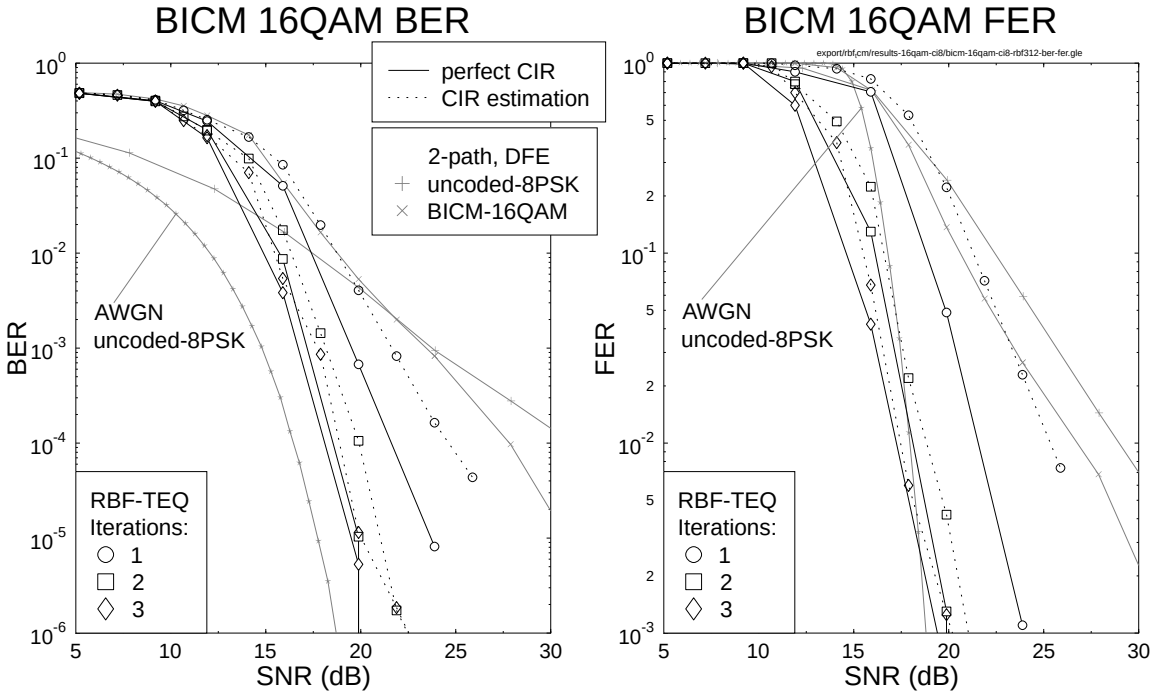

Figure 4.25: The BER and FER versus channel SNR performance of the **RBF-TEQ-BICM** 16QAM scheme, when communicating over the equally-weighted two-path Rayleigh fading CIR. The initial LMS CIR estimation step-size used was 0.05, which was reduced to 0.01 for the second and the subsequent iterations. Our simulation results using perfect CIR estimation are also shown for comparison. The normalised Doppler frequency was 3.25×10^{-5}.

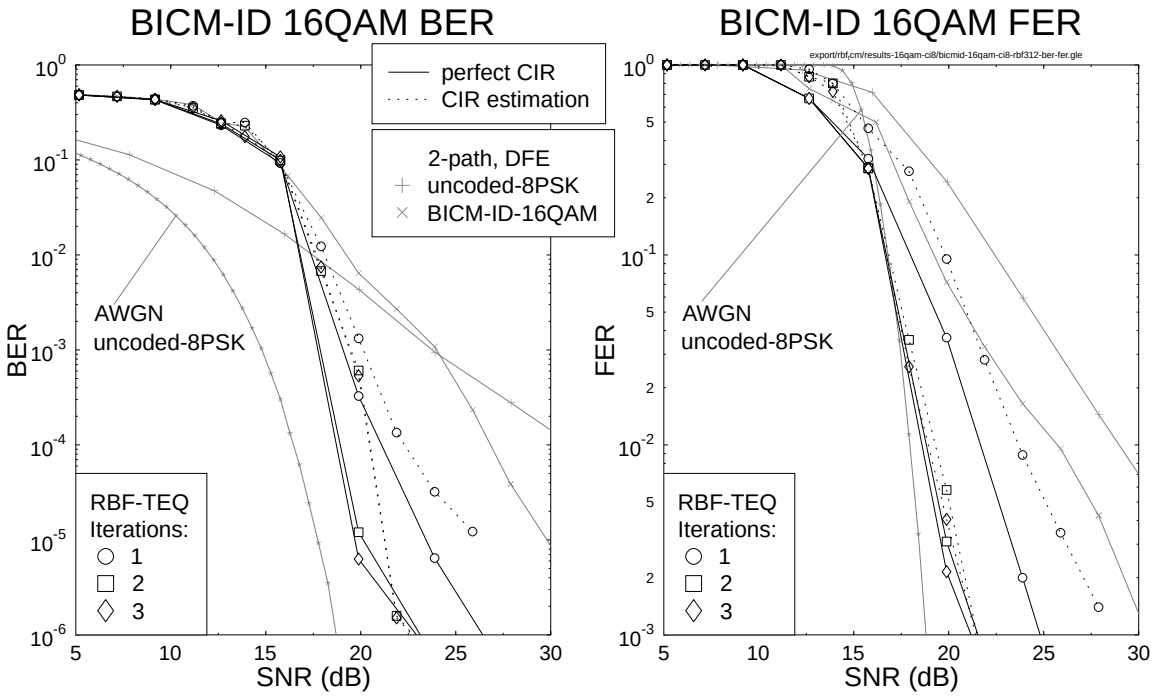

Figure 4.26: The BER and FER versus channel SNR performance of the **RBF-TEQ-BICM-ID** 16QAM scheme, when communicating over the equally-weighted two-path Rayleigh fading CIR. The initial LMS CIR estimation step-size used was 0.05, which was reduced to 0.01 for the second and the subsequent iterations. Our simulation results using perfect CIR estimation are also shown for comparison. The normalised Doppler frequency was 3.25×10^{-5}.

that of the benchmarker at low SNR values. Furthermore, it was found from our simulations that the achievable performance gain remained only marginal, when more than three TEQ iterations were employed.

In order to compare the performance of the RBF-TEQ assisted CM scheme to that of the conventional DFE assisted CM scheme extensively studied in Section 4.4, in Figures 4.23 to 4.26 we have plotted the BER and FER performance of the conventional DFE assisted uncoded-8PSK and those of the CM-16QAM schemes, when communicating over the two-path Rayleigh fading channels considered, where perfect CIR knowledge was assumed. The conventional DFE's feedforward order m and feedback order n were set to seven and one, respectively, since we found from our simulations that further increasing the values of m and n yielded no further performance improvement when communicating over the two-path Rayleigh fading channels considered. Specifically, the conventional DFE exhibits a lower complexity than that of the RBF-DFE. However, the performance of the conventional DFE scheme is lower than that of its RBF-DFE counterpart owing to experiencing an error floor in the high SNR region [103]. From Figures 4.23 to 4.26 we noticed that the conventional DFE assisted CM-16QAM schemes exhibited approximately 2 to 3 dB coding/SNR gain [3] compared to the identical-throughput conventional DFE assisted uncoded-8PSK scheme at a BER of 10^{-4}. However, the achievable coding gain of the various CM schemes was significantly increased, when the RBF-TEQ scheme was employed, although this was achieved at a concomitantly higher complexity owing to employing an increased number of iterations. Explicitly, a coding gain in excess of 10 dB was achievable at a BER of 10^{-4} by the various CM schemes against the identical-throughput conventional DFE assisted uncoded-8PSK scheme, when the RBF-TEQ scheme invoked 3 iterations.

Figure 4.27 shows the BER and FER versus channel SNR performance of RBF-TEQ for various CM aided 16QAM schemes, when communicating over the equally-weighted two-path Rayleigh fading CIR and utilising iterative LMS-based CIR estimation. It is illustrated in Figure 4.27 that the RBF-TEQ-BICM scheme attained the highest TEQ gain compared to its counterparts. The RBF-TEQ-BICM scheme is also the best performer in terms of the achievable FER, but the RBF-TEQ-TTCM arrangement is the best performer in terms of the BER attained.

4.7.3 Conclusions

We found in Figure 4.27 that the BER performance of the TTCM, BICM and BICM-ID assisted RBF-TEQ schemes was only about 2 dB away from that of the identical-throughput uncoded 8PSK scheme communicating over AWGN channels. The achievable coding gain of the various CM schemes was significantly increased, when employing the RBF-TEQ scheme of Section 4.7 rather than the conventional DFE. However, the achievable performance gain remained only marginal, when more than three TEQ iterations were employed. The RBF-TEQ-BICM scheme is the best performer in

[3] In our investigation we will be consistently plotting BER versus SNR as well as FER versus SNR curves. These curves may be readily converted to BER versus E_b/N_0 and FER versus E_b/N_0 curves by shifting them according to the associated coding rate. However, all curves would have to be shifted by the same amount and hence, the achievable coding gain remains identical to the achievable SNR gain. This is because coding gain is defined on the E_b/N_0 scale, while E_b represents the energy of the useful information bits. Therefore, in our further discourse we will refers to SNR gain and coding gain interchangeably. More specifically, in order to convert the SNR scale to E_b/N_0 scale, all curves require a shift of $10\log(3) = 4.77$ dB to the left of the SNR scale when the effective throughput is 3 BPS.

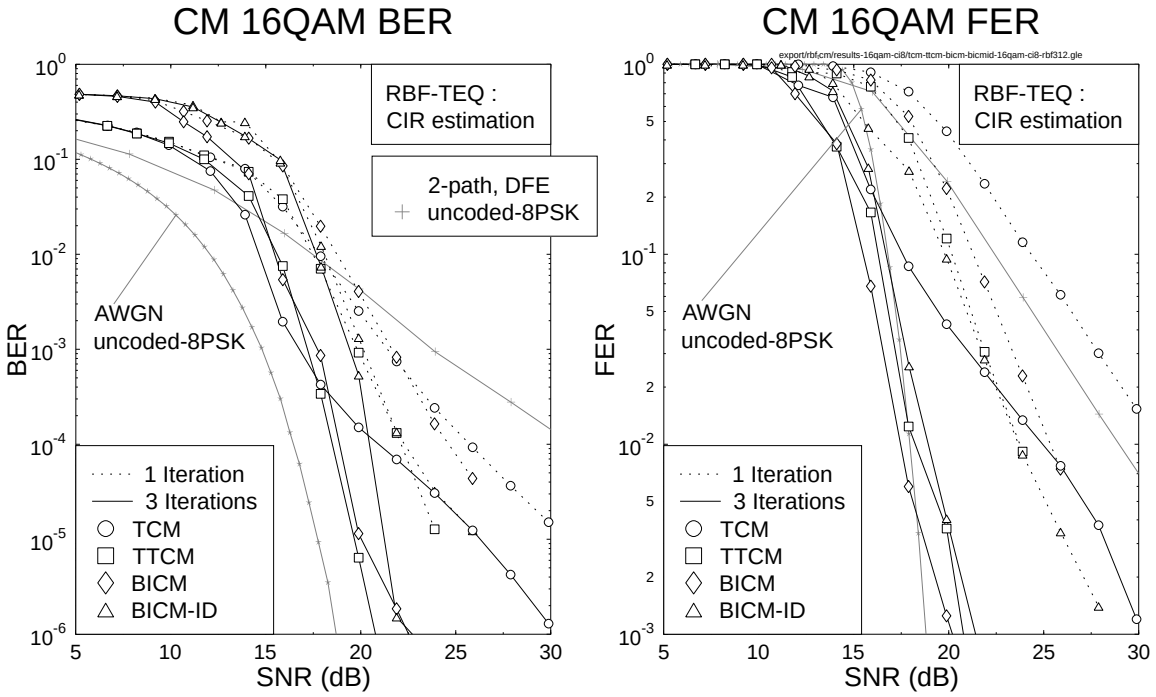

Figure 4.27: The BER and FER versus channel SNR performance of the **RBF-TEQ for various CM** 16QAM scheme, when communicating over the equally-weighted two-path Rayleigh fading CIR. The initial LMS CIR estimation step-size used was 0.05, which was reduced to 0.01 for the second and the subsequent iterations. The iteration gains of TEQ can be observed by comparing the performance of the first and third TEQ iteration of the systems. The normalised Doppler frequency was 3.25×10^{-5}.

terms of the achievable FER, but the RBF-TEQ-TTCM arrangement has the edge in terms of the BER attained.

Having studied the performance of the RBF-TEQ arrangement employing various CM schemes, let us now commence our discourse on employing CM schemes in the context of the reduced complexity In-phase/Quadrature-phase TEQ [103, 123] system to be described in Section 4.8.

4.8 In-phase/Quadrature-phase Turbo Equalisation

In this section, we denote the modulated signal by $s(t)$, which is transmitted over the dispersive channel characterised by the CIR $h(t)$. The signal is also contaminated by the zero-mean Additive White Gaussian Noise (AWGN) $n(t)$ exhibiting a variance of $\sigma_N^2 = N_0/2$, where N_0 is the single-sided noise power spectral density. The received signal $r(t)$ is then formulated as:

$$\begin{aligned} r(t) &= s(t) * h(t) + n(t) \\ &= [s_I(t) + js_Q(t)] * [h_I(t) + jh_Q(t)] \\ &+ n_I(t) + jn_Q(t) \\ &= r_I(t) + jr_Q(t), \end{aligned} \tag{4.29}$$

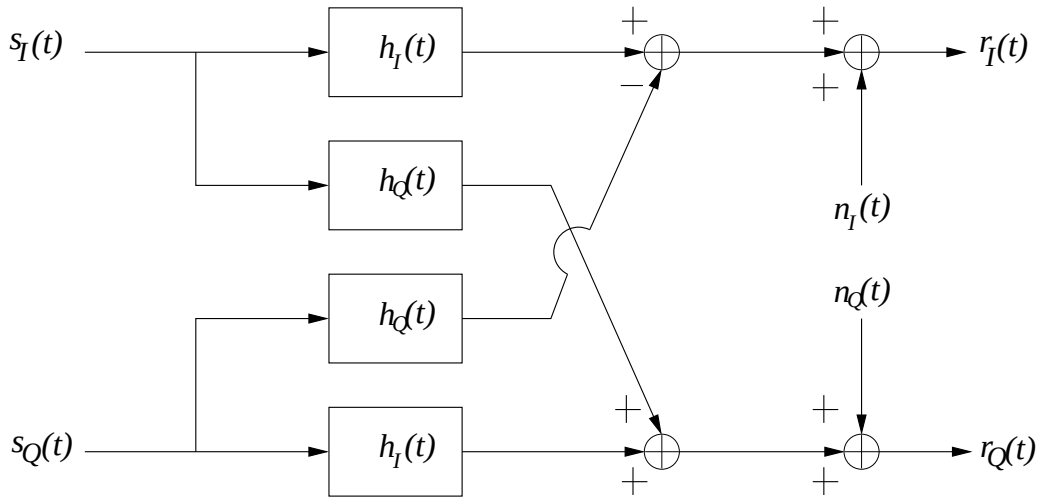

Figure 4.28: The complex channel model. After transmission over the complex channel $h(t)$, the received signal $r(t)$ becomes dependent on the in-phase component $s_I(t)$ and quadrature-phase component $s_Q(t)$ of the transmitted signal, as expressed in Equations 4.29 and 4.30.

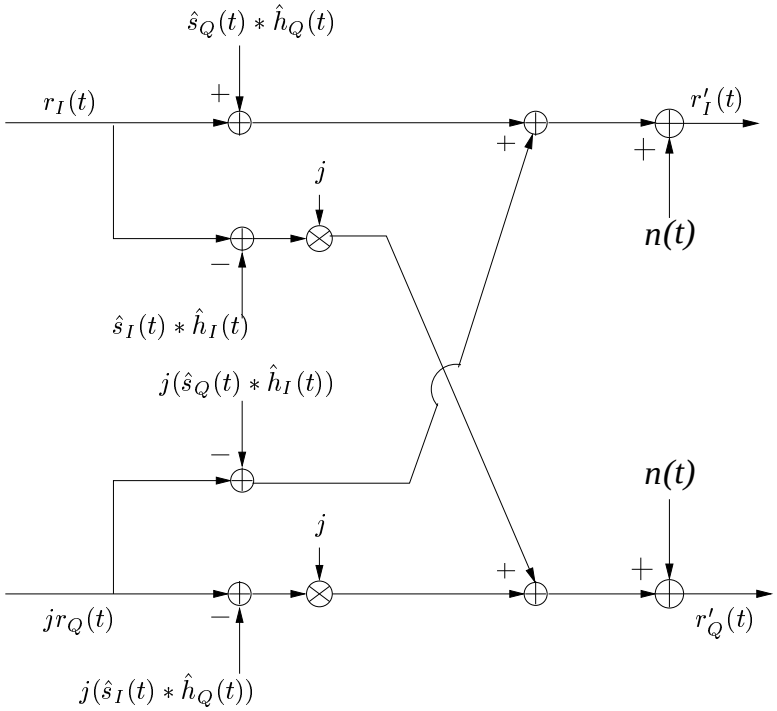

Figure 4.29: The process of removing the dependency of $r_I(t)$ and $r_Q(t)$ on the quadrature components of the transmitted signals, namely on $s_I(t)$ and $s_Q(t)$, to give $r'_I(t)$ and $r'_Q(t)$, respectively. In this figure, it is assumed that the CIR estimation is perfect, *i.e.* that we have $\hat{h}_I(t) = h_I(t)$ as well as $\hat{h}_Q(t) = h_Q(t)$ and that the transmitted signals are known, giving $\hat{s}_I(t) = s_I(t)$ and $\hat{s}_Q(t) = s_Q(t)$. In this case, perfect decoupling is achieved. However, in practice these estimates have to be generated at the receiver.

where we have:

$$\begin{aligned} r_I(t) &= s_I(t) * h_I(t) - s_Q(t) * h_Q(t) + n_I(t) \\ r_Q(t) &= s_I(t) * h_Q(t) + s_Q(t) * h_I(t) + n_Q(t), \end{aligned} \tag{4.30}$$

since the CIR $h(t)$ is complex-valued and therefore consists of the I component $h_I(t)$ and Q component $h_Q(t)$. On the same note, $s_I(t)$ and $s_Q(t)$ are the I and Q components of $s(t)$ in Figure 4.28, while $n_I(t)$ and $n_Q(t)$ denote the corresponding AWGN components. Both of the received I/Q signals, namely $r_I(t)$ and $r_Q(t)$ of Equation 4.30 become dependent on both $s_I(t)$ and $s_Q(t)$ due to the cross-coupling effect imposed by the complex channel. Hence a conventional channel equaliser, regardless of whether it is an iterative or non-iterative equaliser, would have to consider the effects of this cross-coupling.

4.8.1 In-phase/Quadrature-phase Turbo Equalisation Principle

Initially we can neglect the channel-induced cross-coupling of the received signal's quadrature components and then we compensate for this gross simplification with the aid of the turbo equaliser. More explicitly, this simplification would result in an unacceptable performance degradation in the context of conventional non-iterative channel equalisation. However, the employment of the iterative turbo equalisation technique allows us to compensate for the above simplification during the consecutive iterations. Therefore we can compute the I and Q components of the decoupled channel output $r'(t)$, as though they were dependent on $s_I(t)$ or $s_Q(t)$ only, as portrayed in Figure 4.29 in the context of the following equations:

$$\begin{aligned} r'_I(t) &= s_I(t) * h(t) + n_I(t) \\ &= s_I(t) * h_I(t) + j[s_I(t) * h_Q(t)] + n(t) \\ r'_Q(t) &= -s_Q(t) * h(t) + n_Q(t) \\ &= -\left(s_Q(t) * h_I(t) + j[s_Q(t) * h_Q(t)]\right) + n(t). \end{aligned} \tag{4.31}$$

More explicitly, the removal of the cross-coupling is facilitated by generating the estimates $\hat{s}_I(t)$ and $\hat{s}_Q(t)$ of the transmitted signal [117] with the aid of the reliability information generated by the channel decoder and then by cancelling the cross-coupling effects imposed by the channel, yielding $r'_I(t)$ and $r'_Q(t)$, respectively, as seen in Figure 4.29. In the ideal scenario, where perfect knowledge of both the CIR and that of the transmitted signal is available, it is plausible that the channel-induced cross-coupling between the quadrature components can be removed. However, when unreliable symbol estimates are generated owing to the channel-impaired low-confidence reliability values, errors are introduced in the decoupling operation. Nonetheless, we will show that the associated imperfect decoupling effects are compensated with the aid of the iterative turbo equalisation process in its consecutive iterations.

Following the above decoupling operation, the modified complex channel outputs, namely $r'_I(t)$ and $r'_Q(t)$ of Figure 4.29, respectively, can be viewed as the result of convolving both quadrature components independently with the complex CIR on each quadrature arm. Consequently, we can equalise $s_I(t)$ and $s_Q(t)$ independently, hence reducing the number of channel states and the associated complexity quite significantly. Again, note that in Equation 4.31 we have assumed that perfect signal

regeneration and perfect decoupling is achieved at the receiver, in order to highlight the underlying principle of the reduced complexity equaliser.

4.9 RBF Assisted Reduced Complexity In-phase/Quadrature-phase Turbo Equalisation of Coded Modulation Schemes

In the RBF-I/Q-EQ scheme we utilised the principle of separate I/Q equalisation outlined as in Section 4.8, where two separate RBF equalisers was used for the in-phase and quadrature component of the transmitted symbols. The in-phase-RBF-EQ has RBF centres, which consist of the in-phase decoupled channel output $r'_I(t)$ of Equation 4.30 and vice-versa for the quadrature-RBF-EQ. The number of possible channel output states is reduced, since the decoupled channel output $r'(t)$ is dependent on $\sqrt{\mathsf{M}}$ number of possible in-phase or quadrature-phase transmitted symbols instead of the original M number of possible symbols.

4.9.1 System Overview

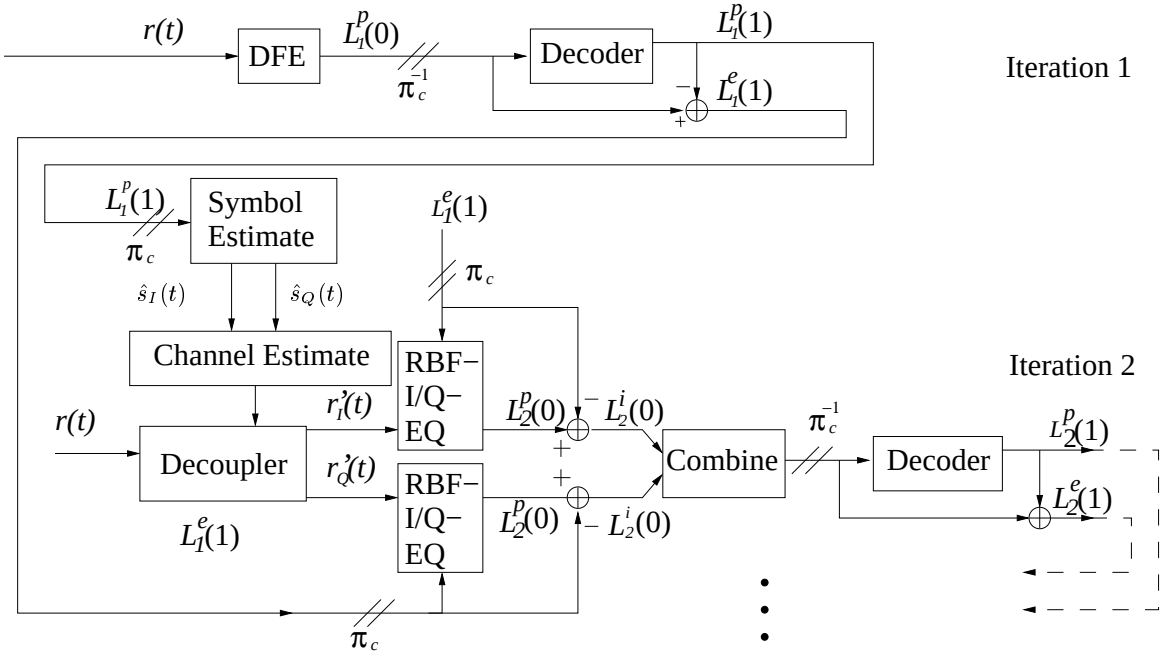

Figure 4.30: Schematic of the turbo equaliser employing a DFE and a SISO channel decoder in the first turbo equalisation iteration. In subsequent iterations, two RBF-I/Q-EQs and one SISO channel decoder are employed. The notation π_c represents a channel interleaver, while π_c^{-1} is used to denote a channel deinterleaver.

Figure 4.30 illustrates the schematic of the turbo equaliser utilising two reduced-complexity RBF-I/Q equalisers. The same notations employed in Section 4.6 is used in this section. The subscripts in Figure 4.30 are used for representing the iteration index, while the argument within the brackets ( ) indicates the index of the receiver stage, where the equalisers are denoted as receiver stage 0, while the channel decoder as receiver stage 1.

The conventional minimum mean square error DFE seen at the top left corner of Figure 4.30 is

used for the first turbo equalisation iteration for providing soft decisions in the form of the LP $L_1^p(0)$ to the CM decoder. Invoking the DFE at the first iteration constitutes a low-complexity approach to providing an initial estimate of the transmitted symbols, as compared to the more complex RBF-I/Q-EQ. The symbol-based MAP channel decoder of Figure 4.30 generates the *a posteriori* LP $L_1^p(1)$ and from that, the *extrinsic* information of the encoded symbols $L_1^e(1)$ is extracted. In the next iteration, the *a posteriori* LP $L_1^p(1)$ is used for regenerating estimates of the I and Q components of the transmitted signal, namely $\hat{s}_I(t)$ and $\hat{s}_Q(t)$, as seen in the 'Symbol Estimate' block of Figure 4.30. The *a posteriori* information was transformed from the logarithmic domain to modulated symbols using the approach employed in [117]. The estimated transmitted quadrature components $\hat{s}_I(t)$ and $\hat{s}_Q(t)$ are then convolved with the estimate of the CIR $h(t)$. At the decoupler block of Figure 4.30, the resultant signal is used for removing the cross-coupling effect, as seen in Equation 4.30, according to Equation 4.31 from both quadrature components of the transmitted signal, yielding $r'_I(t)$ and $r'_Q(t)$.

After the decoupling operation, $r'_I(t)$ and $r'_Q(t)$ are passed to the RBF-I/Q-EQ in the schematic of Figure 4.30. In addition to these received quadrature signals, the RBF-I/Q-EQ also processes the *a priori* information received, which is constituted by the *extrinsic* LPs $L_1^e(1)$ derived from the previous iteration, and generates the *a posteriori* information $L_2^p(0)$. Subsequently, the combined channel and *extrinsic* information $L_2^i(0)$ is extracted from both RBF-I/Q-EQs in Figure 4.30 and combined, before being passed to the Log-MAP channel decoder. As in the first turbo equalisation iteration, the *a posteriori* and *extrinsic* information of the encoded symbol, namely $L_2^p(1)$ and $L_2^e(1)$, respectively, are evaluated. Subsequent turbo equalisation iterations obey the same sequence of operations, until the iteration termination criterion is met.

4.9.2 Simulation Results and Discussions

In this section, we will study the performance of a number of RBF-I/Q-TEQ schemes employing various CM schemes. Similar simulation parameters to those outlined in Section 4.7.2 are used. The RBF-DFE based TEQ is specified by the equaliser's decision delay τ, the feedforward order m and the feedback order n. The number of RBF nodes is $n_{s,i} = \bar{\mathsf{M}}^{\bar{L}+m-n}$ and the number of scalar channel states of the Jacobian RBF equaliser is $n_{s,f} = \bar{\mathsf{M}}^{\bar{L}+1}$, where we have $\bar{\mathsf{M}}$=M for the non-I/Q based full-complexity RBF-TEQ system, while $\bar{\mathsf{M}}$=$\sqrt{\mathsf{M}}$ for the I/Q based RBF-TEQ system. The estimated computational complexity of generating the *a posteriori* LP for the Jacobian RBF equaliser is summarised in Table 4.2, where $n_{s,i}(m+2) - 2\bar{\mathsf{M}} + n_{s,f}$ number of additions/subtractions and $2n_{s,f}$ multiplications/divisions are required. Here, we employed τ=2, m=3 and n=1 for the RBF-TEQ, as well as m=7 and n=1 for the conventional DFE. Therefore, the 'per-iteration' complexity of the full-RBF-TEQ expressed in terms of the number of additions/subtractions and multiplications/divisions is about 20704 and 512, respectively, while that of the RBF-I/Q-TEQ is about 328 and 32, respectively.

Figures 4.31 to 4.34 illustrate the BER and FER versus channel SNR performance of the RBF-I/Q-TEQ scheme incorporating into 16QAM-based TCM, TTCM, BICM and BICM-ID, when communicating over the equally-weighted two-path Rayleigh fading CIR. As we can see from the figures, the systems employing LMS-based CIR estimation exhibited only marginal performance losses compared to the ideal systems employing perfect CIR estimation. This is because the RBF-I/Q-TEQ scheme reduces the effect of error propagation, since the set of RBF centres to be selected using

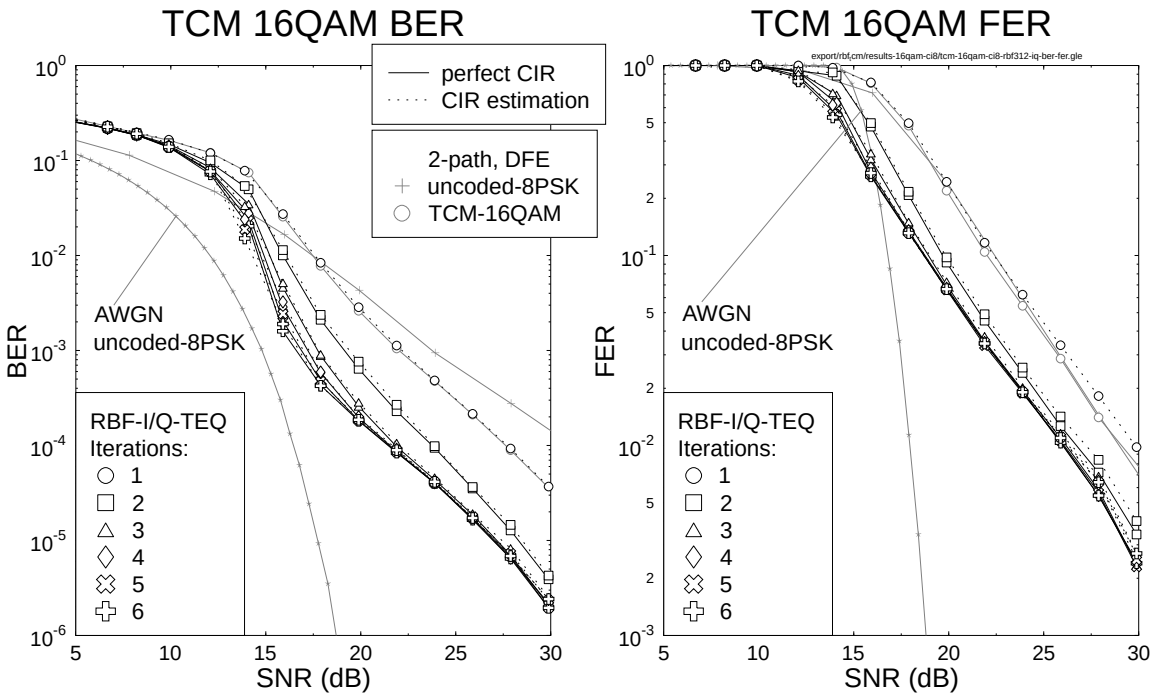

Figure 4.31: The BER and FER versus channel SNR performance of the **RBF-I/Q-TEQ-TCM** 16QAM scheme, when communicating over the equally-weighted two-path Rayleigh fading CIR. The initial LMS CIR estimation step-size used was 0.05, which was reduced to 0.01 for the second and the subsequent iterations. Our simulation results using perfect CIR estimation are also shown for comparison. The normalised Doppler frequency was 3.25×10^{-5}.

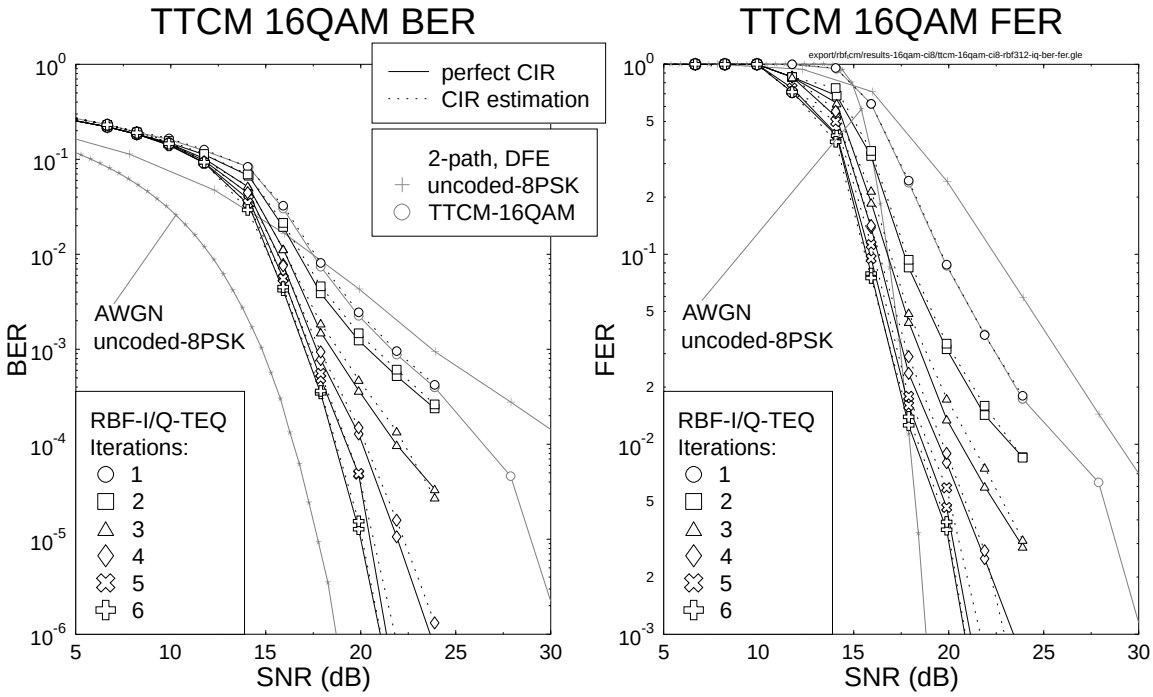

Figure 4.32: The BER and FER versus channel SNR performance of the **RBF-I/Q-TEQ-TTCM** 16QAM scheme, when communicating over the equally-weighted two-path Rayleigh fading CIR. The initial LMS CIR estimation step-size used was 0.05, which was reduced to 0.01 for the second and the subsequent iterations. Our simulation results using perfect CIR estimation are also shown for comparison. The normalised Doppler frequency was 3.25×10^{-5}.

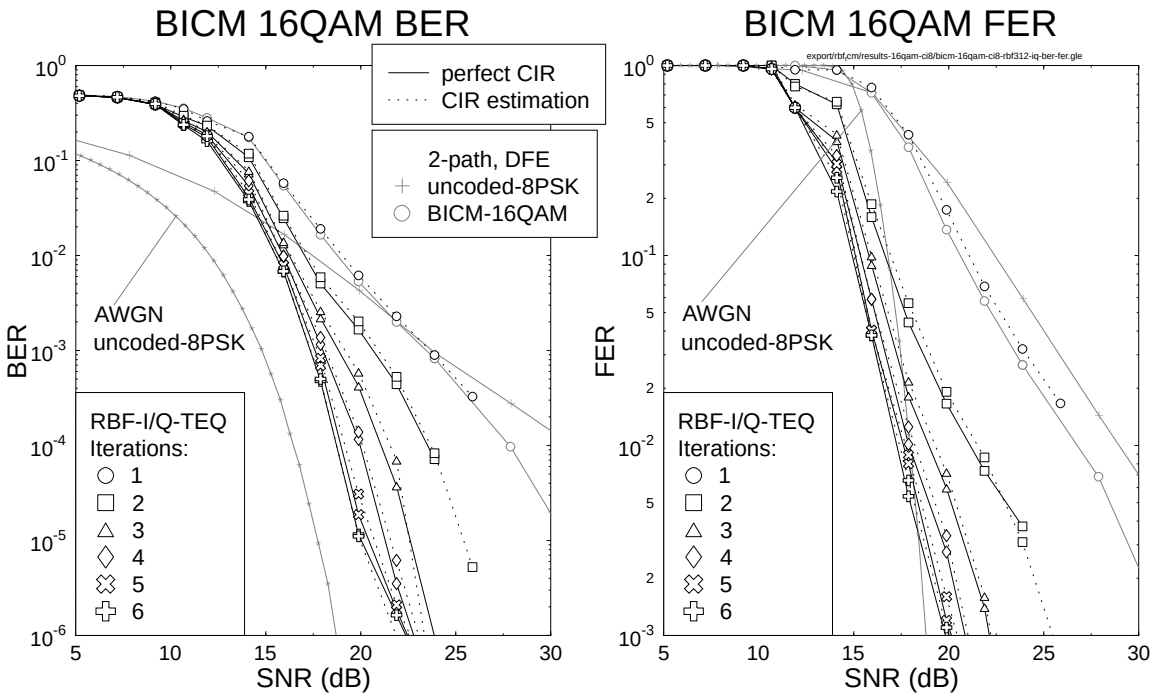

Figure 4.33: The BER and FER versus channel SNR performance of the **RBF-I/Q-TEQ-BICM** 16QAM scheme, when communicating over the equally-weighted two-path Rayleigh fading CIR. The initial LMS CIR estimation step-size used was 0.05, which was reduced to 0.01 for the second and the subsequent iterations. Our simulation results using perfect CIR estimation are also shown for comparison. The normalised Doppler frequency was 3.25×10^{-5}.

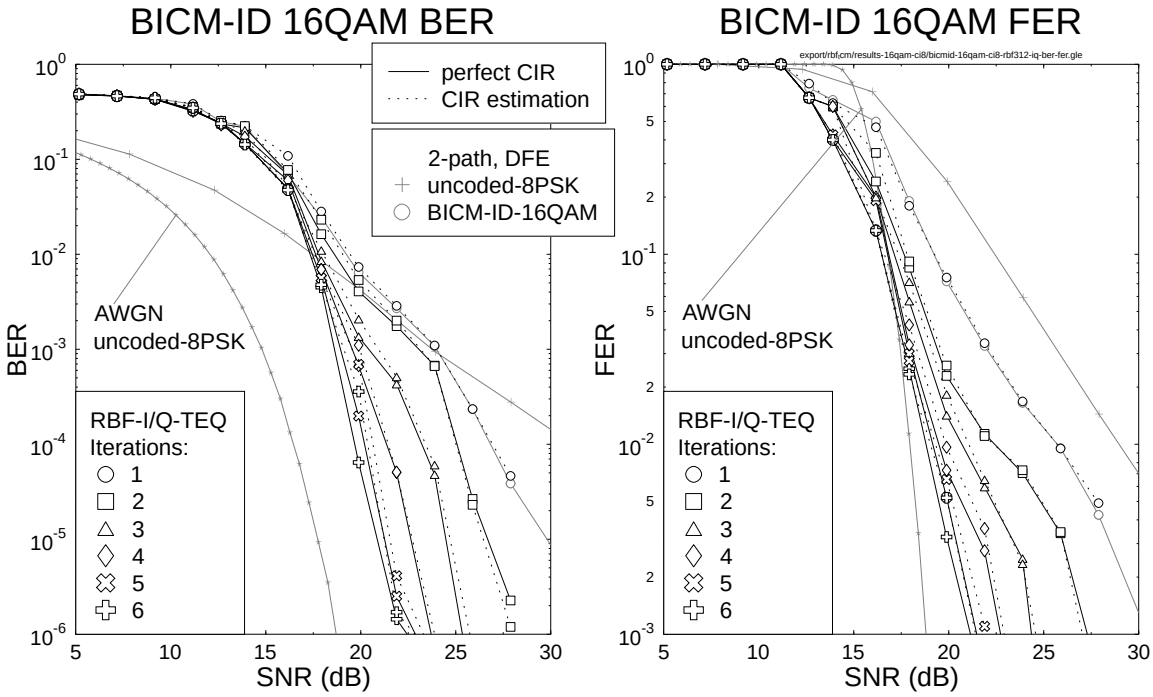

Figure 4.34: The BER and FER versus channel SNR performance of the **RBF-I/Q-TEQ-BICM-ID** 16QAM scheme, when communicating over the equally-weighted two-path Rayleigh fading CIR. The initial LMS CIR estimation step-size used was 0.05, which was reduced to 0.01 for the second and the subsequent iterations. Our simulation results using perfect CIR estimation are also shown for comparison. The normalised Doppler frequency was 3.25×10^{-5}.

the DFE mechanism is reduced from $\mathcal{M}^n$ to $\mathcal{M}^{n/2}$ [103, 118]. Again the BER performance of the identical-throughput uncoded 8PSK scheme communicating over the non-dispersive AWGN channels was used as a benchmarker for the 16QAM-based RBF-I/Q-TEQ arrangement using various CM schemes, which communicated over the dispersive two path Rayleigh fading channels. It was found from our simulations that the achievable performance gain remained only marginal, when more than six TEQ iterations were employed.

The BER and FER performance of the conventional DFE assisted uncoded-8PSK and CM-16QAM schemes employing perfect CIR knowledge was also plotted in Figures 4.31 to 4.34 for comparison to the RBF-I/Q-TEQ assisted CM scheme when communicating over the two-path Rayleigh fading channels considered. Explicitly, the first iteration of the RBF-I/Q-TEQ-CM scheme employed a conventional DFE rather than the RBF-DFE, hence the corresponding performance is identical to that of the conventional DFE assisted CM-16QAM schemes characterised in Figures 4.31 to 4.34. Specifically, the achievable coding gain of the various 16QAM-based RBF-I/Q-TEQ assisted CM schemes against the identical-throughput conventional DFE assisted uncoded-8PSK scheme increases, as the number of iterations increases. Again, the achievable coding gain of the various RBF-I/Q-TEQ assisted CM schemes is significantly higher than that of the conventional DFE assisted CM schemes, albeit this is achieved at a higher complexity. Nonetheless, the complexity of the RBF-I/Q-TEQ scheme still remains lower than that of the conventional trellis-based TEQ as argued in [103, 105].

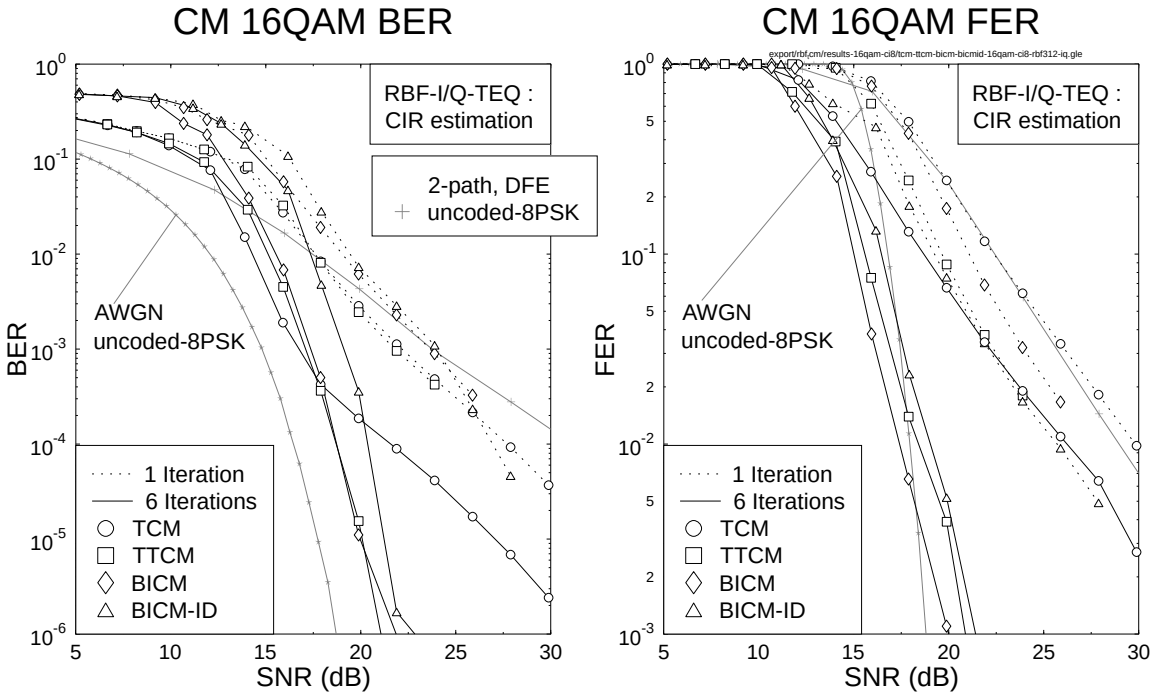

Figure 4.35: The BER and FER versus channel SNR performance of the **RBF-I/Q-TEQ for various CM** 16QAM scheme, when communicating over the equally-weighted two-path Rayleigh fading CIR. The initial LMS CIR estimation step-size used was 0.05, which was reduced to 0.01 for the second and the subsequent iterations. The iteration gains of TEQ can be observed by comparing the performance of the first and third TEQ iteration of the systems. The normalised Doppler frequency was 3.25×10^{-5}.

Figure 4.35 shows the BER and FER versus channel SNR performance of RBF-I/Q-TEQ for various CM aided 16QAM schemes, when communicating over the equally-weighted two-path Rayleigh fading

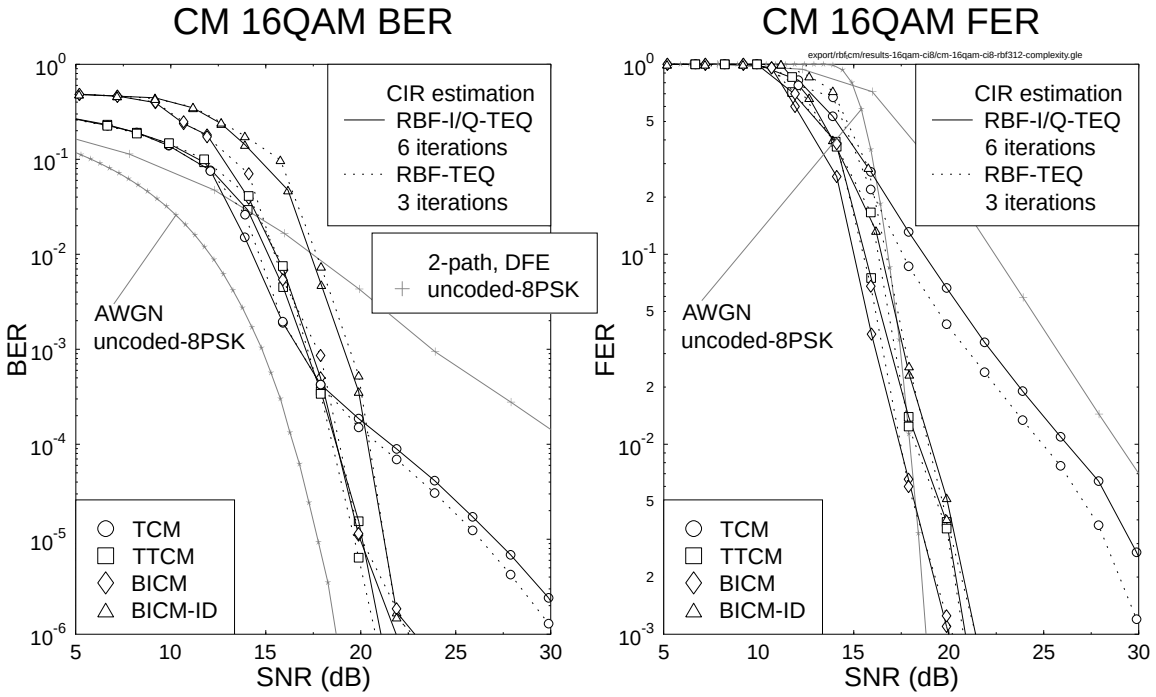

Figure 4.36: The BER and FER versus channel SNR performance of the **RBF-I/Q-TEQ** and **RBF-TEQ** for various CM 16QAM scheme, when communicating over the equally-weighted two-path Rayleigh fading CIR. The initial LMS CIR estimation step-size used was 0.05, which was reduced to 0.01 for the second and the subsequent iterations. The RBF-I/Q-TEQ-CM scheme employs six iterations and the RBF-TEQ-CM scheme employs three iterations. The normalised Doppler frequency was 3.25×10^{-5}.

CIR and utilising the iterative LMS-based CIR estimation of [103]. It is explicit in Figure 4.35 that RBF-I/Q-TEQ-BICM scheme obtained the highest TEQ gains compared to its counterparts. The RBF-I/Q-TEQ-BICM scheme is also the best performer in terms of the achievable FER, but the RBF-I/Q-TEQ-TTCM scheme is the best performer in terms of the BER attained. Let us now compare the performance of the RBF-I/Q-TEQ-CM scheme to that of the RBF-TEQ-CM scheme in Figure 4.36. It is found from Figure 4.36 that the performance of the RBF-I/Q-TEQ-CM scheme having six iterations is similar to that of RBF-TEQ-CM having three iterations, except for the RBF-I/Q-TEQ-TCM scheme, where the achievable FER performance is about one dB inferior in comparison to that of the RBF-TEQ-TCM scheme.

Figure 4.37 illustrates the BER and FER versus channel SNR performance of the TTCM assisted RBF-I/Q-TEQ and RBF-TEQ schemes on an iteration by iteration basis. In terms of the attainable BER, the performance of the first three iterations of RBF-I/Q-TEQ-TTCM is inferior to that of the first iteration of RBF-TEQ-TTCM for BER values below 10^{-4}. In terms of the achievable FER, the performance of the first two iterations of RBF-I/Q-TEQ-TTCM is inferior to that of the first iteration of RBF-TEQ-TTCM for FER values below 10^{-2}. This is due to the employment of a conventional DFE during the first iteration of the RBF-I/Q-TEQ-TTCM scheme, as well as owing to the imperfect I/Q decoupling effects, when unreliable symbol estimates are employed. However, more reliable symbol estimates become available with the aid of the iterative TEQ scheme during the forthcoming iterations and the performance of RBF-I/Q-TEQ-TTCM becomes comparable to that of

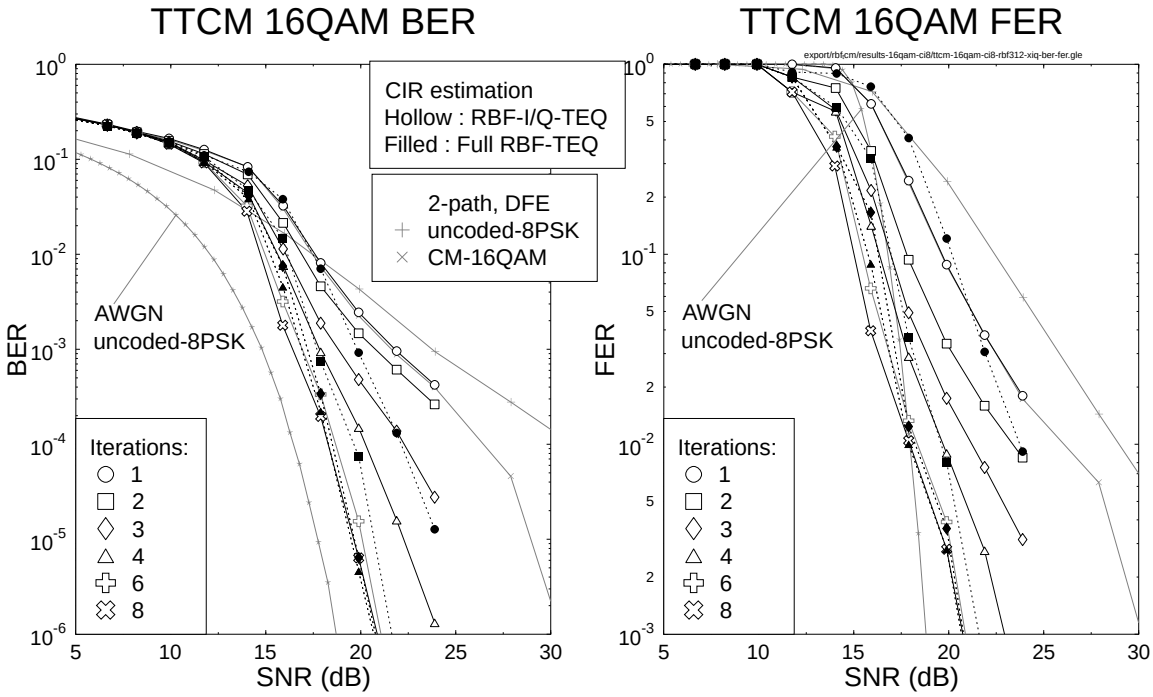

Figure 4.37: The BER and FER versus channel SNR performance of the **RBF-I/Q-TEQ-TTCM** and **RBF-TEQ-TTCM** 16QAM scheme, when communicating over the equally-weighted two-path Rayleigh fading CIR. The initial LMS CIR estimation step-size used was 0.05, which was reduced to 0.01 for the second and the subsequent iterations. The normalised Doppler frequency was 3.25×10^{-5}.

the full-complexity RBF-TEQ-TTCM arrangement eventually, where the performance of RBF-I/Q-TEQ-TTCM having eight iterations is identical to that of RBF-TEQ-TTCM having four iterations for BER values below 10^{-4} and FER values below 10^{-2}, as shown in Figure 4.37. Note that the complexity imposed by the conventional DFE during the first RBF-I/Q-TEQ iteration is insignificant compared to that of the remaining RBF based iterations. Hence, we should compare the complexity of the RBF-DFE assisted scheme using seven iterations in the eight-iteration aided RBF-I/Q-TEQ-TTCM scheme shown in Figure 4.37, to that of the four-iteration full RBF-TEQ-TTCM scheme shown in Figure 4.37. Therefore, it can be shown that complexity reduction factors of $\frac{4}{7} \cdot \frac{20704}{328} \approx 36$ and $\frac{4}{7} \cdot \frac{512}{32} \approx 9$ were obtained in terms of the required number of additions/subtractions and multiplications/divisions, respectively.

4.9.3 Conclusions

We found that the RBF-I/Q-TEQ scheme employing LMS-based CIR estimation exhibited only marginal performance losses compared to the ideal systems employing perfect CIR estimation. This is because the effect of error propagation was reduced significantly, when employing the RBF-I/Q-TEQ scheme, compared to that of the complex-valued RBF-I/Q-TEQ scheme. The achievable performance gain remained only marginal, when more than six TEQ iterations were employed by the CM assisted RBF-I/Q-TEQ scheme.

A significant complexity reduction was obtained by the RBF-I/Q-TEQ-CM scheme, when compared to the complex-valued RBF-TEQ-CM arrangement, while achieving virtually the same perfor-

mance. Specifically, complexity reduction factors of 36 and 9 were achieved in terms of the required number of additions/subtractions and multiplications/divisions, respectively.

4.10 Chapter Conclusions

In this chapter the performance of four single-carrier coded modulation schemes employing channel equalisers was evaluated for transmissions over wideband channels. Specifically, the performance of the BbB adaptive conventional DFE-assisted coded modulation scheme was investigated in Section 4.4, where an improved BER and BPS performance was attained in comparison to that of the fixed-mode based coded modulation schemes. It was found that the employment of a channel interleaver having a memory of one transmission burst was insufficient for randomising the bursty channel errors induced by the slowly-fading COST207 TU channels. Systems that employ a channel interleaver having a longer memory will attain a higher diversity gain, but suffer from a reduced flexibility in terms of modulation mode switching. However, the diversity gain achieved by employing a channel interleaver spanning over four transmission bursts compensated for the loss of switching flexibility, ultimately providing a better performance in terms of both the achievable BER and BPS, as seen in Figure 4.12. TTCM was found to be the best performer, followed by BICM-ID, TCM and BICM in the context of the conventional DFE-assisted adaptive coded modulation scheme.

In Section 4.7, RBF-based turbo equaliser was amalgamated with the coded modulation schemes communicating over wideband fading channels. Specifically, both the proposed RBF-TEQ-CM and the RBF-I/Q-TEQ-CM schemes were investigated under dispersive Rayleigh fading channel conditions using 16QAM for maintaining an effective throughput of 3 BPS as discussed in Sections 4.7 and 4.9, respectively. In general, the BER performance of both the 16QAM-based RBF-TEQ-CM and RBF-I/Q-TEQ-CM schemes when communicating over wideband fading channels, was found to be only about 2 dB away from that of the identical-throughput uncoded 8PSK scheme communicating over AWGN channels. Our simulation results show significant complexity reductions for the RBF-I/Q-TEQ-CM scheme when compared to complex-valued RBF-TEQ-CM, while achieving virtually the same performance. This was demonstrated in Figures 4.36 and 4.37. Amongst the four CM schemes, the best performer was TTCM followed by BICM, BICM-ID and TCM in terms of the achievable BER, as shown in Figure 4.27 for the RBF-TEQ scheme and in Figure 4.35 for the RBF-I/Q-TEQ scheme. However, in terms of the FER attained the best performer was BICM, followed by TTCM, BICM-ID and TCM, as it was demonstrated in Figures 4.27 and 4.35.

We have also compared the performance of the RBF-TEQ-CM and RBF-I/Q-TEQ-CM schemes to that of the conventional DFE assisted CM scheme which was characterised in Section 4.4. More specifically, the conventional DFE assisted CM scheme was integrated into a burst-by-burst adaptive CM system in Section 4.4 based on the corresponding fixed mode's performance. Although the adaptive CM system was not investigated in the context of RBF-TEQ, nonetheless we can expect that the RBF-TEQ assisted adaptive CM system maintains a significantly better performance compared to that of the conventional DFE assisted adaptive CM system of Section 4.4, since the coding gain of the fixed mode RBF-TEQ-CM and RBF-I/Q-TEQ-CM schemes is significantly higher than that of their conventional DFE based counterpart, as we have demonstrated in Sections 4.7 and 4.9. Although the complexity of the RBF-TEQ is higher than that of the conventional DFE, the RBF assisted

schemes are capable of maintaining a lower complexity than that of their conventional trellis-based counterparts, when communicating over both dispersive Gaussian and Rayleigh fading channels, while maintaining a similar performance [103, 105].

In summary, the coding gain exhibited by the coded modulation schemes studied in this chapter was summarised in Tables 4.3, 4.4 and 4.5. Specifically, in Table 4.3 we summarise the performance gain exhibited by the DFE-based coded modulation schemes of Section 4.4, when communicating over the COST207 TU Rayleigh fading channel. Furthermore, the performance gain of the OFDM-based coded modulation schemes of Section 3.4 employing a similar set of parameters and communicating also over the COST207 TU Rayleigh fading channel was incorporated in Table 4.3 for comparison. Specifically, the total number of OFDM subcarriers was 1024 (1K mode [75]) and the number of effective subcarriers was 684. From Table 4.3 we can see that the DFE-based coded modulation schemes of Section 4.4 perform better than the OFDM-based coded modulation schemes of Section 3.4, when targetting a BER of 10^{-3} and 10^{-5}. In Tables 4.4 and 4.5 the coding gain exhibited by the RBF-TEQ-CM and RBF-I/Q-TEQ-CM schemes communicating over 2-path Rayleigh fading channels was tabulated.

COST207 TU Rayleigh fading channels		DFE				OFDM			
Code	Modulation/ BPS	E_b/N_o (dB) BER		Gain (dB)		E_b/N_o (dB) BER		Gain (dB)	
		10^{-3}	10^{-5}	10^{-3}	10^{-5}	10^{-3}	10^{-5}	10^{-3}	10^{-5}
uncoded	BPSK/1	12.35	18.10	0.00	0.00	25.00	44.85	0.00	0.00
TCM	QPSK/1	7.02	11.20	5.33	6.90	11.76	16.00	13.24	28.85
TTCM	QPSK/1	6.35	**8.62**	6.00	9.48	**10.72**	**11.65**	14.28	33.20
BICM	QPSK/1	6.67	9.72	5.68	8.38	11.16	14.09	13.84	30.76
BICM-ID	QPSK/1	**6.21**	9.58	6.14	8.52	10.88	14.34	14.12	30.51
uncoded	QPSK/2	12.71	18.59	0.00	0.00	25.00	44.85	0.00	0.00
TCM	8PSK/2	10.57	14.74	2.14	3.85	14.96	19.84	10.04	25.01
TTCM	8PSK/2	**10.36**	**13.07**	2.35	5.52	14.18	**15.97**	10.82	28.88
BICM	8PSK/2	11.04	14.04	1.67	4.55	14.88	17.97	10.12	26.88
BICM-ID	8PSK/2	10.91	**13.07**	1.80	5.52	**14.05**	16.98	10.95	27.87
uncoded	8PSK/3	16.91	22.31	0.00	0.00	27.34	47.10	0.00	0.00
TCM	16QAM/3	13.18	17.05	3.73	5.03	18.20	36.10	9.14	11.00
TTCM	16QAM/3	**13.13**	**15.81**	3.78	6.50	16.36	**18.56**	10.98	28.54
BICM	16QAM/3	13.65	16.99	3.26	5.53	17.07	20.37	10.27	26.73
BICM-ID	16QAM/3	14.12	16.15	2.79	6.16	**16.32**	19.20	11.02	27.90
uncoded	16QAM/4	17.98	23.75	–	–	28.00	47.85	–	–
TCM	64QAM/5	**18.12**	21.80	–	–	24.48	43.62	–	–
TTCM	64QAM/5	**18.12**	**21.03**	–	–	24.28	43.50	–	–
BICM	64QAM/5	19.01	22.91	–	–	22.55	**26.66**	–	–
BICM-ID	64QAM/5	19.33	21.08	–	–	**21.30**	26.82	–	–
uncoded	64QAM/6	20.42	27.42	–	–	31.61	51.28	–	–

Table 4.3: Coding gain values of the various DFE-based coded modulation schemes studied in this chapter, when communicating over the COST207 TU Rayleigh fading channel. All of the coded modulation schemes exhibited a similar decoding complexity in terms of the number of decoding states, which was equal to 64 states. An interleaver block length of $4 \times 684 = 2736$ symbols was employed and the corresponding simulation parameters were shown in Section 4.4.2. Furthermore, the performance of the OFDM-based coded modulation schemes employing a similar set of parameters, when communicating over the COST207 TU Rayleigh fading channel was also considered here for comparison. Specifically, the total number of OFDM subcarriers was 1024 (1K mode [75]) and the number of effective subcarriers was 684. The performance of the best scheme is printed in bold.

RBF-TEQ, 2-path Rayleigh Fading Channels		First iteration performance				Third iteration performance			
Code	Modulation/ BPS	E_b/N_o (dB) BER		Gain (dB)		E_b/N_o (dB) BER		Gain (dB)	
		10^{-3}	10^{-5}	10^{-3}	10^{-5}	10^{-3}	10^{-5}	10^{-3}	10^{-5}
Uncoded/AWGN	8PSK/3	10.03	12.97	–	–	10.03	12.97	–	–
Uncoded/DFE	8PSK/3	18.88	31.63	0.00	0.00	18.88	31.63	0.00	0.00
TCM	16QAM/3	16.63	25.83	2.25	5.80	**11.98**	21.48	6.90	10.15
TTCM	16QAM/3	**15.03**	**19.23**	3.85	12.40	12.42	**14.88**	6.46	16.75
BICM	16QAM/3	16.87	23.43	2.01	8.20	12.95	15.23	5.93	16.40
BICM-ID	16QAM/3	15.35	21.43	3.53	10.20	14.64	16.47	4.24	15.16

Table 4.4: Coding gain values of the various RBF-TEQ assisted coded modulation schemes studied in this chapter, when communicating over 2-path Rayleigh fading channels. All of the coded modulation schemes exhibited a similar decoding complexity in terms of the number of decoding states, which was equal to 64 states. An interleaver block length of $8 \times 684 = 5472$ symbols was employed and the corresponding simulation parameters were summarised in Section 4.7.2. The performance of the best scheme is printed in bold.

RBF-I/Q-TEQ, 2-path Rayleigh Fading Channels		First iteration performance				Sixth iteration performance			
Code	Modulation/ BPS	E_b/N_o (dB) BER		Gain (dB)		E_b/N_o (dB) BER		Gain (dB)	
		10^{-3}	10^{-5}	10^{-3}	10^{-5}	10^{-3}	10^{-5}	10^{-3}	10^{-5}
Uncoded/AWGN	8PSK/3	10.03	12.97	–	–	10.03	12.97	–	–
Uncoded/DFE	8PSK/3	18.88	31.63	0.00	0.00	18.88	31.63	0.00	0.00
TCM	16QAM/3	17.38	27.13	1.50	4.50	**11.97**	22.28	6.91	9.35
TTCM	16QAM/3	**17.00**	26.75	1.88	4.88	12.32	15.30	6.56	16.33
BICM	16QAM/3	18.88	26.73	0.00	4.90	12.59	**15.19**	6.29	16.44
BICM-ID	16QAM/3	19.20	**24.73**	-0.32	6.90	14.33	16.28	4.55	15.35

Table 4.5: Coding gain values of the various RBF-I/Q-TEQ assisted coded modulation schemes studied in this chapter, when communicating over 2-path Rayleigh fading channels. All of the coded modulation schemes exhibited a similar decoding complexity in terms of the number of decoding states, which was equal to 64 states. An interleaver block length of $8 \times 684 = 5472$ symbols was employed and the corresponding simulation parameters were summarised in Sections 4.7.2 and 4.9.2. The performance of the best scheme is printed in bold.

Chapter 5

Coded Modulation Assisted Code-Division Multiple Access

5.1 Introduction

In this chapter we embark on studying the performance of Coded Modulation (CM) assisted Direct Sequence (DS) Code-Division Multiple Access (CDMA) systems. Two sub-optimum Multi-User Detection (MUD) schemes will be utilised, namely the Minimum Mean Square Error based Decision Feedback Equaliser (MMSE-DFE) MUD and Genetic Algorithm (GA) based MUD.

Joint Detection (JD) [124] receivers are derivatives of the family of well-known single-user channel equalisers, which were originally designed for equalising signals that have been impaired by Inter-Symbol Interference (ISI) due to traversing through multipath channels. The MMSE-DFE based JD (JD-MMSE-DFE) scheme constitutes a powerful approach to mitigating the effects of Multiple Access Interference (MAI) and ISI [125], while at the same time improving the system's performance by benefiting from the multipath diversity provided by dispersive channels. In the literature, TCM and BICM schemes have been investigated in the context of a coherent DS-CDMA receiver using an MMSE receiver, when communicating over flat Rayleigh fading channels [126]. However, in this chapter a JD-MMSE-DFE arrangement will be employed for assisting the operation of the TCM, TTCM, BICM and BICM-ID schemes invoked for transmissions over dispersive Rayleigh fading channels in the context of a DS-CDMA system.

On the other hand, GAs have been used for efficiently solving combinatorial optimisation problems in numerous applications [127]. Recently, GA assisted MUD has been studied using Binary-Phase-Shift-Keying (BPSK) in the context of a CDMA system [128–130]. When compared to Verdu's optimum MUD scheme [131], the GA-MUD is capable of significantly reducing the computational complexity imposed.

The rest of this chapter is organised as follows. The CM assisted JD-MMSE-DFE based MUD is presented in Section 5.2, while an Adaptive CM assisted JD-MMSE-DFE based MUD is investigated in Section 5.3. Finally, the performance of CM assisted GA based MUD is evaluated in Section 5.4.

5.2 CM Assisted JD-MMSE-DFE Based CDMA

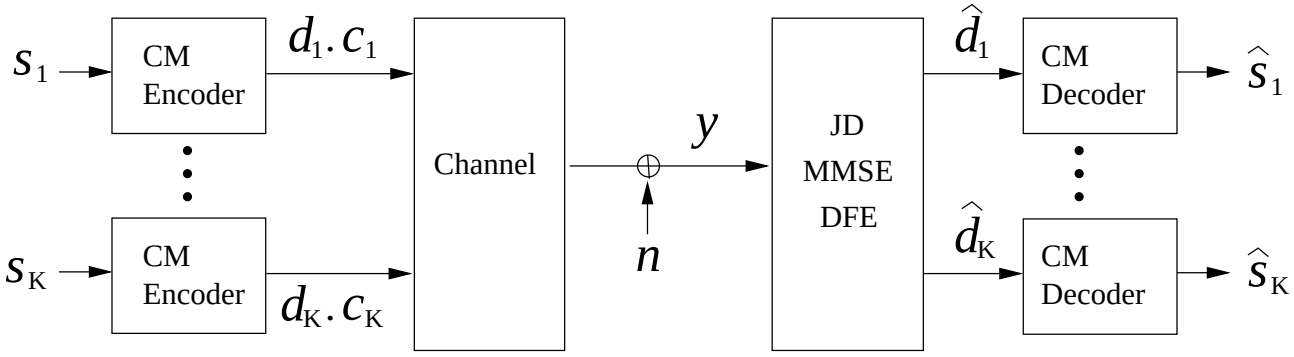

Figure 5.1: Block diagram of the concatenated CM and JD-MMSE-DFE scheme.

The block diagram of the CM-assisted Joint Detection based CDMA (CM-JD-CDMA) system is shown in Figure 5.1. There are K users in the system, where each user is assigned a spreading code. At first, the $2^{\bar{m}}$-ary information symbol S_k of user k, is encoded by the CM encoder to an $2^{\bar{m}+1}$-ary signal, d_k, by adding a parity bit to the original information symbol of $\bar{m}$ information bits. Then, d_k is spread by the spreading code c_k of user k before transmission through the channel. In this uplink scenario each user transmits his/her signal through different channels using a single transmit antenna per user. At the Base Station (BS), we consider one receive antenna for all users. The JD-MMSE-DFE subsystem of the BS's receiver jointly detects all users' signals. The estimate of the signal $\hat{d}_k$ of user k, is then fed from JD-MMSE-DFE to the CM decoder for generating the decoded output $\hat{S}_k$.

5.2.1 The JD-MMSE-DFE Subsystem

The conventional detector used for DS-CDMA systems is the classic matched filter [131]. The matched filter is capable of maximising the SNR at the required sampling instant at its output for a given received waveform [63]. The Whitening Matched Filter (WMF) [124, 132] is an extension of the conventional data estimation technique that uses a bank of matched filters, one for each user. JD schemes can be viewed as extensions to the WMF.

5.2.1.1 DS-CDMA System Model

Before highlighting the structure of the JD-MMSE-DFE subsystem, let us consider the structure of the system matrix **A** for the K-user CDMA system in Figure 5.2. A synchronous system was considered here for simplicity. However, an asynchronous system matrix can also be constructed with the knowledge of the users' delays, provided that the value of the delay can be exactly determined. The combined impulse response $\mathbf{b}_n^{(k)}$ of user k, constituted by the convolution of the spreading sequence

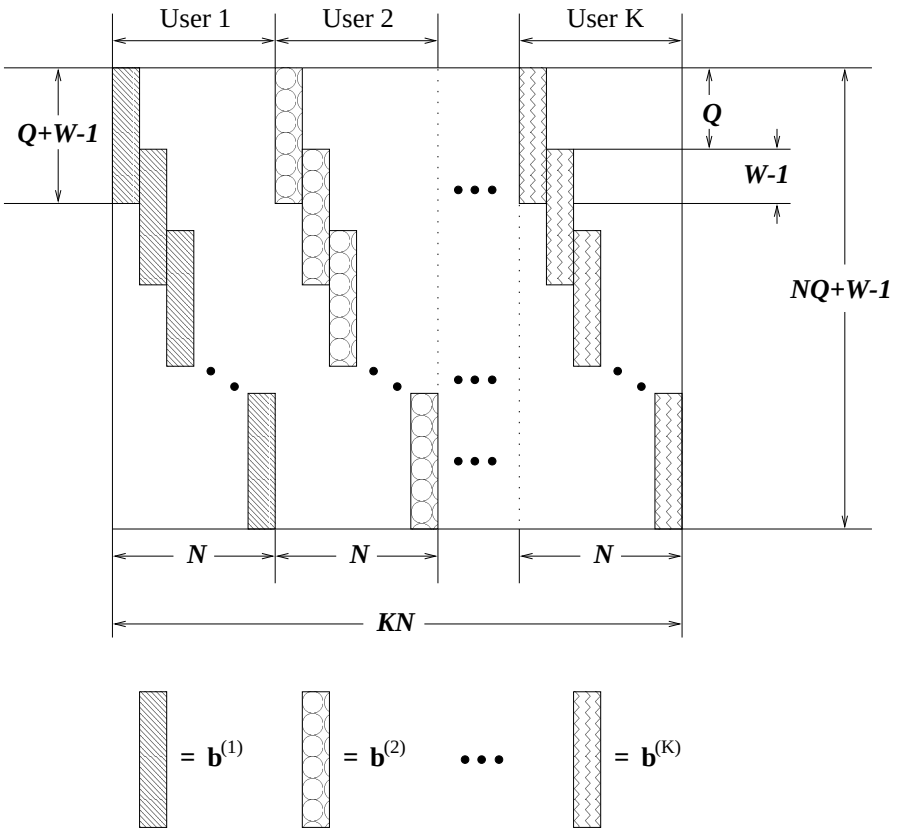

Figure 5.2: Example of the system matrix $\mathbf{A}$ for a K-user CDMA system, where $\mathbf{b}^{(1)}$, $\mathbf{b}^{(2)}$ and $\mathbf{b}^{(\mathsf{K})}$ are column vectors representing the combined impulse responses of user 1, 2 and K respectively in Equation 5.2. The notations are as follows : N denotes the number of coded symbols transmitted by each transmitter, Q represents the number of chips in each spreading sequence and W indicates the length of the wideband Channel Impulse Response (CIR).

$\mathbf{c}^{(k)}$ and the Channel Impulse Response (CIR) $\mathbf{h}_n^{(k)}$ formulated as:

$$\begin{aligned} \mathbf{b}_n^{(k)} &= (b_n^{(k)}(1), b_n^{(k)}(2), \ldots, \\ &\quad b_n^{(k)}(l), \ldots, b_n^{(k)}(Q+W-1))^T \qquad (5.1) \\ &= \mathbf{c}^{(k)} * \mathbf{h}_n^{(k)}, \qquad (5.2) \\ &\quad \text{for } k = 1 \ldots \mathsf{K}; \quad n = 1, \ldots N, \end{aligned}$$

where K represents the total number of users, N denotes the number of coded symbols transmitted by each transmitter, Q represents the number of chips in each spreading sequence and W indicates the length of the wideband CIR. The system matrix of user k, $\mathbf{A}^{(k)}$ is represented by:

$$[\mathbf{A}^{(k)}]_{in} = \begin{cases} b_n^{(k)}(l) & \text{for } i = (n-1)Q + l; \\ & \quad n = 1, \ldots, N; \\ & \quad l = 1, \ldots, Q+W-1; \\ 0 & \text{otherwise.} \end{cases} \qquad (5.3)$$

The overall system matrix can be constructed by appending the matrix $\mathbf{A}^{(k)}$ of each of the K users column-wise:

$$\mathbf{A} = (\mathbf{A}^{(1)}, \mathbf{A}^{(2)}, \ldots, \mathbf{A}^{(k)}, \ldots, \mathbf{A}^{(\mathsf{K})}). \qquad (5.4)$$

Therefore, the discretised received composite signal can be represented in matrix form as:

$$\begin{aligned} \mathbf{y} &= \mathbf{Ad} + \mathbf{n}, \\ \mathbf{y} &= (y_1, y_2, \ldots, y_{NQ+W-1})^T, \end{aligned} \tag{5.5}$$

where $\mathbf{n} = (n_1, n_2, \ldots, n_{NQ+W-1})^T$, is the noise sequence having a variance of σ^2. The covariance matrix of the noise is given by:

$$\mathbf{R}_n = E[\mathbf{n}.\mathbf{n}^H] = \sigma^2 \mathbf{I}_{(NQ+W-1)}, \tag{5.6}$$

where $\mathbf{I}_{(NQ+W-1)}$ is the identity matrix having the dimension of $[NQ+W-1] \times [NQ+W-1]$. The composite signal vector $\mathbf{y}$ has $(NQ+W-1)$ elements for a transmission burst of length N symbols.

The basic concept of joint detection is centred around processing the received composite signal vector, $\mathbf{y}$, in order to determine the transmitted data vector, $\mathbf{d}$ of the K number of users supported. This concept is encapsulated in the following equation:

$$\hat{\mathbf{y}} = \mathbf{S}\hat{\mathbf{d}} = \mathbf{My}, \tag{5.7}$$

where $\mathbf{S}$ is a square matrix having dimensions of $(\mathsf{K}N \times \mathsf{K}N)$ and the matrix $\mathbf{M}$ is a $[\mathsf{K}N \times (NQ+W-1)]$ dimensional matrix. These two matrices determine the type of joint detection algorithm.

Having considered the system model describing the DS-CDMA system, let us now proceed to the description of the joint detection algorithm employed during our further studies.

5.2.1.2 Minimum Mean Square Error Decision Feedback Equaliser Based Joint Detection Algorithm

The principle behind MMSE estimation is the minimisation of the error between the data vector estimate, $\hat{\mathbf{d}}$, and the actual data vector, $\mathbf{d}$. Hence the MMSE algorithm jointly minimises the effects of both MAI, ISI and noise. Explicitly, the MMSE estimator minimises the simple quadratic form [132]:

$$Q(\hat{\mathbf{d}}) = E[(\mathbf{d} - \hat{\mathbf{d}})^H (\mathbf{d} - \hat{\mathbf{d}})]. \tag{5.8}$$

Upon invoking the well-known Orthogonality Principle [80], in order to minimise the Mean Squared Error (MSE), the error vector $\mathbf{e} = \mathbf{d} - \hat{\mathbf{d}}$ has to be set orthogonal by the MMSE equaliser to the estimator's input vector $\mathbf{y}$. This implies that:

$$E[(\mathbf{d} - \hat{\mathbf{d}})\mathbf{y}^H] = \mathbf{0}, \tag{5.9}$$

where $\mathbf{0}$ is a matrix with all of its elements being zero-valued. If we let $\hat{\mathbf{d}} = \mathbf{My}$, where $\mathbf{M}$ is a linear estimator, then:

$$\begin{aligned} E[(\mathbf{d} - \mathbf{My})\mathbf{y}^H] &= \mathbf{0} \\ E[(\mathbf{dy}^H - \mathbf{Myy}^H)] &= \mathbf{0} \\ E[(\mathbf{dy}^H)] - \mathbf{M}\ E[\mathbf{yy}^H] &= \mathbf{0} \\ \mathbf{R}_{dy} - \mathbf{MR}_y &= \mathbf{0} \\ \therefore \mathbf{M} &= \mathbf{R}_{dy}\mathbf{R}_y^{-1}, \end{aligned} \tag{5.10}$$

where $\mathbf{R}_{dy} = E[\mathbf{d}\mathbf{y}^H]$ and $\mathbf{R}_y = E[\mathbf{y}\mathbf{y}^H]$. For the special case of Equation 5.5, i.e. when $\mathbf{y} = \mathbf{A}\mathbf{d} + \mathbf{n}$, we have [133]:

$$\begin{aligned} \mathbf{R}_{dy} &= E[\mathbf{d}(\mathbf{A}\mathbf{d} + \mathbf{n})^H] \\ &= E[\mathbf{d}\mathbf{d}^H\mathbf{A}^H + \mathbf{d}\mathbf{n}^H], \end{aligned} \tag{5.11}$$

and assuming that the transmitted data vector, $\mathbf{d}$, and the noise vector, $\mathbf{n}$, are uncorrelated with each other, i.e. when $E[\mathbf{d}\mathbf{n}^H] = 0$, we arrive at:

$$\begin{aligned} \mathbf{R}_{dy} &= E[\mathbf{d}\mathbf{d}^H\mathbf{A}^H] \\ &= \mathbf{R}_d\mathbf{A}^H, \end{aligned} \tag{5.12}$$

where $\mathbf{R}_d = E[\mathbf{d}\mathbf{d}^H]$. Furthermore, the covariance matrix, $\mathbf{R}_y$, of the received vector $\mathbf{y}$ in Equation 5.10 is given by:

$$\begin{aligned} \mathbf{R}_y &= E[(\mathbf{A}\mathbf{d} + \mathbf{n})(\mathbf{A}\mathbf{d} + \mathbf{n})^H] \\ &= E[\mathbf{A}\mathbf{d}\mathbf{d}^H\mathbf{A}^H + \mathbf{n}\mathbf{n}^H] \\ &= \mathbf{A}\mathbf{R}_d\mathbf{A}^H + \mathbf{R}_n. \end{aligned} \tag{5.13}$$

Substituting Equations 5.12 and 5.13 into Equation 5.10, we get:

$$\mathbf{M} = \mathbf{R}_d\mathbf{A}^H(\mathbf{A}\mathbf{R}_d\mathbf{A}^H + \mathbf{R}_n)^{-1} \tag{5.14}$$

$$= (\mathbf{A}^H\mathbf{R}_n^{-1}\mathbf{A} + \mathbf{R}_d^{-1})^{-1}\mathbf{A}^H\mathbf{R}_n^{-1}. \tag{5.15}$$

Finally, by substituting the MMSE detector expression of Equation 5.15 into the Equation $\hat{\mathbf{d}} = \mathbf{M}\mathbf{y}$, we arrive at:

$$\hat{\mathbf{d}}_{\text{MMSE-BLE}} = (\mathbf{A}^H\mathbf{R}_n^{-1}\mathbf{A} + \mathbf{R}_d^{-1})^{-1}\mathbf{A}^H\mathbf{R}_n^{-1}\mathbf{y}, \tag{5.16}$$

which is the data estimate generated by the MMSE Block Linear Equaliser (MMSE-BLE) or, in other words, the output of the feed-forward filter of the MMSE-DFE. On the other hand, the output of the WMF is given by [134]:

$$\hat{\mathbf{d}}_{\mathbf{WMF}} = \mathbf{A}^H\mathbf{R}_n^{-1}\mathbf{y}. \tag{5.17}$$

Observing Equations 5.17 and 5.16, the output of the MMSE-BLE is given by the output of the WMF in Equation 5.17, multiplied by the matrix $(\mathbf{A}^H\mathbf{R}_n^{-1}\mathbf{A} + \mathbf{R}_d^{-1})$. The Cholesky decomposition [135] is performed on the matrix $(\mathbf{A}^H\mathbf{R}_n^{-1}\mathbf{A} + \mathbf{R}_d^{-1})$ [132] giving:

$$\mathbf{A}^H\mathbf{R}_n^{-1}\mathbf{A} + \mathbf{R}_d^{-1} = (\mathbf{D}\mathbf{U})^H\mathbf{D}\mathbf{U}, \tag{5.18}$$

where $\mathbf{U}$ is an upper triangular matrix, where all the elements on its main diagonal have the value of one and $\mathbf{D}$ is a diagonal matrix having real-valued elements. With the aid of Equation 5.5, the output of the WMF from Equation 5.17 can be rearranged as:

$$\begin{aligned} \hat{\mathbf{d}}_{\text{WMF}} &= \mathbf{A}^H\mathbf{R}_n^{-1}\mathbf{A}\mathbf{d} + \mathbf{A}^H\mathbf{R}_n^{-1}\mathbf{n} \\ &= (\mathbf{A}^H\mathbf{R}_n^{-1}\mathbf{A} + \mathbf{R}_d^{-1})\mathbf{d} - \mathbf{R}_d^{-1}\mathbf{d} + \mathbf{A}^H\mathbf{R}_n^{-1}\mathbf{n}. \end{aligned} \tag{5.19}$$

Applying the matrix $((\mathbf{DU})^H)^{-1}$ to both sides of Equation 5.19 and invoking Equation 5.18, yields:

$$\begin{aligned}((\mathbf{DU})^H)^{-1}\hat{\mathbf{d}}_{\text{WMF}} &= ((\mathbf{DU})^H)^{-1}(\mathbf{A}^H\mathbf{R}_n^{-1}\mathbf{A}+\mathbf{R}_d^{-1})\mathbf{d} - ((\mathbf{DU})^H)^{-1}\mathbf{R}_d^{-1}\mathbf{d} + \\ &\quad ((\mathbf{DU})^H)^{-1}\mathbf{A}^H\mathbf{R}_n^{-1}\mathbf{n} \\ &= \mathbf{DUd} - ((\mathbf{DU})^H)^{-1}\mathbf{R}_d^{-1}\mathbf{d} + \\ &\quad ((\mathbf{DU})^H)^{-1}\mathbf{A}^H\mathbf{R}_n^{-1}\mathbf{n}. \end{aligned} \tag{5.20}$$

Again, since $\mathbf{D}$ is a diagonal matrix, it can be treated as a scaling factor and removed by multiplying both sides of Equation 5.20 with its inverse, giving the resultant vector of $\hat{\mathbf{y}}$ as:

$$\begin{aligned}\hat{\mathbf{y}} &= (\mathbf{D})^{-1}((\mathbf{DU})^H)^{-1}\hat{\mathbf{d}}_{\text{WMF}} &(5.21)\\ &= (\mathbf{D})^{-1}\mathbf{DUd} - (\mathbf{D})^{-1}((\mathbf{DU})^H)^{-1}\mathbf{R}_d^{-1}\mathbf{d} + \\ &\quad (\mathbf{D})^{-1}((\mathbf{DU})^H)^{-1}\mathbf{A}^H\mathbf{R}_n^{-1}\mathbf{n} \\ &= \mathbf{Ud} - \mathbf{e} + \mathbf{z} \\ &= \mathbf{d} + (\mathbf{U} - \mathbf{I}_{\mathsf{K}N})\mathbf{d} - \mathbf{e} + \mathbf{z}, &(5.22)\end{aligned}$$

where

$$\mathbf{e} = (\mathbf{D})^{-1}((\mathbf{DU})^H)^{-1}\mathbf{R}_d^{-1}\mathbf{d}, \tag{5.23}$$

and

$$\mathbf{z} = (\mathbf{D})^{-1}((\mathbf{DU})^H)^{-1}\mathbf{A}^H\mathbf{R}_n^{-1}\mathbf{n}. \tag{5.24}$$

Therefore, in the MMSE-DFE, the received vector, $\mathbf{y}$, is processed by a WMF, followed by the feed-forward filter that is represented by the matrix $(\mathbf{D})^{-1}((\mathbf{DU})^H)^{-1}$. The output of the feed-forward filter is given as [124]:

$$\begin{aligned}\hat{\mathbf{y}} &= (\mathbf{D})^{-1}((\mathbf{DU})^H)^{-1}\mathbf{A}^H\mathbf{R}_n^{-1}\mathbf{y} &(5.25)\\ &= \mathbf{My}, &(5.26)\end{aligned}$$

where

$$\mathbf{M} = (\mathbf{D})^{-1}((\mathbf{DU})^H)^{-1}\mathbf{A}^H\mathbf{R}_n^{-1}. \tag{5.27}$$

The matrix $\mathbf{M}$ represents the combination of the WMF and feed-forward filter. Since $\mathbf{U}$ is an upper triangular matrix having ones on its main diagonal, $(\mathbf{U} - \mathbf{I}_{\mathsf{KN}})$ is an upper triangular matrix having zeros on its main diagonal. Therefore, from Equation 5.22 the i-th element of the vector $\hat{\mathbf{y}}$ is given by:

$$\hat{y}_i = d_i + \sum_{j=i+1}^{J} [\mathbf{U} - \mathbf{I}_{\mathsf{K}N}]_{i,j}\ d_j - e_i + z_i, \tag{5.28}$$

where $J = \mathsf{K}N$. The summation is only from $j = i+1$ to J, since $(\mathbf{U} - \mathbf{I}_{\mathsf{K}N})$ is an upper triangular matrix having zeros on its main diagonal. For $i = J$, we have:

$$\hat{y}_J = d_J - e_J + z_J. \tag{5.29}$$

The i-th data estimate is $Q(\hat{y}_J)$, where $Q\{.\}$ is the thresholding or quantisation operator performed in a threshold detector. For $i = 1, \ldots, J-1$, if the estimates of the data are obtained in decreasing order of i, then for each $\hat{y}_i$, the data estimates $\hat{d}_{i+1}, \ldots, \hat{d}_J$ have already been obtained. Therefore, the data estimate, $\hat{d}_i$ is given by:

$$\hat{d}_i = d_i + \sum_{j=i+1}^{J} [\mathbf{U} - \mathbf{I}_{\mathsf{K}N}]_{i,j} \ (d_j - \hat{d}_j) - e_i + z_i. \tag{5.30}$$

If the data estimates, $\hat{d}_j$ are accurately estimated, i.e. if we have $\hat{d}_j = d_j$, Equation 5.30 becomes:

$$\hat{d}_i = d_i - e_i + z_i, \tag{5.31}$$

giving an MMSE estimate of the data symbol. For the MMSE-DFE, the feedback operator, $\mathbf{S}$ can be derived from Equation 5.30 as:

$$\mathbf{S} = \mathbf{U} - \mathbf{I}_{\mathsf{K}N}, \tag{5.32}$$

where $\mathbf{S}$ is an upper diagonal matrix and all the elements on its main diagonal have values of zero. If the data symbols are estimated in descending order of j, the previously estimated data symbols of $\hat{d}_j$ are fed into the threshold detector for obtaining a hard decision value of $\hat{t}_j$. The hard decision value $\hat{t}_j$ is multiplied with the feedback operator $\mathbf{S}$ and then deducted from the feed-forward filter's output $\hat{y}_i$, yielding [124]:

$$\begin{aligned} \hat{d}_{i(\text{MMSE-DFE})} &= \hat{y}_i - \sum_{j=i+1}^{J=\mathsf{K}N} [\mathbf{U} - \mathbf{I}_{\mathsf{K}N}]_{ij} \ \hat{t}_j \\ &= \hat{y}_i - \sum_{j=i+1}^{J=\mathsf{K}N} ([\mathbf{U}]_{ij} - [\mathbf{I}_{\mathsf{K}N}]_{ij}) \ \hat{t}_j \\ &= \hat{y}_i - \sum_{j=i+1}^{J=\mathsf{K}N} [\mathbf{U}]_{ij} \ \hat{t}_j, \end{aligned} \tag{5.33}$$

where we have $[\mathbf{I}_{\mathsf{K}N}]_{ij} = 0$ for $i \neq j$.

5.2.1.3 Algorithm Summary

The schematic of the MMSE-DFE is shown in Figure 5.3. The operations required for obtaining the JD-MMSE-DFE data estimates can be summarised as follows. First we construct the system matrix $\mathbf{A}$ in Equation 5.4. Then we obtain the output of the WMF as in Equation 5.17:

$$\hat{\mathbf{d}}_{\mathbf{WMF}} = \mathbf{A}^H \mathbf{R}_n^{-1} \mathbf{y},$$

where $\mathbf{A}^H$ is the conjugate transpose of $\mathbf{A}$ and $\mathbf{R}_n^{-1}$ is the inverse of the noise covariance matrix $\mathbf{R}_n$. Next, Cholesky decomposition [136] of the matrix $(\mathbf{A}^H \mathbf{R}_n^{-1} \mathbf{A} + \mathbf{R}_d^{-1})$ is performed as in Equation 5.18:

$$\mathbf{A}^H \mathbf{R}_n^{-1} \mathbf{A} + \mathbf{R}_d^{-1} = (\mathbf{D}\mathbf{U})^H \mathbf{D}\mathbf{U},$$

where $\mathbf{R}_d^{-1}$ is the inverse of the signal's covariance matrix $\mathbf{R}_d$, $\mathbf{D}$ is a diagonal matrix having real-valued elements and $\mathbf{U}$ is an upper triangular matrix, where all the elements on the main diagonal have

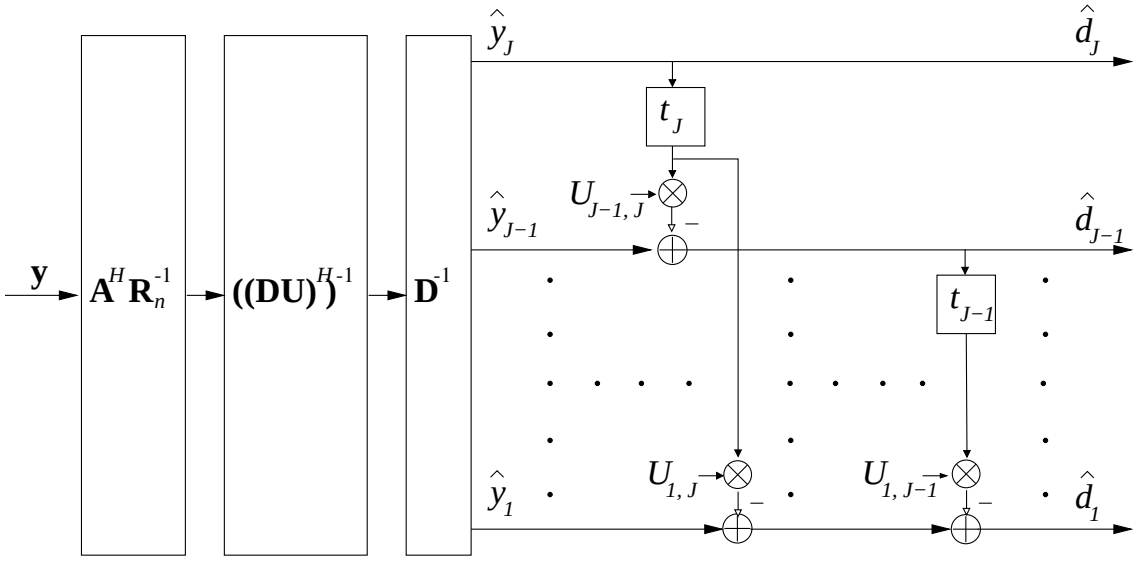

Figure 5.3: Structure of the MMSE-DFE-based receiver. The composite received vector, $\mathbf{y}$, is processed through the WMF, which is represented by the matrix $(\mathbf{A}^H\mathbf{R}_n^{-1})$ and this operation is expressed in Equation 5.17. The output of the WMF is then passed through the feed-forward filter which is constructed by the lower triangular matrix of $((\mathbf{DU})^H)^{-1}$ and the scaling factor matrix of $\mathbf{D}^{-1}$. These two operations were expressed in Equation 5.21. The output of the feed-forward filter is then processed, in order to obtain the data estimates, $\hat{\mathbf{d}}_j$, where the estimates are obtained in the order of $j = J, J-1, \ldots, 1$. As the data estimates, $\hat{\mathbf{d}}_j$, are obtained, they are fed back into the receiver, where they are multiplied by the elements in the upper triangular matrix, $[\mathbf{U}]_{ij} = U_{ij}$, as shown in Equation 5.33.

the value of one. Consequently, the feed-forward filter output is obtained by solving Equation 5.25:

$$\begin{aligned}\hat{\mathbf{y}} &= (\mathbf{D})^{-1}((\mathbf{DU})^H)^{-1}\,\mathbf{A}^H\mathbf{R}_n^{-1}\mathbf{y} \\ &= (\mathbf{D})^{-1}((\mathbf{DU})^H)^{-1}\,\hat{\mathbf{d}}_{\mathbf{WMF}}.\end{aligned}$$

Finally the feedback operation from Equation 5.33 is invoked for producing the final estimate of the coded symbol, yielding:

$$\hat{d}_i(\text{MMSE-DFE}) = \hat{y}_i - \sum_{j=i+1}^{J=\mathsf{K}N} [\mathbf{U}]_{ij}\hat{t}_j.$$

5.2.2 Simulation Parameters

Let us now investigate the performance of the proposed schemes using the simulation parameters shown in Table 5.1, where 16-chip random spreading codes were utilised by each user. The transmission frame structure used is the FMA1 spread speech/data burst of the FRAMES proposal [137], which is shown in Figure 5.4. The channel model used is the COST 207 [72] seven path Bad Urban channel shown in Figure 5.5. Each path is faded according to independent Rayleigh fading statistics, as described by the parameters of Table 5.1. We assumed that the receiver perfectly knows the CIRs although in reality this has to be estimated with the aid of the training sequence of the transmission frame shown in Figure 5.4. The fading envelope was kept constant for the duration of the transmission burst of

Parameter	Value
Doppler frequency	80 Hz
Spreading ratio, Q	16
Chip rate	2.167 MBaud
Normalised Doppler frequency	$80/(2.167\times10^6) = 3.69\times10^{-5}$ Hz
Frame burst structure	FRAMES Mode 1 Spread burst 1 [137] in Figure 5.4
No. of symbols per JD block, N	28
Modulation mode	QPSK, 8PSK, 16QAM
CM subsystem	TCM (ν=6)
	BICM (ν=6)
	TTCM (ν=3, 4 iterations)
	BICM-ID (ν=3, 8 iterations)

Table 5.1: Simulation parameters of the CM-JD-CDMA system.

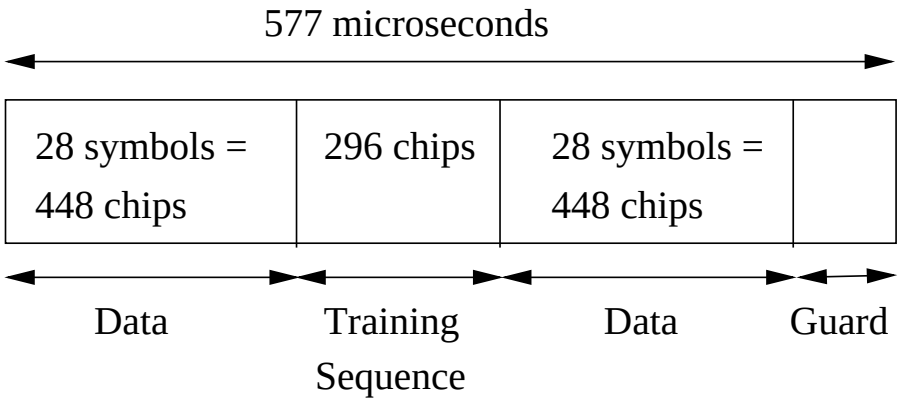

Figure 5.4: Transmission burst structure of the FMA1 spread speech/data burst of the FRAMES proposal [137].

577 μs and it was faded immediately before the next transmission burst. The CM subsystems shown in Table 5.1 exhibit a similar complexity, where their corresponding generator polynomials can be found from Tables 2.1, 2.2, 2.3 and 2.4.

In our performance evaluations, the uncoded QPSK system was compared to the CM assisted 8PSK system when aiming for an effective throughput of 2 information Bits Per Symbol (BPS). Similarly, the uncoded 8PSK system was compared to the CM assisted 16QAM system for a throughput of 3 BPS. Channel interleavers of length 112 symbols or 1120 symbols were utilised, which correspond to 2 transmission burst duration of 1.154 ms or 20 transmission burst durations of 11.54 ms, respectively.

5.2.3 Simulation Results and Discussions

Figure 5.6 shows the Bit Error Ratio (BER) versus Signal to Noise Ratio (SNR) performance of CM-JD-CDMA schemes for transmissions over the COST 207 [72] seven path Bad Urban channel shown in Figure 5.5 using the transmission burst structure of the FMA1 spread speech/data burst of the FRAMES proposal [137] shown in Figure 5.4, when utilising the simulation parameters of

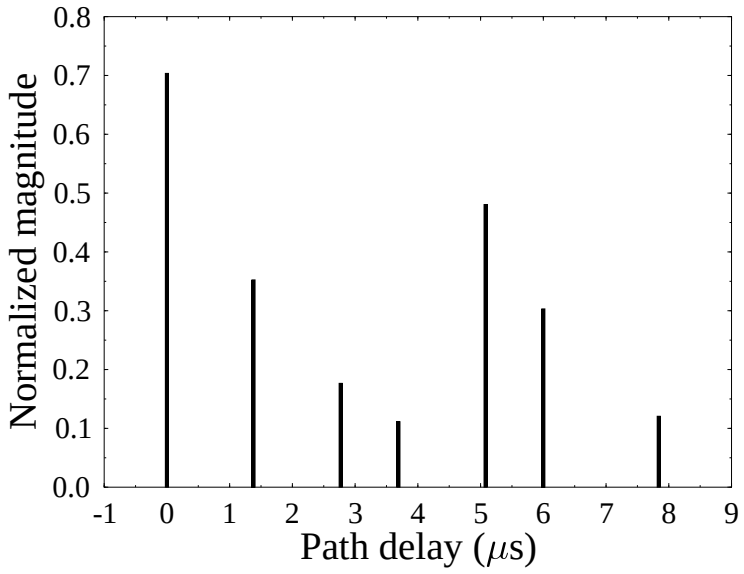

Figure 5.5: Normalised channel impulse response of the COST 207 [72] **seven path Bad Urban channel**.

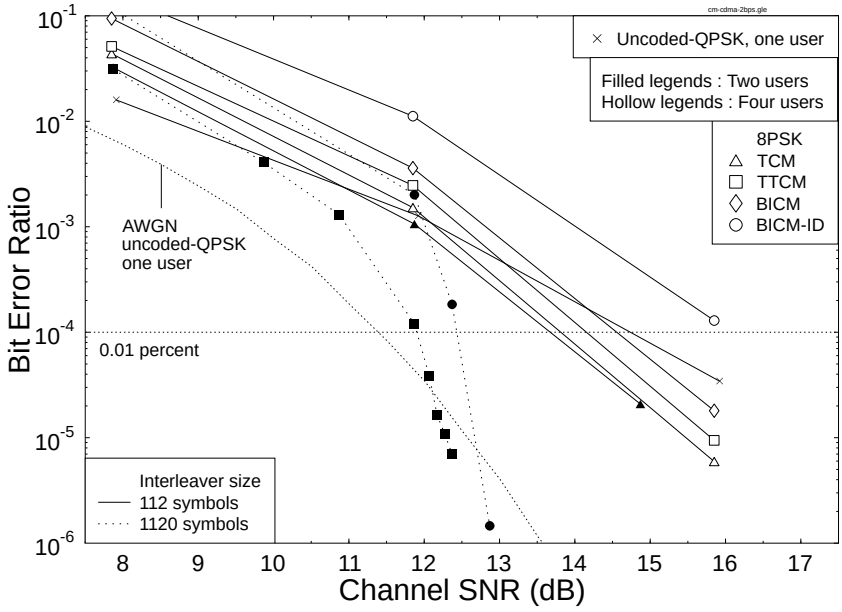

Figure 5.6: Bit Error Ratio (BER) versus Signal to Noise Ratio (SNR) performance of the various CM-JD-CDMA schemes for transmissions over the COST 207 [72] seven path Bad Urban channel of Figure 5.5 using the transmission burst structure of the FMA1 spread speech/data burst of the FRAMES proposal [137] shown in Figure 5.4 utilising the simulation parameters of Table 5.1 for a throughput of **2 BPS**.

Table 5.1 and maintaining a throughput of **2 BPS**. Considering the performance of the TCM-JD-CDMA scheme using 8PSK modulation, the performance difference between the two- and four-user scenario is marginal indicated by the hollow and filled triangles in Figure 5.6 due to employing the powerful JD-MMSE-DFE scheme. Comparing the single-user uncoded-QPSK scheme represented by the cross, with the four-user CM-8PSK schemes utilising an interleaver length of 112 symbols at BER=10^{-4}, performance gains can be observed for all CM-8PSK schemes over the uncoded-QPSK scheme, except for the BICM-ID-8PSK scheme. It can be also observed in Figure 5.6 that the TCM-8PSK scheme constitutes the best candidate, showing an SNR gain of 1 dB at BER=10^{-4}. Due to the short interleaver length used, the TTCM and BICM-ID iterative decoding schemes were unable to perform efficiently. By contrast, the interleaver length does not dramatically affect the performance of the non-iterative TCM and BICM schemes [20]. Comparing the two-user TCM-8PSK scheme with the two-user TTCM-8PSK and BICM-ID-8PSK schemes utilising an interleaver length of 1120 symbols at BER=10^{-4}, TTCM-8PSK and BICM-ID-8PSK show a 1.8 dB and 1.2 dB SNR gain over TCM-8PSK, respectively. For a throughput of 2BPS, TTCM-8PSK utilising an interleaver length of 1120 symbols is the best candidate, exhibiting an SNR gain of 2.9 dB over the uncoded-QPSK scheme at BER=10^{-4}. The performance of the single-user uncoded QPSK system communicating over the non-dispersive AWGN channel is also plotted in Figure 5.6 as a benchmarker. This benchmarker is outperformed by both the TTCM-8PSK and BICM-ID-8PSK schemes at low BERs, when an interleaver length of 1120 symbols was utilised.

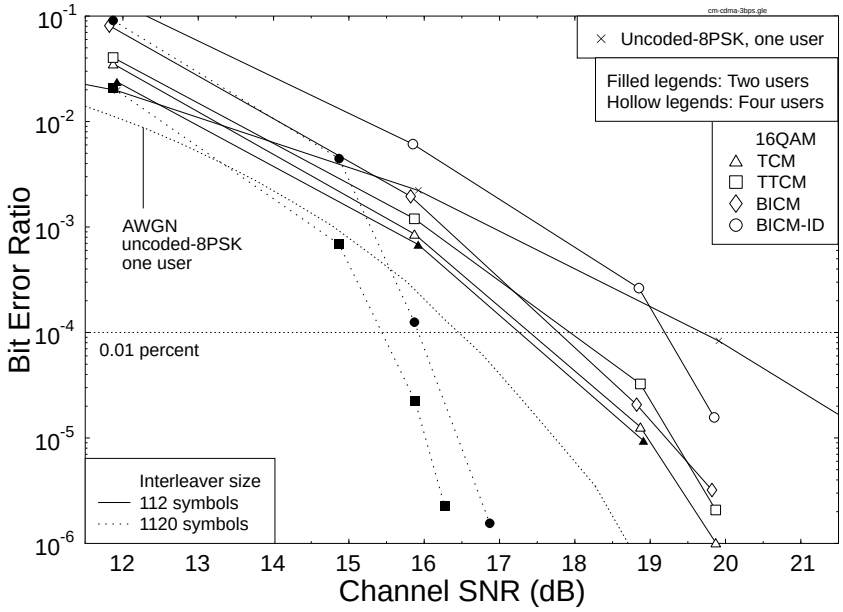

Figure 5.7: BER versus SNR performance of the various CM-JD-CDMA schemes for transmissions over the COST 207 [72] seven path Bad Urban channel of Figure 5.5 using the transmission burst structure of the FMA1 spread speech/data burst of the FRAMES proposal [137] shown in Figure 5.4 utilising the simulation parameters of Table 5.1 for a throughput of **3 BPS**.

Figure 5.7 shows the BER versus SNR performance of CM-JD-CDMA schemes for transmissions over the COST 207 [72] seven path Bad Urban channel shown in Figure 5.5 using the transmission burst structure of the FMA1 spread speech/data burst of the FRAMES proposal [137] shown in Figure 5.4 utilising the simulation parameters of Table 5.1. In this the effective throughput is **3 BPS**. Comparing

the performance of the TCM-JD-CDMA scheme using 16QAM, the performance difference between the scheme supporting two- and four-user is again marginal due to invoking the powerful JD-MMSE-DFE scheme. Comparing the single-user uncoded-8PSK scheme with the four-user CM-16QAM schemes utilising an interleaver length of 112 symbols at BER=10^{-4}, performance gains can be observed for all CM-16QAM schemes over the uncoded-8PSK scheme. The TCM-16QAM scheme constitutes the best candidate, showing an SNR gain of 2.3 dB. Comparing the two-user TCM-16QAM scheme with the two-user TTCM-16QAM and BICM-ID-16QAM schemes utilising an interleaver length of 1120 symbols at BER=10^{-4}, TTCM-16QAM and BICM-ID-16QAM show 1.8 dB and 1.3 dB SNR gains over TCM-16QAM, respectively. For the effective throughput of 3BPS, TTCM-16QAM utilising an interleaver length of 1120 symbols is the best candidate showing an SNR gain of 4.2 dB over the uncoded 8PSK scheme at BER=10^{-4}. The performance of the single-user uncoded 8PSK scheme communicating over the non-dispersive AWGN channel is also plotted in Figure 5.7 as a benchmarker. The benchmarker is outperformed by both the TTCM-16QAM and BICM-ID-16QAM schemes utilising an interleaver length of 1120 symbols.

5.2.4 Conclusions

In this section, TCM, TTCM, BICM and BICM-ID assisted JD-MMSE-DFE based CDMA schemes were proposed and evaluated in performance terms over the COST 207 [72] seven path Bad Urban channel. For systems using a short interleaver length of 112 symbols, TCM was found to be the best candidate when providing a throughput of 2 and 3 BPS. However, for systems that can afford a longer delay due to utilising a long interleaver length, TTCM was found to be the best candidate for providing a throughput of 2 and 3 BPS.

5.3 Adaptive CM Assisted JD-MMSE-DFE Based CDMA

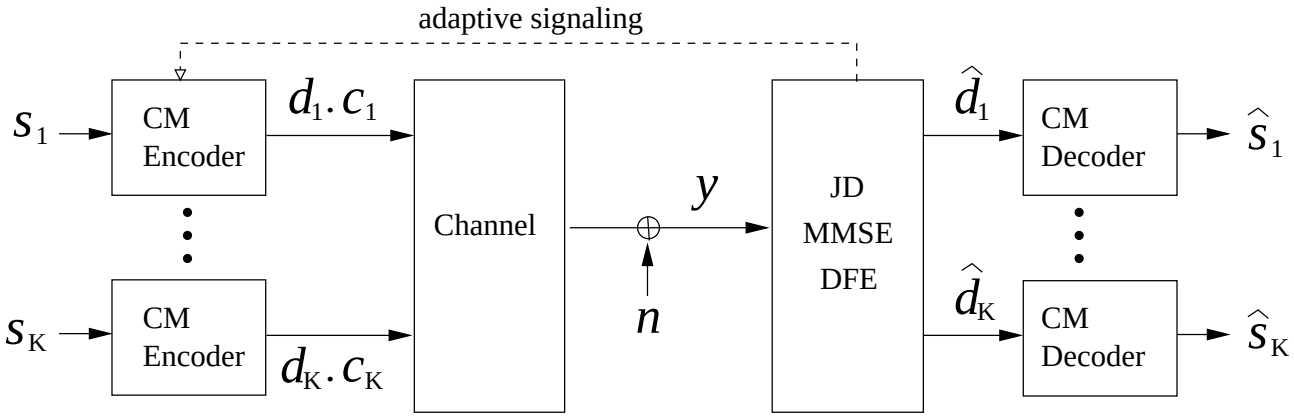

Figure 5.8: Block diagram of the BbB ACM-JD-CDMA scheme.

In this section, a Burst-by-Burst Adaptive Coded Modulation-Aided Joint Detection-Based CDMA (ACM-JD-CDMA) scheme is proposed for wireless communications and characterised in performance terms, when communicating over the UMTS Terrestrial Radio Access (UTRA) wideband vehicular Rayleigh fading channel. The block diagram of the ACM-JD-CDMA system is shown in Figure 5.8,

which is similar to that shown in Figure 5.1 of Section 5.2 except for the adaptive signalling link used by the JD-MMSE-DFE for informing the CM-encoder regarding the choice of the suitable modulation mode.

More explicitly, the instantaneous channel quality is estimated by the JD-MMSE-DFE and the index or identifier of the highest-throughput modulation mode still capable of maintaining the required target BER or FER can then be communicated to the transmitter via explicit signalling in a closed-loop scheme. Conversely, in an open-loop scheme, by assuming reciprocity in the uplink and downlink channels of Wideband Time Division Duplex (TDD) CDMA systems, the modulation mode required for downlink transmission is chosen according to the channel quality estimate related to the uplink and vice versa. Channel reciprocity issues in TDD/CDMA systems have been investigated by Miya *et al.* [138], Kato *et al.* [139] and Jeong *et al.* [140].

In adaptive modulation schemes the issue of modulation mode signalling between the transmitter and receiver is of salient importance, especially in the context of Symbol-by-Symbol (SbS) adaptive systems [141], where the transmitter is capable of transmitting symbols in different modem modes, depending on the channel conditions. Naturally, the receiver has to synchronise with the transmitter in terms of the SbS-adapted mode sequence, in order to correctly demodulate the received symbols. However, in slow-fading pedestrian indoor channels in conjunction with a high transmission rate, the channel conditions do not change dramatically during a transmission burst. Hence a Burst-by-Burst (BbB) -rather than SbS- adaptive scheme can be employed, where the same modulation mode is used throughout one transmission burst. As a benefit, the mode signalling mechanism of the BbB adaptive scheme is simpler, than that of the SbS adaptive scheme, since the BbB adaptive scheme signals one modulation mode per burst, while the SbS adaptive scheme has to signal and/or predict a sequence of modulation modes per burst [141].

To elaborate a little further, the design issues of modulation mode signalling between the transmitter and receiver were discussed for example in the contributions of Lau *et al.* [141, 142], Otsuki *et al.* [143] and Torrance *et al.* [144]. Given the above range of AQAM mode signalling solutions in the literature, in this section we refrained from considering this issue and have assumed perfect modulation mode signalling. More specifically we employed a closed-loop controlled BbB adaptive scheme, where the receiver requests the highest-throughput modulation mode capable of maintaining the target-FER from the remote transmitter for the next transmission burst according to the expected channel conditions. The associated signalling delay will result in a slight performance degradation, since during this time the channel-quality will change. A range of long-term channel-quality prediction techniques were proposed by Duel-Hallen *et al.* in [99]. The impact of signalling delay will be investigated in Section 5.3.4. A range of other important design issues of adaptive CDMA can be found in [63, 141, 145–148].

5.3.1 Modem Mode Adaptation

Joint detection CDMA is suitable for combining with ACM, because the implementation of the joint detection algorithms does not require any knowledge of the modulation mode used. The system matrix required for joint detection is constructed by using only the Channel Impulse Response (CIR) estimates and the spreading sequences of all the users. Therefore, the joint detection receiver does

not have to be reconfigured, when the modulation mode is switched and its complexity is essentially independent of the modulation mode used.

In joint detection systems the Signal to Interference and Noise Ratio (SINR) of each user at the output of the MMSE-DFE can be calculated by using the channel estimates and the spreading sequences of all the users. By assuming that the transmitted data symbols and the noise samples are uncorrelated, the expression for calculating the SINR, γ_o, of the n-th symbol transmitted by the k-th user was given by Klein *et al.* [132] as:

$$\begin{aligned} \gamma_o(j) &= \frac{\text{Wanted Signal Power}}{\text{Res. MAI and ISI Power + Eff. Noise Power}} \\ &= g_j^2[\mathbf{D}]_{j,j}^2 - 1, \qquad \text{for} \quad j = n + N(k-1), \end{aligned} \tag{5.34}$$

where SINR is the ratio of the wanted signal power to the residual MAI and ISI power plus the effective noise power. The number of users in the system is K and each user transmits N symbols per transmission burst. The matrix $\mathbf{D}$ is a diagonal matrix that is obtained with the aid of the Cholesky decomposition [135] of the matrix used for linear MMSE equalisation of the CDMA system [132]. The notation $[\mathbf{D}]_{j,j}$ represents the elements in the j-th row and j-th column of the matrix $\mathbf{D}$ and the value g_j is the amplitude of the j-th symbol.

After the output SINR is calculated, the best-matching modulation mode maximising the throughput, while maintaining the required target BER or FER is chosen accordingly and communicated to the transmitter. Let us denote the choice of modulation modes by V_m, where the total number of modulation modes is $M_o = 4$ and $m = 1, 2, \ldots, M_o$. The modulation mode having the lowest number of constellation points is V_1 and the one associated with the highest is V_{M_o}. The rules used for switching the modulation modes are as follows:

$$\begin{aligned} \Gamma_o(k) \leq t_1 &\implies V_1 = 4QAM \\ t_1 < \Gamma_o(k) \leq t_2 &\implies V_2 = 8PSK \\ t_2 < \Gamma_o(k) \leq t_3 &\implies V_3 = 16QAM \\ t_3 \leq \Gamma_o(k) &\implies V_4 = 64QAM, \end{aligned}$$

where $\Gamma_o(k)$ is the SINR of the k-th user at the output of the MMSE-DFE, which was calculated by using Equation 5.34 and $\Gamma_o(k) = \frac{1}{N}\sum_{n=1}^{N}\gamma_o(j)$, $j = n + N(k-1)$. The values $(t_1, \cdots, t_{M_o-1})$ represent the switching thresholds used for activating the modulation modes, where we have $t_1 < t_2 < \cdots < t_{M_o-1}$.

The mode switching thresholds were adjusted for maintaining the target performance requirements, such as a fixed BER or FER. In 1996 Torrance *et al.* [149] proposed a set of mode switching levels $\mathbf{s}$ optimised for achieving the highest average BPS throughput while maintaining the target average BER. The method was based on defining a specific combined cost-function for transmission over narrowband Rayleigh fading channels, which incorporated both the BPS throughput as well as the target average BER of the system. Powell's optimisation was invoked for finding a set of mode switching thresholds, which were constant, regardless of the actual channel Signal to Noise Ratio (SNR) encountered, i.e. irrespective of the prevalent instantaneous channel conditions. However, in 2001 Choi *et al.* [150] have recognised that a higher BPS throughput can be achieved, if under high channel SNR conditions

the activation of high-throughput AQAM modes is further encouraged by lowering the switching thresholds. More explicitly, a set of SNR-dependent mode switching levels was proposed [150], which keeps the average BER constant, while maximising the achievable throughput. We note that, the set of switching levels derived in [98, 149] is based on Powell's multidimensional optimisation technique [151] and hence the optimisation process may become trapped in a local minimum. This problem was overcome by Choi *et al.* upon deriving an optimum set of switching levels [150], when employing the Lagrangian multiplier technique. It was shown that this set of switching levels results in the global optimum in a sense that the corresponding AQAM scheme obtains the maximum possible average BPS throughput, while maintaining the target average BER. A further approach was proposed by Lau *et al.* in [141], where an eight-mode adaptive modulation scheme was proposed for DS-CDMA using an adaptive M-ary orthogonal modulator. More specifically, a rate-1/9 channel code and a 2^9-ary orthogonal modulator were employed in Mode-0, while a rate-1/2 channel code and a 2^2-ary orthogonal modulator were employed in Mode-7. The adaptive mode thresholds in this scheme were chosen in 3 dB steps, where the overall performance was controlled by a single parameter, which was the threshold value of mode 1.

However, the optimum switching thresholds depend on the accuracy of the instantaneous channel estimation. Specifically, the accuracy of the channel estimation depends on the channel quality prediction method employed and also on the signalling delay incurred, where the longer the signalling delay the more 'outdated' the channel estimation. As mentioned above, efficient channel quality prediction techniques have been proposed by Duel-Hallen *et al.* in [99]. On the other hand, the effects of outdated channel estimation have been investigated in [91]. In this section we considered the practical scenario, where the channel estimation is outdated. In general, this deficiency could be caused by an inaccurate channel quality prediction or due to the associated signalling delay. More specifically, the modulation mode signalling in our system is delayed by one transmission frame duration and hence the channel estimation is outdated by $10ms$, which is the UTRA frame length, as shown in Table 5.3. The switching thresholds of the system studied here were set experimentally by finding the SINR values, where the constituent fixed-mode QAM schemes were capable of maintaining the required target FER, when communicating over the UTRA Rayleigh fading channel. On the other hand, the switching thresholds of the idealistic benchmark system used in conjunction with perfect channel estimation and zero signalling delay were set experimentally by finding the SINR values, where the constituent fixed-mode QAM schemes were capable of maintaining the required target FER, when communicating over the non-fading, non-dispersive Gaussian channel. In general, these two systems represent two extreme cases, where the former system provides the worst performance and the latter system the best possible performance.

5.3.2 Channel Model and System Parameters

Table 5.2 shows the modulation and channel parameters employed. The multipath channel model is characterised by its discretised chip-spaced UTRA vehicular channel A [152]. The corresponding CIR is shown in Figure 5.9, where each path is faded independently according to the Rayleigh distribution. The CM subsystems shown in Table 5.2 exhibit a similar complexity and their corresponding generator polynomials can be found from Tables 2.1, 2.2, 2.3 and 2.4. The transmission burst structure of the modified UTRA Burst 1 [148] using a spreading factor of eight is shown in Figure 5.10. The number

Parameter	Value
Carrier Frequency	1.9 GHz
Vehicular Speed	30 mph
Doppler frequency	85 Hz
System Baud rate	3.84 MBd
Normalised Doppler frequency	$85/(3.84\times10^6)=2.21\times10^{-5}$ Hz
Channel type	UMTS Vehicular Channel A
Number of paths in channel	6
Receiver type	JD-MMSE-DFE
No. of symbols per JD block	20
Data modulation	Adaptive Coded Modulation (4QAM, 8PSK, 16QAM, 64QAM)
CM subsystem	TCM (ν=6)
	BICM (ν=6)
	TTCM (ν=3, 4 iterations)
	BICM-ID (ν=3, 8 iterations)

Table 5.2: CM and channel parameters.

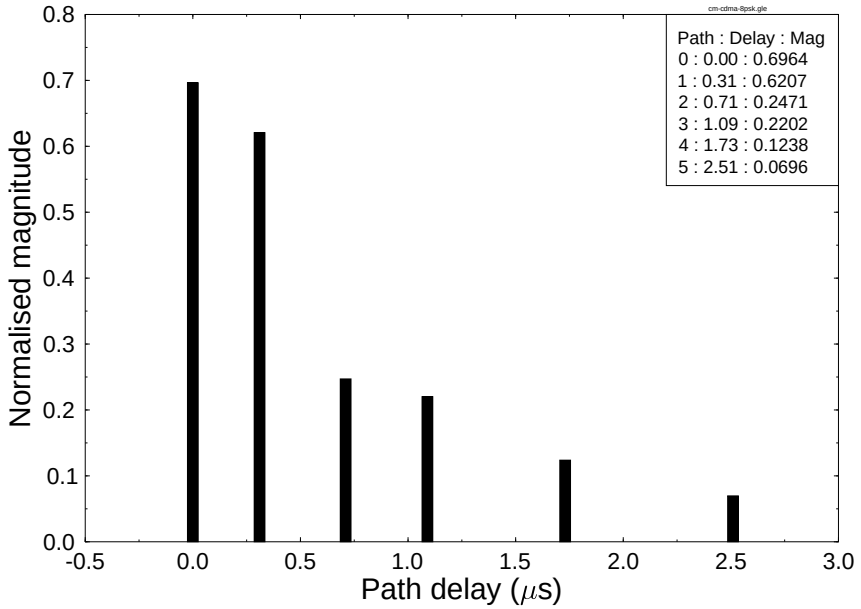

Figure 5.9: UTRA vehicular channel A [152].

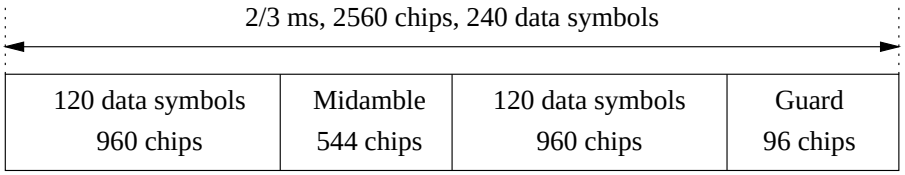

Figure 5.10: A modified UTRA Burst 1 [148] with a spreading factor of 8. The original UTRA burst has 244 data symbols.

Features	**Value**
Multiple access	CDMA, TDD
No. of Slots/Frame	15
Spreading factor	8
Frame length	10 ms
Slot length	2/3 ms
Data Symbols/Slot/User	240
No. of Slot/Group	1
User Data Symbol Rate (KBd)	240/10 = 24
System Data Symbol Rate (KBd)	24x15 = 360
Chips/Slot	2560
Chips/Frame	2560x15=38400
User Chip Rate (KBd)	2560/10 = 256
System Chip Rate (MBd)	38.4/10 = 3.84
System Bandwidth (MHz)	3.84 x 3/2 = 5.76
Eff. User Bandwidth (kHz)	5760/15 = 384

Table 5.3: Generic system features of the reconfigurable multi-mode transceiver, using the spread data burst 1 of UTRA proposal [148, 152] shown in Figure 5.10.

Features	Multi-rate System			
Mode	4QAM	8PSK	16QAM	64QAM
Transmission Symbols	240			
Bit/Symbol	2	3	4	6
Transmission bits	480	720	960	1440
Code Termination Symbols	6			
Data Symbols	234			
Coding Rate	1/2	2/3	3/4	5/6
Information Bit/Symbol	1	2	3	5
Information Bits	234	468	708	1170

Table 5.4: Operational-mode specific transceiver parameters for TTCM.

of data symbols per JD block is 20, hence the original 244-symbol long UTRA Burst 1 was slightly modified to host a burst of 240 data symbols, which is a multiple of 20. The remaining system parameters are shown in Table 5.3, where there are 15 time slots in one UTRA frame and we assign one slot for one group of CDMA users. More specifically, each group employed a similar system configuration but communicated with the base station employing different time slots.

In general, the total number of users supportable by the uplink CDMA system can be increased by using a higher spreading factor at the cost of a reduced throughput, since the system's chip rate was fixed at 3.84 Mcps as shown in Table 5.2. Another option for increasing the number of users supported is by assigning more uplink time slots for new groups of users. In our study, we investigate the proposed system using one time slot only. Hence the data symbol rate per slot per user is 24 KBd for a spreading factor of eight. Table 5.4 shows the operational-mode specific transceiver parameters for the TTCM-assisted ACM-JD-CDMA scheme. Specifically, the corresponding lowest bitrate is 23.4 Kbit/s in the 4QAM mode and the highest bitrate is 117 Kbit/s in the 64QAM mode.

5.3.3 Performance of the Fixed Modem Modes

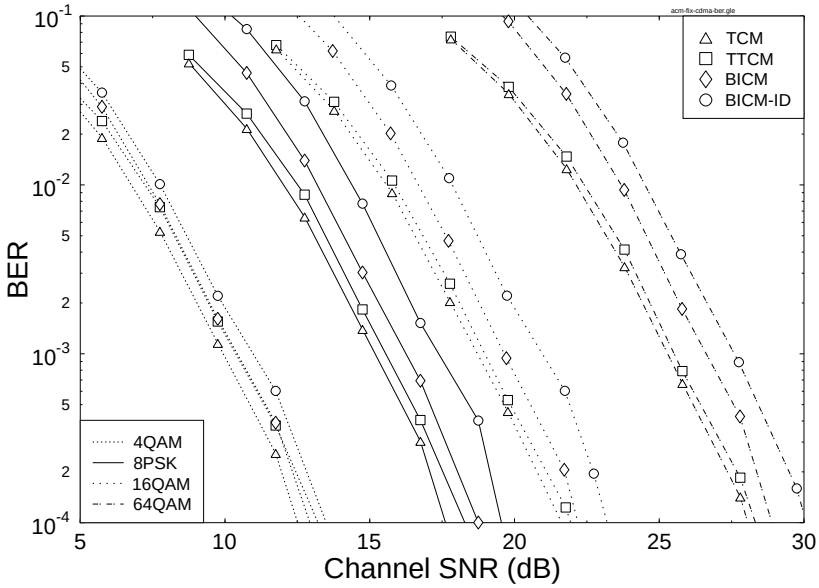

Figure 5.11: BER versus channel SNR performance of the four fixed modem modes, using the TCM, TTCM, BICM and BICM-ID coded modulation schemes, when supporting K=2 users. The simulation parameters are listed in Table 5.2 and the simulations were conducted over the six-path UTRA vehicular channel A of Figure 5.9.

Let us investigate the BER and FER performance of the various CM schemes using the fixed modulation modes of 4QAM, 8PSK, 16QAM and 64QAM in Figures 5.11 and 5.12, respectively. In terms of BER, TCM assisted JD-CDMA scheme exhibits the best performance followed by TTCM, BICM and BICM-ID. However, in terms of FER, the TTCM assisted JD-CDMA scheme exhibits the best performance followed by TCM, BICM-ID and BICM. More specifically, TTCM exploits the time-diversity imposed by the turbo interleaver. However, a turbo interleaver length of 240 symbols is insufficient for TTCM to attain its optimum BER performance when communicating over slow Rayleigh fading channels due to the limited time-diversity experienced. On the other hand, TTCM is

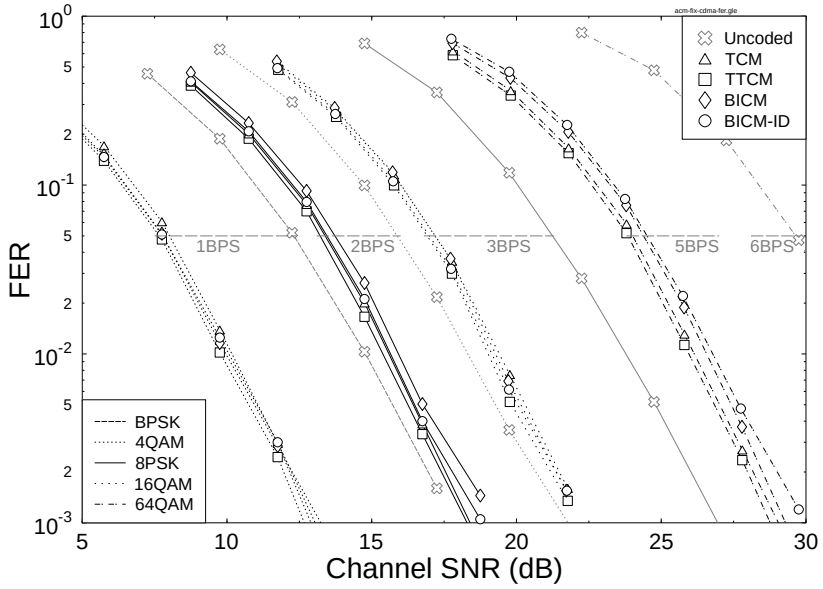

Figure 5.12: FER versus channel SNR performance of the four fixed modem modes, using the TCM, TTCM, BICM and BICM-ID coded modulation schemes, when supporting K=2 users. The simulation parameters are listed in Table 5.2 and the simulations were conducted when communicating over the six-path UTRA vehicular channel A of Figure 5.9.

a powerful scheme employing iterative turbo decoding, which is capable of correcting all the bit errors in moderately corrupted frames, but which increases the BER in the severely corrupted frames due to the error precipitation effects encountered in the iterative turbo decoding process. Hence the BER of TTCM is far from its optimum, when the time-diversity of the system is limited. By contrast, its FER is always better, than that of the other CM schemes at the same decoding complexity. BICM-ID is another scheme employing iterative decoding. However, it was found in [18, 20] that BICM-ID typically requires a higher order of time-diversity, and hence a longer channel interleaver, than the TTCM scheme in order to achieve its optimum performance. Therefore, its BER becomes the worst, while its FER is better than that of BICM in our system. As for the non-iterative TCM and BICM schemes, TCM performs better than BICM in the slow Rayleigh fading channels studied.

Figure 5.12 also illustrates the FER performance of the uncoded fixed modulation modes of BPSK, 4QAM, 8PSK and 64QAM having a throughput of 1, 2, 3 and 6 BPS, respectively. For a throughput of 1 information BPS at 5% FER, TTCM-4QAM is about 5 dB more power efficient, than the uncoded BPSK scheme while requiring the same bandwidth, as shown in Figure 5.12. Similarly, the coding gain of TTCM at throughputs of 2 and 3 BPS is about 3 dB and 4 dB respectively, at the same bandwidth requirement, while maintaining a FER of 5%. It is clear that the employment of CM schemes allow us to mitigate the effects of transmission errors effectively without any bandwidth expansion.

Based on these fixed-mode performance trends, we set the switching thresholds for our system experimentally by finding the corresponding average SINR values, where the constituent fixed-mode QAM schemes were capable of maintaining the required target FER, when communicating over the UTRA Rayleigh fading channels. More specifically, the thresholds required for maintaining a given target FER can be obtained by plotting the FER versus SINR curves for the constituent fixed-mode QAM schemes, when communicating over the UTRA Rayleigh fading channel, where the intersections

of the curves with a horizontal line at a specific target FER are the switching thresholds. The switching thresholds of the system benefiting from perfect channel estimation and a zero signalling delay were obtained by plotting the FER versus SINR curves for the constituent fixed-mode QAM schemes when communicating over non-fading, non-dispersive Gaussian channels.

5.3.4 Adaptive Modes Performance

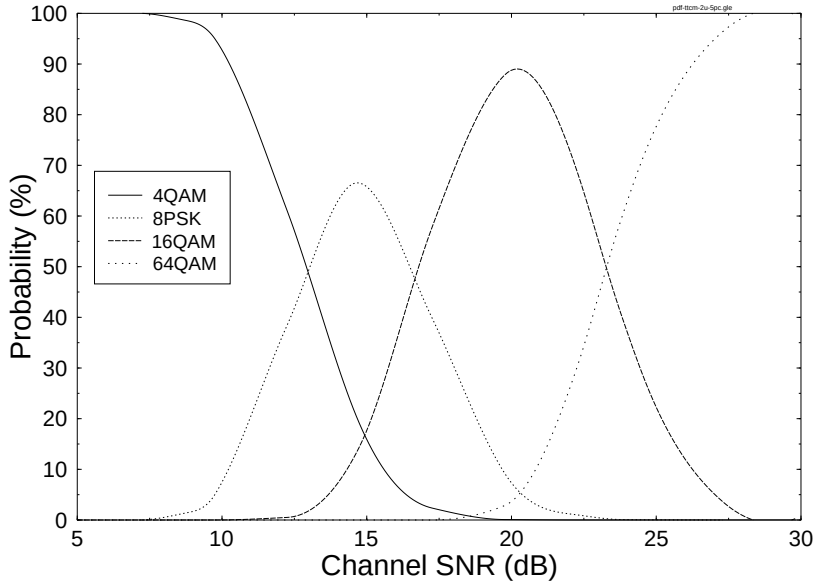

Figure 5.13: The probability of each modulation mode being chosen versus channel SNR for transmission in the TTCM-assisted ACM-JD-CDMA system when maintaining a target FER of 5% supporting K=2 users. The simulation parameters are listed in Table 5.2 and the simulations were conducted when communicating over the six-path UTRA vehicular channel A of Figure 5.9.

In this section, we will investigate the performance of the TTCM-assisted ACM-JD-CDMA scheme, when communicating over the UTRA Rayleigh fading channels. For maintaining a target FER of 5% in conjunction with a mode signalling delay of $10ms$, the probability of each modulation mode being chosen versus the channel SNR for transmission in the TTCM-assisted ACM-JD-CDMA system is illustrated in Figure 5.13. As we can observe from the figure, at low values of the channel SNR, the 4QAM mode was chosen with the highest probability, thus predominantly having a throughput of 1 information BPS. However, as the channel quality improved the channel SNR increased, thus allowing the 8PSK, 16QAM and eventually 64QAM modes to be activated more often, which resulted in an increased average BPS performance.

The FER and BPS performance of the TTCM-assisted ACM-JD-CDMA scheme designed for a target FER of 5% and for supporting $K = 2$ and 4 users is shown in Figure 5.14. The FER was below the target FER of 5% and the BPS throughput improved, as the channel SNR increased. Since we employed switching thresholds which are constant over the SNR range, in the region of SNR=10 dB the FER followed the trend of 4QAM. Similarly, for SNRs between 17 and 20 dB FER trend of 16QAM was predominantly obeyed. In both of these SNR regions a significantly lower FER was achieved than the target FER. We note, however that it is possible to increase the FER to the value of the target FER, at these SNR regions for the sake of obtaining extra BPS gains by employing a set of switching

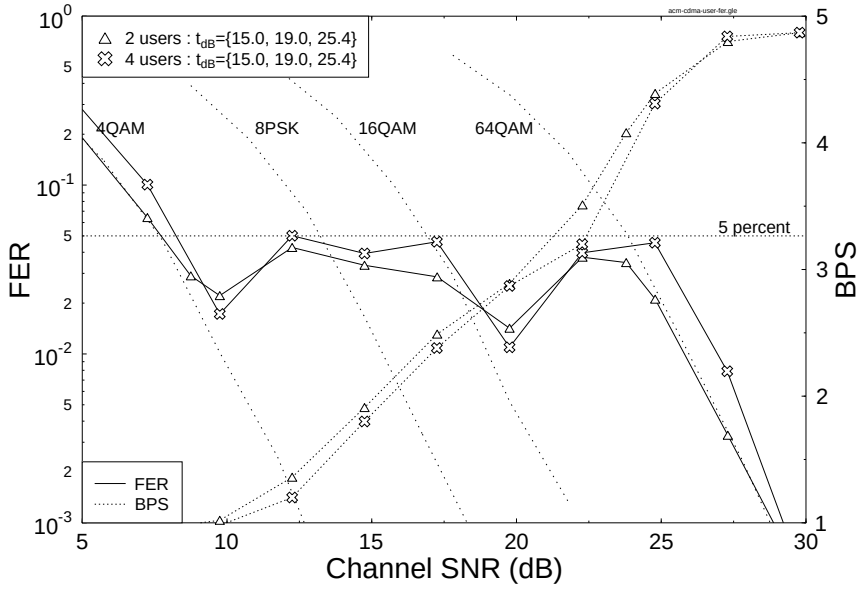

Figure 5.14: The average FER and BPS performance versus channel SNR of the TTCM-assisted ACM-JD-CDMA system supporting $\mathsf{K} = 2$ and 4 users. The same set of switching thresholds t_{dB} was employed as shown in the legend. The FER curves for the same system but using fixed modulation modes of 4QAM, 8PSK, 16QAM and 64QAM for $\mathsf{K} = 2$ users are also shown. The simulation parameters are listed in Table 5.2 and the simulations were conducted when communicating over the six-path UTRA vehicular channel A of Figure 5.9.

thresholds, where the thresholds are varied as a function of the SNR [150], but this was set aside for further research.

From Figure 5.14 we also notice that the performance difference between the $\mathsf{K} = 2$ and 4 scenario is only marginal with the advent of the powerful JD-MMSE-DFE scheme. Specifically, there was only about one dB SNR penalty, when the number of users increased from two to four for the 4QAM and 64QAM modes at both low and high SNRs, respectively. The FER of the system supporting $\mathsf{K} = 4$ users was still below the target FER, when the switching thresholds derived for $\mathsf{K} = 2$ users were employed. In general, the SNR penalty is less than one dB, when the number of users supported is increased from $\mathsf{K} = 2$ to 4 users. Note that the delay spread of the chip-spaced UTRA vehicular channel A in Figure 5.9 is 2.51 μs corresponding to $2.51 \times 3.84 \approx 10$ chip duration for the 3.84 MBd Baud rate of our system, as seen in Table 5.2. Hence the delay spread is longer than the spreading code length ($Q = 8$ chips) used in our system and therefore the resultant ISI in the system is significantly higher, than that of the system employing a higher spreading factor, such as $Q > 10$ chips. These findings illustrated the efficiency of the JD-MMSE-DFE scheme in combating the high ISI and MAI of the system. More importantly, the employment of the JD-MMSE-DFE scheme in our system generalised our results recorded for the $\mathsf{K} = 2$ users scenario to that of a higher number of users, since the performance penalty associated with supporting more users was found marginal.

5.3.5 Effects of Estimation Delay and Switching Thresholds

Let us now investigate the effect of mode signalling delay on the performance of the TTCM-assisted ACM-JD-CDMA scheme in Figure 5.15. The performance of the ideal scheme, where the channel

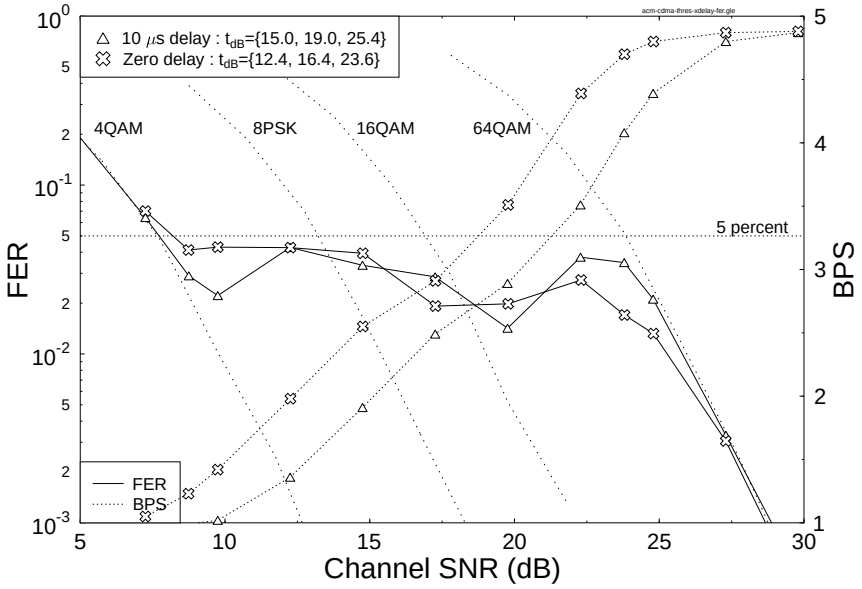

Figure 5.15: The average FER and BPS performance versus channel SNR of the TTCM-assisted ACM-JD-CDMA system supporting $\mathsf{K} = 2$ users. Two different sets of switching thresholds t_{dB} were employed as shown in the legend for systems having zero and $10\mu s$ mode signalling delay. The FER curves for the same system but using fixed modulation modes of 4QAM, 8PSK, 16QAM and 64QAM for $\mathsf{K} = 2$ users are also shown. The simulation parameters are listed in Table 5.2 and the simulations were conducted when communicating over the six-path UTRA vehicular channel A of Figure 5.9.

quality estimation is perfect without any signalling delay is compared to that of the more practical scheme, where the channel quality estimation is imperfect and outdated by the delay of one frame duration of $10\mu s$. For a target FER of 5%, the ideal scheme exhibited a higher BPS throughput than the practical scheme. More specifically, at a target FER of 5%, about 2.5 dB SNR gain is achieved by the ideal scheme in the SNR region spanning from 8 dB to 27 dB. A channel quality signalling delay of one frame duration certainly represents the worst case scenario. In general, the shorter the signalling delay the better the performance of the adaptive system. Hence the performance of the zero-delay and one-frame delay schemes represent the lower-bound and upper-bound performance, respectively, for practical adaptive systems.

Let us now investigate the performance of the practical one-frame delay TTCM-assisted ACM-JD-CDMA system using three switching threshold sets designed for maintaining target FER of 10%, 5% and 1% in Figure 5.16. As the values of the switching thresholds increases, the FER and/or the BPS throughput of the system reduces. The FER performance trends observed in Figure 5.14 also appear in Figure 5.16 for the various switching threshold sets. More explicitly, the FER curves seen in Figure 5.16 exhibit undulations, where the ACM-JD-CDMA FER curves tend to follow those of the predominant fixed modes at a given channel SNR, before gradually switching to the higher throughput modem mode. This is a consequence of the employment of SNR-independent switching thresholds in the one-frame mode signalling delay system. These three schemes illustrate the associated tradeoffs between the achievable BPS and FER performance of the system. Specifically, systems that are capable of tolerating a higher FER exhibit the benefit of a higher BPS throughput.

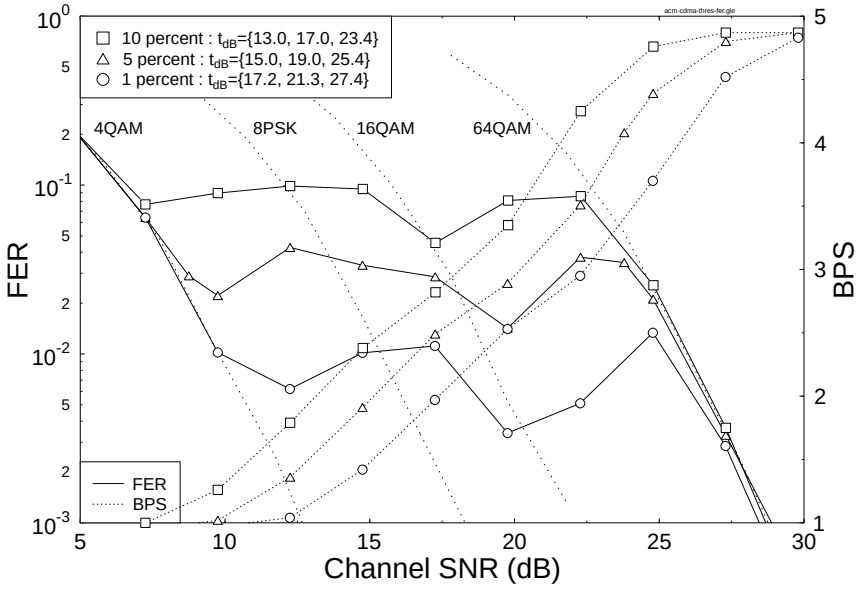

Figure 5.16: The average FER and BPS performance versus channel SNR of the TTCM-assisted ACM-JD-CDMA system supporting $\mathsf{K} = 2$ users. Three different sets of switching thresholds t_{dB} were employed as shown in the legend for maintaining target FERs of 10%, 5% and 1%. The FER curves for the same system but using fixed modulation modes of 4QAM, 8PSK, 16QAM and 64QAM for $\mathsf{K} = 2$ users are also shown. The simulation parameters are listed in Table 5.2 and the simulations were conducted when communicating over the six-path UTRA vehicular channel A of Figure 5.9.

5.3.6 Conclusions

In this section, TTCM-assisted burst-by-burst adaptive coded modulation aided joint detection based CDMA has been studied, when communicating over the UTRA wideband vehicular Rayleigh fading channel. The adaptive transceiver is capable of operating in four different CM modes, namely using 4QAM, 8PSK, 16QAM and 64QAM. Various CM schemes were used in our experiments. It was shown in Figure 5.12 that the CM schemes exhibited significant SNR gains over a wide range of BPS throughputs, while the JD-MMSE-DFE was shown to be robust against both the MAI and ISI in Figure 5.14.

The advantage of the adaptive coded modulation scheme is that when invoking higher-order modulation modes in case of encountering a higher instantaneous channel quality, the coding rate approaches unity. For example, the coding rate of 4QAM was 1/2, while that of 64QAM was 5/6. As a result, this near-unity coding rate allows the system to maintain a high effective throughput, while maintaining the required transmission integrity. More explicitly, the proposed scheme guaranteed the same performance, as the lowest- and highest-order fixed-mode modulation schemes in the low and high channel SNR range, respectively. As an added benefit, between these extreme SNRs the effective bitrate increased smoothly, as the channel SNR increased, whilst maintaining a near-constant FER. In this study, the lower and upper performance bounds of the TTCM-assisted ACM-JD-CDMA scheme have been provided in Figure 5.15 and the tradeoff between the achievable BPS and FER performance has been studied in Figure 5.16 by employing different mode switching threshold sets.

The proposed TTCM-assisted ACM-JD-CDMA scheme constitutes a promising practical com-

munication system guaranteeing reliable transmission providing an effective bitrate ranging from 23.4 Kbit/s/slot to 117 Kbit/s/slot.

Next, we will proceed to study the performance of the CM assisted CDMA system using the GA Based MUD.

5.4 CM Assisted GA Based CDMA

In this section we propose a novel M-ary Coded Modulation assisted Genetic Algorithm based Multiuser Detection (CM-GA-MUD) scheme for synchronous CDMA systems. The performance of the proposed scheme was investigated using QPSK, 8PSK and 16QAM when communicating over AWGN and narrowband Rayleigh fading channels. When compared with the optimum MUD scheme, the GA-MUD subsystem is capable of reducing the computational complexity significantly. On the other hand, the CM subsystem is capable of obtaining considerable coding gains despite being fed with sub-optimal information provided by the GA-MUD output.

5.4.1 Introduction

The optimal CDMA MUD [131, 153] based on the Maximum-Likelihood (ML) detection rule performs an exhaustive search of all the possible combinations of the users' transmitted bit or symbol sequences and then selects the most likely combination as the detected bit or symbol sequence. Since an exhaustive search is conducted, the computational complexity of the detector increases exponentially with the number of users as well as with the number of levels in the modulation scheme employed. Since a CDMA system is required to support a large number of users, the optimum ML multiuser detector is impractical to implement due to its excessive complexity. This complexity constraint led to numerous so-called suboptimal multiuser detection [154] proposals.

GAs have been used for efficiently solving combinatorial optimisation problems in many applications [127]. Recently, GA assisted MUD has been studied using BPSK modulation in the context of a CDMA system [128–130]. In an afford to increase the system's performance with the aid of channel coding, but without increasing the required bandwidth, in this section we will investigate the performance of the CM assisted Genetic Algorithm Based Multiuser Detection (CM-GA-MUD) using M-ary modulation modes.

5.4.2 System Overview

In our study, each user invokes a CM encoder, which provides a block of N modulated symbols before spreading. We consider a synchronous CDMA uplink as illustrated in Figure 5.17, where K users simultaneously transmit data packets of equal length using M-ary modulation to a single receiver. The transmitted signal of the kth user can be expressed in an equivalent lowpass representation as :

$$\tilde{s}_k(t) = \sum_{n=0}^{N-1} b_k^n a_k(t - nT_b), \quad \forall k = 1, \ldots, \mathsf{K} \tag{5.35}$$

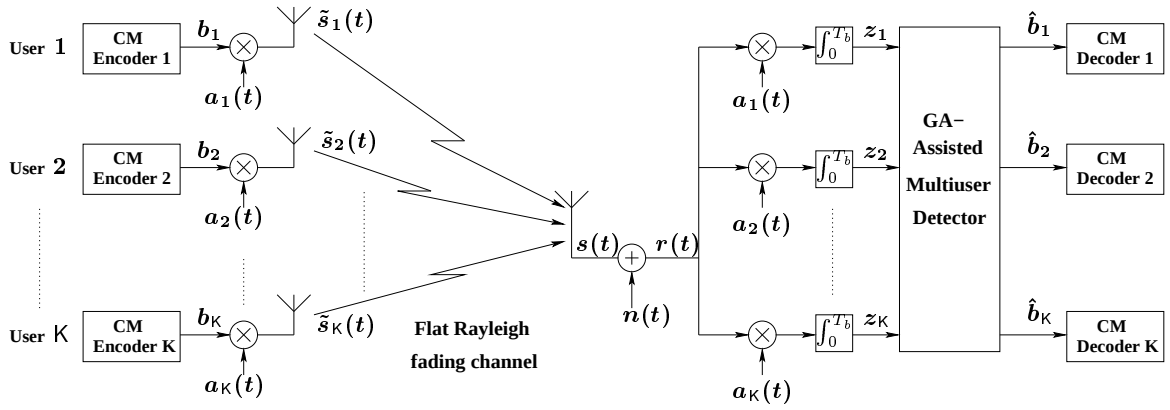

Figure 5.17: Block diagram of the K-user synchronous CDMA uplink model in a flat Rayleigh fading channel.

where $a_k(t)$ is the kth user's signature sequence, T_b is the data symbol duration, N is the number of data symbols transmitted in a packet and $b_k^n = \sqrt{\xi_k^n} e^{j\theta_k^n}$ represents the n^{th} coded-modulated M-ary symbol of the kth user, where ξ_k^n and θ_k^n are the kth user's signal energy and phase of the n^{th} transmitted symbol, respectively. More explicitly, b_k^n denotes a complex CM-coded symbol in the range of $0, 1, \ldots, \mathsf{M}-1$, where M is the number of possible constellation points in the M-ary modulation, which is equals to 4, 8 and 16 for QPSK, 8PSK and 16QAM. The superscript n can be omitted, since no dispersion-induced interference is inflicted by symbols outside a single symbol duration T_b in narrowband channel.

Each user's signal $\tilde{s}_k(t)$ is assumed to propagate over a narrowband slowly Rayleigh fading channel, as shown in Figure 5.17 and the fading envelope of each path is statistically independent for all users. The complex lowpass CIR for the link between the kth user's transmitter and the base station's receiver, as shown in Figure 5.17, can be written as :

$$h_k(t) = \alpha_k(t) e^{j\phi_k(t)} \delta(t), \quad \forall k = 1, \ldots, \mathsf{K} \tag{5.36}$$

where the amplitude $\alpha_k(t)$ is a Rayleigh distributed random variable and the phase $\phi_k(t)$ is uniformly distributed between $[0, 2\pi)$.

Hence, when the kth user's spread spectrum signal $\tilde{s}_k(t)$ given by Equation 5.35 propagates through a Rayleigh fading channel having an impulse response given by Equation 5.36, the resulting output signal $s_k(t)$ over a single symbol duration can be written as :

$$s_k(t) = \alpha_k b_k a_k(t) e^{j\phi_k}, \quad \forall k = 1, \ldots, \mathsf{K} \tag{5.37}$$

Upon combining Equation 5.37 for all K users, the received signal at the receiver, which is denoted by $r(t)$ in Figure 5.17, can be written as :

$$r(t) = s(t) + n(t), \tag{5.38}$$

where $s(t) = \sum_{k=1}^{\mathsf{K}} s_k(t)$ is the sum of the resultant output signals of all users and $n(t)$ is the zero-mean AWGN having independent real and imaginary components, each having a double-sided power spectral density of $\sigma^2 = N_0/2$.

The joint optimum decision rule for the M-ary modulated K-user CDMA system based on the synchronous system model can be derived from that of the BPSK-modulated system [131], which is

expressed in vectorial notation as:

$$\Omega\left(\boldsymbol{b}\right) = 2\Re\left[\boldsymbol{b}^H \boldsymbol{C}^* \boldsymbol{Z}\right] - \boldsymbol{b}^H \boldsymbol{C}^* \boldsymbol{R} \boldsymbol{C} \boldsymbol{b}, \tag{5.39}$$

where

$$\begin{aligned} \boldsymbol{C} &= \text{diag}\left[\alpha_1 e^{j\phi_1}, \ldots, \alpha_K e^{j\phi_K}\right] \\ \boldsymbol{b} &= \left[b_1, \ldots, b_K\right]^T, \\ \boldsymbol{Z} &= \textit{ouput vector of the matched filters.} \end{aligned}$$

More specifically, $(.)^H$ is the complex conjugate transpose of the matrix (.) and $(.)^*$ is the complex conjugate of the matrix (.). For BPSK modulation the term $\boldsymbol{b}^H$ in Equation 5.39 is substituted by $\boldsymbol{b}^T$, which is the transpose of the matrix $\boldsymbol{b}$, since only the real component is considered in the context of BPSK modulation.

The decision rule for the optimum CDMA multiuser detection scheme based on the maximum likelihood criterion is to choose the specific symbol combination $\boldsymbol{b}$, which maximises the correlation metric of Equation 5.39, yielding:

$$\hat{\boldsymbol{b}} = \arg\left\{\max_{\boldsymbol{b}}\left[\Omega\left(\boldsymbol{b}\right)\right]\right\}. \tag{5.40}$$

Here, the optimum decision vector $\hat{\boldsymbol{b}}$ represents the *hard decision* values for a specific K-symbol combination of the K users during a symbol period. Based on the *hard decision* vector component $\hat{b}_k$ of vector $\hat{\boldsymbol{b}}$, we derived the log-likelihood channel metrics for the kth user's CM decoder for all the M possible M-ary modulated symbols as:

$$P_{k,m}(\hat{b_k}|b_{k,m}) = -\frac{|\hat{b_k} - b_{k,m}|^2}{2\sigma^2}, \tag{5.41}$$

where $b_{k,m}$ is the m^{th} phasor of user k in the constellation space and $m \in \{0, \ldots, \mathsf{M}-1\}$. Note that it is possible to obtain the *soft decision* metrics for the optimum-MUD, although its employment imposes a higher complexity. Specifically, given $r(t)$ and all possible $\Omega\left(\boldsymbol{b}\right)$ values, we derived the *soft decision* metrics as:

$$\begin{aligned} P_{k,m}(r(t)|b_{k,m}) &= ln\left\{\sum_{if\ b_{k,m}=b_k}^{all\ possible\ \boldsymbol{b}} exp\left(-\frac{1}{2\sigma^2}\int_0^{T_b}|r(t)-s(t)|^2\,dt\right)\right\} \\ &= ln\left\{\sum_{if\ b_{k,m}=b_k}^{all\ possible\ \boldsymbol{b}} exp\left(-\frac{1}{2\sigma^2}\int_0^{T_b}|r(t)|^2\,dt - \Omega\left(\boldsymbol{b}\right)\right)\right\}. \end{aligned} \tag{5.42}$$

The maximisation of Equation 5.39 is a combinatorial optimisation problem. Specifically, Equation 5.39 has to be evaluated for each of the M^K possible combinations of the M-ary modulated symbols for the K users, in order to find the vector $\boldsymbol{b}$ that maximises the correlation metric of Equation 5.39. Explicitly, since there are M^K different possible vectors $\boldsymbol{b}$, the optimum multiuser detection has a complexity that increases exponentially with the number of users K and the modulation mode employed M.

In this section, we aim at reducing the complexity of the optimum MUD, which performs M^K full search, by employing the sub-optimum GA-based MUD, which performs only a partial search. Hence,

the sub-optimum decision vector $\hat{\mathrm{b}}$ output by the GA-MUD is input to the CM decoder for generating the final estimate of the information. Note that the *hard decision* metric of Equation 5.41 is based on using only the optimum correlation metric of $\Omega(\boldsymbol{b})$, which is operated by the low-complexity GA-MUD. However, the *soft decision* metric of Equation 5.42 is based on evaluating all possible correlation metrics $\Omega(\boldsymbol{b})$ according to Equation 5.39, which requires a full search. Hence, the proposed reduced-complexity CM-GA-MUD scheme employed the lower-complexity *hard decision* metric.

5.4.3 The GA-assisted Multiuser Detector Subsystem

For a detailed description of the GA-MUD, the interested readers are referred to the literature [14, 128]. A brief description of the GA-MUD is given below.

The flowchart depicting the structure of the genetic algorithm adopted for our GA-assisted multiuser detection technique is shown in Figure 5.18. Firstly, an initial population consisting of P number of so-called *individuals* is created, where P is known as the population size. Each individual represents a legitimate K-dimensional vector of M-ary modulated symbols constituting the solution of the given optimisation problem. In other words, an individual can be considered as a K-dimensional vector consisting of the M-ary modulated symbol's decision variables to be optimised.

In order to aid our GA-assisted search at the beginning, we employed the hard decisions offered by the matched filter outputs $\boldsymbol{Z}$ which were denoted as:

$$\hat{\boldsymbol{b}}_{MF} = \left[\hat{b}_{1,MF}, \hat{b}_{2,MF}, \ldots, \hat{b}_{\mathsf{K},MF}\right], \tag{5.43}$$

where $\hat{b}_{l,MF}$ for $l = 1, \ldots, \mathsf{K}$ is given by:

$$\hat{b}_{l,MF} = arg\left\{\min_{b}\left|z_l - \alpha_l e^{j\phi_l} b\right|\right\}. \tag{5.44}$$

In Equation 5.44 a multiplication by $\alpha_l e^{j\phi_l}$ is necessary for coherent detection, because the phase rotation introduced by the channel has to be taken into account. A different randomly 'mutated' version [128, 155] of the hard decision vector $\hat{\boldsymbol{b}}_{MF}$ of Equation 5.43 was assigned to each of the individuals in the initial population, where the same probability of mutation, namely p_m was adopted for all individuals. Note that we cannot assign the same hard decision vector $\hat{\boldsymbol{b}}_{MF}$ to all the individuals, since the process of incest prevention [156] is invoked, which will not allow identical individuals to mate.

The so-called fitness value [127] associated with each individual in the population is evaluated by substituting the candidate solution represented by the individual under consideration into the objective function, as indicated by the 'Evaluation' block of Figure 5.18. Individuals having the T number of highest fitness values are then placed in a so-called *mating pool* [127, 128] where $2 \leq \mathsf{T} \leq \mathsf{P}$. Using a kind of natural selection scheme [127] together with the genetically-inspired operators of *crossover* [155] and *mutation* [155], the individuals in the mating pool are then evolved to a new population. Our objective function, or synonymously, fitness value is defined by the correlation metric of Equation 5.39. Here, the legitimate solutions are the M^{K} possible combinations of the K-symbol vector $\boldsymbol{b}$, where there are $log_2(\mathsf{M})$ bits in each of the M-ary symbols. Hence, each individual will take the form of a K-symbol vector corresponding to the K users' M-ary symbols during a single symbol

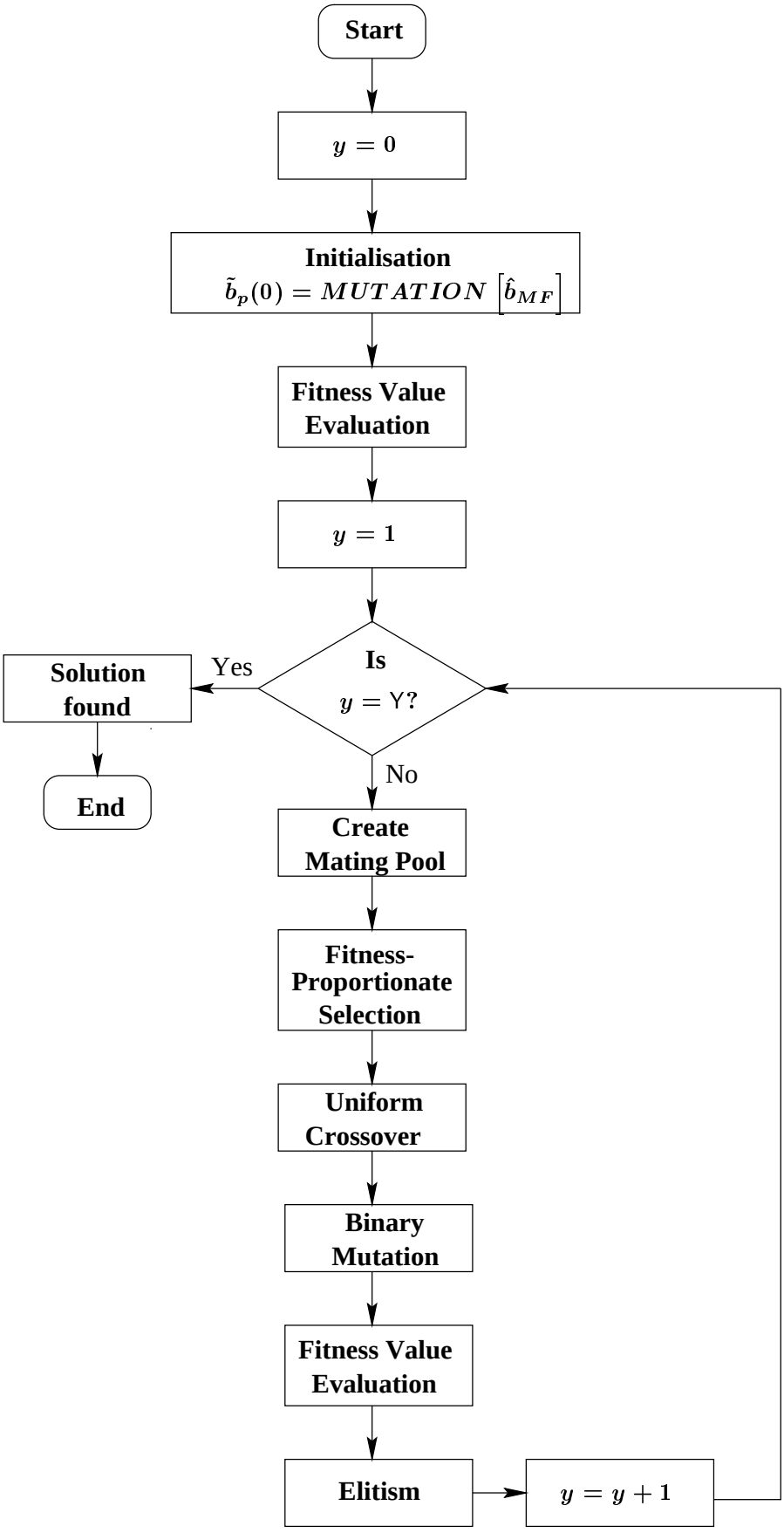

Figure 5.18: A flowchart depicting the structure of the genetic algorithm adopted for our GA-assisted multiuser detection technique.

interval. We will denote the p^{th} individual here as $\tilde{\boldsymbol{b}}_p(y) = \left[\tilde{b}_{p,1}(y), \ldots, \tilde{b}_{p,\mathsf{K}}(y)\right]$, where y denotes the y^{th} generation. Our goal is to find the specific individual that corresponds to the highest fitness value in the sense of Equation 5.39. In order to ensure that the fitness values are positive for all combinations of $\boldsymbol{b}$ for the so-called *fitness-proportionate* selection scheme [127], we modify the correlation metric of Equation 5.39 according to [157]:

$$\exp\left\{\Omega\left(\boldsymbol{b}\right)\right\} = \exp\left\{2\Re\left[\boldsymbol{b}^H \boldsymbol{C}^* \boldsymbol{Z}\right] - \boldsymbol{b}^H \boldsymbol{C}^* \boldsymbol{R} \boldsymbol{C} \boldsymbol{b}\right\}. \tag{5.45}$$

The associated probability of fitness-proportionate selection p_i of the ith individual is defined as [127]:

$$p_i = \frac{f_i}{\sum_j^T f_j}, \tag{5.46}$$

where f_i is the fitness value associated with the ith individual. Once a pair of parents is selected, the *uniform crossover* [128, 155, 158] and *binary mutation* [155] operations are then applied to this pair of parents.

The *crossover* [155] operation is a process in which arbitrary decision variables are exchanged between a pair of selected parents, 'mimicking the biological recombination process between two single-chromosome organisms'. Hence, the crossover operation creates two new individuals, known as *offspring* in GA parlance [127], which have a high probability of having better fitness values than their parents. In order to generate P number of new offspring, $\mathsf{P}/2$ number of crossover operations are required. A new pair of parents is selected from the mating pool for each crossover operation. The newly created offspring will form the basis of the new population. In a *uniform crossover* operation [158], a so-called *crossover mask* is invoked. The crossover mask is a vector consisting of randomly generated 1s and 0s of equal probability, having a length equal to that of the individuals. Bits or M-ary symbols are exchanged between the selected pair of parents at locations corresponding to a 1 in the crossover mask. While it was shown in [159] that the uniform crossover operation has a higher probability of destroying a schema, it is also capable of creating new schemata.

During the *mutation* operation [155], each decision variable in the offspring is perturbed, i.e. corrupted, with a probability of p_m, by either a predetermined or a random value. This allows new areas in the search space to be explored. The mutation probability of a decision variable is usually low, in the region of 0.1-0.01 [127]. This value is often reduced throughout the search, when the optimisation is likely to approach the final solution. In a *binary mutation* operation [155], there are only two possible values for each binary decision variable hosted by an individual. Hence, when mutation is invoked for a particular bit, the value of the bit is toggled to the other possible value. For example, a bit of logical '1' is changed to a logical '0' and vice versa.

In order to ensure that high-merit individuals are not lost from one generation to the next, the best or a few of the best individuals are copied into the forthcoming generation, replacing the worst offspring of the new population. This technique is known as *elitism* [155]. In our application, we will terminate the GA-assisted search at the Y^{th} generation and the individual associated with the highest fitness value at this point will be the detected solution.

Setup/Parameter	Method/Value
Individual initialisation method	Mutation of $\hat{\boldsymbol{b}}_{MF}$ of Equation 5.43
Selection method	Fitness-proportionate
Crossover operation	Uniform crossover
Mutation operation	Standard binary mutation
Elitism	Yes
Incest Prevention	Yes
Population size, P	$\mathsf{K} \cdot \mathsf{M}$
Mating pool size, T	$\mathsf{T} \leq \mathsf{P}$ depends on the no. of non-identical individuals
Probability of mutation, p_m	0.1
Termination generation, Y	$\frac{1}{2}\mathsf{K} \cdot \mathsf{M}$

Table 5.5: The configuration of the GA employed in our system, where K is the number of CDMA users and M is the number of modulation levels.

5.4.4 Simulation Parameters

The configuration of the GA employed in our system is shown in Table 5.5. Soft decision trellis decoding utilising the Log-MAP algorithm [53] was invoked for channel decoding. The similar complexity CM schemes utilised are: TCM using a code memory of six, BICM using a code memory of six, TTCM using a code memory of three in conjunction with four decoding iterations and finally, BICM-ID using a code memory of four employing four decoding iterations. Their corresponding code generator polynomials can be found from Tables 2.1, 2.2, 2.3 and 2.4.

5.4.5 Simulation Results And Discussions

Our performance metric is the average BER evaluated over the course of several GA generations. The detection time of the GA is governed by the number of generations Y required, in order to obtain a reliable decision. The computational complexity of the GA, quantified in the context of the total number of objective function evaluations, is related to $\mathsf{P} \times \mathsf{Y}$. Since our GA-assisted multiuser detector is based on optimising the modified correlation metric of Equation 5.45, the computational complexity is deemed to be acceptable, if there is a significant amount of reduction in comparison to the optimum multiuser detector, which requires M^{K} objective function evaluations, in order to reach the optimum decision.

The BER versus E_b/N_0, performance of the QPSK-based CM-GA-MUD schemes is shown in Figures 5.19 and 5.20 for transmissions over AWGN channel and uncorrelated Rayleigh fading channel, respectively. The simulation parameters were summarised in Table 5.5. A 'codeword length' of 1000 symbols and a spreading factor of 31 chips were employed. As determined by the 'codeword length', the turbo interleaver of TTCM and the internal bit interleavers of BICM and BICM-ID had a memory of 1000 symbol duration. The employment of an uncorrelated Rayleigh fading channel implies ideal channel interleaving, which has an infinitely long interleaver depth.

It is widely recognised that a QPSK signal consists of two orthogonal BPSK signals in a single-user

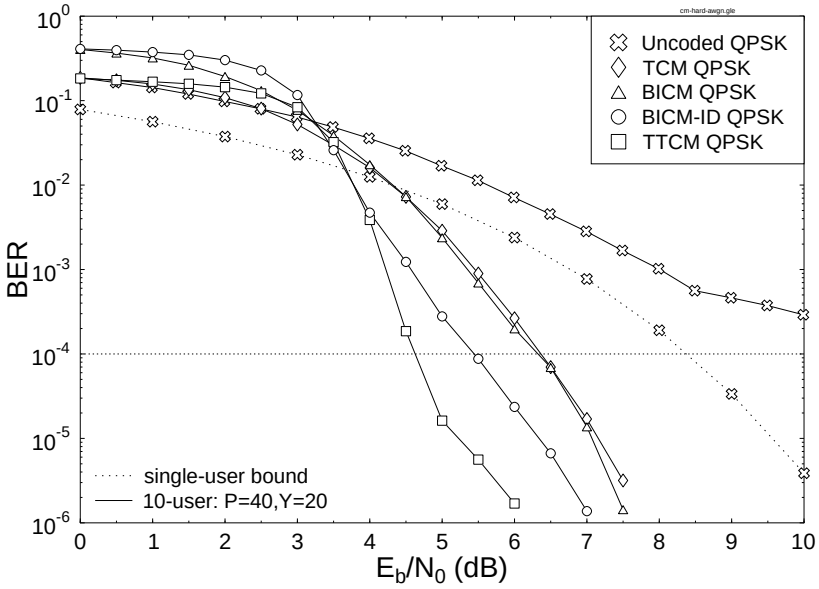

Figure 5.19: BER versus E_b/N_0 performance of the various CM-GA-MUD schemes for transmissions over the AWGN channel employing QPSK and utilising the simulation parameters of Table 5.5. A codeword length of 1000 symbols and a spreading factor of 31 chips were employed.

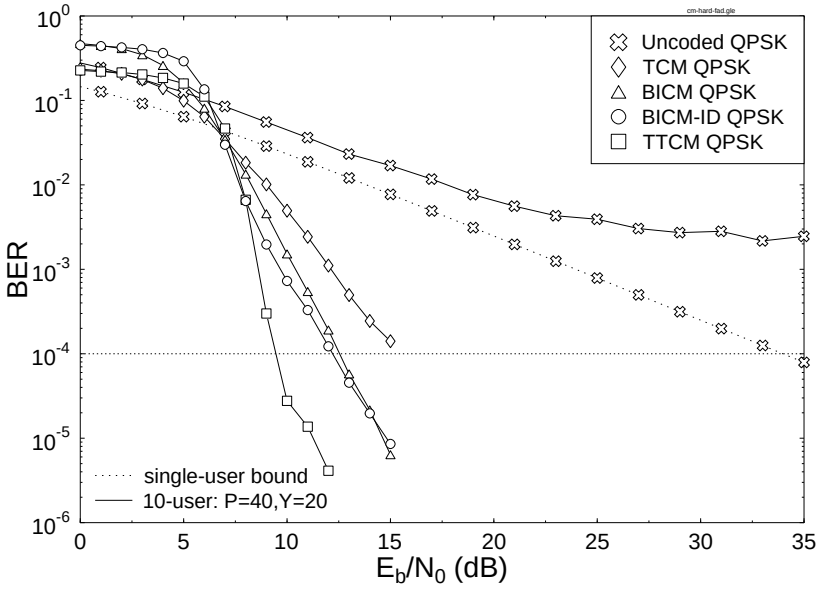

Figure 5.20: BER versus E_b/N_0 performance of the various CM-GA-MUD schemes for transmissions over the uncorrelated Rayleigh fading channel employing QPSK and utilising the simulation parameters of Table 5.5. A codeword length of 1000 symbols and a spreading factor of 31 chips were employed.

scenario and that the associated BERs of BPSK and QPSK are identical in terms of E_b/N_0. Hence the single-user bounds for QPSK modulation shown in Figure 5.19 for AWGN channel and Figure 5.20 for uncorrelated Rayleigh fading channel, are identical to that of the BPSK modulation. However, the orthogonality of the in-phase and quadrature-phase BPSK signals is corrupted by the MAI when a QPSK signal is transmitted in a CDMA system. Hence the BER of QPSK signal is not identical to that of BPSK signals in the context of a MAI-limited CDMA environment. Therefore, the uncoded QPSK performance of a $\mathsf{K} = 10$-user CDMA system is worse than that of the single-user bounds illustrated in Figures 5.19 and 5.20.

Note that the computational complexity of the GA-MUD is $\frac{\mathsf{M}^{\mathsf{K}}}{\mathsf{P}\times\mathsf{Y}} = 1310.72$ times lower, than that of the optimum MUD, when supporting $\mathsf{K} = 10$ users employing QPSK modulation [1]. The penalty for this complexity reduction is the BER error floor experienced by the GA-MUD schemes at high SNRs, as shown in Figures 5.19 and 5.20. However, this disadvantage is eliminated, when the CM schemes are utilised. In particular, the TTCM assisted GA-MUD constitutes the best candidate, followed by the BICM-ID assisted GA-MUD, as evidenced in Figures 5.19 and 5.20 for transmissions over the AWGN and uncorrelated Rayleigh fading channels encountered. More specifically, for a throughput of 1 BPS and a target BER of 10^{-4}, the $\mathsf{K} = 10$-user TTCM-GA-MUD assisted CDMA system is capable of providing SNR gains of about 4 and 25 dB in AWGN and perfectly interleaved narrowband Rayleigh fading channels, respectively, against the single-user bounds of the uncoded BPSK scheme.

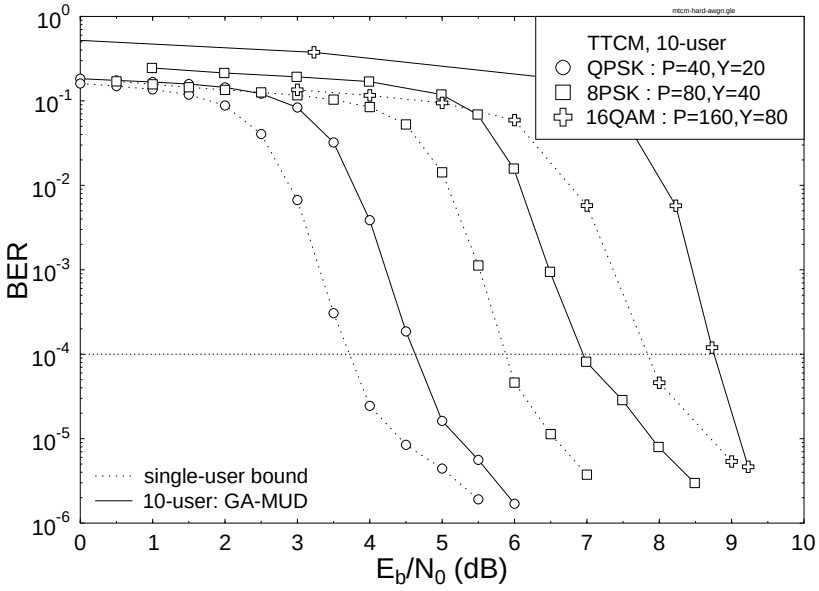

Figure 5.21: BER versus E_b/N_0 performance of the TTCM-GA-MUD scheme for transmissions over the AWGN channel employing QPSK, 8PSK and 16QAM and utilising the simulation parameters of Table 5.5. A codeword length of 1000 symbols and a spreading factor of 31 chips were employed.

[1] We note that Verdu's full-search based optimum MUD exhibits an excessive complexity and hence it is not a practical benchmarker. However, it exhibits a performance which is similar to the achievable single-user performance. Therefore our benchmarker is the single-user performance which may be approach using a variety of different reduced-complexity MUD schemes. The GA-MUD's complexity may be best characterised by quantifying the number of objective function evaluation required for achieving near single-user performance. The closest relative of the GA-based MUD family is that of the M-algorithm [160, 161] and T-algorithm [162, 163], both of which would constitute an appropriate benchmarker scheme.

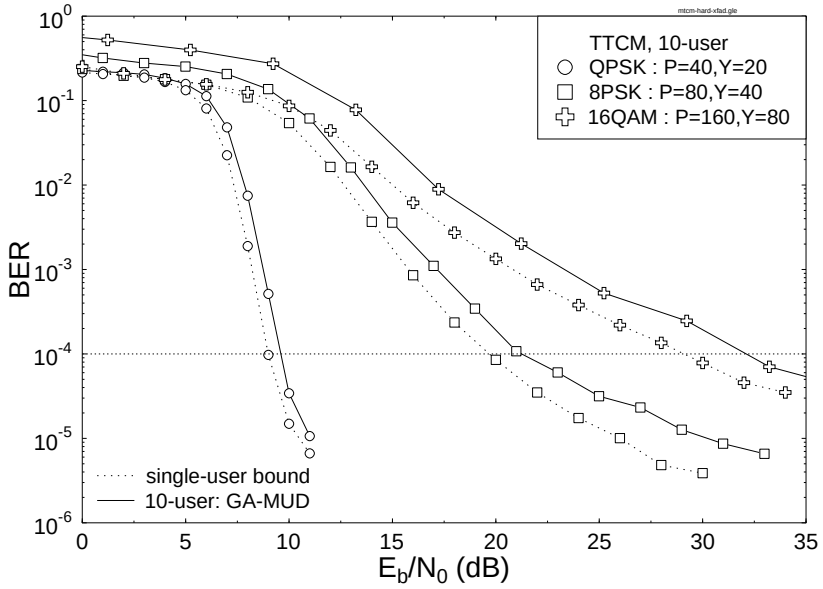

Figure 5.22: BER versus E_b/N_0 performance of the TTCM-GA-MUD scheme for transmissions over the uncorrelated Rayleigh fading channel employing QPSK, 8PSK and 16QAM and utilising the simulation parameters of Table 5.5. A codeword length of 1000 symbols and a spreading factor of 31 chips were employed.

Next, let us study the performance of the TTCM-GA-MUD scheme in conjunction with QPSK, 8PSK and 16QAM in Figures 5.21 and 5.22 for transmissions over both AWGN and uncorrelated Rayleigh fading channels, respectively. The *hard decision*-based single-user performance bounds for TTCM are also plotted in Figures 5.21 and 5.22 as benchmarkers. We found that the performance of the TTCM-GA-MUD scheme, which supports 10 users is comparable to that of the single-user TTCM benchmarker, in the 1, 2 and 3 BPS effective throughput modes associated with QPSK, 8PSK and 16QAM, respectively. In the higher-throughput modes, it was achievable by doubling the population size P and the number of generations Y of the TTCM-GA-MUD, every time when the BPS throughput was increased by one, as shown in the legends of Figures 5.21 and 5.22. More specifically, we found that for detecting K users each employing M-ary modulation, the rule of thumb quantifying the required complexity of the specific TTCM-GA-MUD scheme considered is given by $\mathsf{P} \times \mathsf{Y} \approx \frac{1}{2}\mathsf{K}^2\mathsf{M}^2$, where we require $\mathsf{P} \approx \mathsf{KM}$ and $\mathsf{Y} \approx \frac{1}{2}\mathsf{KM}$, which attains a performance similar to that of the optimum MUD. **Hence, the computational complexity reductions obtained by the TTCM-GA-MUD compared to that of the optimum MUD can be construed to be about** $F \approx \frac{\mathsf{M}^\mathsf{K}}{\frac{1}{2}\mathsf{K}^2\mathsf{M}^2} = 2\mathsf{M}^{\mathsf{K}-2}\mathsf{K}^{-2}$**.** For the specific example of K=10 users, the complexity reduction factors F for QPSK, 8PSK and 16QAM were 1.3×10^3, 6.7×10^5 and 8.6×10^7, respectively. Despite these huge complexity reduction gains, the BER penalty for TTCM-GA-MUD was only around 0.5 to 2 dB at a BER of 10^{-4} compared to the single-user benchmarker, when communicating over the AWGN and uncorrelated Rayleigh fading channels employing QPSK, 8PSK and 16QAM, as evidenced by Figures 5.21 and 5.22.

In Figure 5.23, we show the BER versus E_b/N_0 performance of the TTCM-GA-MUD and that of the TTCM-optimum-MUD schemes, when communicating over AWGN channels using QPSK, 8PSK and 16QAM TTCM. It is shown in Figure 5.23 that the optimum-MUD exhibits an approximately

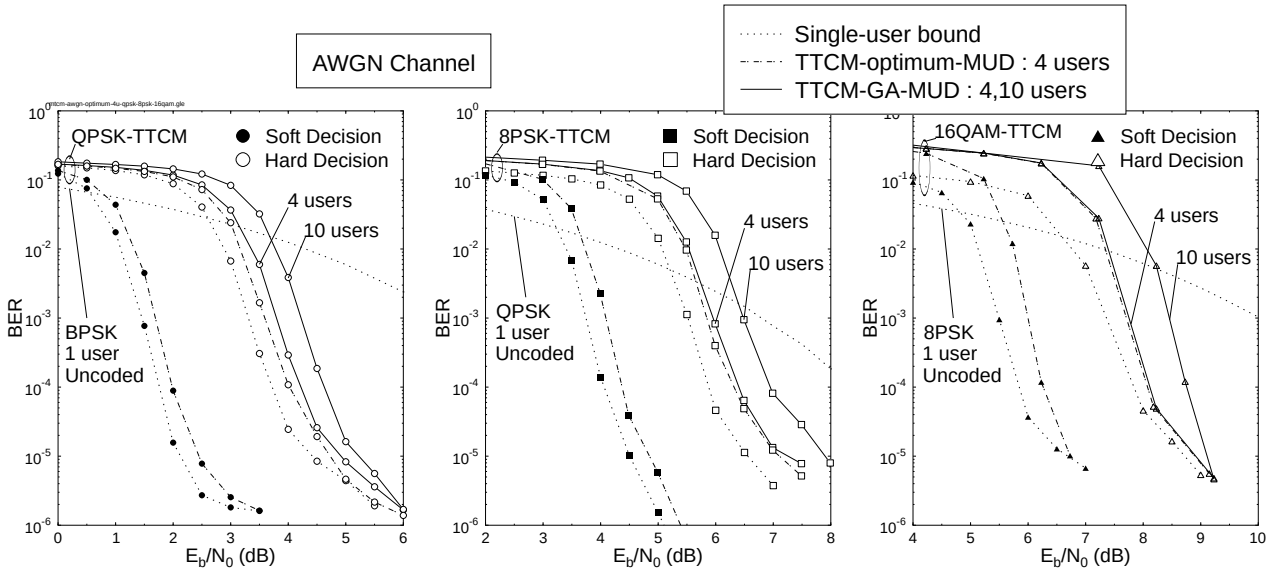

Figure 5.23: BER versus E_b/N_0 performance of the TTCM-GA-MUD and TTCM-optimum-MUD schemes, when communicating over non-dispersive AWGN channels; left: effective throughput of 1 BPS; middle: effective throughput of 2 BPS; right: effective throughput of 3 BPS.

0.3 dB performance loss both in conjunction with *hard-* and *soft decisions*, when K increased from one to four. For K=10 users the performance loss of TTCM-GA-MUD was about 1 and 3 dB, as shown in Figure 5.23, compared to the TTCM-assisted single-user schemes employing *hard-* and *soft decisions*, respectively, regardless whether QPSK, 8PSK or 16QAM modulation schemes were used. The TTCM-GA-MUD aided QPSK, 8PSK and 16QAM systems supporting K=10 users achieved an SNR-reduction of 3.8, 1.4 and 2.9 dB at the effective throughputs of 1, 2 and 3 BPS in comparison to the single-user bounds of the uncoded schemes of BPSK, QPSK and 8PSK, respectively, without extending the required bandwidth.

Similar performances trend can also be observed in Figure 5.24 for the TTCM-GA-MUD and TTCM-optimum-MUD schemes, when communicating over uncorrelated Rayleigh fading channels. Despite the huge complexity reduction and the support of K=10 users, the TTCM-GA-MUD aided QPSK, 8PSK and 16QAM systems were still capable of achieving an SNR-reduction of 25, 13 and 4 dB at the effective throughputs of 1, 2 and 3 BPS in comparison to the single-user bounds of the uncoded schemes of BPSK, QPSK and 8PSK, respectively, within the same bandwidth.

5.4.6 Conclusions

In this section, TCM, TTCM, BICM and BICM-ID assisted GA-based MUD schemes were proposed and evaluated in performance terms when communicating over the AWGN and narrowband Rayleigh fading channels encountered. It was shown that the GA-MUD is capable of significantly reducing the computational complexity of the optimum-MUD, but experiences a GA-induced error floor at high SNRs due to invoking an insufficiently large population size and a low number of generations as demonstrated in Figures 5.19 and 5.20. However, with the advent of the bandwidth efficient CM schemes proposed, this problem is eliminated. When comparing the four CM schemes at the same decoding complexity, TTCM was found to be the best candidate for assisting the operation of the

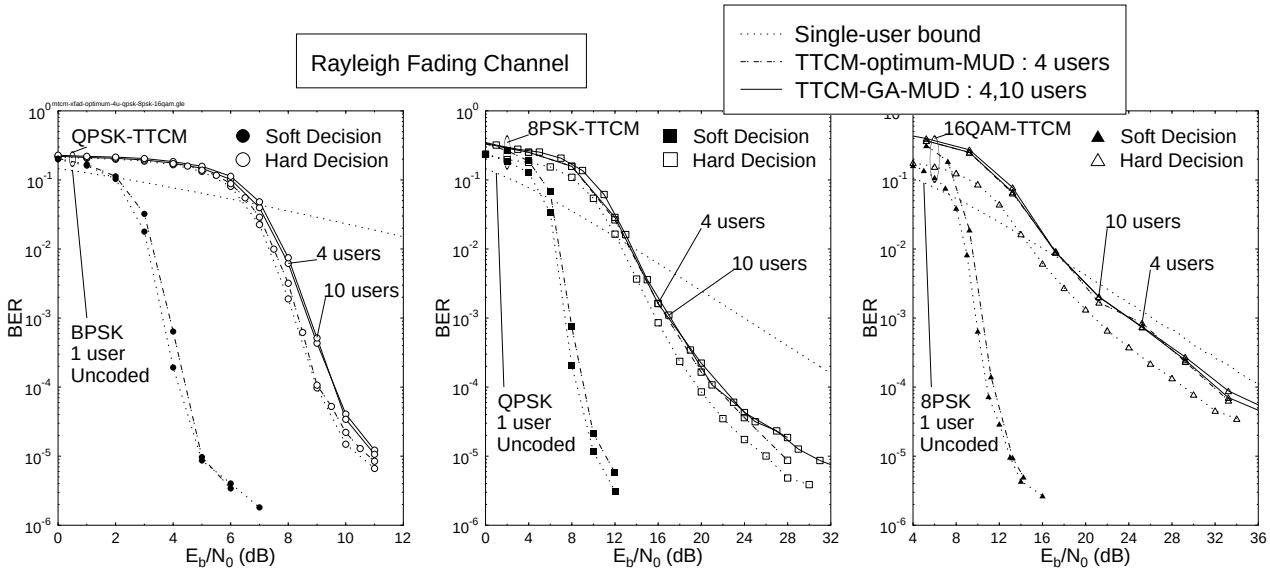

Figure 5.24: BER versus E_b/N_0 performance of the TTCM-GA-MUD and TTCM-optimum-MUD schemes, when communicating over non-dispersive Rayleigh fading channels; left: effective throughput of 1 BPS; middle: effective throughput of 2 BPS; right: effective throughput of 3 BPS.

GA-MUD system.

When higher throughput M-ary modulation schemes were investigated with the advent of TTCM-GA-MUD arrangements, we found that the complexity of TTCM-GA-MUD was dramatically lower than that of the optimum-MUD, with the penalty of only 0.5 to 2 dB SNR loss compared to that of the TTCM single-user bound as evidenced in Figures 5.21 and 5.22. Furthermore, the reduced-complexity TTCM-GA-MUD schemes are capable of attaining further coding gains with respect to the uncoded single-user modulation schemes while maintaining a similar throughput and bandwidth, even when supporting a high number of users, as shown in Figures 5.23 and 5.24. We note furthermore that the BER curves of TTCM-GA-MUD in Figures 5.23 and 5.24 also show a tendency to have a residual BER, which is the characteristic of all turbo coding-based arrangements.

5.5 Chapter Conclusions

In this chapter the CM schemes introduced in Chapter 2 were investigated in the context of CDMA environments with the aid of JD-MMSE-DFE based MUD scheme in Sections 5.2 and 5.3, and with the aid of GA-MUD in Section 5.4.

It was found in Section 5.2 that the TCM-assisted JD-MMSE-DFE based MUD scheme was the best candidate for employment in systems using a short channel interleaver, while the TTCM-assisted JD-MMSE-DFE based MUD was the best candidate for systems using a long channel interleaver. The burst-by-burst adaptive TTCM-assisted JD-MMSE-DFE based MUD was investigated in Section 5.3, where the complexity of the joint detection algorithms remained constant upon changing the CM modes. The proposed adaptive scheme constitutes a promising practical communication system, guaranteeing reliable transmission while providing an effective bitrate ranging from 23.4 Kbit/s/slot to 117 Kbit/s/slot for transmission over the UTRA environment of Figure 5.9 and Table 5.2.

A reduced complexity M-ary CM-GA-MUD scheme was proposed and investigated in Section 5.4. It was shown in Section 5.4 that the CM-GA-MUD scheme is capable of attaining further coding gains with respect to the uncoded single-user modulation schemes at a similar throughput and in the same bandwidth, when supporting a high number of CDMA users. At the same time, the CM-GA-MUD scheme also attains a significant complexity reduction with respect to the optimum-MUD.

In summary, the coding gain values exhibited by the coded modulation schemes studied in this chapter were collated in Tables 5.6 and 5.7. Specifically, we summarised the performance gains exhibited by the JD-DFE assisted coded modulation schemes of Section 5.3 communicating over the UTRA Rayleigh fading channels in Tables 5.6. By contrast, the coding gains exhibited by the GA-MUD-CM schemes of Section 5.4 communicating over non-dispersive AWGN channels and uncorrelated Rayleigh fading channels were summarised in Table 5.7.

Code	Modulation/ BPS	JD-DFE, UTRA Rayleigh fading channels							
		E_b/N_o (dB)		Gain (dB)		E_b/N_o (dB)		Gain (dB)	
		BER				FER			
		10^{-3}	10^{-5}	10^{-3}	10^{-5}	10^{-1}	10^{-2}	10^{-1}	10^{-2}
uncoded	BPSK/1	11.42	17.40	0.00	0.00	11.00	14.79	0.00	0.00
TCM	QPSK/1	**10.00**	**14.19**	1.42	3.21	6.79	10.17	4.21	4.62
TTCM	QPSK/1	10.41	**14.19**	1.01	3.21	**6.36**	**9.77**	4.64	5.02
BICM	QPSK/1	10.41	14.80	1.01	2.60	6.48	9.96	4.52	4.83
BICM-ID	QPSK/1	10.98	14.34	0.44	3.06	6.48	10.06	4.52	4.73
uncoded	QPSK/2	11.52	17.39	0.00	0.00	11.74	15.31	0.00	0.00
TCM	8PSK/2	**12.19**	**16.42**	-0.67	0.97	9.19	12.58	2.55	2.73
TTCM	8PSK/2	12.54	16.52	-1.02	0.87	**9.03**	**12.37**	2.71	2.94
BICM	8PSK/2	13.25	17.13	-1.73	0.26	9.57	12.91	2.17	2.40
BICM-ID	8PSK/2	14.38	17.84	-2.86	-0.45	9.27	12.64	2.47	2.67
uncoded	8PSK/3	14.49	20.63	0.00	0.00	15.27	19.01	0.00	0.00
TCM	16QAM/3	**13.96**	**18.38**	0.53	2.25	11.23	14.63	4.04	4.38
TTCM	16QAM/3	14.23	18.54	0.26	2.09	**11.00**	**14.25**	4.27	4.76
BICM	16QAM/3	14.89	18.93	-0.40	1.70	11.23	14.50	4.04	4.51
BICM-ID	16QAM/3	16.21	19.07	-1.72	1.56	11.06	14.38	4.21	4.63
uncoded	16QAM/4	15.11	21.23	–	–	15.98	19.58	–	–
TCM	64QAM/5	**18.31**	**22.78**	–	–	15.79	19.15	–	–
TTCM	64QAM/5	18.53	23.09	–	–	**15.61**	**18.96**	–	–
BICM	64QAM/5	19.65	23.21	–	–	16.26	19.57	–	–
BICM-ID	64QAM/5	20.62	24.01	–	–	16.39	19.79	–	–
uncoded	64QAM/6	19.25	25.20	–	–	20.59	24.22	–	–

Table 5.6: Coding gain values attained by the various JD-DFE assisted coded modulation schemes studied in this chapter, when communicating over the UTRA Rayleigh fading channels. All of the coded modulation schemes exhibited a similar decoding complexity in terms of the number of decoding states, which was equal to 64 states. An interleaver block length of 240 symbols was employed and the corresponding simulation parameters were summarised in Section 5.3.2. The performance of the best scheme is printed in bold.

CM-GA-MUD		AWGN Channels				Flat Uncorrelated Rayleigh Fading Channels			
Code	Modulation/ BPS	E_b/N_o (dB) BER		Gain (dB)		E_b/N_o (dB) BER		Gain (dB)	
		10^{-3}	10^{-5}	10^{-3}	10^{-5}	10^{-3}	10^{-5}	10^{-3}	10^{-5}
Uncoded	BPSK/1	6.75	9.52	0.00	0.00	24.00	43.50	0.00	0.00
TCM	QPSK/1	5.45	7.15	1.30	2.37	12.12	21.00	11.88	22.50
TTCM	QPSK/1	**4.22**	**5.22**	2.53	4.30	**8.76**	**11.00**	15.24	32.50
BICM	QPSK/1	5.35	7.06	1.40	2.46	10.40	14.62	13.60	28.88
BICM-ID	QPSK/1	4.57	6.34	2.18	3.18	9.68	14.80	14.32	28.70
Uncoded	QPSK/2	6.75	9.52	0.00	0.00	24.00	43.50	0.00	0.00
TTCM	8PSK/2	**6.48**	**7.90**	0.27	1.62	**17.15**	**30.10**	6.85	13.40
Uncoded	8PSK/3	10.02	12.95	0.00	0.00	26.15	46.00	0.00	0.00
TTCM	16QAM/3	**8.45**	**9.11**	1.57	3.84	**24.00**	**45.00**	2.15	1.00

Table 5.7: Coding gain values of the various of GA-MUD assisted coded modulation schemes studied in this chapter, when communicating over non-dispersive AWGN channels and uncorrelated Rayleigh fading channels. All of the coded modulation schemes exhibited a similar decoding complexity in terms of the number of decoding states, which was equal to 64 states. An interleaver block length of 1000 symbols was employed and the corresponding simulation parameters were summarised in Section 5.4.4. The performance of the best scheme is printed in bold.

Chapter 6

Coded Modulation Assisted Space Time Block Coding

6.1 Introduction

In this chapter, we will further develop the Coded Modulation (CM) schemes studied in Chapter 2 by amalgamating them with Space Time Block Coding (STBC) [164, 165] and investigate the achievable performance improvements in the light of the complexity investments required.

In numerous practical situations the wireless channels are neither highly time selective nor significantly frequency selective. This motivated numerous researchers to investigate space diversity techniques with the aim of improving the system's performance. Classic receiver diversity [166] has been widely used at the base stations of both the GSM and IS-136 systems. As an additional performance enhancement, recently the family of transmit diversity techniques [14, 167] has been studied extensively for employment at the base station, since it is more practical to have multiple transmit antennas at the base station, than at the mobile station. Furthermore, upgrading the base station instead of the mobile stations has the potential of benefiting numerous mobile stations in a cost efficient manner. Space-Time Trellis Coding (STTC) pioneered by Tarokh *et. al.* [168] incorporates jointly designed channel coding, modulation, transmit diversity and optional receiver diversity [14]. In an attempt to reduce the associated decoding complexity, Alamouti proposed STBC employing two transmit antennas. Alamouti's scheme was later generalised to an arbitrary number of transmit antennas [165].

Furthermore, in this chapter we will argue that further diversity gain may also be attained by exploiting the independent nature of the fading experienced by the In-phase (I) and Quadrature-phase (Q) components of the complex-valued transmitted signal with the aid of two independent IQ interleavers. Alternatively, the multipath components exhibited by the dispersive Rayleigh fading channel constitute a further often-used source of useful diversity potential.

This chapter is organised as follows. The proposed STBC aided IQ-interleaved CM (IQ-CM) scheme will be studied in Section 6.2, while the novel concept of a STBC assisted double-spread Rake receiver assisted CDMA scheme will be studied in Section 6.3. Finally, an amalgamated system based on the combination of the above two schemes with be investigated in Section 6.4 and our conclusions

are offered in Section 6.5.

6.2 Space-Time Block Coded IQ-Interleaved Coded Modulation

6.2.1 Introduction

In this section we will present the philosophy of a set of STBC-assisted IQ-interleaved TCM and TTCM schemes designed for transmission over both non-dispersive AWGN and for flat Rayleigh fading channels. Specifically, we will demonstrate that the proposed schemes are capable of quadrupling the achievable diversity order of the conventional symbol-interleaved TCM and TTCM schemes, when two transmit antennas are employed. The increased diversity order of the proposed schemes provides significant additional coding gains, when communicating over non-dispersive Rayleigh fading channels, which is achieved without compromising the coding gain attainable over Gaussian channels. This is a significant achievement, since the design criteria of schemes destined for those different channels are also different. Hence in general a scheme optimised for one of these channels is typically suboptimum, when communicating over the other. The BICM as well as BICM-ID schemes introduced in Sections 2.5 and 2.6, respectively, are also incorporated into the proposed system and their performance is compared to that of TCM and TTCM schemes highlighted in Sections 2.2 and 2.4, respectively.

To elaborate a little further, it was shown in [37] that the maximisation of the minimum Hamming distance measured in terms of the number of different symbols between any two transmitted symbol sequences is the key design criterion of TCM schemes contrived for flat Rayleigh fading channels, in particular when communicating at high Signal-to-Noise Ratios (SNR). In an effort to increase the achievable time diversity, a multidimensional TCM scheme utilising a symbol interleaver and two encoders was proposed by S. Al-Semari and T. Fuja in [169], where the individual encoders generate the I and Q components of the complex transmitted signal, respectively. Another efficient TCM scheme using constellation rotation was proposed by B. D. Jelicic and S. Roy in [170], which utilised two separate channel interleavers for interleaving the I and Q components of the complex-valued transmitted signals, but assumed the absence of I/Q *cross-coupling*, which can only be realistically expected when communicating over fading channels exhibiting a real-valued Channel Impulse Response (CIR).

In order to improve the performance of the existing state-of-the-art systems, in this section we proposed a novel system, which amalgamates STBC [164] with IQ-interleaved TCM, TTCM, BICM and BICM-ID schemes using no constellation rotation.

6.2.2 System Overview

The block diagram of the STBC based IQ-interleaved (STBC-IQ) TCM/TTCM system is shown in Figure 6.1. Specifically, we employ two transmitters and one receiver in the STBC scheme. Furthermore, we invoke two independent IQ interleavers in the TCM/TTCM arrangement, which are denoted as π_I and π_Q in the block diagram of Figure 6.1. We denote the IQ-interleaved modulated signal by $\tilde{s} = \tilde{s}_I + j\tilde{s}_Q$, which is transmitted over the flat Rayleigh fading channel having a complex fading coefficient of $h = \alpha e^{j\theta}$ with the aid of two STBC transmitters [14]. As seen in Figure 6.1, during the

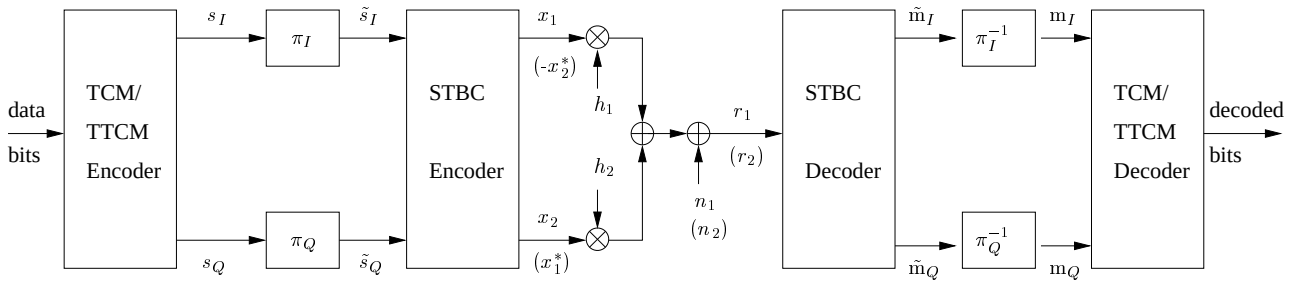

Figure 6.1: Block diagram of the STBC-based IQ-interleaved system. The notations π and π^{-1} denote the interleaver and deinterleaver, while the variables in the round brackets () denote the STBC signals transmitted during the second symbol period.

first symbol period of the STBC transmission the signals $x_1 = \tilde{s}_1$ and $x_2 = \tilde{s}_2$ are transmitted, while during the second symbol period, the signals -x_2^* and x_1^* are emitted from the transmit antennas 1 and 2, respectively, as in Alamouti's G_2 code [164]. Specifically, G_2 is defined as [164, 165]:

$$G_2 = \begin{pmatrix} x_1 & x_2 \\ -x_2^* & x_1^* \end{pmatrix}, \tag{6.1}$$

where two symbols, x_1 and x_2, were transmitted using two transmit antennas over the duration of two symbol periods. Hence, a coding rate of unity was achieved. We assume that both the fading envelope and the phase of the CIR taps remains constant across the two STBC time slots. The signal is also contaminated by the zero-mean AWGN n, exhibiting a variance of $\sigma^2 = N_0/2$, where N_0 is the single-sided noise power spectral density. It can be readily seen from Figure 6.2 that the two signals received during the two consecutive symbol periods of the STBC scheme can be represented in a matrix form as $\mathbf{r} = \mathbf{A} \cdot \mathbf{x} + \mathbf{n}$:

$$\begin{pmatrix} r_1 \\ r_2^* \end{pmatrix} = \begin{pmatrix} h_1 & h_2 \\ h_2^* & -h_1^* \end{pmatrix} \begin{pmatrix} x_1 \\ x_2 \end{pmatrix} + \begin{pmatrix} n_1 \\ n_2^* \end{pmatrix}, \tag{6.2}$$

where $\mathbf{A}$ is termed the system matrix and x^* denotes the complex conjugate of the transmitted symbol x. At the combiner/decoupler block of Figure 6.2, the received vector $\mathbf{r}$ is multiplied with the conjugate transpose of $\mathbf{A}$, namely with $\mathbf{A^H}$, yielding:

$$\begin{aligned} \hat{\mathbf{x}} &= \mathbf{A^H} \cdot \mathbf{r} \\ \begin{pmatrix} \hat{x}_1 \\ \hat{x}_2 \end{pmatrix} &= (\alpha_1^2 + \alpha_2^2) \begin{pmatrix} x_1 \\ x_2 \end{pmatrix} + \begin{pmatrix} \hat{n}_1 \\ \hat{n}_2 \end{pmatrix}, \end{aligned} \tag{6.3}$$

where the terms $\hat{n}_1 = h_1^* n_1 + h_2 n_2^*$ and $\hat{n}_2 = h_2^* n_1 + h_1 n_2^*$ represent the resultant noise.

Note that as usual, owing to the complex-valued nature of the CIR, the I (or Q) component of the received signal r_i, namely $r_{i,I}$ (or $r_{i,Q}$) where we have $i \in \{1, 2\}$, is dependent on both the I and Q components of x_1 and x_2, namely on $x_{1,I}$, $x_{1,Q}$, $x_{2,I}$ and $x_{2,Q}$. This phenomenon is often referred to as IQ crosscoupling. More explicitly, we have:

$$r_{1,I} = h_{1,I}x_{1,I} - h_{1,Q}x_{1,Q} + h_{2,I}x_{2,I} - h_{2,Q}x_{2,Q} + n_{1,I}, \tag{6.4}$$

owing to the cross-coupling effect imposed by the complex-valued CIR. It is however desirable to decouple them, so that we can compute the I (or Q) branch metrics m_I (or m_Q) in Figure 6.1 for a

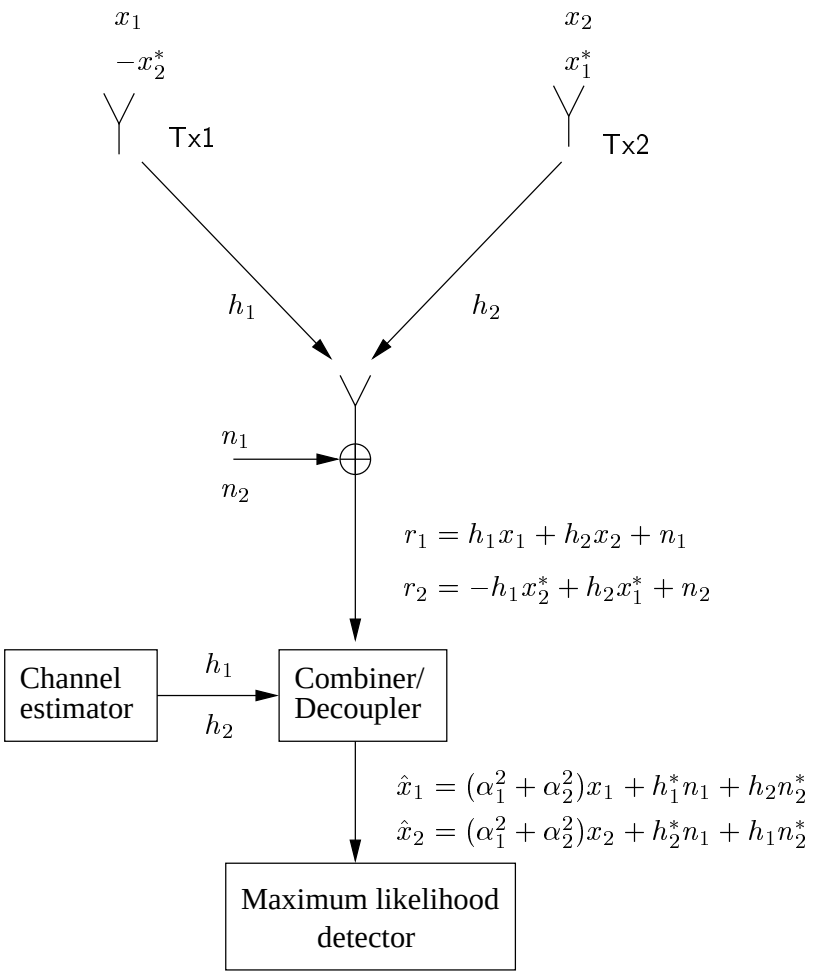

Figure 6.2: Baseband representation of the STBC G_2 code employing two transmitters and one receiver.

particular transmitted symbol x_i independently, as a function of only $x_{1,I}$ and $x_{2,I}$ (or $x_{1,Q}$ and $x_{2,Q}$). Surprisingly, this may be achieved without carrying out any explicit decoupling operation for the STBC based IQ-interleaved TCM/TTCM scheme. More specifically, this is achieved because the signals already have been decoupled during the STBC decoding operation at the combiner/decoupler block of Figure 6.2, when the received vector $\mathbf{r}$ is multiplied with $\mathbf{A^H}$, yielding $\hat{\mathbf{x}} = \mathbf{A^H} \cdot \mathbf{r}$ in Equation 6.3. Explicitly, the transmitted signal estimate of $\hat{x}_1 = (\alpha_1^2 + \alpha_2^2)x_1 + \hat{n}_1$ is the decoupled version of r_1, where $\hat{x}_{1,I}$ (or $\hat{x}_{1,Q}$) is independent of $x_{1,Q}$ and $x_{2,Q}$ (or $x_{1,I}$ and $x_{2,I}$).

Before we proceed further to the computation of the branch metrics for the STBC based IQ-TCM/TTCM scheme, let us first derive the branch metrics for the single-transmitter based IQ-TCM/TTCM scheme. For a single-transmitter scheme emitting the signal $x = x_I + jx_Q$, which is conveyed over narrowband fading channels exhibiting a complex-valued CIR of $h = \alpha e^{j\theta}$, the corresponding received signal is $r = hx + n$ and the I/Q-decoupled signal can be computed from:

$$\begin{aligned} \hat{x} &= h^*r, \\ &= \alpha^2 x + h^*n. \end{aligned} \tag{6.5}$$

The corresponding symbol-based branch metrics can be calculated from:

$$\tilde{\mathrm{m}}(x|\hat{x},h) = -\frac{\left|r-hx\right|^2}{2\sigma^2}, \tag{6.6}$$

$$= -\frac{\left|h^*r-h^*hx\right|^2}{2\sigma^2|h^*|^2}, \tag{6.7}$$

$$= -\frac{\left|\hat{x}-\alpha^2x\right|^2}{2\sigma^2\alpha^2}, \tag{6.8}$$

$$= -\frac{\left|\hat{x}-Dx\right|^2}{2\sigma^2D}, \tag{6.9}$$

where we have $D=\alpha^2$, which can be physically interpreted as a fading envelope-related variable or a diversity quantity. Since $\hat{x}$, which was computed from Equation 6.5, is the decoupled version of the received signal r, we can compute the corresponding I and Q branch metrics based on Equation 6.9 as:

$$\begin{aligned}\tilde{\mathrm{m}}(x|\hat{x},h) &= -\frac{\left|\hat{x}_I-D_Ix_I\right|^2}{2\sigma^2D_I}-\frac{\left|\hat{x}_Q-D_Qx_Q\right|^2}{2\sigma^2D_Q}\\ &= \tilde{\mathrm{m}}_I(x_I|\hat{x}_I,D_I)+\tilde{\mathrm{m}}_Q(x_Q|\hat{x}_Q,D_Q),\end{aligned} \tag{6.10}$$

where $\tilde{\mathrm{m}}_I$ and $\tilde{\mathrm{m}}_Q$ denote the I and Q branch metrics, respectively, before the IQ interleavers as shown in Figure 6.1. Furthermore, we have $D_I=D_Q=D=\alpha^2$.

Let us now compute the I and Q branch metrics for the STBC scheme by first studying the similarity between $\hat{x}=h^*r$ of Equation 6.5 and $\hat{\mathbf{x}}=\mathbf{A}^{\mathbf{H}}\cdot\mathbf{r}$ of Equation 6.3. Clearly, $\hat{x}$ and $\hat{\mathbf{x}}$ are the decoupled versions of their corresponding received signals, hence the branch metrics for the STBC scheme can be computed similarly to that of the single-transmitter scheme. Although, in the STBC scheme we cannot employ a relationship similar to Equation 6.6, we can directly utilise a relationship similar to Equation 6.9. Specifically, the symbol-based branch metrics for x_i, $i\in\{1,2\}$ of the STBC scheme can be calculated from:

$$\tilde{\mathrm{m}}(x_i|\hat{x}_i,D) = -\frac{\left|\hat{x}_i-Dx_i\right|^2}{2\sigma^2D}, \tag{6.11}$$

where we have $D=\left(\alpha_1^2+\alpha_2^2\right)$ for the STBC G_2 scheme. Hence, the associated IQ branch metrics of the STBC coded signal $x_i=x_{i,I}+jx_{i,Q}$ can be derived from $\hat{x}_i=\hat{x}_{i,I}+j\hat{x}_{i,Q}$ as:

$$\begin{aligned}\tilde{\mathrm{m}}(x_i|\hat{x}_i,D) &= -\frac{\left|\hat{x}_{i,I}-D_Ix_{i,I}\right|^2}{2\sigma^2D_I}-\frac{\left|\hat{x}_{i,Q}-D_Qx_{i,Q}\right|^2}{2\sigma^2D_Q}\\ &= \tilde{\mathrm{m}}_I(x_{i,I}|\hat{x}_{i,I},D_I)+\tilde{\mathrm{m}}_Q(x_{i,Q}|\hat{x}_{i,Q},D_Q),\end{aligned} \tag{6.12}$$

where again, we have $D_I=D_Q=D=\left(\alpha_1^2+\alpha_2^2\right)$. The effect of the associated second-order transmit diversity attained may be observed in the context of the term $(\alpha_1^2+\alpha_2^2)$ in Equation 6.3.

Note that $\tilde{\mathrm{m}}_I$ and $\tilde{\mathrm{m}}_Q$ share the same fading channel-envelope related D value for the same transmitted signal of $x(=\tilde{s})$ before the IQ interleavers, as seen in Figure 6.1. However, owing to rearranging the transmitted IQ components by the IQ deinterleavers of π_I^{-1} and π_Q^{-1} seen in Figure 6.1, m_I and

m_Q will be associated with different fading envelope values of $D_I \neq D_Q$ after the IQ deinterleavers. The branch metrics of the TCM/TTCM-coded complex-valued signal s can be computed by summing the I and Q branch metrics as follows:

$$m(s) = m_I(x_I = s_I) + m_Q(x_Q = s_Q). \tag{6.13}$$

Since there are two independent IQ components for a complex-valued TCM/TTCM symbol and since they are independently interleaved by the interleavers π_I and π_Q in Figure 6.1, m_I and m_Q are exposed to independent fading and hence they have the potential of providing independent diversity for a particular symbol. More explicitly, **since we have $D_I \neq D_Q$ for a particular coded symbol s, the IQ-interleaved TCM/TTCM scheme may be expected to double the achievable diversity order compared to its symbol-interleaved counterpart.** Therefore the achievable Hamming distance between the transmitted symbol sequences of the proposed IQ-interleaved TCM/TTCM scheme is based on the sum of the number of different I and Q components between the different transmitted messages, rather than on the number of different complex-valued symbols, which was the case in the context of conventional symbol-interleaved TCM/TTCM.

We have also amalgamated the proposed STBC-IQ scheme of Figure 6.1 with the BICM and BICM-ID schemes of Sections 2.5 and 2.6. More specifically, in addition to their internal bit-interleavers [14], two extra random interleavers were invoked for separately interleaving the I and Q components of their bit-interleaved complex symbol $s = s_I + js_Q$ for yielding $\tilde{s} = \tilde{s}_I + j\tilde{s}_Q$, as it was illustrated in Figure 6.1.

6.2.3 Simulation Results And Discussions

We evaluated the performance of the proposed schemes using 16QAM in the context of the non-iterative 64-state TCM and BICM schemes, as well as in conjunction with the iterative 8-state TTCM arrangement using four decoding iterations and along with the 8-state BICM-ID arrangement using eight decoding iterations. As in Section 3.2.2, the rationale of using 64 and 8 states, respectively, was that the TCM/BICM and TTCM/BICM-ID schemes considered here exhibit a similar decoding complexity expressed in terms of the total number of trellis states. Explicitly, since there are two 8-state TTCM decoders, which are invoked in four iterations, we encounter a total of $2 \times 8 \times 4 = 64$ TTCM trellis states. By contrast, only a single 8-state BICM-ID decoder is required, which is invoked in eight iterations, involving a total of $8 \times 8 = 64$ BICM-ID trellis states. The effective throughput was 3 Bits Per Symbol (BPS) for all the 16QAM based CM schemes, since a coding rate of 3/4 was used.

In Figure 6.3, we portray the Bit Error Ratio (BER) versus signal to noise ratio per bit, namely E_b/N_0, performance of the 16QAM based TCM and BICM schemes, when communicating over AWGN as well as over uncorrelated flat Rayleigh fading channels[1]. An interleaved codeword length of 1000 symbols was used and the BER performance curve of the uncoded 8PSK scheme is also plotted for benchmarking the schemes, all having an effective throughput of 3 BPS. As illustrated in Figure 6.3, all the TCM/BICM schemes associated with the conventional CM, STBC-CM, IQ-CM and STBC-IQ-CM arrangements exhibit a similar performance in AWGN channels. This is because no space

[1] CM: the conventional CM scheme; STBC-CM: the STBC based conventional CM scheme; IQ-CM: the proposed IQ-interleaved CM scheme using no STBC; STBC-IQ-CM: the proposed STBC-based IQ-interleaved CM scheme.

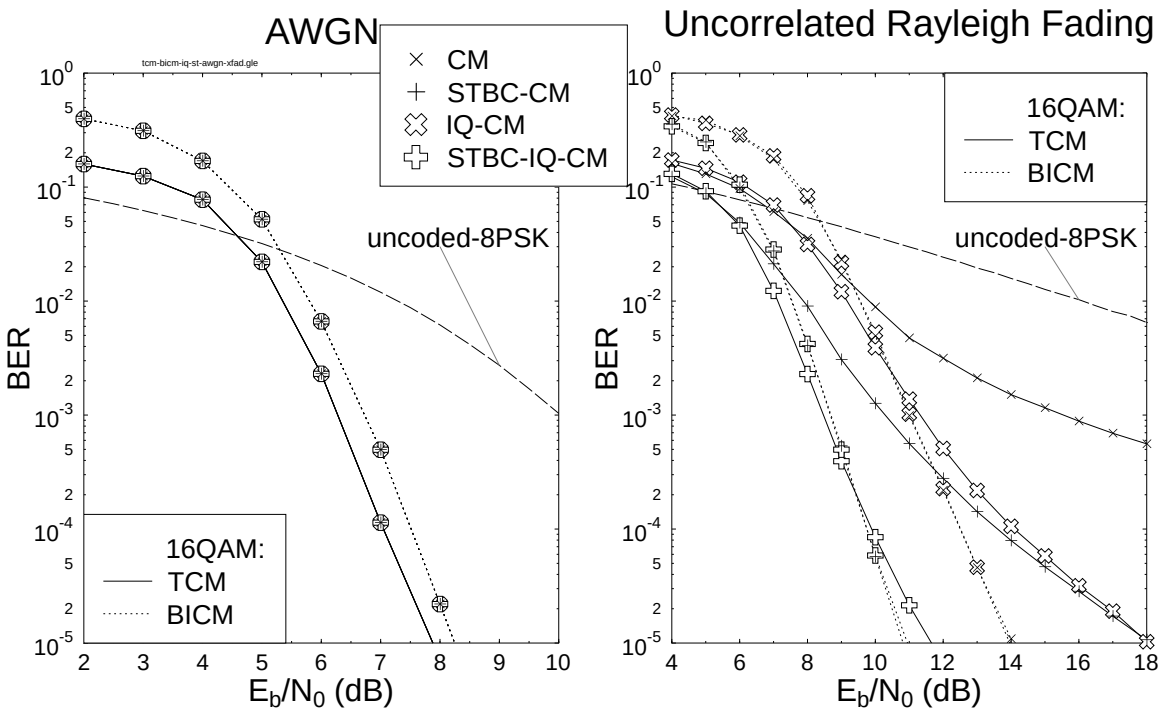

Figure 6.3: BER versus E_b/N_0 performance of the 16QAM based **TCM** and **BICM** schemes, when communicating over AWGN and uncorrelated flat Rayleigh fading channels. The legends are described in Footnote 1. An interleaved codeword length of 1000 symbols was used and the performance of the uncoded 8PSK scheme is also plotted for benchmarking the CM schemes, all having an effective throughput of **3 BPS**.

diversity or time diversity is attainable over Gaussian channels despite using multiple transmitters and interleaving. On the other hand, the TCM scheme performs approximately 0.5 dB better, than the BICM scheme, when communicating over AWGN channels, since it has a higher Euclidean distance than that of BICM, which is the decisive criterion in the context of AWGN channels.

By contrast, when communicating over uncorrelated flat Rayleigh fading channels, the BER curve of IQ-TCM merged with that of STBC-TCM in the high-SNR region of Figure 6.3, since they both exhibit twice the diversity potential compared to conventional TCM. As seen in Figure 6.3, with the advent of STBC-IQ-TCM a further 6.4 dB gain can be obtained at a BER of 10^{-5} compared to the IQ-TCM and STBC-TCM schemes. By contrast, the BICM scheme exhibits only transmit diversity gain but no IQ diversity gain, as we can observe in Figure 6.3. This is because when further randomising the output bit-sequence of a random interleaver, we simply arrive at a different but similarly randomised bit-sequence. In the context of 16QAM BICM having four bits per symbol, four bit-interleavers were employed for interleaving the four modulated bits in parallel. On the other hand, each of the I and Q interleavers will be further randomising two BICM output bit-sequences in parallel. Therefore, no interleaving gain is attainable, when employing extra I and Q interleavers in the context of 16QAM BICM. However, this will not be true in the context of 8PSK BICM, as we will argue in Section 6.4.3. Upon returning to Figure 6.3, since in BICM the bit-based minimum Hamming distance of the codewords is maximised [14], which is the decisive criterion in the context of Rayleigh fading channels, BICM will benefit from a lower bit error probability in Rayleigh fading channels than that of TCM, because TCM maximises the free Euclidean distance of bits within the modulated signal

constellation. Note that the performance of the conventional TCM scheme is significantly lower than that of conventional BICM owing to the existence of unprotected bits in the 16QAM TCM symbol. However, the achievable coding gain of the STBC-IQ-TCM scheme is only about 0.8 dB less than that of the STBC-IQ-BICM scheme at a BER of 10^{-5}.

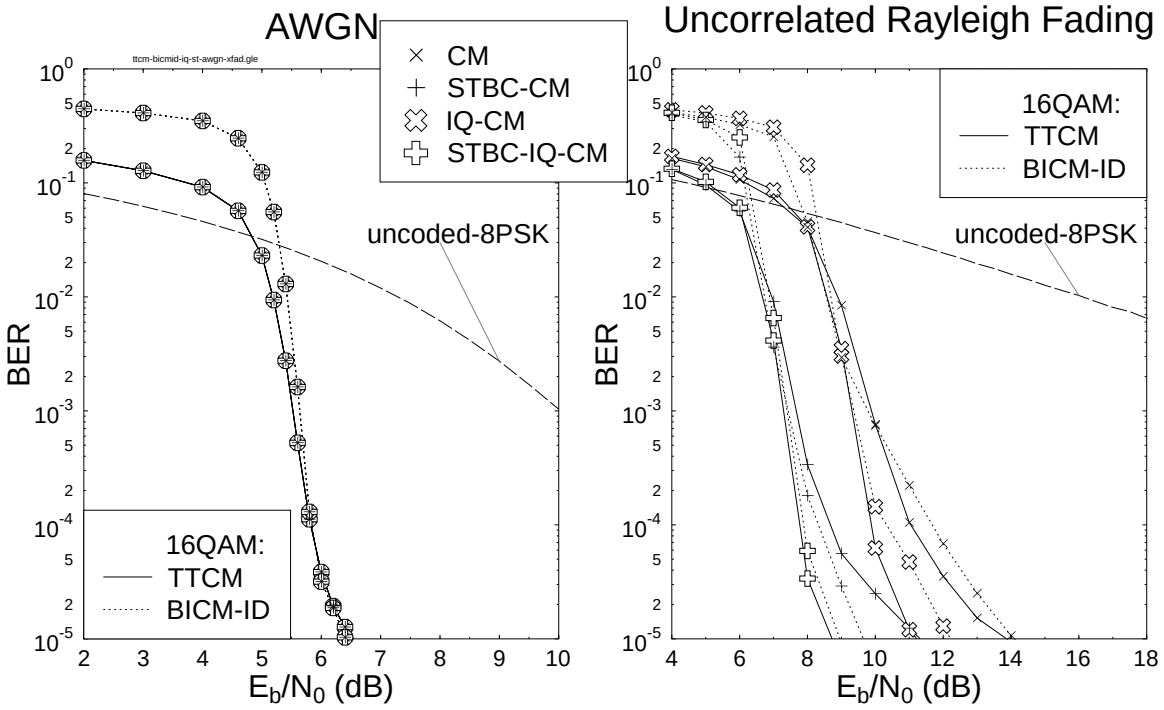

Figure 6.4: BER versus E_b/N_0 performance of the 16QAM based **TTCM** and **BICM-ID** schemes, when communicating over AWGN and uncorrelated flat Rayleigh fading channels. The legends are described in Footnote 1. An interleaved codeword length of 1000 symbols was used and the performance of the uncoded 8PSK scheme is also plotted for benchmarking the CM schemes, all having an effective throughput of **3 BPS**.

Let us now study in Figure 6.4 the BER versus E_b/N_0 performance of the 16QAM based iterative TTCM and BICM-ID schemes, when communicating over AWGN and uncorrelated flat Rayleigh fading channels, again, in the context of the conventional CM, STBC-CM, IQ-CM and STBC-IQ-CM arrangements defined in Footnote 1. An interleaved codeword length of 1000 symbols was used and the performance of the uncoded 8PSK scheme was also plotted as a benchmarker. As portrayed in Figure 6.4, the TTCM scheme exhibits a better performance than BICM-ID in the low SNR region, when communicating over AWGN channels, although their BER curves converge beyond $E_b/N_0 = 5.8$ dB. Again, no space and no time diversity gain was achieved, when communicating over Gaussian channels.

From Figure 6.4 we infer that similarly to the performance trends observed for the TCM schemes of Figure 6.3, the BER curve of IQ-TTCM merged with that of STBC-TTCM in the high-SNR region, when communicating over the uncorrelated flat Rayleigh fading channels, since they both exhibit twice the diversity potential compared to conventional TTCM. However, the achievable diversity/coding gain of TTCM was found lower than that of TCM owing to the fact that TTCM has already achieved part of its total attainable diversity gain with the aid of its iterative turbo decoding procedure, assisting in achieving time diversity. Nonetheless, at a BER of 10^{-5} the performance of STBC-IQ TTCM is

about 5.1 dB better than that of the conventional TTCM scheme. Note from Figure 6.4 that the BICM-ID scheme is capable of exploiting the IQ diversity owing to employing iterative detection, when communicating over uncorrelated flat Rayleigh fading channels. Although IQ-BICM-ID exhibits a performance, which is about 1 dB lower than that of IQ-TTCM at BER=10^{-5}, nonetheless the coding gain of STBC-IQ-BICM-ID is only marginally lower than that of STBC-IQ-TTCM. However, unlike in the context of the TCM and TTCM schemes, the BER performance of the IQ-BICM-ID scheme – which benefits from IQ diversity – was lower than that of the STBC-BICM-ID scheme in the high-SNR region, where the latter exhibits a transmit diversity of order two. This is because the IQ diversity gain potential of IQ-BICM-ID is a benefit that is turned into reality by the iterative decoding, rather than accruing automatically from employing IQ interleaving alone. This observations may be confirmed in Figure 6.4.

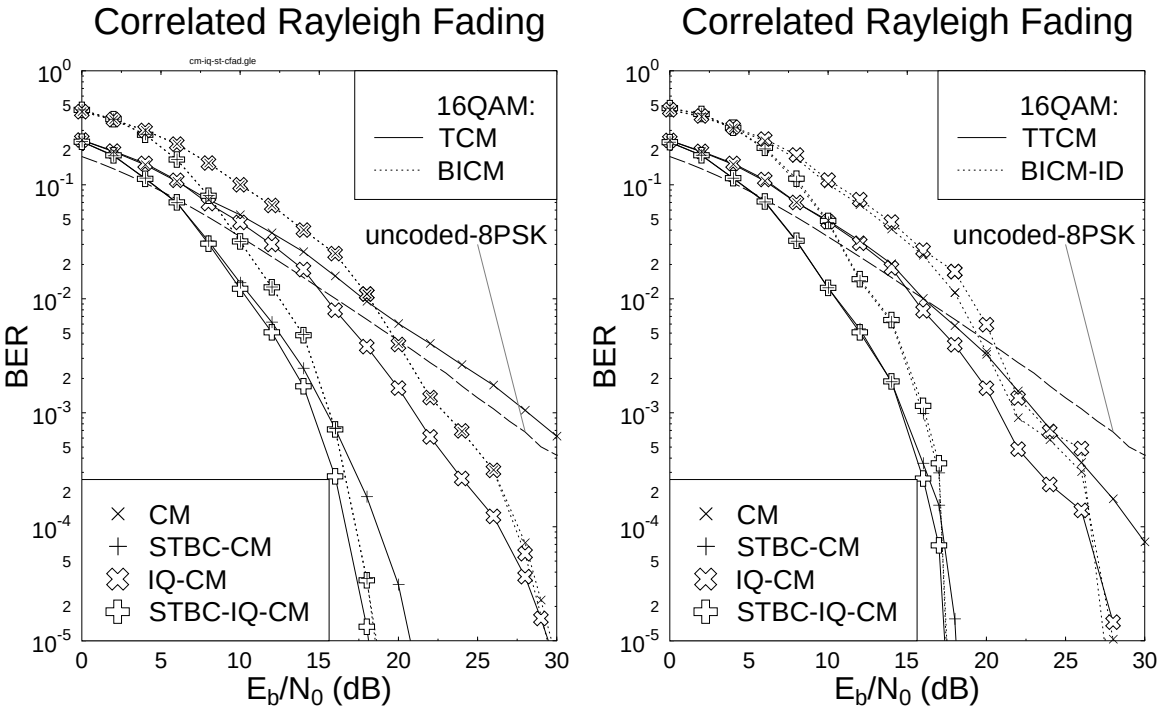

Figure 6.5: BER versus E_b/N_0 performance of the 16QAM based **TCM**, **BICM**, **TTCM** and **BICM-ID** schemes, when communicating over correlated flat Rayleigh fading channels having a normalised Doppler frequency of 3.25×10^{-5}. The legends are described in Footnote 1. An interleaved codeword length of 10000 symbols was used and the performance of the uncoded 8PSK scheme is also plotted for benchmarking the CM schemes, all having an effective throughput of **3 BPS**.

Note that encountering uncorrelated flat Rayleigh fading channels would imply that the channel interleaving has an infinitely long memory or that the vehicular speed is infinite. However, practical Rayleigh fading channels exhibit correlated fading and the degree of the correlation experienced depends on the associated normalised Doppler frequency. Let us now investigate the performance of the proposed schemes under correlated flat Rayleigh fading channel conditions having a normalised Doppler frequency of 3.25×10^{-5} in Figure 6.5, where an interleaved codeword length of 10000 symbols was used. Note that the BER performance of the uncoded 8PSK benchmarker is the same, when communicating over uncorrelated and correlated flat Rayleigh Fading channels. However, the performance of the CM schemes degrades, when the fading exhibits a high degree of correlation. As portrayed at the left of Figure 6.5, the performance of the conventional TCM scheme becomes lower than that

of the uncoded 8PSK benchmarker, when communicating over correlated flat Rayleigh fading channels. However, with the advent of IQ interleaving, the performance of the IQ-TCM scheme improved significantly and it becomes better than that of BICM (or IQ-BICM) under these conditions. On the other hand, STBC-IQ-TCM performs better than STBC-BICM (or STBC-IQ-BICM), although STBC-TCM performs worse than STBC-BICM, when the slowly fading channel exhibits a normalised Doppler frequency of 3.25×10^{-5}, as evidenced in Figure 6.5. However, IQ-TCM is outperformed by STBC-TCM, when communicating over correlated flat Rayleigh fading channels. This is because, the two STBC transmitter antennas were arranged sufficiently far apart, so that their transmitted signals experience independent channel fading, whereas the IQ-interleaved signals suffer from correlated channel fading, as a result of the limited-memory 10000-symbol interleaver.

The performance of the TTCM and BICM-ID schemes communicating over correlated flat Rayleigh fading channels was also shown at the right of Figure 6.5. Specifically, IQ-BICM-ID (or STBC-IQ-BICM-ID) shows no advantage over its conventional BICM-ID (or STBC-BICM-ID) counterpart, when communicating over slowly fading channels. By contrast, IQ-TTCM still outperforms conventional TTCM by approximately 2 dB under these conditions. However, the performance of the STBC-IQ-TTCM arrangement is only marginally better than that of its STBC-TTCM counterpart.

6.2.4 Conclusions

In this section we proposed a set of novel STBC-IQ aided CM schemes for transmissions over both AWGN and Rayleigh fading channels. The STBC-IQ-TCM, STBC-IQ-TTCM and STBC-IQ-BICM-ID schemes are capable of providing significant diversity gains over their conventional counterparts. Specifically, in case of the uncorrelated flat Rayleigh fading channel, coding gains of 26.1 dB, 28.2 dB, 26.9 dB and 28.1 dB were achieved over the identical-throughput uncoded 8PSK benchmarker at a BER of 10^{-4} by the STBC-IQ-TCM, STBC-IQ-TTCM, STBC-IQ-BICM and STBC-IQ-BICM-ID schemes, respectively. All schemes achieved an effective throughput of 3 BPS without bandwidth expansion. From Figures 6.3, 6.4 and 6.5 STBC-IQ-TTCM was found to be the best scheme, when communicating over AWGN as well as over uncorrelated and correlated flat Rayleigh fading channels.

For systems requiring the reduced complexity of a single-transmitter scheme, the IQ-interleaved TCM/TTCM scheme is still capable of doubling the achievable diversity potential of conventional symbol-interleaved TCM/TTCM with the aid of a single transmit antenna, although the IQ diversity attainable decreased, when the fading channel exhibited a higher correlation.

Having studied the proposed STBC-IQ aided CM schemes for transmission over both AWGN and non-dispersive Rayleigh fading channels, we will now invoke Direct Sequence (DS) spreading and study a STBC-based CDMA system designed for transmission over dispersive Rayleigh fading channels in the following section. Then in Section 6.4 we will amalgamate it with STBC-IQ CM schemes.

6.3 Space-Time Block Coding-Assisted Double-Spread Rake Receiver-Based CDMA

6.3.1 Introduction

In this section we will present a novel STBC-assisted Double-Spread Rake Receiver (DoS-RR) based CDMA scheme designed for downlink (base to mobile) transmissions over dispersive Rayleigh fading channels, where all the transmitted user signals arriving at a particular mobile station experience identical propagation conditions. The design philosophy of this system is that of achieving the maximum possible diversity gain, when communicating over dispersive fading channels. This is achieved by systematically incorporating performance enhancements, which is capable of providing transmit diversity, time diversity and multipath diversity. Specifically, the proposed STBC-assisted DoS-RR (STBC-DoS-RR) scheme invokes Turbo Convolutional (TC) [11] channel coding and STBC for achieving both time and space diversity gains in addition to the path diversity gain provided by the dispersive Rayleigh fading environments. We will demonstrate that the double-spreading mechanism of the STBC-DoS-RR scheme is capable of detecting the wanted user's channel-impaired wideband signals with the aid of a low-complexity Rake receiver, without resorting to employing a complex interference cancellation scheme. The performance of the proposed scheme was investigated using Quadrature-Phase-Shift-Keying (QPSK), when communicating over dispersive channels. It will be shown that the wideband scheme advocated is capable of achieving E_b/N_0 gains up to 35 dB in comparison to an uncoded single-transmitter scheme communicating over narrowband channels.

Space-Time Coding (STC) schemes [14, 164, 165, 168] were originally proposed for transmissions over narrowband fading channels. When encountering wideband channels, Multi-Carrier Code Division Multiple Access (MC-CDMA) and Orthogonal Frequency Division Modulation (OFDM) [63] can be utilised for converting the wideband channel to numerous narrowband channels. However, a detrimental effect of employing STTCs or STBCs is that not only the desired signal, but also the Multiple Access Interference (MAI) and the Co-Channel Interference (CCI) are enhanced due to the multiple antenna based transmission diversity scheme and hence the effective average SNR and SIR may not be substantially improved. Nonetheless, the fading-induced fluctuation of the SNR and SIR are improved, which results in overall performance improvements. These are the most important limiting factors of employing space-time coding in CDMA systems [171]. By contrast, Multi-User Detection (MUD) and Interference Cancellation (IC) constitute two efficient ways of combating the MAI and CCI, although their complexity may become excessive, especially, when the number of users supported is high. On the other hand, a low-complexity Rake receiver can be used for obtaining path diversity in CDMA systems, provided that the maximum propagation path delay is shorter than a fraction of the original symbol period, and hence the ISI can be neglected but still sufficiently high for encountering a number of resolvable multipath components after Direct Sequence (DS) spreading. Furthermore, the multipath intensity profile typically has an exponentially decaying shape in realistic channel conditions, where the longer the path delay, the lower the magnitude of the path. Hence the ISI induced by a long-delay path is typically insignificant and can be neglected. It is worth noting that in [172], an adaptive Space-Time Spreading (STS) assisted DS-CDMA scheme was proposed, which is capable of maintaining an arbitrary diversity order and transmission integrity by adaptively controlling the amount of STS. Based on these arguments the employment of a simple Rake receiver

is often more practical, than that of a complex IC scheme, especially in a downlink scenario imposing identical propagation conditions on all users.

In our proposed system, a double-spreading assisted Rake receiver is used. Specifically, in the first spreading operation Walsh code based unique user signatures are used for distinguishing the users and hence for mitigating the effects of MAI, while in the second spreading step a random code is employed for DS spreading and hence for attaining path diversity. Additionally, STBC is invoked for achieving transmit diversity, while a power efficient TC channel code [11] is used for obtaining time diversity.

6.3.2 System Description

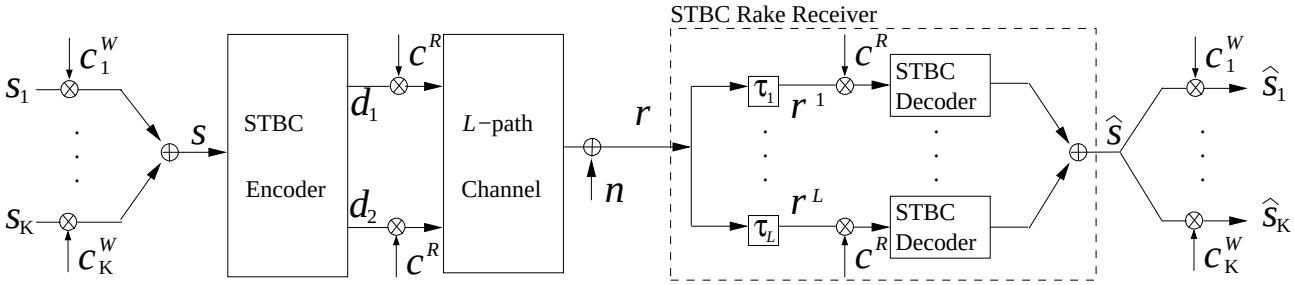

Figure 6.6: Block diagram of the space-time block coding assisted double-spread Rake receiver based downlink CDMA scheme.

The block diagram of the STBC-DoS-RR based CDMA scheme proposed for downlink (base to mobile) transmissions is shown in Figure 6.6. The information destined for user-i, where we have $i \in \{1 \dots \mathsf{K}\}$, is first encoded by the TC channel encoder to yield S_i. Then, S_i is spread by the Walsh code c_i^W, where each user is assigned a unique Walsh code. The sum S of the signals of all users is then passed to the STBC encoder on a chip by chip basis. Here Alamouti's G_2 code [164] associated with two transmit antennas is used for STBC. The STBC encoder yields two chips, namely d_1 and d_2, one for each transmit antenna. Both chips are then DS spread by the same random code for the sake of attaining multipath diversity, namely c^R, before transmission through the L-path dispersive Rayleigh fading channels associated with the two transmission antennas. A single STBC-based Rake receiver is utilised at the mobile station. In the Rake receiver we have L number of delayed replicas of the transmitted signal, resulting in the received signals $r^1 \dots r^L$, where r^i is synchronised to the ith resolvable path having a path delay of τ_i. Each of the signals $r^1 \dots r^L$ will be DS despread by the random code c^R. Due to the employment of the G_2 STBC encoder, each of the L number of DS despread signals benefits from a transmit diversity order of two. Consequently, the STBC decoder is invoked L times, namely once for each of the L number of DS despread signals for obtaining a path diversity of order L. The L number of STBC decoded signals are summed, yielding $\hat{S}$ of Figure 6.6, which benefits from a total diversity order of $2L$. Then, the signal $\hat{S}_i$ of user-i can be obtained by despreading $\hat{S}$ with the aid of the unique Walsh signature sequence c_i^W. Finally, $\hat{S}_i$ is channel decoded by the TC channel decoder in order to yield the estimate of the information transmitted by user-i.

6.3.2.1 Double-Spreading Mechanism

The family of orthogonal Walsh codes is well-known for its attractive zero cross-correlation property [173] expressed as:

$$\sum_{l=1}^{Q} c_i^W[l] \cdot c_j^W[l] \quad = \quad 0; \text{ for } i \neq j, \tag{6.14}$$

where $i, j \in \{1 \dots \mathsf{K}\}$ and $c_i[l] \in \{+1, -1\}$. There are Q chips in a code and the maximum number of Walsh codes of length Q is Q, which allows us to support a maximum number of $\mathsf{K} = Q$ users. Therefore, it is possible to support Q users employing Walsh codes of length Q, without encountering any MAI, provided that the codes' orthogonality is not destroyed by the channel. However, the off-peak auto-correlation of Walsh codes is relatively high [173], which is quantified as:

$$\sum_{l=1}^{Q} c_i^W[m] \cdot c_i^W[l] \quad \neq \quad 0; \text{ for } m, i \in \{1 \dots Q\}. \tag{6.15}$$

Hence, the good cross-correlation properties of orthogonal Walsh codes may be destroyed by the multipath interference encountered in dispersive channels. In contrast to orthogonal Walsh codes, random codes exhibit high cross-correlation, but low off-peak auto-correlation values [173]. Therefore non-orthogonal random codes can be processed by a Rake receiver for obtaining path diversity as a benefit of their low auto-correlation value. However, without additional Walsh-spreading they are only applicable for single user scenarios, since the associated high cross-correlation will result in excessive MAI, i.e. poor 'user-separation'.

To elaborate a little further, the double-spreading mechanism introduced here is different from the conventional method of combining orthogonal Walsh codes with non-orthogonal random or Pseudo-Noise (PN) scrambling codes. The mechanism of both methods is illustrated in Figure 6.7. Specifically, in the context of the conventional method the chip duration of the Walsh code is identical to that of the random code. For the transmission of a B-symbol burst using orthogonal Walsh codes having a spreading factor of Q, there are Q chips per information symbol, resulting in $B \times Q$ chips per transmission block. After each of the information symbols has been DS spread by the Q-chip orthogonal Walsh code, a non-orthogonal random code of length $B \times Q$ chips is multiplied by the $B \times Q$-chip transmission block on a chip-by-chip basis in order to decrease the auto-correlation of the orthogonal Walsh codes. Although the resultant spread signal exhibits a reduced auto-correlation, the cross-correlation of the various users' signals is no longer zero.

By contrast, the proposed double-spreading mechanism invokes $\bar{\mathsf{Q}}$-chip orthogonal Walsh codes for supporting $\mathsf{K} = \bar{\mathsf{Q}}$ users with the aid of DS spreading of each symbol to $\bar{\mathsf{Q}}$ chips. Then each of the $\bar{\mathsf{Q}}$ chips is further spread by a $\tilde{\mathsf{Q}}$-chip non-orthogonal random code for attaining multipath diversity, where there are a total of Q chips per information symbol and we have $\bar{\mathsf{Q}} \times \tilde{\mathsf{Q}} = Q$. The first spreading operation spreads each information symbol of user-i to $\bar{\mathsf{Q}}$ chips, using the Walsh code c_i^W. Then the $\tilde{\mathsf{Q}}$-chip random code further spreads each of the $\bar{\mathsf{Q}}$ number of resultant chips to $\tilde{\mathsf{Q}}$ chips. Hence there are a total of $\bar{\mathsf{Q}} \times \tilde{\mathsf{Q}} = Q$ chips per information symbol also according to the conventional method highlighted in the previous paragraph, although the spreading mechanism used is different. In other words, here the same $\tilde{\mathsf{Q}}$-chip random code repeats itself every $\bar{\mathsf{Q}}$ chips, namely for each of the Walsh-code chips. Note that the l^{th} chip of the $\bar{\mathsf{Q}}$-chip Walsh code of all users is spread by the same random

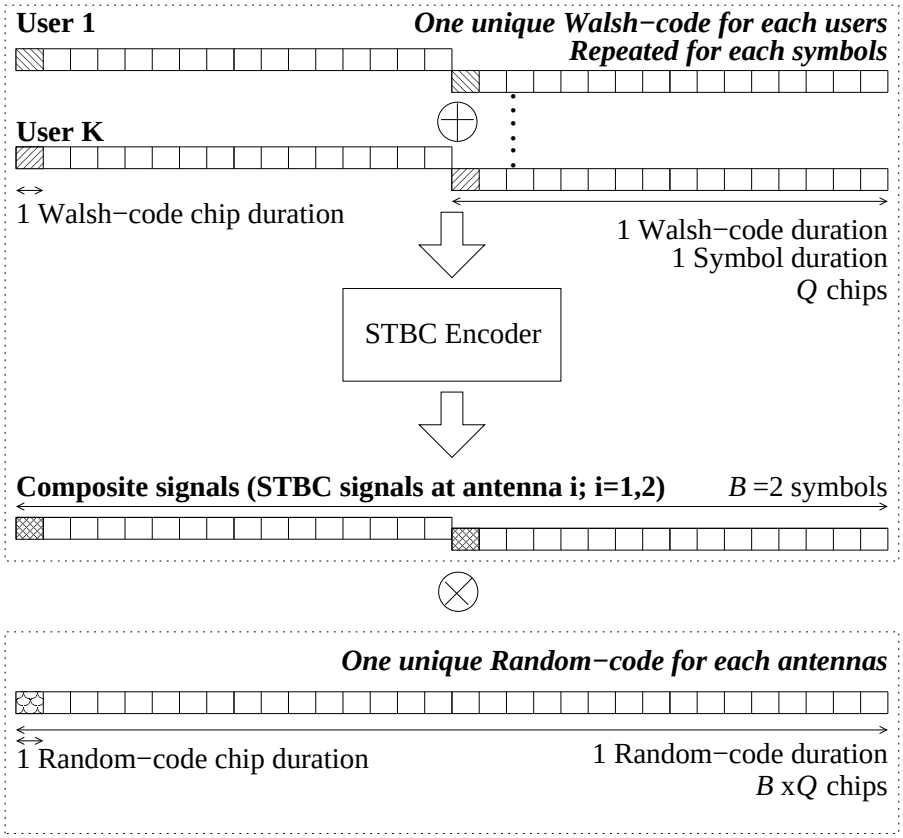

(a) Conventional-spreading mechanism.

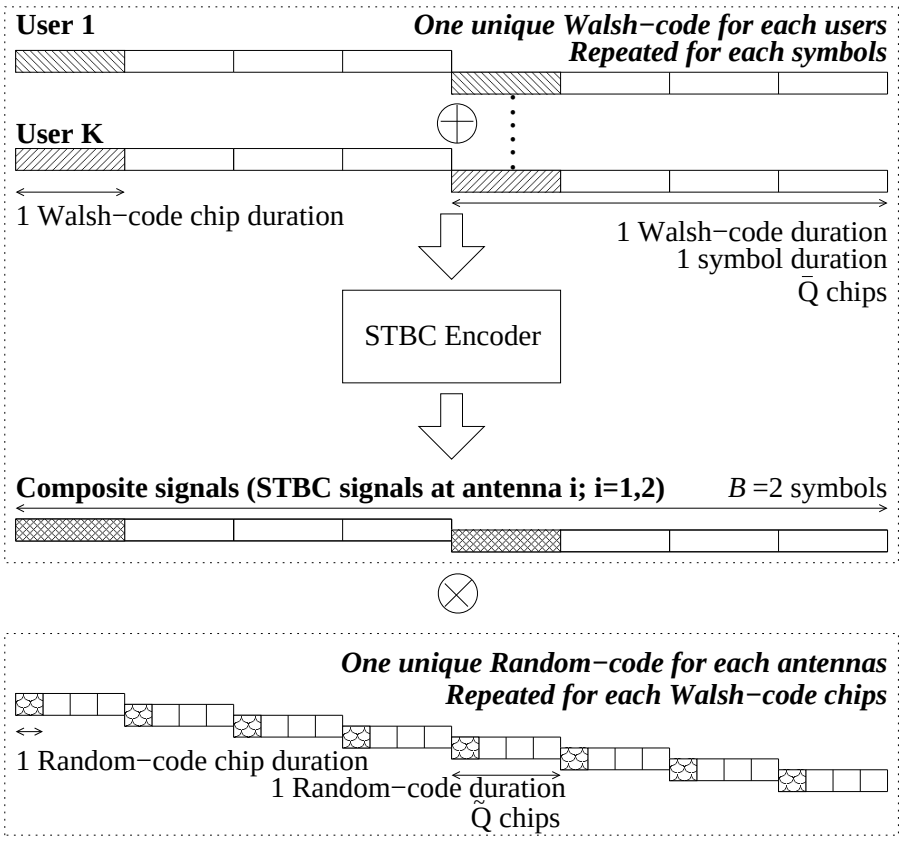

(b) Double-spreading mechanism.

Figure 6.7: Mechanism of conventional-spreading and double-spreading employing Walsh codes and Random codes.

code, which are conveyed via the same channel and experience an identical multipath interference of:

$$I[l] = I_k[l] = I_i[l], \tag{6.16}$$

where $k, i \in \{1 \dots \bar{\mathsf{Q}}\}$ and $I_k[l]$ is the interference imposed on the l^{th} chip of the Walsh code of user-k, $c_k^W[l]$. If a slow fading channel is encountered, the Channel Impulse Response (CIR) of the multipath components of the channel can be assumed to be time-invariant for the duration of $Q = \bar{\mathsf{Q}} \times \tilde{\mathsf{Q}}$ chips. Since each chip of the $\bar{\mathsf{Q}}$-chip Walsh code is further spread by the same random code as seen in Figure 6.7(b), each of the $\bar{\mathsf{Q}}$ chips, again, experiences identical multipath interference in the slow fading channels considered, yielding:

$$I = I[l] = I[m]; \quad l, m \in \{1 \dots \bar{\mathsf{Q}}\}. \tag{6.17}$$

With the aid of Equations 6.14, 6.16 and 6.17 the resultant cross-correlation of the Q-chip codes used by the double-spreading mechanism of Figure 6.7(b) can be shown to be zero, which is expressed as:

$$\begin{aligned} \sum_{l=1}^{\bar{\mathsf{Q}}} (c_i^W[l] \cdot I_i[l]) \cdot (c_k^W[l] \cdot I_k[l]) &= I^2 \cdot \sum_{l=1}^{\bar{\mathsf{Q}}} c_i^W[l] \cdot c_k^W[l], \\ &= 0; \text{ for } i \neq k. \end{aligned} \tag{6.18}$$

This implies encountering no MAI, hence requiring no IC. Therefore attaining near-single-user performance is feasible with the advent of this simple double-spreading method without the employment of complex IC schemes in slow-fading dispersive channels, provided that the factor $\bar{\mathsf{Q}}$ lower user capacity is tolerable. If the user-capacity is at premium, a factor $\bar{\mathsf{Q}}$ higher user-capacity can be maintained by tolerating the high complexity of the IC.

6.3.2.2 Space-Time Block Coded Rake Receiver

The main idea behind Rake receivers [174] is that of capturing the energy of several multipath components of the channels in a spread spectrum system, provided that the different multipath delays are multiples of the chip duration. The number of resolvable multipath components can be increased by increasing the spreading factor used. The Rake receiver consists of a number of matched filters, often referred to as Rake fingers. The maximum number of Rake fingers required is equal to the number of the resolvable paths. These Rake receiver fingers are synchronised to each path and the corresponding delayed replicas of the transmitted signals are combined coherently or noncoherently. Assuming a perfect knowledge of the CIR and multipath delays, the Rake receiver is equivalent to a Maximal Ratio Combining (MRC) scheme having a diversity order L [175]. In a conventional single-transmitter scenario the ith delayed replica of the transmitted signal, r^i, is first DS despread and then multiplied with the complex conjugate of the corresponding CIR tap. However, when using transmit diversity, each of the DS despread signals is conveyed to one of the STBC decoders shown in Figure 6.6. In other words, there are L number of STBC decoders, each corresponding to one resolvable path of the dispersive channel.

In the STBC scheme using Alamouti's G_2 code [164], the encoding requires two time slots and two transmit antennas for transmitting two symbols, namely x_1 and x_2. Specifically, G_2 was defined in

Equation 6.1 [164, 165], but we repeated it here for the sake of the reader's convenience:

$$G_2 = \begin{pmatrix} x_1 & x_2 \\ -x_2^* & x_1^* \end{pmatrix},$$

where, x^* denotes the complex conjugate of the signal x. In time slot 1, signals x_1 and x_2 are transmitted, while in time slot 2, signals -x_2^* and x_1^* are emitted from the transmit antennas 1 and 2, respectively. We assume that the fading amplitude is constant across the two STBC time slots, where each time slot has a duration of $\tilde{\mathrm{Q}}$ chips, or one chip of c^W. Hence we can write:

$$h_p^i(t) = h_p^i(t+T) = h_p^i = \alpha_p^i e^{j\theta_p^i}; \quad p \in \{1, 2\}, \tag{6.19}$$

where T is the time slot duration, while h_p^i is the CIR associated with path i and transmit antenna p. The received signals after despreading are:

$$\begin{aligned} r_1^i = r^i(t) &= h_1^i \cdot x_1 + h_2^i \cdot x_2 + n_1^i, \\ r_2^i = r^i(t+T) &= -h_1^i \cdot x_2^* + h_2^i \cdot x_1^* + n_2^i, \end{aligned} \tag{6.20}$$

where r_t^i is the received signal at instant t for path i, while n_t^i is the random variable representing the sum of the receiver noise at instant t and the multipath interference imposed by path i after despreading. Equivalently, the two signals received over path i can be represented in matrix form as:

$$\begin{aligned} \begin{pmatrix} r_1^i \\ (r_2^i)^* \end{pmatrix} &= \begin{pmatrix} h_1^i & h_2^i \\ (h_2^i)^* & -(h_1^i)^* \end{pmatrix} \begin{pmatrix} x_1 \\ x_2 \end{pmatrix} + \begin{pmatrix} n_1^i \\ (n_2^i)^* \end{pmatrix} \\ \mathbf{r^i} &= \mathbf{A^i} \cdot \mathbf{x} + \mathbf{n^i}, \end{aligned} \tag{6.21}$$

where $\mathbf{A^i}$ is termed the system matrix associated with path i. Since the transmitted signal vector $\mathbf{x}$ can be factorised out from the STBC received signal vector $\mathbf{r^i}$, as shown in Equation 6.21, due to the orthogonality of the G_2 code, transmit diversity can be obtained by multiplying $\mathbf{r^i}$ with the conjugate transpose of $\mathbf{A^i}$, namely with $\mathbf{A_i^H}$ during the STBC decoding process. With the aid of the Rake receiver we can sum all the L number of STBC decoded outputs for generating the estimate of:

$$\begin{aligned} \hat{\mathbf{x}} &= \sum_{i=1}^{L} (\mathbf{A_i^H} \cdot \mathbf{r^i}), \\ \begin{pmatrix} \hat{x}_1 \\ \hat{x}_2 \end{pmatrix} &= \left(\sum_{i=1}^{L} \left((\alpha_1^i)^2 + (\alpha_2^i)^2 \right) \right) \begin{pmatrix} x_1 \\ x_2 \end{pmatrix} + \mathbf{N}, \end{aligned} \tag{6.22}$$

where $\mathbf{N}$ is the resultant noise plus interference for all the L paths, while the diversity of order $2L$ can be observed in the context of the term $\sum_{i=1}^{L} \left((\alpha_1^i)^2 + (\alpha_2^i)^2 \right)$.

Having exploited both the space and multipath diversity, now the TC decoder is invoked for attaining further time diversity. Based on Equation 6.22 the soft inputs of the TC decoder can be readily computed. Finally, the estimates of the original information symbols are obtained at the output of the TC decoder. Here, two identical 1/2-rate Recursive Systematic Convolutional (RSC) codes having a constraint length of three were utilised by the turbo encoder, while soft decision trellis decoding utilising the binary Log-Maximum A Posteriori (Log-MAP) algorithm [53] was invoked for turbo decoding. For detailed discussions on TC channel coding the interested reader is referred to [11].

Parameter	Value
Doppler frequency (Hz)	80
Vehicular velocity (mph)	30
First Spreading ratio, $\bar{Q}$	4
Second Spreading ratio, $\tilde{Q}$	8
Total Spreading ratio, Q	32
Chip rate (MBaud)	2.167
Modulation mode	QPSK
STBC code	G_2 [165]
Number of transmitters	2
Number of receivers	1
TC coding rate	1/2
TC constraint length	3
TC decoding iterations	8
TC interleaver length (bit)	1000
Channel A power profile	Equal/Constant
Channel B power profile	Exponential decay
Number of resolvable paths (chip-spaced)	1 to 5

Table 6.1: Parameters of the STBC-DoS-RR CDMA scheme for downlink transmissions.

6.3.2.3 Channel Model and System Parameter Design

In this section the performance of the proposed scheme will be evaluated using the simulation parameters shown in Table 6.1. We denote the conventional single-transmitter scenario as the 'G_1-coded' scheme, which is invoked for comparison with the two-transmitter based G_2 code. We assumed that the receiver determined the CIRs perfectly, while the fading envelope and phase was maintained at a constant level for the duration of two STBC timeslots or for $2Q$=64 chip duration. Two different channels were used in our investigation. Channel A exhibits a CIR having equal-power chip-spaced taps, while the CIR of Channel B exhibits an exponentially decaying power for each of the multipath components. Each path was faded according to independent Rayleigh fading statistics, as described by the parameters of Table 6.1. Figure 6.8 shows the normalised magnitude versus chip delay profile for the 5-path CIR of Channel A and Channel B, where the total power of the paths was normalised to unity. The delay of each path is expressed in terms of chip durations, where the chip duration is equal to the reciprocal of the system's chip rate. We will consider the presence of one to five resolvable paths for Channel A and Channel B.

6.3.3 Simulation Results And Discussions

Let us now compare the performance of the proposed double-spreading scheme and that of the conventional spreading scheme. Figure 6.9 shows the Bit Error Ratio (BER) versus signal to noise ratio per information bit (E_b/N_0) performance of both the double-spreading and that of the conventional spreading schemes in a multi-user scenario for transmissions over Channel A, when using only two

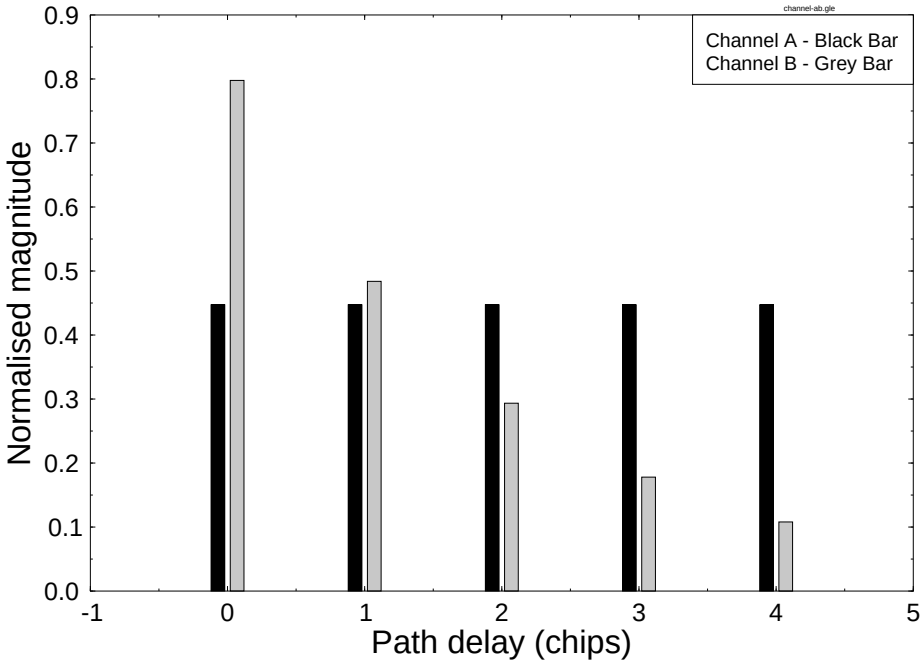

Figure 6.8: The normalised magnitude versus chip delay profile for the 5-path Channel A and Channel B.

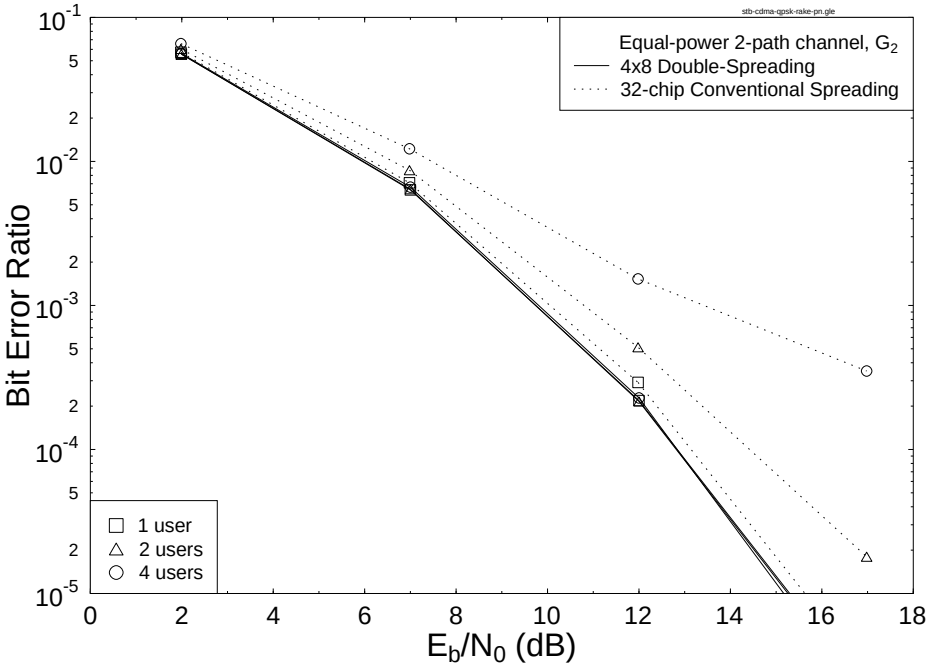

Figure 6.9: Bit Error Ratio (BER) versus signal to noise ratio per information bit (E_b/N_0) performance of both the double-spreading and conventional spreading schemes assisted by a Rake receiver in a multi-user scenario for transmissions over Channel A exhibiting two resolvable paths, utilising the simulation parameters of Table 6.1. The separation of the two CIR taps was one chip interval.

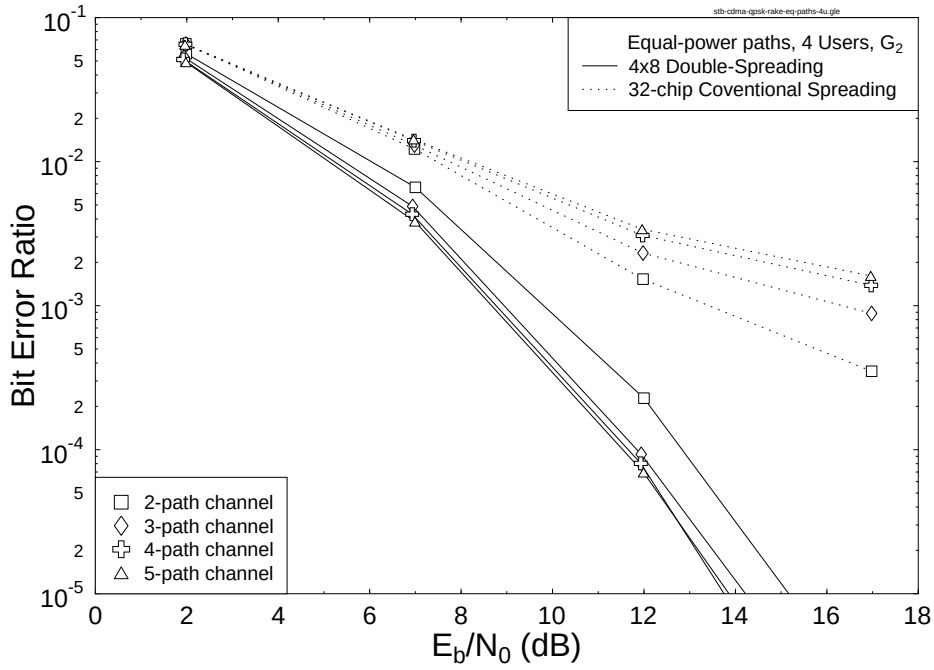

Figure 6.10: BER versus E_b/N_0 performance of both the double-spreading and conventional spreading schemes assisted by a Rake receiver in a multipath scenario for transmissions over Channel A, utilising the simulation parameters of Table 6.1.

resolvable paths, utilising the simulation parameters of Table 6.1. The separation of the two CIR taps was one chip duration.

We observe in Figure 6.9 that conventional spreading experienced performance degradations, when the number of users increased, since the orthogonality of the 32-chip Walsh codes used by the conventional spreading scheme was destroyed by the multipath interference imposed by the two-path channel. By contrast, the double-spreading scheme experienced no performance degradations, when supporting up to $\bar{Q}$=4 users, since the multipath interference can be rejected, as suggested by Equation 6.18. Hence the orthogonality of the 4-chip Walsh codes was preserved by the double-spreading scheme.

Although the conventional spreading method is also capable of attaining multipath diversity with the aid of the signal spreading imposed by the random scrambling code, the multipath components will inflict severe interference, rather than yielding beneficial path diversity, when the number of users is high. This is illustrated in Figure 6.10, where the performance of the conventional spreading scheme degrades, as the channel exhibits an increasing number of multipath components, when supporting four users. By contrast, the performance of the double-spreading scheme improved, as the channel exhibited a higher number of multipath components, although the path diversity gains eventually saturated, when a high number of paths was encountered.

Having investigated the performance gains achieved using the double-spreading scheme, let us now apply the double-spreading scheme in conjunction with the G_2 STBC arrangement utilising two transmitters, as well as along with the single transmitter scenario, which we have denoted as the 'G_1-coded' scheme in Section 6.3.2.3. Explicitly, the G_2 code exhibits twice the diversity gain in comparison to its 'G_1-coded' counterpart. For example, the performance of the G_2 code in single-path Rayleigh channel is identical to that of the G_1 code in the two-path Channel A, as seen from

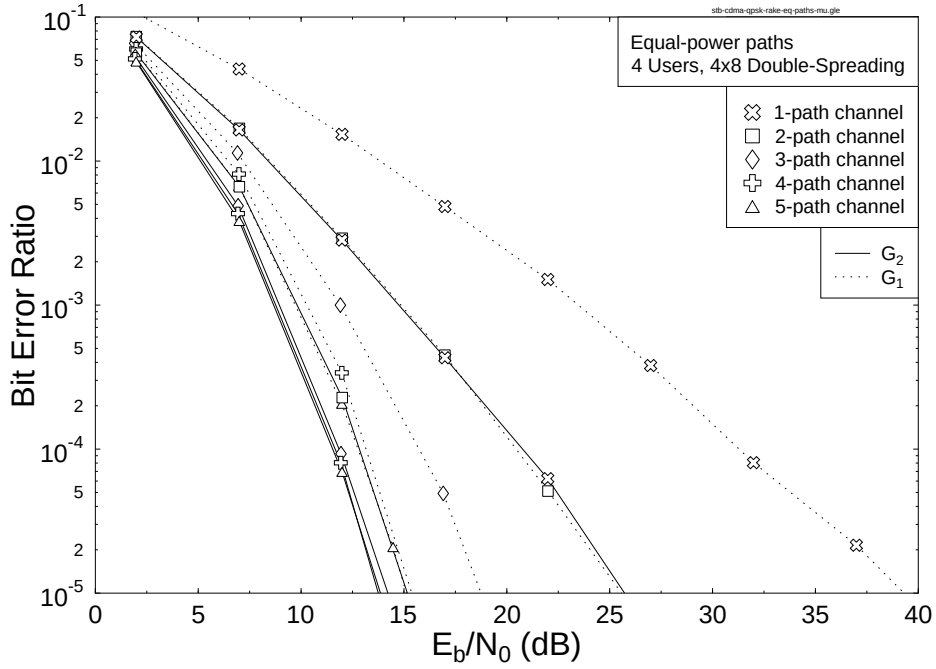

Figure 6.11: BER versus E_b/N_0 performance of the STBC-DoS-RR scheme without TC channel code using the G_2 code of Equation 6.1 and the G_1 code defined in Section 6.3.2.3, for transmissions over Channel A, utilising the simulation parameters of Table 6.1, when supporting four users.

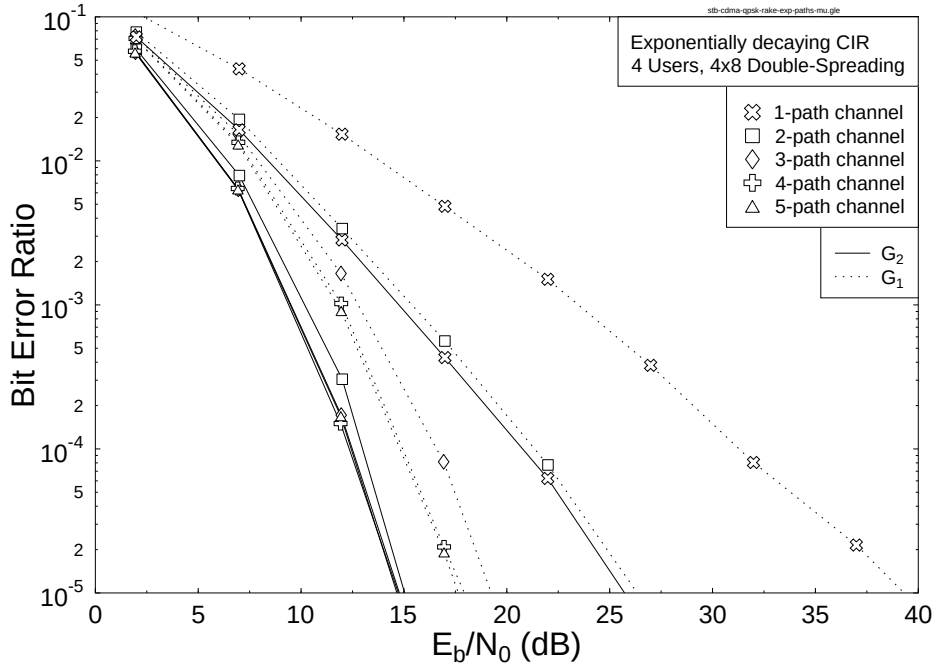

Figure 6.12: BER versus E_b/N_0 performance of STBC-DoS-RR scheme without TC channel code using the G_2 code of Equation 6.1 and the G_1 code defined in Section 6.3.2.3, for transmissions over Channel B, utilising the simulation parameters of Table 6.1, when supporting four users.

Figure 6.11. However, when targeting a total diversity order of four, the performance of the G_2 code used for transmission over the chip-spaced two-path Channel A is slightly better, than that of the G_1 code in the chip-spaced four-path Channel A. This is because the equal power paths in Channel A result in a higher multipath interference, when the channel exhibits a longer delay spread, where the delay spreads of the four-path and two-path channels constitute 50% and 25% of the total duration of the 8-chip random code, respectively. Hence, when aiming for attaining a certain diversity gain, the multipath interference associated with G_2 is less severe, than that in conjunction with G_1, when communicating over dispersive channels having longer delay spreads.

When transmitting over Channel B, where the power of the paths decays exponentially with time, the multipath interference will be less severe in a long-delay-spread environment, although the achievable multipath diversity gain will be decreased. These effects can be studied in Figure 6.12, where the performance of the G_2 code recorded in a single-path scenario is seen to be better than that of the G_1 code employed for transmission over the two-path Channel B. Similarly, the performance of the G_2 code used for transmission over the two-path Channel B is significantly better than that of the G_1 code in the four-path Channel B. Hence, we conclude that the diversity gain of G_2 is higher than that of G_1 in a realistic dispersive channel having negative exponentially decaying CIR, which exhibits a reduced power for the longer delay multipath components.

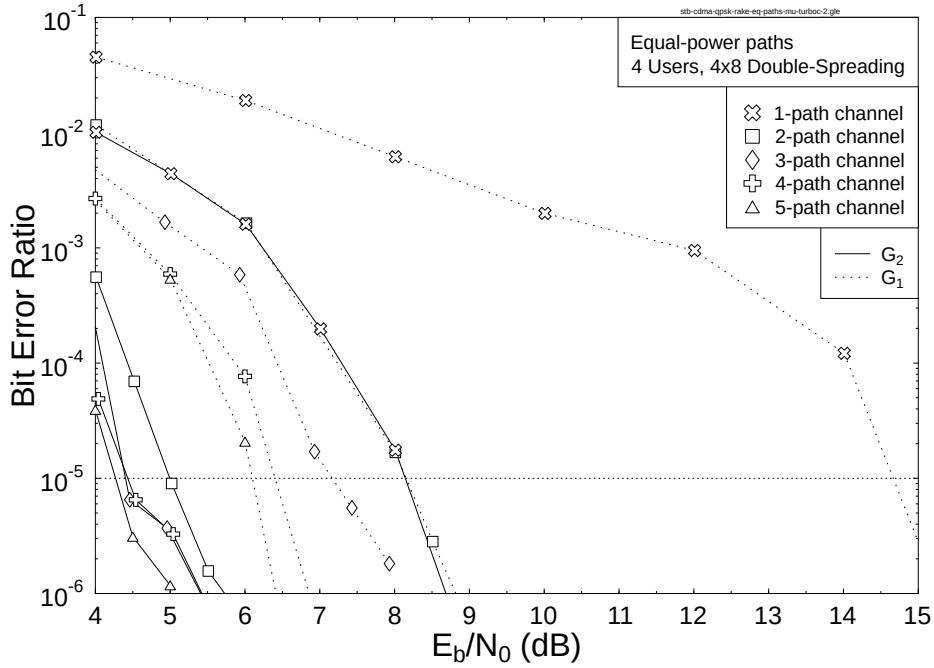

Figure 6.13: BER versus E_b/N_0 performance of the STBC-DoS-RR scheme in conjunction with TC channel coding using the G_2 and G_1 codes for transmissions over Channel A, utilising the simulation parameters of Table 6.1, when supporting four users.

The employment of power efficient TC channel coding further enhances the achievable coding gain of the STBC-DoS-RR scheme. As we can see from Figures 6.13 and 6.14, a high coding gain was obtained by the TC-coded systems compared to the uncoded systems characterised in Figures 6.11 and 6.12. We can observe that at a BER of 10^{-5}, the TC-coded STBC-DoS-RR schemes utilising the G_2 code required only E_b/N_0=4.25 dB, when communicating over the 5-path Channel A, as shown in Figure 6.13. By contrast, the uncoded STBC-DoS-RR scheme utilising G_1 required an E_b/N_0 of

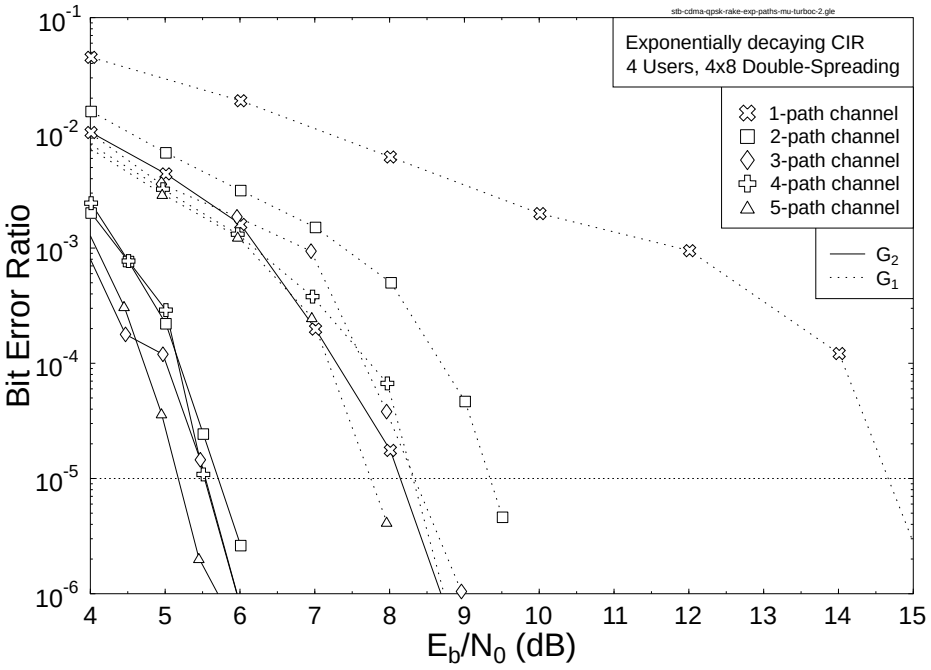

Figure 6.14: BER versus E_b/N_0 performance of the STBC-DoS-RR scheme in conjunction with TC channel coding using the G_2 and G_1 codes for transmissions over Channel B, utilising the simulation parameters of Table 6.1, when supporting four users.

39.3 dB in a narrowband channel, as shown in Figure 6.11, resulting in a total diversity plus coding gain of 35.05 dB. However, we observed from Figure 6.13 that most of this total diversity plus coding gain was already achieved in the 3-path Channel A. Furthermore, we can see from Figure 6.14 that the total gain achieved in the 5-path Channel B for the TC-coded STBC-DoS-RR scheme utilising G_2 was 33.2 dB. By observing Figures 6.13 and 6.14, we notice that the relative performance gain attained is the highest, when the diversity is on the order of two, either utilising G_2 in a narrowband channel for attaining transmit diversity, or utilising G_1 in a 2-path channel for achieving multipath diversity.

The coding plus diversity gain versus the number of resolvable paths at a BER of 10^{-5} for the STBC-DoS-RR scheme against the benchmarker of the uncoded STBC-DoS-RR scheme utilising G_1 in a narrowband channel are summarised in Figure 6.15. The benchmarker required an E_b/N_0 of 39.3 dB for a BER of 10^{-5} as shown in Figure 6.11. It is clear from the figure that the additional path diversity gain attainable is only marginal, when having more than three resolvable paths for the TC or STBC assisted schemes.

6.3.4 Conclusions

In this section, a novel space-time coding-assisted double-spreading aided Rake receiver-based CDMA scheme was proposed and characterised in performance terms, which was contrived for downlink transmissions over dispersive Rayleigh fading channels. The double-spreading mechanism is capable of attaining a near-single-user performance, when using a low-complexity Rake-receiver, rather than a complex IC scheme. Additionally, it is capable of yielding a performance equivalent to that of maximal ratio combining of order L in L-path channels, even when utilising only a single Rake receiver.

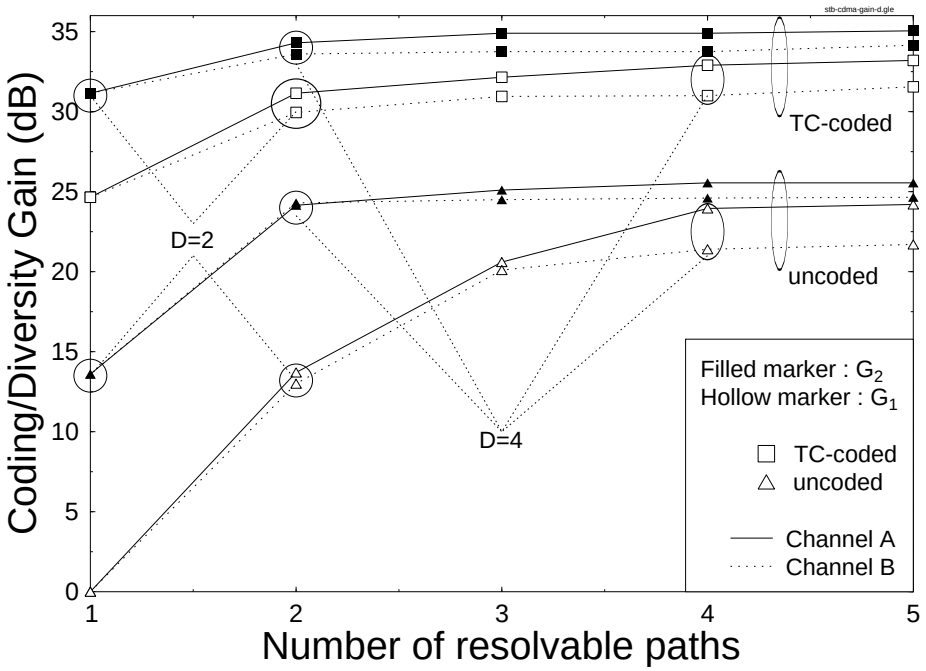

Figure 6.15: Coding plus diversity gain versus the number of resolvable paths at a BER of 10^{-5} for the STBC-DoS-RR scheme. The notation D denotes the diversity order and the uncoded STBC-DoS-RR scheme utilising the G_1 code, when communicating over a narrowband channel was used as the benchmarker exhibiting zero coding/diversity gain. The simulation parameters of Table 6.1 were utilised and the number of users was four.

Explicitly, the transmit diversity and path diversity constitute two independent sources of diversity gain, capable of acting in unison.

It was shown in Figures 6.12 and 6.15 that the employment of transmit diversity is more advantageous than that of multipath diversity in practical dispersive Rayleigh fading channels exhibiting an exponentially decaying CIR. When targeting a certain diversity gain, the multipath interference sensitivity of STBC is lower, than that of a single-transmitter based scheme, especially when communicating over wideband channels having a long delay spread, as investigated in Figures 6.11 and 6.15. With the advent of TC channel coding the proposed scheme required a low bit energy for attaining a low BER. **In conclusion, near-single-user performance can be achieved even with the aid of a single Rake receiver, i.e. without complex IC schemes, at the cost of supporting a factor of $\tilde{\mathbf{Q}}$ reduced number of users.**

Having introduced the STBC-IQ aided CM scheme in Section 6.2 and the STBC-DoS-RR scheme in Section 6.3, we will now amalgamate these two schemes for the sake of jointly exploiting their benefits and investigate the achievable performance in the next section.

6.4 STBC IQ-Interleaved Coded Modulation assisted Double-Spread Rake Receiver-Based CDMA

6.4.1 Introduction

In Section 6.2 we argue that STBC-based IQ-interleaved CM schemes are capable of providing significant diversity gains over their conventional counterparts, when communicating over flat Rayleigh fading channels using a 16QAM modulation scheme. It is important to emphasise that this can be achieved without compromising the coding gain attainable over Gaussian channels. It was found that the achievable transmit diversity was maintained, although the IQ diversity was decreased, when the fading channel exhibited correlation.

Furthermore in Section 6.3, we demonstrated that the STBC-based scheme designed for transmission over non-dispersive fading channels can also be invoked for transmission over dispersive fading channels for the sake of benefiting from multipath diversity. Specifically, when a double-spreading aided Rake receiver is employed, near-single-user performance may be achieved without the aid of complex IC schemes, when transmitting from the base station to the mobile station over dispersive fading channels using QPSK modulation.

In this section, the STBC-IQ-CM scheme proposed in Section 6.2 will be amalgamated with the DoS-RR scheme proposed in Section 6.3 for downlink transmission over 1-path and 2-path Rayleigh fading channels, when supporting four CDMA users, each using 8PSK modulation.

6.4.2 System Description

The block diagram of the amalgamated system can be readily constructed by concatenating the schematics of Figures 6.1 and 6.6, which is shown in Figure 6.16. More specifically, the channel coded signal S_1 of user one, which is shown in Figure 6.16, is generated from the signals $\tilde{s}_I$ and $\tilde{s}_Q$ of Figures 6.1 and 6.16, where we have $S_1 = \tilde{s}_I + j\tilde{s}_q$. At the decoder side, the I and Q components of the signal $\hat{S}_1$, which are shown in Figures 6.6 and 6.16, will be used for computing the signals $\tilde{m}_I$ and $\tilde{m}_Q$ according to Equation 6.12, which are seen in both Figure 6.1 and Figure 6.16.

The CM schemes employed are the non-iterative 64-state TCM and BICM schemes, the iterative 8-state TTCM arrangement using four decoding iterations and the 8-state BICM-ID arrangement invoking eight decoding iterations. Furthermore, we will also employ Turbo Coded Modulation (TuCM) [16] for this study. More specifically, TuCM is an extension of TC codes, where the output bits of a binary TC encoder are suitably punctured and multiplexed before the Gray-labelled signal mapper, for achieving the desired number of information bits per transmitted symbol. For example, two 1/2-rate RSC codes are used for generating a total of four turbo coded bits and this bit stream may be punctured for generating three bits, which are mapped to an 8PSK modulation scheme. By contrast, in separate coding and modulation scheme, any modulation schemes for example BPSK, may be used for transmitting the channel coded bits. Finally, without puncturing, 16QAM transmission would have to be used for maintaining the original transmission bandwidth. Explicitly, a TuCM arrangement employing two 1/2-rate and 4-state RSC component codes using eight decoding iterations will be employed. All the CM schemes exhibit a similar decoding complexity expressed in terms of the total

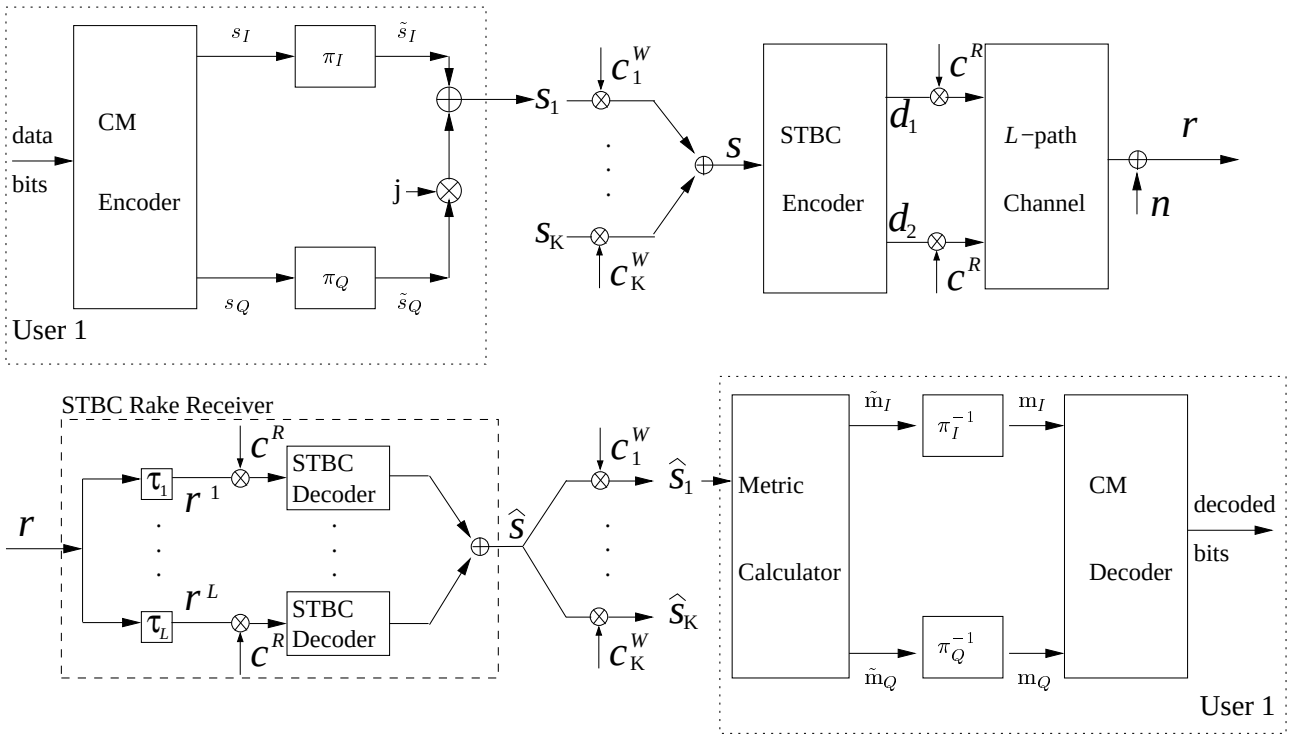

Figure 6.16: Block diagram of the STBC-IQ-CM assisted DoS-RR scheme. The notations π and π^{-1} denote the interleaver and deinterleaver.

number of trellis states, as detailed in Section 6.2.3. The effective throughput of all the 8PSK-based CM schemes is 2 BPS and hence the performance of the uncoded QPSK scheme communicating over flat Rayleigh fading channels will be used as a benchmarker. A codeword length of 1000 symbols was used.

6.4.3 Simulation Results And Discussions

Let us now characterise the performance of the STBC-IQ-CM assisted DoS-RR scheme using the channel parameters and CDMA parameters shown in Table 6.1. The 2-path channel exhibits two equal-power, chip-spaced CIR taps. Specifically, four arrangements will be studied in conjunction with each of the CM schemes, which are denoted in the legends of Figures 6.17 to 6.17 as CM: the conventional CM scheme; STBC-CM: the STBC based conventional CM scheme; IQ-CM: the proposed IQ-interleaved CM scheme using no STBC; and STBC-IQ-CM: the proposed STBC-based IQ-interleaved CM scheme. A codeword length of 1000 symbols was used and the performance of the uncoded QPSK(8PSK) scheme communicating over AWGN and flat Rayleigh fading channels is also plotted for benchmarking the CM schemes having an effective throughput of **2(3) BPS**. Note that the BER performance of the uncoded QPSK/8PSK benchmarker is the same, when communicating over both uncorrelated and correlated flat Rayleigh Fading channels.

In Figure 6.17, we portray the BER versus E_b/N_0 performance of the 8PSK-based non-iterative TCM and BICM schemes, when communicating over correlated flat Rayleigh fading channels exhibiting either one or two resolvable paths. As we can infer from Figure 6.17, that across most of the SNR region the TCM schemes perform slightly better than the corresponding BICM arrangements, al-

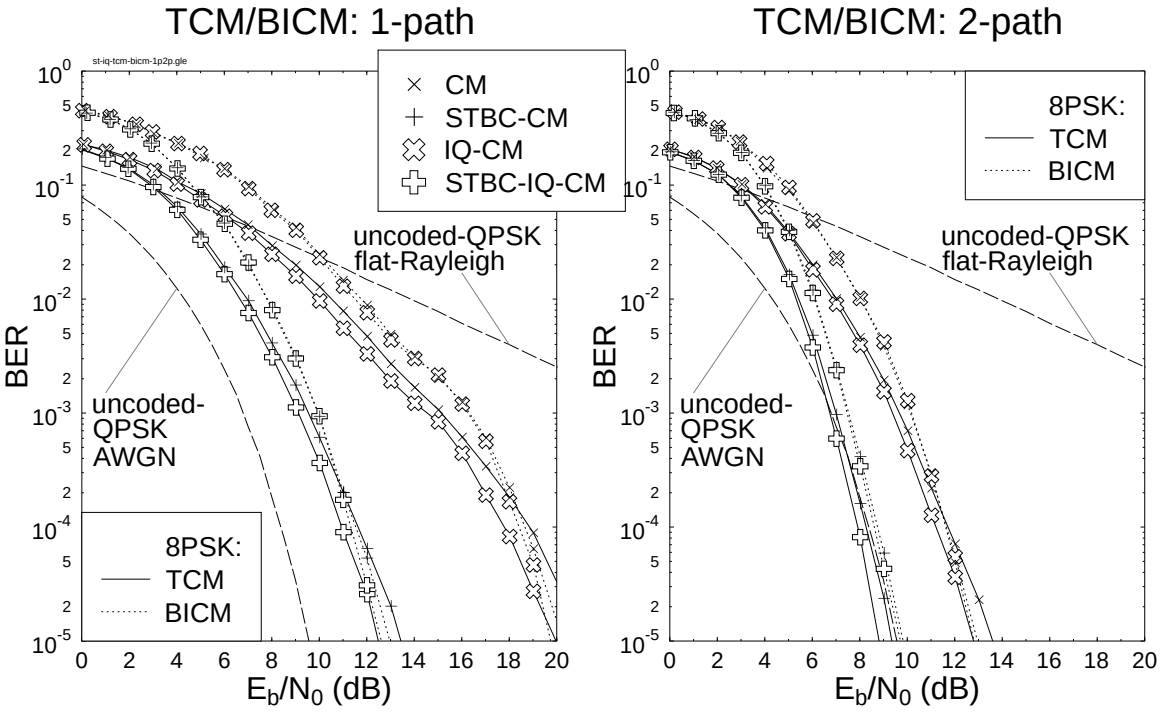

Figure 6.17: BER versus E_b/N_0 performance of the 8PSK based non-iterative **TCM** and **BICM** schemes, when communicating over correlated Rayleigh fading channels exhibiting either one or two resolvable chip-spaced, equal weight paths. The legends are described in Footnote 1. A codeword length of 1000 symbols was used and the performance of the uncoded QPSK scheme communicating over AWGN and flat Rayleigh fading channels is also plotted for benchmarking the CM schemes having an effective throughput of **2 BPS**.

though the BICM arrangements marginally outperform the non-IQ-interleaved TCM arrangements in the high SNR region. However, the channel-properties become more Gaussian-like, when the diversity gain of the system is high. To elaborate a little further, the main contributors of diversity gain in the system are the transmit-diversity and path-diversity, when communicating over slowly fading channels. Therefore, the STBC-TCM arrangement outperforms its STBC-BICM counterpart, when communicating over the 2-path channels, since the TCM schemes originally contrived for AWGN channels outperform the BICM schemes designed for Rayleigh fading channels, in the context of Gaussian-like channels. On the other hand the IQ-interleaved TCM arrangements perform similar to or better than their BICM counterparts, owing to the extra IQ diversity gain achieved as evidenced by Figure 6.17. Note that the performance of the STBC-CM schemes communicating over single-path channels, is similar to that of the corresponding CM schemes communicating over 2-path channels, owing to the independent/uncorrelated nature of the fading experienced by the signals arriving from two different transmit antennas or received via two independent paths.

Note also that in the context of 16QAM studied in Figure 6.3, there was no IQ-interleaving gain for the 16QAM IQ-BICM scheme, since the I (or Q) interleaver will only further randomise two BICM output bit-sequences in parallel, resulting in two similarly randomised bit-sequences. By contrast, in the context of 8PSK, the bits representing the I and Q components cannot be bit-interleaved, while the 8PSK-based BICM scheme seen in Figure 2.15 employed three independent random parallel bit-interleavers. As a result, the I and Q random interleavers of the 8PSK scheme randomise the

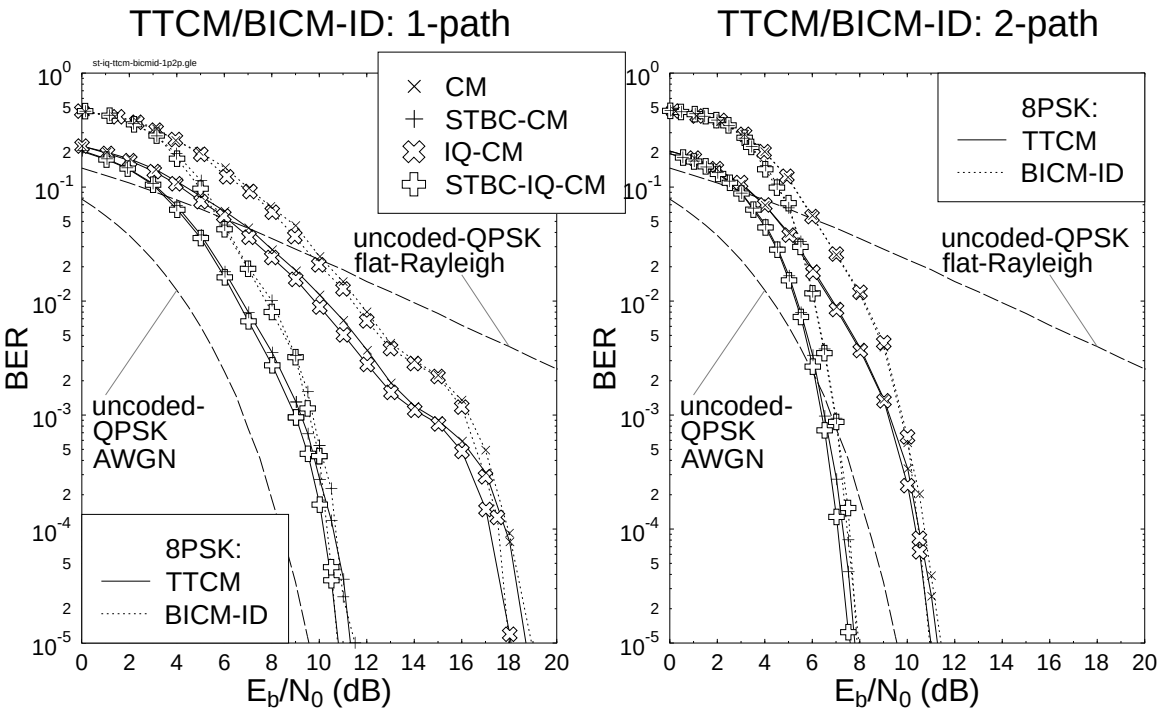

Figure 6.18: BER versus E_b/N_0 performance of the 8PSK based iterative **TTCM** and **BICM-ID** schemes, when communicating over correlated Rayleigh fading channels exhibiting either one or two resolvable chip-spaced, equal weight paths. The legends are described in Footnote 1. A codeword length of 1000 symbols was used and the performance of the uncoded QPSK scheme communicating over AWGN and flat Rayleigh fading channels is also plotted for benchmarking the CM schemes having an effective throughput of **2 BPS**.

quadrature components, rather than randomising the BICM bit-sequences. Therefore this scheme contributes another source of interleaving and hence potentially improves the achievable diversity. As it was evidenced in Figure 6.17, the IQ-interleaved 8PSK-based BICM arrangements benefit from an additional IQ diversity gain in comparison to the BICM arrangements, although this gain is only marginal due to communicating over the slowly fading channels of Table 6.1.

Let us now investigate the achievable performance of the iterative TTCM and BICM-ID arrangements in Figure 6.18. Again, the main contributors of diversity gain in the system are the transmit-diversity and path-diversity, when communicating over the slowly fading channels of Table 6.1. Nonetheless, up to 0.8 dB and 1.0 dB gains may be provided by IQ-TTCM and IQ-BICM-ID, respectively, compared to conventional TTCM and BICM-ID, when communicating over the slowly fading single-path channels of Table 6.1. On the other hand, the TTCM arrangements perform better than or equal to the BICM-ID arrangements. It is also shown in Figures 6.17 and 6.18 that the TTCM scheme is the best performer in the set of TCM, BICM and BICM-ID schemes.

Below we will continue our discourse by comparing the performance of the TTCM and TuCM arrangements in Figure 6.19. Explicitly, the TuCM scheme employs only one bit-interleaver for supporting the operation of the 3-bit based 8PSK modulation, unlike the 8PSK BICM scheme of Figure 2.15 where the modulated bits were randomised in parallel using three bit-interleavers. The TuCM arrangement exhibits no further IQ-diversity gain, when employing two extra IQ interleavers, as we can observe in Figure 6.19. More explicitly, as portrayed in Figure 6.19, the TuCM arrangements –

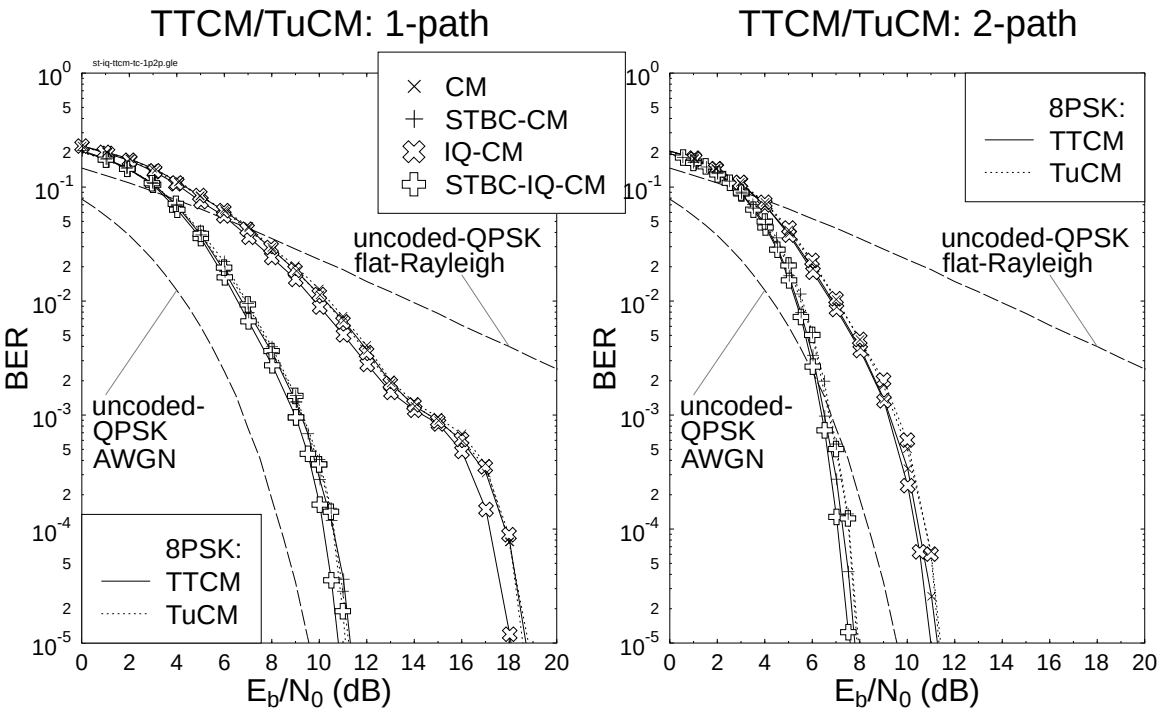

Figure 6.19: BER versus E_b/N_0 performance of the 8PSK based non-iterative **TCM** and **TuCM** schemes, when communicating over correlated Rayleigh fading channels exhibiting either one or two resolvable chip-spaced, equal weight paths. The legends are described in Footnote 1. A codeword length of 1000 symbols was used and the performance of the uncoded QPSK scheme communicating over AWGN and flat Rayleigh fading channels is also plotted for benchmarking the CM schemes having an effective throughput of **2 BPS**.

both with or without IQ-interleaving – perform worse than or similarly to the TTCM arrangements refraining from using IQ-interleaving. This implies that the IQ-interleaved BICM-ID scheme is expected to outperform the TuCM scheme for transmission over the slowly fading channels of Table 6.1.

Based on Figures 6.17 to 6.19, we concluded that that TTCM is the best performer amongst the various CM schemes. Let us now compare the performance of the 8PSK and 16QAM based TTCM schemes, when communicating over correlated Rayleigh fading channels exhibiting either one or two resolvable chip-spaced, equal-weight paths using Figure 6.20. Explicitly, a further coding gain of 7 to 8 dB can be attained by the 8PSK-based STBC-(IQ)-TTCM scheme, when communicating over channels exhibiting a single resolvable path, or by (IQ-)TTCM when communicating over channels exhibiting two resolvable paths, with respect to (IQ-)TTCM when communicating over channels exhibiting one resolvable path, as shown at the left of Figure 6.20. This is owing to doubling the diversity order with the aid of transmit-diversity or multipath-diversity. However, as evidenced by Figure 6.20, the achievable further coding gain with respect to the performance of the TTCM schemes exhibiting a diversity order of two was reduced to about 3.5 to 4 dB, when the diversity order was quadrupled. Similar trends can also be observed for the 16QAM-based TTCM arrangements, as shown at the right of Figure 6.20, when providing an effective throughput of 3 BPS.

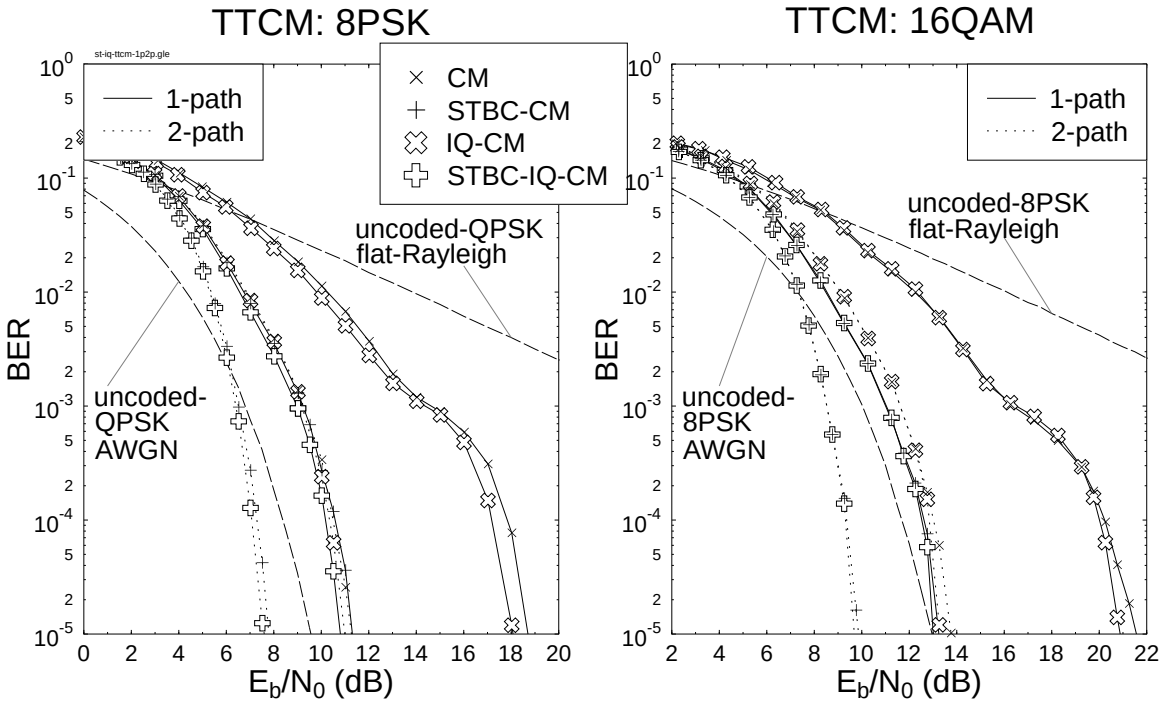

Figure 6.20: BER versus E_b/N_0 performance of the 8PSK and 16QAM based iterative **TTCM** schemes, when communicating over correlated Rayleigh fading channels exhibiting either one or two resolvable chip-spaced, equal weight paths. The legends are described in Footnote 1. A codeword length of 1000 symbols was used and the performance of the uncoded QPSK(8PSK) scheme communicating over AWGN and flat Rayleigh fading channels is also plotted for benchmarking the CM schemes having an effective throughput of **2(3) BPS**.

6.4.4 Conclusions

In conclusion, in these section we have demonstrated that the proposed STBC-IQ-CM assisted DoS-RR scheme is capable of exploiting transmit-diversity, multipath-diversity and IQ-diversity and hence provides significant coding/diversity gains over the identical-throughput uncoded schemes without bandwidth expansion, while supporting multiple downlink CDMA users. Near single-user performance was also achieved without using complex IC schemes. It was shown that the STBC-IQ-CM scheme designed for square QAM modulation in Section 6.2 can also be employed in the context of 8PSK modulation. Furthermore, we have shown in Section 6.3 that the DoS-RR scheme of Figure 6.6 employing QPSK modulation can also be extended to 8PSK and 16QAM for achieving a higher effective throughput without experiencing any BER error floor, although only a simple Rake receiver is employed for supporting multiple downlink CDMA users in dispersive Rayleigh fading channels.

6.5 Chapter Conclusions

In this chapter we have proposed two schemes for achieving diversity gain. Specifically, in Section 6.2 a combination of transmit-diversity and IQ-diversity was exploited for achieving a substantial diversity gain using high-order modulation schemes, while in Section 6.3, we have exploited transmit-diversity and multipath-diversity using a simple Rake receiver benefiting from the proposed double spreading

in the context of low-level modulation scheme. Finally, the two designs were amalgamated for yielding a new scheme which is capable of exploiting transmit-diversity, IQ-diversity and multipath-diversity by employing the CM schemes studied in Chapter 2.

Specifically, coding gains of 26.1 dB, 28.2 dB, 26.9 dB and 28.1 dB were achieved over the identical-throughput uncoded 8PSK benchmarker at a BER of 10^{-4} by the 16QAM based STBC-IQ-TCM, STBC-IQ-TTCM, STBC-IQ-BICM and STBC-IQ-BICM-ID schemes, respectively, when communicating over the uncorrelated flat Rayleigh fading channel, as evidenced in Figures 6.3 and 6.4. It was shown in Figures 6.3 and 6.4 that the IQ-TCM and IQ-TTCM schemes were capable of doubling the achievable diversity potential of the conventional symbol-interleaved TCM and TTCM schemes. Explicitly, similar performances were achieved by both IQ-TCM and STBC-TCM, as well as by IQ-TTCM and STBC-TTCM. However, it was shown in Figure 6.5 that the IQ diversity attainable decreased, when the fading channel envelope exhibited correlation.

It was illustrated in Section 6.3.3 that with the advent of the double-spreading based Rake receiver, near-single-user performance can be achieved without employing complex interference cancellation schemes, although this complexity reduction is achieved at the cost of supporting a factor of $\tilde{Q}$ reduced number of users. Specifically, transmit diversity and path diversity constitute two independent sources of diversity gain in the context of the STBC-DoS-RR CDMA downlink. It was shown in Figures 6.12 and 6.15 that the employment of transmit diversity is more advantageous than that of the multipath diversity in practical dispersive Rayleigh fading channels exhibiting an exponentially decaying CIR.

The proposed STBC-IQ-CM assisted DoS-RR scheme was capable of exploiting transmit-diversity, multipath-diversity and IQ-diversity, hence providing a significant coding/diversity gain over the similar throughput uncoded scheme, which is achieved without bandwidth expansion, while supporting a number of CDMA users. It was shown in Section 6.4.3 that the main contributors of diversity gain in the system were the transmit-diversity and path-diversity, when communicating over the slowly fading channels of Table 6.1. Based on Figures 6.17 to 6.19, the STBC-IQ-TTCM assisted DoS-RR scheme was found to be the best performer amongst the various CM schemes studied.

In summary, the coding gain values exhibited by the various coded modulation schemes studied in this chapter were tabulated in Tables 6.2 and 6.3. Specifically, in Tables 6.2 we summarised the performance gain exhibited by the STBC-assisted and/or IQ-interleaved coded modulation schemes of Section 6.2 communicating over non-dispersive uncorrelated as well as correlated correlated Rayleigh fading channels. The coding gains exhibited by the STBC-assisted and/or IQ-interleaved DoS-RR-based coded modulation schemes of Section 6.4 communicating over both 1-path and 2-path Rayleigh fading channels were summarised in Table 6.3.

STBC-IQ-CM		Flat Uncorrelated Rayleigh Fading Channels				Flat Correlated Rayleigh Fading Channels			
Code	Modulation/ BPS	E_b/N_o (dB) BER		Gain (dB)		E_b/N_o (dB) BER		Gain (dB)	
		10^{-3}	10^{-5}	10^{-3}	10^{-5}	10^{-3}	10^{-5}	10^{-3}	10^{-5}
Uncoded	8PSK/3	26.15	46.00	0.00	0.00	26.15	46.00	0.00	0.00
TCM	16QAM/3	15.54	34.00	10.61	12.00	28.15	45.00	-2.00	1.00
IQ-TCM	16QAM/3	11.32	18.10	14.83	27.90	21.00	29.45	5.15	16.55
STBC-TCM	16QAM/3	10.29	18.10	15.86	27.90	15.47	20.75	10.68	25.25
STBC-IQ-TCM	16QAM/3	8.47	11.65	17.68	34.35	**14.58**	18.11	11.57	27.89
TTCM	16QAM/3	9.88	13.86	16.27	32.14	23.15	32.85	3.00	13.15
IQ-TTCM	16QAM/3	9.31	11.22	16.84	34.78	20.80	28.20	5.35	17.80
STBC-TTCM	16QAM/3	7.66	11.30	18.49	34.70	14.75	18.07	11.40	27.93
STBC-IQ-TTCM	16QAM/3	**7.30**	**8.72**	18.85	37.28	14.65	**17.36**	11.50	28.64
BICM	16QAM/3	11.00	14.00	15.15	32.00	22.90	29.66	3.25	16.34
IQ-BICM	16QAM/3	11.00	13.96	15.15	32.04	22.90	29.45	3.25	16.55
STBC-BICM	16QAM/3	8.66	10.90	17.49	35.10	15.66	18.60	10.49	27.40
STBC-IQ-BICM	16QAM/3	8.66	10.85	17.49	35.15	15.66	18.55	10.49	27.45
BICM-ID	16QAM/3	9.78	14.03	16.37	31.97	21.85	27.45	4.30	18.55
IQ-BICM-ID	16QAM/3	9.36	12.20	16.79	33.80	22.88	28.01	3.27	17.99
STBC-BICM-ID	16QAM/3	7.44	9.65	18.71	36.35	16.00	17.50	10.15	28.50
STBC-IQ-BICM-ID	16QAM/3	7.40	8.95	18.75	37.05	16.12	17.45	10.03	28.55

Table 6.2: Coding gain values of the STBC-assisted and/or IQ-interleaved coded modulation schemes of Section 6.2 when communicating over non-dispersive uncorrelated and correlated Rayleigh fading channels. The coded modulation schemes exhibited a similar decoding complexity in terms of the number of decoding states, which was equal to 64 states. A turbo interleaver block length of 1000 symbols was employed when communicating over uncorrelated Rayleigh fading channels and an interleaver block length of 10000 symbols was employed when communicating over correlated Rayleigh fading channels. The correlated Rayleigh fading channels exhibit a normalised Doppler frequency of 3.25×10^{-5}. The corresponding simulation parameters were summarised in Section 6.2.3 The performance of the best scheme is printed in bold.

STBC-IQ-CM DoS-RR CDMA		1-path Correlated Rayleigh Fading Channels				2-path Correlated Rayleigh Fading Channels			
Code	Modulation/ BPS	E_b/N_o (dB) BER		Gain (dB)		E_b/N_o (dB) BER		Gain (dB)	
		10^{-3}	10^{-5}	10^{-3}	10^{-5}	10^{-3}	10^{-5}	10^{-3}	10^{-5}
Uncoded (1-path)	QPSK/2	24.00	43.50	0.00	0.00	24.00	43.50	0.00	0.00
TCM	8PSK/2	15.13	21.49	8.87	22.01	9.67	13.60	14.33	29.90
IQ-TCM	8PSK/2	13.55	19.96	10.45	23.54	9.38	12.79	14.62	30.71
STBC-TCM	8PSK/2	9.54	13.44	14.46	30.06	7.00	9.35	17.00	34.15
STBC-IQ-TCM	8PSK/2	9.12	12.48	14.88	31.02	6.74	8.81	17.26	34.69
TTCM	8PSK/2	14.62	18.70	9.38	24.80	9.25	11.27	14.75	32.23
IQ-TTCM	8PSK/2	14.35	18.06	9.65	25.44	9.18	10.99	14.82	32.51
STBC-TTCM	8PSK/2	9.22	11.31	14.78	32.19	6.51	7.79	17.49	35.71
STBC-IQ-TTCM	8PSK/2	**9.00**	**10.80**	15.00	32.70	**6.40**	**7.60**	17.60	35.90
BICM	8PSK/2	16.28	20.23	7.72	23.27	10.15	12.81	13.85	30.69
IQ-BICM	8PSK/2	16.28	19.75	7.72	23.75	10.15	12.95	13.85	30.55
STBC-BICM	8PSK/2	9.96	12.96	14.04	30.54	7.53	9.82	16.47	33.68
STBC-IQ-BICM	8PSK/2	9.96	12.61	14.04	30.89	7.46	9.71	16.54	33.79
BICM-ID	8PSK/2	16.29	18.94	7.71	24.56	9.72	11.42	14.28	32.08
IQ-BICM-ID	8PSK/2	16.12	18.00	7.88	25.50	9.77	10.95	14.23	32.55
STBC-BICM-ID	8PSK/2	9.72	11.50	14.28	32.00	6.98	7.95	17.02	35.55
STBC-IQ-BICM-ID	8PSK/2	9.57	**10.80**	14.43	32.70	6.95	7.90	17.05	35.60
TuCM	8PSK/2	14.70	18.60	9.30	24.90	11.39	11.39	12.61	32.11
IQ-TuCM	8PSK/2	14.70	18.75	9.30	24.75	9.55	11.35	14.45	32.15
STBC-TuCM	8PSK/2	9.28	11.22	14.72	32.28	6.75	7.94	17.25	35.56
STBC-IQ-TuCM	8PSK/2	9.28	11.11	14.72	32.39	6.75	7.92	17.25	35.58
Uncoded (1-path)	8PSK/3	26.15	46.00	0.00	0.00	26.15	46.00	0.00	0.00
TTCM	16QAM/3	16.30	21.56	9.85	24.44	11.62	13.77	14.53	32.23
IQ-TTCM	16QAM/3	16.30	28.88	9.85	17.12	11.62	13.32	14.53	32.68
STBC-TTCM	16QAM/3	11.00	13.24	15.15	32.76	8.52	9.86	17.63	36.14
STBC-IQ-TTCM	16QAM/3	11.00	13.10	15.15	32.90	8.52	9.69	17.63	36.31

Table 6.3: Coding gain values of the STBC-assisted and/or IQ-interleaved DoS-RR-based coded modulation schemes of Section 6.4 when communicating over both 1-path and 2-path Rayleigh fading channels. The coded modulation schemes exhibited a similar decoding complexity in terms of the number of decoding states, which was equal to 64 states. An interleaver block length of 1000 symbols was employed and the corresponding simulation parameters were summarised in Section 6.3.2.3. The performance of the best scheme is printed in bold.

Chapter 7

Conclusions and Future Work

In this concluding chapter, a summary of the thesis and the main findings of our investigations will be presented. This will be followed by a range of ideas on future research.

7.1 Summary and Conclusions

This thesis investigated the application of coded modulation schemes for transmission over wireless fading channels. Specifically, four coded modulation schemes, namely TCM, TTCM, BICM and BICM-ID, were evaluated in the context of various transceivers.

In Chapter 2, we commenced our discussions by outlining the principles of TCM, TTCM, BICM and BICM-ID. The conceptual differences amongst these coded modulation schemes were outlined in terms of their coding structure, signal labelling philosophy, interleaver type and decoding philosophy. The TCM and TTCM schemes employed a symbol-based interleaver, while the BICM and BICM-ID schemes employed several parallel bit-based interleavers. As for symbol labelling, the BICM scheme employed Gray-coded signal labelling, while the remaining three schemes employed SP-based signal labelling. More specifically, the conventional TCM scheme is designed for maximising the minimum Euclidean distance between the unprotected bits of the constellation. However, this design criterion is only suitable for AWGN channels. By contrast, maximising the free Hamming distance is the main design criterion for fading channels. Therefore, the TCM schemes designed for fading channels avoid having parallel trellis transitions, in order to maximise the associated free Hamming distance between the codewords. By contrast, the conventional BICM scheme is designed for communicating over fading channels, where the bit-based free Hamming distance is maximised. However, the associated minimum Euclidean distance of the various bits of the phasor constellation is considerably lower than that of the TCM scheme. On the other hand, the BICM-ID scheme was designed with a good performance over both AWGN and fading channels. Specifically, the corresponding minimum Euclidean distance of the various bits of the phasor constellation is further increased with the advent of iterative demodulation and BICM decoding, without sacrificing the high free Hamming distance between the codewords obtained by the non-iterative BICM scheme. Another coded modulation scheme designed for attaining a good performance over both AWGN and fading channels is the TTCM scheme, where the turbo coding principle is invoked by employing TCM schemes as the constituent codes. Explicitly, the free

Hamming distance between the codewords is maximised with the advent of the turbo interleaver and two constituent encoders. The symbol-based MAP algorithm was also detailed in this chapter, where a MAP algorithm operating in the logarithmic domain was invoked by the coded modulation schemes throughout the thesis.

In Chapter 3, a comparative study of the TCM, TTCM, BICM and BICM-ID schemes was carried out, while communicating over both AWGN and uncorrelated narrowband Rayleigh fading channels. Explicitly, it was shown in Sections 3.2.2.1 and 3.2.2.2 that at a given complexity TCM performed better than BICM in AWGN channels, but worse than BICM in uncorrelated narrowband Rayleigh fading channels, in the context of 8PSK, 16QAM and 64QAM. However, BICM-ID outperformed both TCM and BICM for transmissions over both AWGN and uncorrelated narrowband Rayleigh fading channels at the same decoding complexity. Finally, TTCM has shown a superior performance in comparison to the other three coded modulation schemes studied. When employing 64QAM, the trends changed. Specifically, TCM and TTCM were outperformed by BICM and BICM-ID in the context of 64QAM scheme, when communicating over uncorrelated narrowband Rayleigh fading channels. This was deemed to be a consequence of the presence of several uncoded information bits in the TCM/TTCM coded 64QAM symbol. When comparing the achievable coding gain plotted against the interleaver length in Section 3.2.2.3, TTCM was the best performer for a variety of interleaver lengths, while the performance of BICM-ID was better than TCM and BICM only when a long interleaver length was employed. In Section 3.4, multi-carrier OFDM was integrated with the various coded modulation schemes, where we assumed that the individual OFDM subcarriers experienced narrowband fading, when communicating over the wideband COST207 HT Rayleigh fading channels. The TTCM scheme was found to constitute the best compromise, followed by BICM-ID, BICM and TCM in the context of the OFDM scheme. In summary, the TTCM assisted scheme was found to represent the most attractive trade-off in terms of its achievable performance and complexity, closely followed by the BICM-ID assisted scheme, which was our conclusion both in the context of the conventional single-carrier system of Section 3.2 as well as the multi-carrier OFDM system of Section 3.4, in the non-dispersive propagation environments. Explicitly, the coding gain values of the coded modulation schemes studied in this chapter were summarised in Tables 3.4 and 3.5.

Based on Tables 3.4 and 3.5, the BPS throughput versus E_b/N_0 performance of the various coded modulation schemes communicating over AWGN channels as well as communicating over OFDM environment was plotted in Figure 7.1. As we can observe in Figure 7.1(a), the performance curve of the TTCM scheme employing a code memory of three and four iterations is about 2 to 3 dB away from the Shannon limit when targeting a BER of 10^{-5} in the context of AWGN channels. When aiming for BER=10^{-3}, these curves are expected to be closer to the Shannon limit, as we can infer from Table 3.4. Figure 7.1(b) portrays the performance of the OFDM-based coded modulation schemes of Section 3.4 when communicating over the COST207 HT Rayleigh fading channel. When the number of subcarriers is sufficiently high, each OFDM subcarrier experiences narrowband, non-dispersive channel conditions. Therefore, the performance trend of the OFDM-based coded modulation schemes communicating over dispersive Rayleigh fading channels is similar to that of the conventional coded modulation schemes communicating over flat uncorrelated Rayleigh fading channels, as we can observe in Tables 3.4 and 3.5. Note that the performance of the uncoded schemes communicating over flat Rayleigh fading channels was very poor, as it is shown in Table 3.4. Therefore, the OFDM-

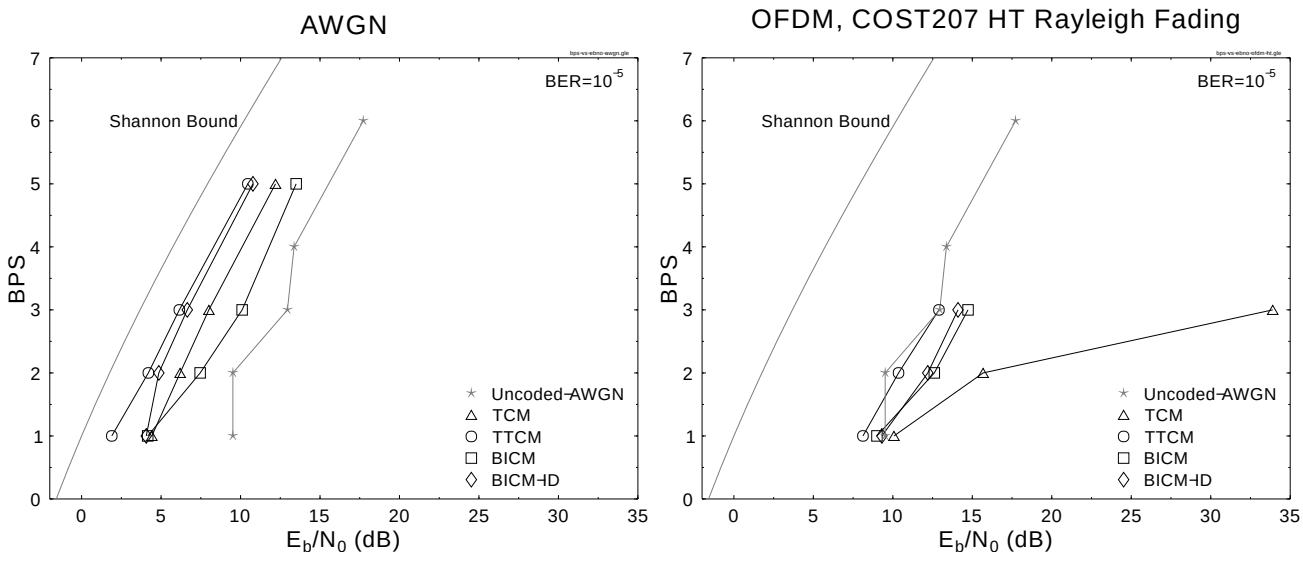

Figure 7.1: The BPS throughput versus E_b/N_0 performance of the coded modulation schemes of Chapter 2 when communicating over (a) AWGN channels and (b) OFDM environment. The corresponding results were extracted from Tables 3.4 and 3.5, respectively, at BER=10^{-5}. The corresponding simulation parameters were summarised in Section 3.2.2 and Table 3.3, respectively.

based uncoded schemes communicating over the COST207 HT Rayleigh fading channel was also very poor, as shown in Table 3.5. However, the performance can be further improved with the advent of employing Walsh-Hadamard spreading [103]. Specifically, when spreading the information carried by each subchannels to all subcarriers with the aid of orthogonal spreading code, the corruption of a few chips owing to low quality subcarriers is unlikely to result in a corrupted subcarrier symbol. Hence, this spreading operation typically improve the achievable OFDM performance.

In Chapter 4, the performance of the various coded modulation schemes was evaluated for transmission over wideband fading channels, by incorporating single-carrier channel equalised arrangements. Specifically, the DFE aided adaptive coded modulation schemes were characterised in performance terms, when communicating over the COST207 TU fading channels in Section 4.4, where the transceivers' performance was optimised by employing channel equalisation and adaptive coded modulation jointly. A delay of one transmission burst duration was incurred in the channel quality estimation process. The MSE at the output of the DFE was used as the metric invoked for switching amongst the various coded modulation modes, in order to combat both the signal power fluctuations as well as the effects of the time-variant ISI imposed by the wideband channel. We found in Sections 4.4.4 that the diversity gain obtained by the employment of a longer channel interleaver spanning over four transmission bursts in the adaptive coded modulation was more than sufficient for compensating for the loss of modem mode switching flexibility imposed by the four-burst duration mode-switching mechanism, ultimately providing a better performance in terms of the achievable BER and BPS performance. The TTCM scheme was found to be the best performer followed by BICM-ID, TCM and BICM in the context of the DFE-assisted adaptive coded modulation schemes. Furthermore, in Sections 4.7 and 4.9, an RBF-based turbo equaliser was also incorporated into the coded modulation schemes designed for transmission over wideband fading channels. Specifically, various RBF-TEQ-CM and RBF-I/Q-TEQ-CM schemes were investigated for transmission over wideband

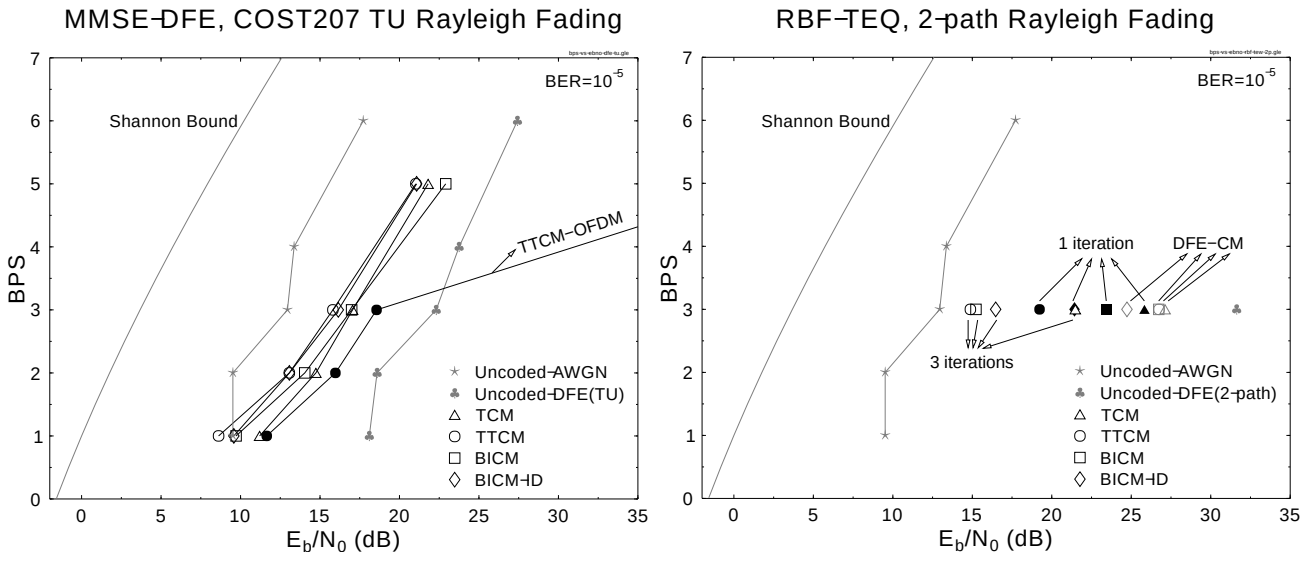

Figure 7.2: The BPS throughput versus E_b/N_0 performance of (a) the DFE-assisted coded modulation schemes of Section 4.4 and of (b) the RBF-TEQ-assisted coded modulation schemes of Section 4.7, when communicating over dispersive Rayleigh fading channels. The corresponding results were extracted from Tables 4.3 and 4.4, respectively, at BER=10^{-5}. The corresponding simulation parameters were summarised in Sections 4.4.2 and 4.7.2, respectively.

Rayleigh fading channels in Sections 4.7 and 4.9, respectively. Our simulation results provided in Sections 4.7.2 and 4.9.2 showed that the BER performance of both the 16QAM-based RBF-TEQ-CM and that of the RBF-I/Q-TEQ-CM schemes communicating over wideband fading channels was only about 2 dB inferior in comparison to that of the identical-throughput uncoded 8PSK scheme communicating over benign AWGN channels. As illustrated in Figure 4.36, a significant complexity reduction was achieved by the RBF-I/Q-TEQ-CM scheme, when compared to the complex-valued RBF-TEQ-CM scheme, while achieving virtually the same performance. In particular, complexity reduction factors of 36 and 9 were attained in terms of the required number of additions/subtractions and multiplications/divisions, respectively, by the RBF-I/Q-TEQ-TTCM scheme, when compared to the RBF-TEQ-TTCM arrangement. As illustrated in Figures 4.27 and 4.35, the best performer was TTCM followed by BICM, BICM-ID and TCM in terms of the achievable BER. However, in terms of the FER attained the best performance was achieved by BICM, followed by TTCM, BICM-ID and TCM in the context of both RBF-TEQ and RBF-I/Q-TEQ. We have also compared the performance of the RBF-TEQ-CM and RBF-I/Q-TEQ-CM schemes to that of the conventional DFE assisted CM scheme in Sections 4.7.2 and 4.9.2. Explicitly, a significant performance gain was achieved by the RBF-TEQ-CM and RBF-I/Q-TEQ-CM schemes in comparison to the conventional DFE assisted coded modulation scheme in the context of 16QAM. The coding gain values of the channel equalised coded modulation schemes characterised in this chapter were summarised in Tables 4.3 and 4.4.

Based on Tables 4.3 and 4.4, the BPS throughput versus E_b/N_0 performance of the DFE and RBF-TEQ assisted coded modulation schemes was illustrated in Figure 7.2 when communicating over dispersive Rayleigh fading channels. Note that the signals at the output of the DFE exhibit Gaussian-like statistics, since the anti-fading effects of the path-diversity were exploited by the channel equaliser. Therefore, the performance of the DFE-assisted uncoded schemes is significantly better than that of

the OFDM-assisted uncoded schemes, as shown in Figure 7.2(a) as well as in Tables 3.5 and 4.3. For the sake of a fair comparison, the performance of the OFDM-based TTCM scheme employing a similar set of parameters for communicating over the COST207 TU Rayleigh fading channel was also plotted in Figure 7.2(a). Specifically, the total number of OFDM subcarriers was 1024 (1K mode) and the number of effective subcarriers was 684. As portrayed in Figure 7.2(a), the performance of OFDM-TTCM is about 3 to 4 dB lower than that of the DFE-TTCM scheme in the context of 4QAM, 8PSK and 16QAM. However, the performance curve of OFDM-TTCM-64QAM exhibits a BER error floor, similar to that of TTCM-64QAM, when communicating over flat uncorrelated Rayleigh fading channels, as we have seen in Figure 3.8. Again, this phenomenon is owing to the presence of several uncoded information bits in the TTCM-coded 64QAM symbol. Furthermore, DFE-TTCM benefits from the dispersion-induced multipath diversity provided by the channel while OFDM-TTCM experiences flat fading in each of the subcarriers and hence no multipath diversity gain is achieved. Next, DFE-CM scheme is compared to the RBF-TEQ-CM arrangement in Figure 7.2(b) in the context of 2-path Rayleigh fading channels. Explicitly, the performance of RBF-TEQ-CM is significantly better than that of the DFE-CM scheme, which is achieved at the expense of a higher complexity owing to the employment of the iterative TEQ.

In Chapter 5, the performance of coded modulation assisted DS-CDMA systems was evaluated. Explicitly, coded modulation assisted JD-MMSE-DFE based CDMA schemes were proposed and evaluated in performance terms, when communicating over the COST 207 seven-path Bad Urban channels in Section 5.2. The powerful JD-MMSE-DFE aided scheme was capable of mitigating the effects of MAI and ISI effectively. We found in Section 5.2.3 that CDMA/TCM was the best candidate, when a short interleaver length was employed, whereas CDMA/TTCM was found to be the best choice for systems that can afford a longer delay owing to utilising a high interleaver length, in the context of CDMA-based slow fading wideband channels. The performance of the JD-MMSE-DFE aided coded modulation schemes has also been evaluated when communicating over the UTRA wideband vehicular Rayleigh fading channels in Section 5.3. It was observed in Section 5.3.3 that the CDMA/TTCM scheme was the best performer in terms of the attainable FER. Therefore, a JD-MMSE-DFE based adaptive CDMA/TTCM scheme was studied in the context of communicating over the UTRA [15] wideband vehicular Rayleigh fading channels. Explicitly, the output SINR of the JD-MMSE-DFE was utilised as the metric invoked for switching the operational modes of the TTCM modem. The effect of modem mode signalling delay was studied in Figure 5.15, where an idealistic scheme having zero signalling delay was compared to a practical scheme having $10\mu s$ signalling delay. It was found that at a target FER of 5%, an approximately 2.5 dB SNR gain was exhibited by the ideal scheme in the SNR region spanning from 8 dB to 27 dB. In Figure 5.16, the systems that were designed for maintaining a higher FER were shown to exhibit the benefit of a higher BPS throughput, which was achieved by invoking a different switching threshold set designed for maintaining a higher FER. The proposed adaptive TTCM-assisted CDMA scheme constitutes a promising practical communication system, which is capable of guaranteeing reliable transmission, while providing an effective bitrate ranging from 23.4 $Kbit/s$ to 117 $Kbit/s$, in the context of the UTRA environment.

As an alternative design, in Section 5.4 an M-ary coded modulation assisted GA-based MUD scheme was proposed and characterised. It was shown in Figures 5.19 and 5.20 that the uncoded GA-MUD was capable of significantly reducing the computational complexity of the optimum-MUD, but

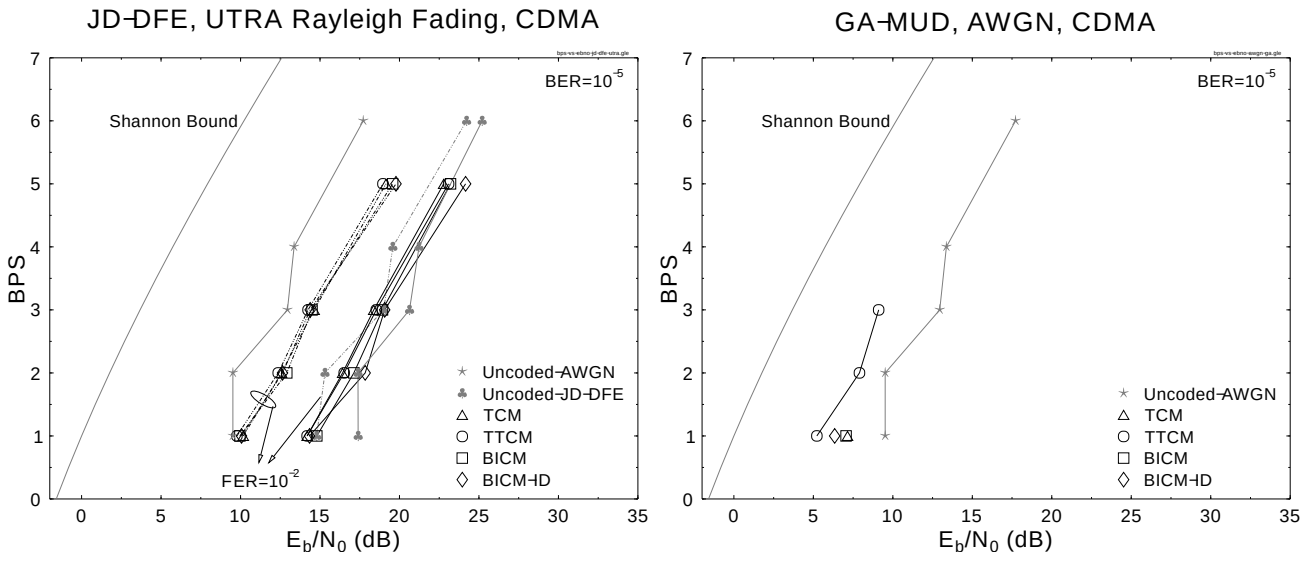

Figure 7.3: The BPS throughput versus E_b/N_0 performance according to Tables 5.6 and 5.7, respectively, at a BER of 10^{-5} for (a) JD-DFE-assisted coded modulation schemes and (b) GA-MUD-assisted coded modulation schemes, when communicating in CDMA environments. The corresponding simulation parameters were summarised in Sections 5.3.2 and 5.4.4, respectively.

experienced an error floor at high SNRs due to invoking an insufficiently large GA population size and a low number of GA generations. However, this problem was eliminated with the aid of CM schemes. Explicitly, the CM-GA-MUD scheme attained a significant complexity reduction with respect to the optimum-MUD and the TTCM scheme was found to be the best candidate amongst the four coded modulation schemes invokes for assisting the operation of the GA-MUD system. Furthermore, it was shown in Figures 5.23 and 5.24 that the CM-GA-MUD scheme was capable of attaining further coding gains with respect to the uncoded single-user schemes, while maintaining a similar throughput and bandwidth, even when supporting a high number of CDMA users. Tables 5.6 and 5.7 summarise the performance gains attained by the coded modulation schemes of Chapter 2 communicating over the CDMA-based fading environment, when employing a JD-MMSE-DFE and a GA-based MUD, respectively.

Based on Tables 5.6 and 5.7, the BPS throughput versus E_b/N_0 performance both the JD-DFE and GA-MUD assisted coded modulation schemes communicating in CDMA environment was illustrated in Figure 7.3[1]. As we can observe in Figure 7.3(a), the coding gain achieved at a BER of 10^{-5} by the JD-DFE-assisted coded modulation schemes against the JD-DFE-assisted uncoded scheme is modest, when communicating over the UTRA Rayleigh fading channel. This performance limitation is a consequence of the employment of a short channel interleaver having a duration of 240 symbols, when communicating over slow Rayleigh fading channels. However, in terms of the achievable FER the coding gain of the JD-DFE-assisted coded modulation schemes is significantly higher. As we can observe from Figure 7.3(a), the BPS performance of the JD-DFE-assisted TTCM scheme is significantly better than that of the JD-DFE-assisted uncoded scheme, when targeting a FER of 10^{-2}. In

[1]Note in Figure 7.3(a) that we have also plotted the achievable BPS performance of the various coded modulation schemes, when aiming for FER=10^{-2} instead of BER=10^{-5}. The BER corresponding to FER=10^{-2} can be inferred from Figures 5.11 and 5.12 for the various coded modulation schemes.

Figure 7.3(b), the performance of the GA-MUD-assisted coded modulation schemes of Section 5.4 was portrayed when communicating over the AWGN channels. Specifically, the BER performance curve of GA-MUD assisted TTCM is about 5 to 6 dB away from the Shannon bound.

Finally, in Chapter 6, we have studied a CM assisted STBC scheme. Explicitly, in Section 6.2 we proposed a set of novel STBC based IQ-interleaved CM schemes designed for transmission over both AWGN and Rayleigh fading channels. Specifically, the associated minimum Hamming distance of the encoded sequences of the CM schemes can be doubled with the advent of employing two separate I and Q interleavers, while the minimum Euclidean distance was not changed. The STBC scheme provided both space and time diversity in conjunction with the employment of multiple transmit antennas. It was observed in Figures 6.3 and 6.4 that coding gains of 26.1 dB, 28.2 dB, 26.9 dB and 28.1 dB were achieved for comparison to the identical-throughput uncoded 8PSK benchmarker at a BER of 10^{-4} by the 16QAM-based STBC-IQ-TCM, STBC-IQ-TTCM, STBC-IQ-BICM and STBC-IQ-BICM-ID schemes, respectively, when communicating over narrowband fading channels. It was found from Figures 6.3 and 6.4 that the IQ-TCM and IQ-TTCM schemes were capable of doubling the achievable diversity potential of the conventional symbol-interleaved TCM and TTCM schemes without requiring STBC. Explicitly, a similar performance was observed for both IQ-TCM and STBC-TCM as well as by IQ-TTCM and STBC-TTCM. However, it was shown in Figure 6.5 that the IQ diversity attainable decreased, when the fading channel exhibited a higher correlation.

On the other hand, a novel STBC-assisted double-spread Rake receiver-based CDMA scheme was proposed and characterised in performance terms for downlink transmissions, when communicating over wideband Rayleigh fading channels, as it was shown in Section 6.3. More specifically, it was illustrated in Section 6.3.3 that the double-spreading mechanism was capable of attaining a near-single-user performance with the aid of a low-complexity Rake receiver, i.e. without employing a complex interference cancellation scheme, at the cost of supporting a reduced number of users. Additionally, the double-spread Rake receiver was capable of yielding a performance equivalent to that of maximal ratio combining of order L when transmitting over L-path channels. Specifically, transmit diversity and path diversity constitute two independent sources of diversity gain in the context of the proposed STBC-assisted double-spreading aided Rake receiver-based CDMA scheme. It was shown in Figures 6.12 and 6.15 that second-order transmit diversity was more advantageous than path diversity having the same order in the context of practical wideband Rayleigh fading channels exhibiting an exponentially decaying CIR. This is plausible, since the low-energy CIR taps contribute only modestly towards improving the achievable path diversity gain. When targeting a certain diversity gain, the multipath interference sensitivity of STBC was lower, than that of a single-transmitter based scheme, when communicating over wideband channels having a long delay spread, as evidenced by Figures 6.11 and 6.15.

Lastly, the STBC-IQ aided CM scheme was amalgamated with a DoS-RR scheme in Section 6.4. Explicitly, the proposed STBC-IQ-CM assisted DoS-RR scheme was capable of exploiting transmit-diversity, multipath-diversity as well as IQ-diversity and hence provided a significant coding/diversity gain over the uncoded scheme, which was achieved without bandwidth expansion, while supporting a number of CDMA users. It was shown in Section 6.4.3 that the main contributors of diversity gain in the system were the transmit-diversity and path-diversity, when communicating over slowly fading channels. We have also invoked TuCM in the proposed scheme, however, the TTCM assisted scheme

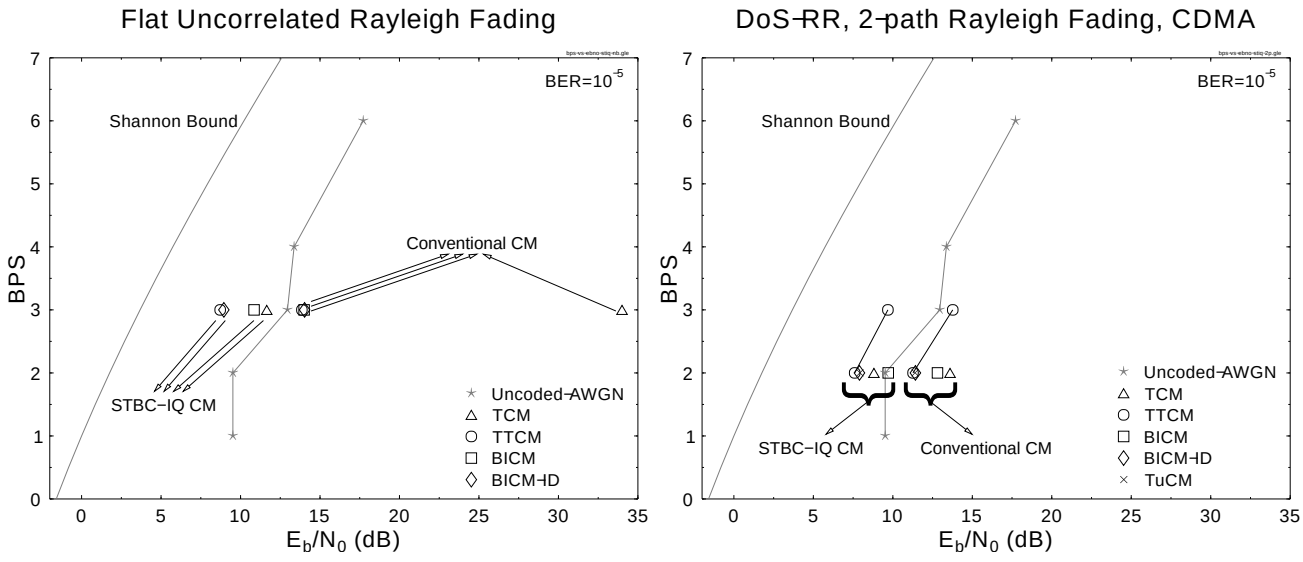

Figure 7.4: The BPS throughput versus E_b/N_0 performance of the STBC-IQ coded modulation scheme of Section 6.2 when communicating over (a) flat uncorrelated Rayleigh fading channels channels and (b) 2-path Rayleigh fading channels. The results were extracted from Tables 6.2 and 6.3, respectively, at BER=10^{-5}. The corresponding simulation parameters were summarised in Sections 6.2.3 and 6.3.2.3, respectively.

once again proved to be the best performer amongst all the schemes studied. Tables 6.2 and 6.3 summarise the diversity/coding gain attained by the coded modulation schemes with the advent of employing IQ-interleaving and multiple transmit antennas of Section 6.2 as well as a double-spread Rake receiver of Section 6.4 in the CDMA environment.

Based on Tables 6.2 and 6.3, the BPS throughput versus E_b/N_0 performance of the STBC-IQ coded modulation schemes of Section 6.2 was plotted in Figure 7.4. These curves were generated for BER=10^{-5}. As we can observed in Figure 7.4(a), the performance of the STBC-IQ assisted coded modulation schemes of Section 6.2 was found to be better than that of the uncoded schemes communicating over AWGN channels, when communicating over flat uncorrelated Rayleigh fading channels. When comparing the performance of STBC-IQ-CM to that of the conventional CM schemes in Figure 7.4(a), an approximately 5 to 6 dB gain was attained by the TTCM and BICM-ID schemes. In the context of CDMA, the performance of the STBC-IQ assisted DoS-RR based coded modulation arrangement of Section 6.4 was illustrated in Figure 7.4(b) when communicating over 2-path Rayleigh fading channels. Explicitly, the performance of the STBC-IQ assisted DoS-RR based coded modulation schemes communicating over 2-path Rayleigh fading channels in a downlink CDMA system was found to be still better than that of the single-user uncoded schemes communicating over AWGN channels.

7.2 Suggestions for Future Work

As demonstrated in Chapter 4, the performance of the RBF-TEQ aided CM schemes is very promising. Therefore, the investigation of coded modulation techniques employing a reduced-complexity MAP-based TEQ [73] schemes as well as TEQ-based iterative MUD [176] schemes may be beneficial. Another

area of promising research is the employment of a TEQ-based scheme in adaptive coded modulation for yielding a better performance in terms of the achievable BER and BPS, which is attained at the cost of a higher complexity. On the other hand, the coded modulation assisted GA-MUD scheme investigated in Section 5.4 may be combined both with space-time coding and multi-carrier CDMA.

As we have proposed in Chapter 6, the IQ-interleaved coded modulation schemes, especially TCM and TTCM, exhibit a better performance than that of the conventional coded modulation schemes with the advent of employing two extra I and Q interleavers, when communicating over fading channels. Therefore, investigations based on IQ-interleaved coded modulation constitute a promising topic for future research. Explicitly, investigations invoking OFDM and multi-carrier CDMA [177] schemes as well as the Multi-Input Multi-Output (MIMO) equaliser [178] in the context of IQ-interleaved coded modulation, are of immediate interest.

Finally, the concept of coded modulation can also be invoked for application in other coding schemes for the sake of achieving a coding gain without bandwidth expansion. Specifically, research into Low Density Parity Check code [179] based block coded modulation is also of interest for transmission over wireless channels. In addition, research on jointly designing IQ-TTCM in conjunction with space-time trellis coding for MIMO schemes and multi-carrier CDMA schemes appears also promising.

List of Symbols

General notation

- The superscript * is used to indicate complex conjugation. Therefore, a^* represents the complex conjugate of the variable a.
- The superscript ^{T} is used to indicate matrix transpose operation. Therefore, $\mathbf{a}^T$ represents the transpose of the matrix $\mathbf{a}$.
- The superscript ^{H} is used to indicate complex conjugate transpose operation. Therefore, $\mathbf{a}^H$ represents the complex conjugate transpose of the matrix $\mathbf{a}$.
- The notation $*$ denotes the convolutional process. Therefore, $a * b$ represents the convolution between variables a and b.
- The notation $\hat{x}$ represents the estimate of x.
- The notation $X(f)$ is the Fourier Transform of $x(t)$.

Special symbols

$\mathbf{A}$: The system matrix in a CDMA system or a ST system.

b_i: The coefficient taps of the backward filters of the Decision Feedback Equalizer.

$\boldsymbol{b}$: A symbol vector, or combination, representing one of the possible transmited symbol sequence.

d_{free}: The minimum free Euclidean distance.

c^W: Walsh spreading code

c^R: Random spreading code.

D: The diversity quantity.

D_I: The diversity quantity of I component.

D_Q: The diversity quantity of Q component.

$\bar{D}$: The signal set dimensionality.

c_k: The coded symbol of the encoder at instance k.

$\mathbf{c}_j^i$: The M-ary multilevel RBF network's centres at node-j and level-i.

C_i: The coefficient taps of the forward filters of the Decision Feedback Equalizer.

E_b: Bit energy.

E_s: Symbol energy.

$E[k]$: The expected value of k.

f_n: The adaptive modem mode switching thresholds at mode n.

f_{RBF}^i: The conditional PDF of the M-ary multilevel RBF equaliser, at level-i.

$G(D)$: The generator polynomials matrix for Convolutional codes.

$H^i(D)$: The coefficients of the generator polynomials for bit i in TCM codes.

h_i: The channel's impulse response.

I_n: The random TTCM symbol-interleaver size in terms of the number of bits for adaptive modem mode n.

K: The number of users.

$\bar{K}$: The Rician fading parameter.

L: The number of resolvable paths in wideband channels.

$\bar{L}$: The memory length of CIR, i.e. $L-1$.

L: The "length" of the shortest error event path or the Hamming distance of a code.

$L(j,m)$: The branch label for transition from state j when the imput symbol is m.

m: The decision feedback equaliser's feedforward order.

m_I: The branch metrics for I component.

m_Q: The branch metrics for Q component.

$\bar{\mathsf{m}}$: The number of information bits in a modulated symbol.

$\tilde{\mathsf{m}}$: The number of encoded information bits in a modulated symbol.

m: The number of bits in a modulated symbol.

M: The number of levels of a multi-level modulation scheme, PSK or QAM.

M: The number of possible values of a source symbol.

M_o: The number of modulation modes in an adaptive modulation scheme.

$\mathcal{M}$: The number of RBF centres or the number of independant basis functions of the RBF equaliser.

n: The decision feedback equaliser's feedback order.

$n_{s,i}$: The number of channel states or the number of hidden nodes, at level-i of M-ary multilevel RBF equaliser.

$n_{s,f}$: The number of scalar centres or channel states, of the reduced complexity RBF equaliser.

N: The number of symbols produced in each transmission interval, or the number of symbols per JD block.

$n(t)$: AWGN added to the transmitted signal.

N_0: Single-sided power spectral density of white noise.

P: The population size of GA.

P_b: Bit error probability.

P_m: The probability of mutation in GA.

Q: The number of chips in each spreading sequence, spreading factor.

$\bar{\mathsf{Q}}$: The first spreading ratio of the DS-RR scheme.

$\tilde{\mathsf{Q}}$: The second spreading ratio of the DS-RR scheme.

R: Coding rate.

r'_I: The I component of the decoupled channel output, in the I/Q-TEQ scheme.

r'_Q: The Q component of the decoupled channel output, in the I/Q-TEQ scheme.

S: The number of coding states, which is equals to 2^ν.

S_n: The trellis state at time instant n.

T: The mating pool size of GA.

u_k: The input symbol to the encoder at instance k.

V_m: The mth modulation mode of the adaptive modulation scheme, which has a total of M_o different modulation modes.

w_j^i: The M-ary multilevel RBF equaliser's weight at node-j and level-i.

x_k: The transmitted symbol at instance k.

y_k: The received symbol at instance k.

Y: The number of generations of GA.

α: The forward variable of a MAP decoder.

β: The backward variable of a MAP decoder.

$\chi(i,b)$: The subset that contains all the phasors for which the position i of the phasor has the binary value b, $b \in \{0,1\}$.

γ: The branch transition metric of a MAP decoder.

γ_{dfe}: The SNR at the output of the DFE.

$\Gamma_o(k)$: The SINR of the user-k at the output of the JD-MMSE-DFE.

ν: The code memory.

$\Omega(\boldsymbol{b})$: The correlation metric of symbol vector $\boldsymbol{b}$.

σ_S^2: The complex signal's variance.

σ_N^2: The complex noise's variance.

π: Interleaver.

π^{-1}: Deinterleaver.

τ: The decision feedback equaliser's decision delay.

φ_i: The nonlinear activation function of multilevel RBF equaliser at level-i.

Glossary

16QAM	16-level Quadrature Amplitude Modulation
3G	Third generation
4QAM	4-level Quadrature Amplitude Modulation
64QAM	64-level Quadrature Amplitude Modulation
8PSK	8-level Phase Shift Keying
APP	A Posteriori Probability
ATM	Asynchronous Transfer Mode
AWGN	Additive White Gaussian Noise
BbB	Burst-by-Burst
BER	Bit error ratio, the number of the bits received incorrectly
BICM	Bit Interleaved Coded Modulation
BICM-ID	Bit-Interleaved Coded Modulation with Iterative decoding
BPS	Bits per modulated symbol
BPSK	Binary Phase Shift Keying
BS	A common abbreviation for Base Station
CCI	Co-Channel Interference
CDMA	Code Division Multiple Access
CIR	Channel Impulse Response
CM	Coded Modulation
CM-GA-MUD	Coded Modulation assisted Genetic Algorithm based Multiuser Detection
CM-JD-CDMA	Coded Modulation-assisted Joint Detection-based CDMA
CT-TEQ	Conventional Trellis-based Turbo Equalisation

D/A	Digital to Analogue
DAB	Digital Audio Broadcasting
DC	Decoding Complexity
DFE	Decision Feedback Equalizer
DFT	Digital Fourier Transform
DoS-RR	Double-Spreading aided Rake Receiver
DS	Direct Sequence
DTTB	Digital Terrestrial Television Broadcast
DVB	Digital Video Broadcasting
ECL	The Effective Code Length or the "length" of the shortest error event path.
EFF	Error Free Feedback
E_b/N_0	Ratio of bit energy to noise power spectral density.
FDM	Frequency Division Multiplexing
FEC	Forward Error Correction
FED	Free Euclidean distance
FER	Frame error rate
FFT	Fast Fourier Transform
G	Coding Gain
GA	Genetic Algorithm
HT	Hilly Terrain, channel impulse response of a hilly terrain environment.
I	The In-phase component of a complex quantity.
I/Q-TEQ	In-phase/Quadrature-phase Turbo Equalisation
IC	Interference Cancellation
IL	interleaver block length
IQ-CM	IQ-interleaved Coded Modulation
ISI	Intersymbol Interference
JD	Joint Detection
JD-MMSE-DFE	Joint Detection scheme employing MMSE-DFE

LMS	Least Mean Square, a stochastic gradient algorithm used in adapting the equalizer's coefficients in a non-stationary environment
log-domain	logarithmic-domain
LP	Logarithmic-domain Probability
MAI	Multiple Access Interference
MAP	Maximum A Posteriori
MC-CDMA	Multi-Carrier Code Division Multiple Access
MIMO	Multi-Input Multi-Output
ML	Maximum Likelihood
MMSE	Minimum Mean Square Error
MMSE-BLE	Minimum Mean Square Error based Block Linear Equaliser
MMSE-DFE	Minimum Mean Square Error based Decision Feedback Equaliser
MPSK	M-ary Phase Shift Keying
MRC	Mixed Radix Conversion
MSE	Mean Square Error, a criterion used to optimised the coefficients of the equalizer such that the ISI and the noise contained in the received signal is jointly minimised.
MUD	Multi-User Detection
OFDM	Orthogonal Frequency Division Multiplexing
OMPX	Orthogonal Multiplexing
PDF	Probability Density Function
PN	Pseudo-Noise
PSD	Power Spectral Density
PSK	Phase Shift Keying
Q	The Quadrature-phase component of a complex quantity.
QAM	Quadrature Amplitude Modulation
QPSK	Quadrature Phase Shift Keying
RBF	Radial Basis Function
RBF-DFE	RBF assisted Decision Feedback Equaliser

RBF-TEQ	Radial Basis Function based Turbo Equalisation
RCPC	Rate-Compatible Puncture Convolutional
RSC	Recursive Systematic Convolutional
SbS	Symbol-by-Symbol
SER	Symbol Error Ratio
SISO	Soft-Input-Soft-Output
SNR	Signal to Noise Ratio, noise energy compared to the signal energy
SOVA	Soft-Output Viterbi Algorithm
SP	Set Partitioning
STBC	Space-Time Block Coding
STBC-DoS-RR	Space-Time Block Coding-assisted Double-Spread Rake Receiver
STBC-IQ	Space-Time Block Coding based IQ-interleaved
STC	Space-Time Coding
STS	Space-Time Spreading
STTC	Space-Time Trellis Coding
TC	Turbo Coding
TCM	Trellis Coded Modulation
TDD	Time Division Duplex
TDMA	Time Division Multiple Access
TEQ	Turbo Equalisation
TTCM	Turbo Trellis Coded Modulation
TU	Typical Urban, channel impulse response of an urban environment.
TuCM	Turbo Coded Modulation
UMTS	Universal Mobile Telecommunication System
UTRA	UMTS Terrestrial Radio Access
VA	Viterbi Algorithm
WMF	Whitening Matched Filter
ZFE	Zero Forcing Equalizer.

Bibliography

[1] C. E. Shannon, "A mathematical theory of communication," *Bell System Technical Journal*, pp. 379–427, 1948.

[2] R. Hamming, "Error detecting and error correcting codes," *Bell System Technical Journal*, vol. 29, pp. 147–160, 1950.

[3] M. Golay, "Notes on digital coding," *Proceedings of the IEEE*, vol. 37, p. 657, 1949.

[4] P. Elias, "Coding for noisy channels," *IRE Conv. Rec. pt.4*, pp. 37–47, 1955.

[5] A. Viterbi, "Error bounds for convolutional codes and an asymptotically optimum decoding algorithm," *IEEE Transactions on Information Theory*, vol. IT-13, pp. 260–269, April 1967.

[6] G. Ungerböck, "Trellis-coded modulation with redundant signal sets. Part 1 and 2," *IEEE Communications Magazine*, vol. 25, pp. 5–21, February 1987.

[7] D. Divsalar and M. K. Simon, "The design of trellis coded MPSK for fading channel: Set partitioning for optimum code design," *IEEE Transactions on Communications*, vol. 36, pp. 1013–1021, September 1988.

[8] C. Schlegel, *Trellis Coding*. The Institute of Electrical and Electronics Engineers, Inc., New York: IEEE Press, 1997.

[9] E. Zehavi, "8-PSK trellis codes for a Rayleigh fading channel," *IEEE Transactions on Communications*, vol. 40, pp. 873–883, May 1992.

[10] G. Caire and G. Taricco and E. Biglieri, "Bit-Interleaved Coded Modulation," *IEEE Transactions on Information Theory*, vol. 44, pp. 927–946, May 1998.

[11] C. Berrou and A. Glavieux and P. Thitimajshima, "Near Shannon limit error-correcting coding and decoding: Turbo codes," in *Proceedings of the International Conference on Communications*, (Geneva, Switzerland), pp. 1064–1070, May 1993.

[12] *Proceedings of the International Symposium on Turbo Codes & Related Topics*, (Brest, France), 3–5 September 1997.

[13] D. J. Costello, A. Banerjee, T. E. Fuja and P. C. Massey, "Some reflections on the design of bandwidth efficient turbo codes," in *Proceedings of 4th ITG Conference on Source and Channel Coding*, no. 170 in ITG Fachbericht, (Berlin), pp. 357–363, VDE–Verlag, 28–30 January 2002.

[14] L. Hanzo, T.H. Liew and B.L. Yeap, *Turbo Coding, Turbo Equalisation and Space Time Coding for Transmission over Wireless channels*. New York, USA: John Wiley IEEE Press, 2002.

[15] R. Steele and L. Hanzo, eds., *Mobile Radio Communications: Second and Third Generation Cellular and WATM Systems*. New York, USA: IEEE Press - John Wiley & Sons, 2nd ed., 1999.

[16] S. L. Goff, A. Glavieux, and C. Berrou, "Turbo-codes and high spectral efficiency modulation," in *Proceedings of IEEE International Conference on Communications*, pp. 645–649, 1994.

[17] P. Robertson and T. Wörz, "Bandwidth-efficient turbo trellis-coded modulation using punctured component codes," *IEEE Journal on Selected Areas in Communications*, vol. 16, pp. 206–218, Feb 1998.

[18] X. Li and J.A. Ritcey, "Trellis-coded modulation with bit interleaving and iterative decoding," *IEEE Journal on Selected Areas in Communications*, vol. 17, April 1999.

[19] X. Li and J.A. Ritcey, "Bit-interleaved coded modulation with iterative decoding using soft feedback," *IEE Electronics Letters*, vol. 34, pp. 942–943, May 1998.

[20] S. X. Ng, T. H. Liew, L-L. Yang and L. Hanzo, "Comparative study of TCM, TTCM, BICM and BICM-ID schemes," in *IEEE Vehicular Technology Conference*, (Rhodes, Greece), pp. 2450–2454, May 2001.

[21] C. S. Lee, S. X. Ng, L. Piazzo and L. Hanzo, "TCM, TTCM, BICM and iterative BICM assisted OFDM-based digital video broadcasting to mobile receivers," in *IEEE Vehicular Technology Conference*, (Rhodes, Greece), pp. 732–736, May 2001.

[22] S. X. Ng, C. H. Wong and L. Hanzo, "Burst-by-burst adaptive decision feedback equalized tcm, ttcm, bicm and bicm-id," in *International Conference on Communications (ICC)*, (Helsinki, Finland), pp. 3031–3035, June 2001.

[23] P. Cherriman, S. X. Ng and L. Hanzo, "Near-Instantaneously Adaptive Decision Feedback Equalized Coded Modulation for Wireless Video Telephony," in *IEEE Eurocon*, (Bratislava, Slovak Republic), pp. 6–10, July 2001.

[24] S. X. Ng, P. Cherriman and L. Hanzo, "Burst-by-Burst Adaptive Decision Feedback Equalised TCM, TTCM and BICM for H.263-Assisted Wireless Video Telephony." Submitted for publication in IEEE Transactions on Vehicular Technology, 2002.

[25] M. S. Yee, S. X. Ng and L. Hanzo, "Iterative radial basis function assisted turbo equalisation of various coded modulation schemes ," in *IEEE Vehicular Technology Conference*, (Birmingham, USA), pp. 1705 –1709, May 2002.

[26] M. S. Yee, S. X. Ng and L. Hanzo, "Radial Basis Function Assisted Reduced Complexity In-phase/Quadrature-phase Turbo Equalisation of Coded Modulation Schemes." Accepted for publication in IEEE Vehicular Technology Conference, 2003.

[27] S. X. Ng, M. S. Yee and L. Hanzo, "Coded Modulation Assisted Radial Basis Function Aided Turbo Equalisation for Dispersive Rayleigh Fading Channels." Submitted for publication in IEEE Transactions on Wireless Communications, 2002.

[28] S. X. Ng, E. L. Kuan and L. Hanzo, "TCM, TTCM, BICM and BICM-ID Assisted Joint Detection Based CDMA," in *Proceedings of 4th ITG Conference on Source and Channel Coding*, (Berlin, Germany), pp. 1317–1321, January 2002.

[29] J. Y. Chung, S. X. Ng and L. Hanzo, "Burst-by-burst adaptive coded modulation-aided joint detection-based CDMA for wireless video telephony," in *IEEE Vehicular Technology Conference*, (Birmingham, USA), pp. 1317–1321, May 2002.

[30] S. X. Ng, K. Yen and L. Hanzo, "TTCM Assisted Genetic-Algorithm Aided Reduced-complexity Multiuser Detection," *IEE Electronics Letters*, vol. 38, pp. 722–724, July 2002.

[31] S. X. Ng, K. Yen and L. Hanzo, "Coded Modulation Assisted Genetic Algorithm Based Multiuser Detection for CDMA Systems ," in *IEEE Proceedings of Wireless*, (Calgary, Canada), pp. 429–433, July 2002.

[32] S. X. Ng, K. Yen and L. Hanzo, "M-ary Coded Modulation Assisted Genetic Algorithm Based Multiuser Detection for CDMA Systems." Accepted for publication in IEEE Proceedings of Wireless Communications and Networking Conference, March 2003.

[33] S. X. Ng and L. Hanzo, "Space-Time IQ-interleaved TCM and TTCM for AWGN and Rayleigh Fading Channels," *IEE Electronics Letters*, vol. 38, pp. 1553–1555, November 2002.

[34] S. X. Ng and L. Hanzo, "Space-Time Block Coded IQ-interleaved Joint Coding and Modulation for AWGN and Rayleigh Fading Channels." Accepted for publication in IEEE Vehicular Technology Conference, 2003.

[35] S. X. Ng, L.-L. Yang and L. Hanzo, "Space-time coding-assisted double-spread rake receiver-based cdma for dispersive rayleigh fading environments," in *IEEE Vehicular Technology Conference*, (Birmingham, USA), pp. 1670–1674, May 2002.

[36] G. Ungerböck, "Channel coding with multilevel/phase signals," *IEEE Transactions on Information Theory*, vol. IT-28, pp. 55–67, January 1982.

[37] D. Divsalar and M. K. Simon, "The design of trellis coded MPSK for fading channel: Performance criteria," *IEEE Transactions on Communications*, vol. 36, pp. 1004–1012, September 1988.

[38] P. Robertson, T. Wörz, "Bandwidth-efficient turbo trellis-coded modulation using punctured component codes," *IEEE Journal on Selected Areas in Communications*, vol. 16, pp. 206–218, February 1998.

[39] X. Li and J.A. Ritcey, "Bit-interleaved coded modulation with iterative decoding," *IEEE Communications Letters*, vol. 1, November 1997.

[40] X. Li and J.A. Ritcey, "Bit-interleaved coded modulation with iterative decoding — Approaching turbo-TCM performance without code concatenation," in *Proceedings of CISS 1998*, (Princeton University, USA), March 1998.

[41] J.-H. Chen and A. Gersho, "Gain-adaptive vector quantization with application to speech coding," *IEEE Transactions on Communications*, vol. 35, pp. 918–930, September 1987.

[42] R. Blahut, *Theory and Practice of Error Control Codes*, ch. 6, pp. 130–160. IBM Corporation, Owego, NY 13827, USA: Addison-Wesley Publishing Company, 1983.

[43] E. Berlekamp, *Algebraic Coding Theory*. New York, USA: McGraw-Hill, 1968.

[44] S. S. Pietrobon, G. Ungerböck, L. C. Perez and D. J. Costello, "Rotationally invariant nonlinear trellis codes for two-dimensional modulation," *IEEE Transactions on Information Theory*, vol. IT-40, pp. 1773–1791, November 1994.

[45] C. Schlegel, "Chapter 3: Trellis coded modulation," in *Trellis Coding*, (New York), pp. 43–89, IEEE Press, September 1997.

[46] J. K. Cavers and P. Ho, "Analysis of the error performance of trellis-coded modulations in Rayleigh-fading channels," *IEEE Transactions on Communications*, vol. 40, pp. 74–83, January 1992.

[47] C. Schlegel and D. J. Costello, "Bandwidth Efficient Coding for Fading Channels: Code Construction and Performance Analysis," *IEEE Journal on Selected Areas in Communications*, vol. 7, pp. 1356–1368, December 1989.

[48] J. Du, B. Vucetic and L. Zhang, "Construction of new MPSK trellis codes for fading channels," *IEEE Transactions on Communications*, vol. 43, pp. 776–784, February/March/April 1995.

[49] G. D. Forney, "The Viterbi Algorithm," in *Proceedings of the IEEE*, vol. 61, pp. 268–277, March 1973.

[50] L.R. Bahl and J. Cocke and F. Jelinek and J. Raviv, "Optimal decoding of linear codes for minimising symbol error rate," *IEEE Transactions on Information Theory*, vol. 20, pp. 284–287, March 1974.

[51] L. Piazzo, "TTCM-OFDM over wideband fading channels," tech. rep., University of Southampton, December 1999.

[52] J. G. Proakis, "Optimum receivers for the additive white Gaussian noise channel," in *Digital Communication*, (New York), pp. 260–274, September 1995.

[53] P. Robertson, E. Villebrun, and P. Höher, "A comparison of optimal and sub-optimal MAP decoding algorithms operating in the log domain," in *Proceedings of the International Conference on Communications*, (Seattle, United States), pp. 1009–1013, June 1995.

[54] K. Abend and B. D. Fritchman, "Statistical detection for communication channels with intersymbol interference," *Proceedings of the IEEE*, vol. 58, pp. 779–785, May 1970.

[55] L. Piazzo, "An algorithm for SBS Receivers/Decoders," *IEE Electronics Letters*, vol. 32, pp. 1058–1060, Jun 1996.

[56] S.S. Pietrobon, R.H. Deng, A. Lafanechére, G. Ungerböck and D.J. Costello, "Trellis-coded multidimensional phase modulation," *IEEE Transactions on Information Theory*, vol. 36, pp. 63–89, January 1990.

[57] L.-F. Wei, "Trellis-coded modulation with multidimensional constellations," *IEEE Transactions on Information Theory*, vol. IT-33, pp. 483–501, July 1987.

[58] P. Robertson, "An overview of bandwidth efficient turbo coding schemes," in ISTC'97 [12], pp. 103–110.

[59] S. Lin and D. Constello Jr., *Error Control Coding: Fundamentals and Applications*. Englewood Cliffs, NJ, USA: Prentice-Hall, October 1982. ISBN: 013283796X.

[60] J. Hagenauer, "Rate-compatible puncture convolutional codes (RCPC) and their application," *IEEE Transactions on Communications*, vol. 36, pp. 389–400, April 1988.

[61] L. Lee, "New rate-compatible puncture convolutional codes for Viterbi decoding," *IEEE Transactions on Communications*, vol. 42, pp. 3073–3079, December 1994.

[62] S. Benedetto, D. Divsalar, G. Montorsi and F. Pollara, "A soft-input soft-output APP module for iterative decoding of concatenated codes," *IEEE Communications Letter*, vol. 1, pp. 22–24, January 1997.

[63] L. Hanzo, W. Webb, and T. Keller, *Single- and Multi-carrier Quadrature Amplitude Modulation*. New York, USA: IEEE Press-John Wiley, April 2000.

[64] R. W. Chang, "Synthesis of band-limited orthogonal signals for multichannel data transmission," *Bell Systems Technical Journal*, vol. 46, pp. 1775–1796, December 1966.

[65] M.S. Zimmermann and A.L. Kirsch, "The AN/GSC-10/KATHRYN/Variable Rate Data Modem for HF Radio," *IEEE Transactions on Communication Technology*, vol. CCM–15, pp. 197–205, April 1967.

[66] L.J. Cimini, "Analysis and simulation of a digital mobile channel using orthogonal frequency division multiplexing," *IEEE Transactions on Communications*, vol. 33, pp. 665–675, July 1985.

[67] F. Mueller-Roemer, "Directions in audio broadcasting," *Journal Audio Engineering Society*, vol. 41, pp. 158–173, March 1993.

[68] M. Alard and R. Lassalle, "Principles of modulation and channel coding for digital broadcasting for mobile receivers," *EBU Review, Technical No. 224*, pp. 47–69, August 1987.

[69] I. Kalet, "The multitone channel," *IEEE Transactions on Communications*, vol. 37, pp. 119–124, February 1989.

[70] L. Piazzo and L. Hanzo, "TTCM-OFDM over dispersive fading channels," *IEEE Vehicular Technology Conference*, vol. 1, pp. 66–70, May 2000.

[71] R.F.H. Fischer, L.H.-J. Lampe and S.H. Muller-Weinfurtner, "Coded modulation for noncoherent reception with application to OFDM," *IEEE Transactions on Vehicular Technology*, vol. 50, pp. 74–88, January 2001.

[72] "COST 207: Digital land mobile radio communications, final report," tech. rep., Luxembourg, 1989.

[73] C. Douillard, A. Picart, M. Jézéquel, P. Didier, C. Berrou, and A. Glavieux, "Iterative correction of intersymbol interference: turbo-equalization," *European Transactions on Communications*, vol. 6, pp. 507–511, 1995.

[74] B. L. Yeap, T. H. Liew and L. Hanzo, "Turbo equalization of serially concatenated systematic convolutional codes and systematic space time trellis codes," *IEEE Vehicular Technology Conference*, p. 119 (CDROM), May 2001.

[75] ETSI, *Digital Video Broadcasting (DVB): Framing Structure, Channel Coding and Modulation for Digital Terrestrial Television*, August 1997. ETS 300 744.

[76] R. Steele and W. Webb, "Variable rate QAM for data transmission over Rayleigh fading channels," in *Proceeedings of Wireless '91*, (Calgary, Alberta), pp. 1–14, IEEE, 1991.

[77] S. Chen, S. McLaughlin, and B. Mulgrew, "Complex-valued radial basis function network, Part II: Application to digital communications channel equalisation," *EURASIP Signal Processing*, vol. 36, pp. 175–188, March 1994.

[78] J. G. Proakis, "Chapter 10: Communication through band-limited channels," in *Digital Communications*, (New York), pp. 583–635, McGraw-Hill International Editions, 3rd Edition, September 1995.

[79] C. H. Wong, *Wideband Adaptive Full Response Multilevel Transceivers and Equalizers.* PhD thesis, University of Southampton, United Kingdom, November 1999.

[80] D.F. Mix, *Random Signal Processing.* Englewood Cliffs, NJ, USA: Prentice-Hall, 1995.

[81] J.C. Cheung, *Adaptive Equalisers for Wideband TDMA Mobile Radio*. PhD thesis, Department of Electronics and Computer Science, University of Southampton, UK, 1991.

[82] S. Sampei and S. Komaki and N. Morinaga, "Adaptive modulation/TDMA scheme for large capacity personal multi-media communication systems," *IEICE Transactions on Communications (Japan)*, vol. E77-B, pp. 1096–1103, September 1994.

[83] J.M. Torrance and L. Hanzo, "Latency and networking aspects of adaptive modems over slow indoors Rayleigh fading channels," *IEEE Transactions on Vehicular Technology*, vol. 48, no. 4, pp. 1237–1251, 1998.

[84] J.M. Torrance and L. Hanzo, "Interference aspects of adaptive modems over slow Rayleigh fading channels," *IEEE Vehicular Technology Conference*, vol. 48, pp. 1527–1545, September 1999.

[85] A.J. Goldsmith and S. Chua, "Variable-rate variable-power MQAM for fading channels," *IEEE Transactions on Communications*, vol. 45, pp. 1218–1230, October 1997.

[86] C. Wong and L. Hanzo, "Upper-bound performance of a wideband burst-by-burst adaptive modem," *IEEE Transactions on Communications*, vol. 48, pp. 367–369, March 2000.

[87] H. Matsuoka and S. Sampei and N. Morinaga and Y. Kamio, "Adaptive Modulation System with Variable Coding Rate Concatenated Code for High Quality Multi-Media Communications Systems," in *Proceedings of IEEE VTC'96*, vol. 1, (Atlanta, GA, USA), pp. 487–491, IEEE, 28 April–1 May 1996.

[88] V.K.N. Lau and M.D. Macleod, "Variable rate adaptive trellis coded QAM for high bandwidth efficiency applications in Rayleigh fading channels," in *Proceedings of IEEE Vehicular Technology Conference (VTC'98)*, (Ottawa, Canada), pp. 348–352, IEEE, 18–21 May 1998.

[89] V.K.N. Lau and M.D. Macleod, "Variable rate adaptive trellis coded QAM for flat-fading channels," *IEEE Transactions on Communications*, vol. 49, pp. 1550–1560, September 2001.

[90] A.J. Goldsmith and S. Chua, "Adaptive coded modulation for fading channels," *IEEE Transactions on Communications*, vol. 46, pp. 595–602, May 1998.

[91] D. Göckel, "Adaptive coding for fading channels using outdated fading estimates," *IEEE Transactions on Communications*, vol. 47, pp. 844–855, June 1999.

[92] P. Ormeci, X. Liu, D. Goeckel and R. Wesel, "Adaptive bit-interleaved coded modulation," *IEEE Transactions on Communications*, vol. 49, pp. 1572–1581, September 2001.

[93] V.K.N. Lau, "Performance analysis of variable rate: symbol-by-symbol adaptive bit interleaved coded modulation for Rayleigh fading channels," *IEEE Transactions on Vehicular Technology*, vol. 51, pp. 537–550, May 2002.

[94] S. Falahati, *Adaptive Modulation and Coding in Wireless Communications with Feedback*. PhD thesis, Communication Systems Group, Department of Signals and Systems, School of Electrical and Computer Engineering, Chalmers University of Technology, Sweden, 2002.

[95] C.H. Wong, T. H. Liew and L. Hanzo, "Burst-by-burst turbo coded wideband adaptive modulation with blind modem mode detection," *Proceedings of 4th ACTS Mobile Communications Summit 1999, Sorrento, Italy*, pp. 303–308, 8–11 June 1999.

[96] "COST 207: Digital land mobile radio communications, final report." Office for Official Publications of the European Communities, 1989. Luxembourg.

[97] A. Klein and R. Pirhonen and J. Skoeld and R. Suoranta, "FRAMES Multiple Access MODE 1 — Wideband TDMA with and without Spreading," in *Proceedings of the IEEE International Symposium on Personal, Indoor and Mobile Radio Communications (PIMRC)*, vol. 1, (Helsinki, Finland), pp. 37–41, 1–4 September 1997.

[98] B. J. Choi, M. Münster, L. L. Yang, and L. Hanzo, "Performance of Rake receiver assisted adaptive-modulation based CDMA over frequency selective slow Rayleigh fading channel," *Electronics Letters*, vol. 37, pp. 247–249, February 2001.

[99] A. Duel-Hallen and S. Hu and H. Hallen, "Long range prediction of fading signals," *IEEE Signal Processing Magazine*, vol. 17, pp. 62–75, May 2000.

[100] A. Naguib, N. Seshdri, and A. Calderbank, "Increasing data rate over wireless channels: Space-time coding for high data rate wireless communications," *IEEE Signal Processing Magazine*, vol. 17, pp. 76–92, May 2000.

[101] S. M. Alamouti and S. Kallel, "Adaptive trellis-coded multiple-phased-shift keying Rayleigh fading channels," *IEEE Transactions on Communications*, vol. 42, pp. 2305–2341, June 1994.

[102] M. Yee, T. Liew, and L. Hanzo, "Radial basis function decision feedback equalisation assisted block turbo burst-by-burst adaptive modems," in *Proceedings of VTC '99 Fall*, (Amsterdam, Holland), pp. 1600–1604, 19-22 September 1999.

[103] L. Hanzo and C. H. Wong and M. S. Yee, *Adaptive Wireless Transceivers: Turbo-Coded, Turbo-Equalized and Space-Time Coded TDMA, CDMA and OFDM Systems.* New York, USA: John Wiley, IEEE Press, 2002.

[104] M. S. Yee, B. L. Yeap, and L. Hanzo, "Turbo equalisation of convolutional coded and concatenated space time trellis coded systems using radial basis function aided equalizers," in *Proceedings of Vehicular Technology Conference*, (Atlantic City, USA), pp. 882–886, Oct 7-11 2001.

[105] M. S. Yee, B. L. Yeap, and L. Hanzo, "Radial basis function assisted turbo equalisation," in *Proceedings of IEEE Vehicular Technology Conference*, (Tokyo, Japan), pp. 640–644, IEEE, 15-18 May 2000.

[106] G. Bauch, H. Khorram, and J. Hagenauer, "Iterative equalization and decoding in mobile communications systems," in *European Personal Mobile Communications Conference*, (Bonn, Germany), pp. 301–312, 30 September - 2 October 1997.

[107] G. J. Gibson, S. Siu, and C. F. N. Cowan, "The application of nonlinear structures to the reconstruction of binary signals," *IEEE Transactions on Signal Processing*, vol. 39, pp. 1877–1884, August 1991.

[108] S. Chen, G. J. Gibson, and C. F. N. Cowan, "Adaptive channel equalisation using a polynomial-perceptron structure," *IEE Proceedings*, vol. 137, pp. 257–264, October 1990.

[109] H. L. V. Trees, *Detection, Estimation and Modulation Theory, Part 1.* New York: John Wiley and Sons, 1968.

[110] S. Chen, B. Mulgrew, and P. M. Grant, "A clustering technique for digital communications channel equalization using radial basis function networks," *IEEE Transactions on Neural Networks*, vol. 4, pp. 570–579, July 1993.

[111] S. Haykin, *Neural Networks: A Comprehensive Foundation.* Basingstoke: Macmillan Publishing Company, 1994.

[112] S. K. Patra and B. Mulgrew, "Computational aspects of adaptive radial basis function equalizer design," in *IEEE International Symposium on Circuits and Systems, ISCAS'97*, vol. 1, pp. 521–524, IEEE, Piscataway, NJ, USA, June 1997.

[113] M. Gertsman and J. Lodge, "Symbol-by-symbol MAP demodulation of CPM and PSK signals on Rayleigh flat-fading channels," *IEEE Transactions on Communications*, vol. 45, pp. 788–799, July 1997.

[114] D. Raphaeli and Y. Zarai, "Combined turbo equalization and turbo decoding," *IEEE Communications Letters*, vol. 2, pp. 107–109, April 1998.

[115] C. Berrou and A. Glavieux, "Near optimum error correcting coding and decoding: Turbo codes," *IEEE Transactions on Communications*, vol. 44, pp. 1261–1271, October 1996.

[116] A. Knickenberg, B. L. Yeap, J. Hamorsky, M. Breiling, and L. Hanzo, "Non-iterative joint channel equalisation and channel decoding," in *Proceedings of Globecom'99*, (Rio de Janeiro, Brazil), pp. 442–446, 5-9 December 1999.

[117] A. Glavieux, C. Laot, and J. Labat, "Turbo equalization over a frequency selective channel," in *Proceedings of the International Symposium on Turbo Codes*, (Brest, France), pp. 96–102, 3-5 September 1997.

[118] M. Yee and L. Hanzo, "Multi-level radial basis function network based equalisers for Rayleigh channel," in *Proceeding of VTC'99 (Spring)*, (Houston, TX, USA), pp. 707–711, IEEE, 16–20 May 1999.

[119] S. Chen, B. Mulgrew, and S. McLaughlin, "Adaptive Bayesian equalizer with decision feedback," *IEEE Transactions on Signal Processing*, vol. 41, pp. 2918–2927, September 1993.

[120] E.-S. Chng, H. Yang, and W. Skarbek, "Reduced complexity implementation of Bayesian equaliser using local RBF network for channel equalisation problem," *Electronics Letters*, vol. 32, pp. 17–19, January 1996.

[121] M. S. Yee, T. H. Liew and L. Hanzo, "Burst-by-burst adaptive turbo-coded radial basis function-assisted decision feedback equalization," *IEEE Transactions on Communications*, vol. 49, pp. 1935–1945, November 2001.

[122] J. G. Proakis, *Digital Communications*. New York: Mc-Graw Hill International Editions, 3rd ed., 1995.

[123] B. L. Yeap, C. H. Wong, and L. Hanzo, "Reduced complexity in-phase/quadrature-phase turbo equalisation with iterative channel estimation," in *IEEE International Communications Conference 2001*, (Helsinki, Finland), pp. 1395–1399, 11-15 June 2001.

[124] P. Jung and J. Blanz, "Joint detection with coherent receiver antenna diversity in CDMA mobile radio systems," *IEEE Transactions on Vehicular Technology*, vol. 44, pp. 76–88, February 1995.

[125] E.L. Kuan and C.H. Wong and L. Hanzo, "Comparative study of joint-detection and interference cancellation based burst-by-burst adaptive CDMA schemes," in *Proceedings of the IEEE Vehicular Technology Conference (VTC Fall)*, (Amsterdam, The Netherlands), pp. 653–657, 19–22 September 1999.

[126] J. R. Foerster and L. B. Milstein, "Coded modulation for a coherent DS-CDMA system employing an mmse receiver in a fading channel," *IEEE Transactions on Communications*, vol. 48, pp. 1909–1918, November 2000.

[127] D. E. Goldberg, *Genetic Algorithms in Search, Optimization, and Machine Learning.* Reading, Massachusetts: Addison-Wesley, 1989.

[128] K. Yen and L. Hanzo, "Hybrid genetic algorithm based multi-user detection schemes for synchronous CDMA systems," in *submitted to the IEEE Vehicular Technology Conference (VTC)*, (Tokyo, Japan), 2000.

[129] K. Yen and L. Hanzo, "Genetic algorithm assisted joint multiuser symbol detection and fading channel estimation for synchronous CDMA systems," *IEEE Journal on Selected Areas in Communications*, vol. 19, pp. 985–998, June 2001.

[130] S. Abedi and R. Tafazolli, "Genetically modified multiuser detection for code division multiple access systems," *IEEE Journal on Selected Areas in Communications*, vol. 20, pp. 463–473, February 2002.

[131] S. Verdú, *Multiuser Detection.* Cambridge: Cambridge University Press, 1998.

[132] A. Klein, G. Kaleh, and P. Baier, "Zero forcing and minimum mean square error equalization for multiuser detection in code division multiple access channels," *IEEE Transactions on Vehicular Technology*, vol. 45, pp. 276–287, May 1996.

[133] A. Whalen, *Detection of Signals in Noise.* New York, USA: Academic Press, 1971.

[134] E.A. Lee and D.G. Messerschmitt, *Digital Communication.* Dordrecht: Kluwer Academic Publishers, 1988.

[135] G. Golub and C. van Loan, *Matrix Computations.* North Oxford Academic, 1983.

[136] W.H. Press and S.A. Teukolsky and W.T. Vetterling and B.P. Flannery, *Numerical Recipes in C.* Cambridge: Cambridge University Press, 1992.

[137] T. Ojanperä, A. Klein, and P.-O. Anderson, "FRAMES multiple access for UMTS," *IEE Colloquium (Digest)*, pp. 7/1–7/8, May 1997.

[138] K. Miya, O. Kato, K. Homma, T. Kitade, M. Hayashi, and T. Ue, "Wideband CDMA systems in TDD-mode operation for IMT-2000," *IEICE Transactions on Communications*, vol. E81-B, pp. 1317–1326, July 1998.

[139] O. Kato, K. Miya, K. Homma, T. Kitade, M. Hayashi, and M. Watanabe, "Experimental performance results of coherent wideband DS-CDMA with TDD scheme," *IEICE Transactions on Communications.*, vol. E81-B, pp. 1337–1344, July 1998.

[140] I. Jeong and M. Nakagawa, "A novel transmission diversity system in TDD-CDMA," *IEICE Transactions on Communications*, vol. E81-B, pp. 1409–1416, July 1998.

[141] V. Lau and S. Maric, "Variable rate adaptive modulation for DS-CDMA," *IEEE Transactions on Communications*, vol. 47, pp. 577–589, April 1999.

[142] V. K. N. Lau and M. Macleod, "Variable-rate adaptive trellis coded QAM for flat-fading channels," *IEEE Transactions on Communications*, vol. 49, pp. 1550–1560, September 2001.

[143] S. Otsuki, S. Sampei, and N. Morinaga, "Square QAM adaptive modulation/TDMA/TDD systems using modulation level estimation with Walsh function," *Electronics Letters*, vol. 31, pp. 169–171, February 1995.

[144] J. Torrance and L. Hanzo, "Demodulation level selection in adaptive modulation," *Electronics Letters*, vol. 32, pp. 1751–1752, 12 September 1996.

[145] T.S. Lee and T.C. Tsai, "A partially adaptive CDMA interference canceller for multipath channels," *IEEE Vehicular Technology Conference*, vol. 2, pp. 917–921, May 2000.

[146] S. Kazi and L. Lucke, "A convolutionally-coded adaptive CDMA receiver architecture," *Signals, Systems and Computers. Thirty-Second Asilomar Conference*, vol. 2, pp. 1199–1203, 1998.

[147] S.W. Lei and V.K.N. Lau, "Adaptive interleaving for OFDM in TDD system," *IEE Proceedings on Communications*, vol. 148, no. 2, pp. 77–80, 2001.

[148] L. Hanzo and P. Cherriman and J. Streit, *Wireless Video Communications: From Second to Third Generation Systems, WLANs and Beyond.* IEEE Press, 2001. (For detailed contents please refer to http://www-mobile.ecs.soton.ac.uk.).

[149] J. Torrance and L. Hanzo, "Optimisation of switching levels for adaptive modulation in a slow Rayleigh fading channel," *Electronics Letters*, vol. 32, pp. 1167–1169, 20 June 1996.

[150] B. J. Choi and L. Hanzo, "Optimum mode-switching levels for adaptive modulation systems," in *Proceedings of IEEE GLOBECOM 2001*, 2001.

[151] W. H. Press, S. A. Teukolsky, W. T. Vetterling, and B. P. Flannery, *Numerical Recipes in C.* Cambridge University Press, 1992.

[152] Special Mobile Group of ETSI, "UMTS: Selection procedures for the choice of radio transmission technologies of the UMTS," tech. rep., European Telecommunications Standard Institute (ETSI), France, 1998.

[153] S. Verdú, "Minimum probability of error for asynchronous Gaussian multiple-access channel," *IEEE Transactions on Communications*, vol. 32, pp. 85–96, January 1986.

[154] S. Moshavi, "Multi-user detection for DS-CDMA communications," *IEEE Communications Magazine*, vol. 34, pp. 124–136, October 1996.

[155] M. Mitchell, *An Introduction to Genetic Algorithms.* Cambridge, Massachusetts: MIT Press, 1996.

[156] L. J. Eshelman and J. D. Schaffer, "Preventing premature convergence in genetic algorithms by preventing incest," in *Proceedings of the Fourth International Conference on Genetic Algorithms* (R. K. Belew and L. B. Booker, eds.), (California, USA), pp. 115–122, Morgan Kaufmann, 1991.

[157] M. J. Juntti, T. Schlösser, and J. O. Lilleberg, "Genetic algorithms for multiuser detection in synchronous CDMA," in *IEEE International Symposium on Information Theory – ISIT'97*, (Ulm, Germany), p. 492, 1997.

[158] G. Syswerda, "Uniform crossover in genetic algorithms," in *Proceedings of the Third International Conference on Genetic Algorithms* (J. D. Schaffer, ed.), (California, USA), pp. 2–9, Morgan Kaufmann, 1989.

[159] W. Spears and K. De Jong, *Foundations of Genetic Algorithms*, ch. An Analysis of Multi-Point Crossover, pp. 301–315. California, USA: G. Rawlins, ed., Morgan Kaufmann, 1991.

[160] J. Anderson and S. Mohan, "Sequential coding algorithms: a survey and cost analysis," *IEEE Transactions on Communications*, vol. 32, pp. 169–176, February 1984.

[161] T. Hashimoto, "A list-type reduced-constraint generalization of the Viterbi algorithm," *IEEE Transactions on Information Theory*, vol. 33, pp. 866–876, November 1987.

[162] S. J. Simmons, "Breadth-first trellis decoding with adaptive effort," *IEEE Transactions on Communications*, vol. 38, pp. 3–12, January 1990.

[163] L. Rasmussen, T. Lim, and T. Aulin, "Breadth-first maximum likelihood detection in multiuser CDMA," *IEEE Transactions on Communications*, vol. 45, pp. 1176–1178, October 1997.

[164] S. M. Alamouti, "A simple transmit diversity technique for wireless communications," *IEEE Journal on Selected Areas in Communications*, vol. 16, pp. 1451–1458, October 1998.

[165] H. J. V. Tarokh and A. Calderbank, "Space-time block codes from orthogonal designs," *IEEE Transactions on Information Theory*, vol. 45, pp. 1456–1467, May 1999.

[166] P. Balaban, J. Salz, "Optimum diversity combining and equalization in digital data transmission with application to cellular mobile radio – Part I: Theoretical considerations," *IEEE Transactions on Communications*, vol. 40(5), pp. 885–894, 1992.

[167] A. Wittneben, "Base station modulation diversity for digital SIMULCAST," in *Proceedings of IEEE Vehicular Technology Conference*, pp. 505–511, May 1993.

[168] V. Tarokh, N. Seshadri, and A. R. Calderbank, "Space-time codes for high data rate wireless communication: Performance criterion and code construction," *IEEE Transactions on Information Theory*, vol. 44, pp. 744–765, March 1998.

[169] S. Al-Semari and T. Fuja, "I-Q TCM: Reliable communication over the Rayleigh fading channel close to the cuttoff rate," *IEEE Transactions on Information Theory*, vol. 43, pp. 250–262, January 1997.

[170] B. D. Jelicic and S. Roy, "Design of trellis coded QAM for flat fading and AWGN channels," *IEEE Transactions on Vehicular Technology*, vol. 44, pp. 192–201, February 1994.

[171] G. Klang, A. F. Naguib, "Transmit diversity based on space-time block codes in frequency selective Rayleigh fading DS-CDMA systems," *IEEE Vehicular Technology Conference*, pp. 264–268, Spring 2000.

[172] L.-L. Yang and L. Hanzo, "Performance of wideband CDMA using adaptive space-time spreading over multipath Nakagami fading channels," *IEEE Vehicular Technology Conference*, pp. 615–619, May 2002.

[173] L. Miller and J. Lee, *CDMA Systems Engineering Handbook*. London, UK: Artech House, 1998.

[174] R. Price and E. Green Jr., "A communication technique for multipath channels," *Proceedings of the IRE*, vol. 46, pp. 555–570, March 1958.

[175] J. Mar and H. Chen, "Performance analysis of cellular CDMA networks over frequency-selective fading channel," *IEEE Transactions on Vehicular Technology*, vol. 47, pp. 1234–1244, November 1998.

[176] M. C. Reed, C. B. Schlegel, P. D. Alexander, and J. A. Asenstorfer, "Iterative multiuser detection for CDMA with FEC: Near single user performance," *IEEE Transactions on Communication*, pp. 1693–1699, December 1998.

[177] R. Prasad and S. Hara, "Overview of multi-carrier CDMA," in *Proceedings of the IEEE International Symposium on Spread Spectrum Techniques and Applications (ISSSTA)*, (Mainz, Germany), pp. 107–114, 22–25 September 1996.

[178] C. Tidestav, A. Ahlén and M. Sternad, "Realiazable MIMO decision feedback equalizer: structure and design," *IEEE Transactions on Signal Processing*, vol. 49, pp. 121–133, January 2001.

[179] R. Gallager, "Low-density parity-check codes," *IEEE Transactions on Information Theory*, pp. 21–28, 1962.

Index

Symbols

E_b/N_0 ..... 169, 170
$\bar{D}$ 28
16QAM 7
3G 2
4QAM 7
64QAM 7
8PSK 7

A

APP 18
ATM 60
AWGN ..... ii, 6

B

BbB 76
BER ..... ii, 1, 6, 123, 124, 169, 170
BICM 2, 6, 33
BICM coding example 37–38
BICM interleaver design 42
BICM phasor labelling 40–42
BICM principle 34–37
BICM-ID 6, 40
BICM-ID coding example 42
bit-interleaved coded modulation 33–38
bit-interleaved coded modulation with iterative decoding 40
BPS 71, 123, 158
BPSK 115
broadcasting 60
BS 116

C

CCI 163
CDMA ..... ii, 4, 115
channel impulse response 139
Cholesky decomposition 119
CIR 72, 94, 117
CM 75, 86, 115, 153
CM-GA-MUD 138
CM-JD-CDMA 116
coded modulation
  fixed-mode-based performance 80–82
coded modulation assisted OFDM 61–68
coded modulation coding gain versus complexity and interleaver block length 55–59
coded modulation in narrowband channels 46–59
coded modulation performance over uncorrelated narrowband Rayleigh fading channels 52–55
coded modulation simulation results and discussions 48–59
coded modulation System I and System II performance 83–85
coded modulation theory 6
coded OFDM simulation parameters 64–65
coded OFDM simulation results and discussions 65–67
convolutional code 7
CT-TEQ 88

D

D/A 61
DAB 60
DC 55
decision feedback equaliser 72–75
decision feedback equaliser aided adaptive coded modulation 76–86
decision feedback equaliser principle 73–75
DFE ..... ii, 3, 71
DFT 60
digital audio 60
DoS-RR 4, 163
DS 4, 115, 162, 163

DTTB 60
DVB 63

E

ECL 15
EFF 50
elitism 143
equaliser signal-to-noise ratio loss 75
European digital audio broadcasting 60

F

FDM 60
FEC 2, 7
FED 12
FER 1
FFT 61
FRAMES Mode 1 burst structure 123
free distance 10

G

G 55
GA ..... ii, 4, 115

H

HT 63, 65

I

I ..... ii, 4, 153
I/Q-TEQ 88
IC 163
IL 55
individual 141
inter-symbol interference 72
IQ-CM 4, 153
ISI 59, 71, 115
Iterative turbo equalisation
    schematic 92
    serially concatenated coded M-ary system 92

J

JD 115
JD-MMSE-DFE 115

L

LMS 97
log-domain 17, 25
LP 93

M

MAI 115, 163
MAP 2, 17, 92
MAP algorithm summary 28
maximum likelihood 138, 140
MC-CDMA 163
MIMO 193
ML 138
MMSE 72
MMSE-BLE 119
MMSE-DFE 115
MPSK 14
MRC 167
MSE 74, 118
MUD ..... ii, 4, 115, 163
mutation
    probability 143

O

OFDM ..... ii, 3, 46, 59, 163
OFDM principle 60–61
offspring 143
OMPX 60
optimum TCM codes 13–14
orthogonal frequency division multiplexing 59–61
Orthogonality Principle 118

P

parallel transitions 10
PDF 43
performance over AWGN channels 49–52
PN 165
population 141
population size 141
PSD 21, 47
PSK 7

Q

Q ..... ii, 4, 153
QAM 7, 88
QPSK 7, 163

R

RBF ..... ii, 3, 71, 86, 89
RBF assisted turbo equalisation of Coded Modulation Schemes 94
RBF networks
schematic 89
RBF-DFE 90
RBF-TEQ 88
RCPC 36, 37
redundant phasors 7
RSC 3, 13, 48, 168

S

SbS 127
selection
fitness-proportionate
probability 143
SER 16, 19
set partitioning 16–17
SISO 42, 92
SNR 6, 123, 124
SOVA 94
SP 2, 6
STBC ..... ii, 4, 153
STBC-DoS-RR 163
STBC-IQ 154
STC 163
STS 163
STTC 153
symbol-based MAP
problem description 17–19
symbol-based MAP algorithm 17–28
Symbol-based MAP Algorithm Description 20–26
Symbol-based MAP algorithm summary 26

T

TC 163
TCM 2, 6, 7
TCM code design for fading channels ... 14–16
TCM principle 8–13
TDD 77, 127
TDMA 77
TEQ ..... ii, 71
trellis diagrams 7
trellis-coded modulation 7–17
TTCM 3, 6, 17, 28
TTCM decoder 30–33
TTCM encoder 28–30
TU 76, 77
TuCM 2, 176
Turbo Trellis-Coded Modulation 28–33

U

UMTS 126
UTRA 126

V

VA 16
Viterbi algorithm 13

W

WMF 116

Z

ZFE 73

Author Index

A

Abedi [130] 115, 138
Abend [54] 28
Al-Semari [169] 154
Alamouti [101] 79
Alamouti [164] 153–155, 163, 164, 167, 168
Alard [68] 60
Alexander [176] 192
Anderson [137] 122–125
Anderson [160] 146
Asenstorfer [176] 192
Aulin [163] 146

B

Bahl [50] 17, 18, 20, 28, 48, 92
Baier [132] 116, 118, 119, 128
Balaban [166] 153
Banerjee [13] 2, 3
Bauch [106] 88, 94
Benedetto [62] 42, 44
Berlekamp [43] 13
Berlekamp [2] 2
Berrou [11] 2, 6, 32, 163, 164, 168
Berrou [73] 64, 91, 92, 94, 192
Berrou [115] 92
Berrou [16] 2, 3, 176
Biglieri [10] 2, 34, 82
Blahut [42] 13
Blanz [124] 115, 116, 120, 121
Breiling [116] 92

C

Caire [10] 2, 34, 82
Calderbank [100] 79
Calderbank [165] 153, 155, 163, 168, 169
Cavers [46] 15, 29, 34, 79
Chang [64] 60
Chen [41] 7
Chen [77] 71, 88
Chen [119] 94
Chen [108] 88
Chen [110] 89, 95
Chen [175] 167
Cherriman [148] 127, 129–131
Cherriman [23] 4
Cherriman [24] 4
Cheung [81] 74, 75, 78
Chng [120] 94
Choi [98] 78, 129
Choi [150] 128, 129, 135
Chua [85] 76
Chua [90] 76
Chung [29] 5
Cimini [66] 60
Cocke [50] 17, 18, 20, 28, 48, 92
Costello [13] 2, 3
Cowan [107] 88
Cowan [108] 88

D

Deng [56] 28
Didier [73] 64, 91, 92, 94, 192
Divsalar [37] 6, 14–16, 29, 79, 154
Divsalar [7] 2, 6
Divsalar [62] 42, 44
Douillard [73] 64, 91, 92, 94, 192
Duel-Hallen [99] 78, 127, 129

E

Elias [4] 2
Eshelman [156] 141
ETSI [152] 129–131

F

Falahati [94] 76
Fischer [71] 63

Flannery [136] 121
Flannery [151] 129
Foerster [126] 115
Forney [49] 16
Fritchman [54] 28
Fuja [169] 154
Fuja [13] 2, 3

G

Gersho [41] 7
Gertsman [113] 91
Gibson [107] 88
Gibson [108] 88
Glavieux [11] 2, 6, 32, 163, 164, 168
Glavieux [117] 94, 103, 105
Glavieux [73] 64, 91, 92, 94, 192
Glavieux [115] 92
Glavieux [16] 2, 3, 176
Goeckel [92] 76
Goff [16] 2, 3, 176
Golay [3] 2
Goldberg [127] 115, 138, 141, 143
Goldsmith [85] 76
Goldsmith [90] 76
Golub [135] 119, 128
Grant [110] 89, 95
Göckel [91] 76, 129

H

Höher [53] .. 25, 26, 32, 48, 91, 92, 96, 144, 168
Hagenauer [106] 88, 94
Hagenauer [60] 36, 37
Hallen [99] 78, 127, 129
Hamming [2] 2
Hamorsky [116] 92
Hanzo [95] 76
Hanzo [15] 2, 14, 15, 43, 65, 72, 189
Hanzo [148] 127, 129–131
Hanzo [86] 76, 78
Hanzo [98] 78, 129
Hanzo [150] 128, 129, 135
Hanzo [103] 88, 89, 91, 94, 96, 97, 100, 101, 108, 109, 112, 187
Hanzo [123] 101
Hanzo [84] 76
Hanzo [83] 76
Hanzo [149] 128, 129
Hanzo [172] 163
Hanzo [70] 63, 80
Hanzo [121] 96
Hanzo [23] 4
Hanzo [24] 4
Hanzo [22] 4, 6
Hanzo [20] 4, 6, 125, 133
Hanzo [29] 5
Hanzo [28] 5
Hanzo [21] 4, 6
Hanzo [27] 5
Hanzo [25] 5
Hanzo [32] 5
Hanzo [31] 5
Hanzo [30] 5
Hanzo [35] 5
Hanzo [34] 5
Hanzo [33] 5
Hanzo [26] 5
Hanzo [63] . 46, 60–64, 72–75, 78, 116, 127, 163
Hanzo [128] 115, 138, 141, 143
Hanzo [14] . 2, 71, 88, 90–92, 95, 141, 153, 154, 158, 159, 163
Hanzo [116] 92
Hanzo [144] 127
Hanzo [105] 88, 108, 112
Hanzo [74] 64
Hanzo [125] 115
Hanzo [118] 94, 96, 108
Hanzo [102] 88
Hanzo [129] 115, 138
Hara [177] 193
Hashimoto [161] 146
Hayashi [139] 127
Hayashi [138] 127
Haykin [111] 89
Ho [46] 15, 29, 34, 79
Homma [139] 127
Homma [138] 127
Hu [99] 78, 127, 129

J

Jézéquel [73] 64, 91, 92, 94, 192
Jafarkhani [165] 153, 155, 163, 168, 169
Jelicic [170] 154
Jelinek [50] 17, 18, 20, 28, 48, 92
Jeong [140] 127
Jong [159] 143
Jr. [174] 167
Jr. [59] 34–37, 49
Jung [124] 115, 116, 120, 121
Juntti [157] 143

K

Kaleh [132] 116, 118, 119, 128
Kalet [69] 60
Kallel [101] 79
Kamio [87] 76
Kato [139] 127
Kato [138] 127
Kazi [146] 127
Keller [63] . 46, 60–64, 72–75, 78, 116, 127, 163
Khorram [106] 88, 94
Kirsch [65] 60
Kitade [139] 127
Kitade [138] 127
Klang [171] 163
Klein [137] 122–125
Klein [97] 77, 97
Klein [132] 116, 118, 119, 128
Knickenberg [116] 92
Komaki [82] 76
Kuan [28] 5
Kuan [125] 115

L

Labat [117] 94, 103, 105
Lafanechére [56] 28
Lampe [71] 63
Laot [117] 94, 103, 105
Lassalle [68] 60
Lau [141] 127, 129
Lau [142] 127
Lau [93] 76
Lau [147] 127
Lau [89] 76
Lau [88] 76
Lee [173] 165
Lee [134] 119
Lee [145] 127
Lee [61] 36, 37, 48, 49
Lee [21] 4, 6
Lei [147] 127
Li [39] 6, 40, 43
Li [40] 6, 42
Li [19] 3, 7, 44, 47
Li [18] 3, 6, 40, 41, 47, 50, 133
Liew [95] 76
Liew [121] 96
Liew [20] 4, 6, 125, 133
Liew [14] ... 2, 71, 88, 90–92, 95, 141, 153, 154, 158, 159, 163
Liew [74] 64
Liew [102] 88
Lilleberg [157] 143
Lim [163] 146
Lin [59] 34–37, 49
Liu [92] 76
Loan [135] 119, 128
Lodge [113] 91
Lucke [146] 127

M

Münster [98] 78, 129
Macleod [142] 127
Macleod [89] 76
Macleod [88] 76
Mar [175] 167
Maric [141] 127, 129
Matsuoka [87] 76
McLaughlin [77] 71, 88
McLaughlin [119] 94
Messerschmitt [134] 119
Miller [173] 165
Milstein [126] 115
Mitchell [155] 141, 143
Mix [80] 74, 118
Miya [139] 127
Miya [138] 127

Mohan [160] 146
Montorsi [62] 42, 44
Morinaga [82] 76
Morinaga [143] 127
Morinaga [87] 76
Moshavi [154] 138
Mueller-Roemer [67] 60
Mulgrew [77] 71, 88
Mulgrew [119] 94
Mulgrew [110] 89, 95
Mulgrew [112] 91, 94
Muller-Weinfurtner [71] 63

N

Naguib [100] 79
Naguib [171] 163
Nakagawa [140] 127
Ng [23] 4
Ng [24] 4
Ng [22] 4, 6
Ng [20] 4, 6, 125, 133
Ng [29] 5
Ng [28] 5
Ng [21] 4, 6
Ng [27] 5
Ng [25] 5
Ng [32] 5
Ng [31] 5
Ng [30] 5
Ng [35] 5
Ng [34] 5
Ng [33] 5
Ng [26] 5

O

Ojanperä [137] 122–125
Ormeci [92] 76
Otsuki [143] 127

P

P. C. Massey [13] 2, 3
Patra [112] 91, 94
Perez [44] 14
Piazzo [55] 28
Piazzo [51] 20
Piazzo [70] 63, 80
Piazzo [21] 4, 6
Picart [73] 64, 91, 92, 94, 192
Pietrobon [56] 28
Pietrobon [44] 14
Pirhonen [97] 77, 97
Pollara [62] 42, 44
Prasad [177] 193
Press [136] 121
Press [151] 129
Price [174] 167
Proakis [122] 97
Proakis [78] 73, 74
Proakis [52] 21, 43

R

Raphaeli [114] 92
Rasmussen [163] 146
Raviv [50] 17, 18, 20, 28, 48, 92
Reed [176] 192
Ritcey [39] 6, 40, 43
Ritcey [40] 6, 42
Ritcey [19] 3, 7, 44, 47
Ritcey [18] 3, 6, 40, 41, 47, 50, 133
Robertson [38] . 6, 16, 17, 29–31, 47, 48, 52, 53, 80
Robertson [53] .. 25, 26, 32, 48, 91, 92, 96, 144, 168
Robertson [58] 29
Robertson [17] 3
Roy [170] 154

S

Salz [166] 153
Sampei [82] 76
Sampei [143] 127
Sampei [87] 76
Schaffer [156] 141
Schlösser [157] 143
Schlegel [45] 14
Schlegel [176] 192
Schlegel [8] 2
Seshdri [100] 79

Shannon [1] 2
Simmons [162] 146
Simon [37] 6, 14–16, 29, 79, 154
Simon [7] 2, 6
Siu [107] 88
Skarbek [120] 94
Skoeld [97] 77, 97
Spears [159] 143
Steele [4] 2
Steele [15] 2, 14, 15, 43, 65, 72, 189
Steele [76] 71, 76
Streit [148] 127, 129–131
Suoranta [97] 77, 97
Syswerda [158] 143

T

Tafazolli [130] 115, 138
Taricco [10] 2, 34, 82
Tarokh [165] 153, 155, 163, 168, 169
Teukolsky [136] 121
Teukolsky [151] 129
Thitimajshima [11] 2, 6, 32, 163, 164, 168
Tidestav [178] 193
Torrance [84] 76
Torrance [83] 76
Torrance [149] 128, 129
Torrance [144] 127
Trees [109] 88, 89
Tsai [145] 127

U

Ue [138] 127
Ungerböck [6] 2, 7–10, 14
Ungerböck [36] 6, 8, 13, 14, 17, 47, 48

V

Verdú [131] 115, 116, 138, 139
Verdú [153] 138
Vetterling [136] 121
Vetterling [151] 129
Villebrun [53] . . . 25, 26, 32, 48, 91, 92, 96, 144, 168
Viterbi [5] 2

W

Wörz [17] 3
Watanabe [139] 127
Webb [76] 71, 76
Webb [63] . . 46, 60–64, 72–75, 78, 116, 127, 163
Wei [57] 28
Wesel [92] 76
Whalen [133] 119
Wittneben [167] 153
Wong [4] 2
Wong [95] 76
Wong [79] 73, 75
Wong [86] 76, 78
Wong [103] 88, 89, 91, 94, 96, 97, 100, 101, 108, 109, 112, 187
Wong [123] 101
Wong [22] 4, 6
Wong [125] 115
Wörz [38] . . . 6, 16, 17, 29–31, 47, 48, 52, 53, 80

Y

Yang [98] 78, 129
Yang [172] 163
Yang [20] 4, 6, 125, 133
Yang [35] 5
Yang [120] 94
Yeap [123] 101
Yeap [14] . . . 2, 71, 88, 90–92, 95, 141, 153, 154, 158, 159, 163
Yeap [116] 92
Yeap [105] 88, 108, 112
Yeap [74] 64
Yee [103] . 88, 89, 91, 94, 96, 97, 100, 101, 108, 109, 112, 187
Yee [121] 96
Yee [27] 5
Yee [25] 5
Yee [26] 5
Yee [105] 88, 108, 112
Yee [118] 94, 96, 108
Yee [102] 88
Yen [32] 5
Yen [31] 5
Yen [30] 5

Yen [128] 115, 138, 141, 143
Yen [129] 115, 138

Z

Zarai [114] 92
Zehavi [9] 2, 6, 33–35, 47, 82
Zimmermann [65] 60